

LITHIUM-RICH TRANSITION METAL OXIDES AS POSITIVE ELECTRODE
MATERIALS IN LITHIUM-ION BATTERIES

by

Andrew van Bommel

Submitted in partial fulfilment of the requirements
for the degree of Doctor of Philosophy

at

Dalhousie University
Halifax, Nova Scotia
November 2010

© Copyright by Andrew van Bommel, 2010

DALHOUSIE UNIVERSITY
DEPARTMENT OF CHEMISTRY

The undersigned hereby certify that they have read and recommend to the Faculty of Graduate Studies for acceptance a thesis entitled “LITHIUM-RICH TRANSITION METAL OXIDES AS POSITIVE ELECTRODE MATERIALS IN LITHIUM-ION BATTERIES” by Andrew van Bommel in partial fulfillment of the requirements for the degree of Doctor of Philosophy.

Dated: November 2, 2010

External Examiner: _____

Research Supervisor: _____

Examining Committee: _____

Departmental Representative: _____

DALHOUSIE UNIVERSITY

DATE: November 2, 2010

AUTHOR: Andrew van Bommel

TITLE: LITHIUM-RICH TRANSITION METAL OXIDES AS POSITIVE
ELECTRODE MATERIALS IN LITHIUM-ION BATTERIES

DEPARTMENT OR SCHOOL: Department of Chemistry

DEGREE: PhD CONVOCATION: May YEAR: 2011

Permission is herewith granted to Dalhousie University to circulate and to have copied for non-commercial purposes, at its discretion, the above title upon the request of individuals or institutions.

Signature of Author

The author reserves other publication rights, and neither the thesis nor extensive extracts from it may be printed or otherwise reproduced without the author's written permission.

The author attests that permission has been obtained for the use of any copyrighted material appearing in the thesis (other than the brief excerpts requiring only proper acknowledgement in scholarly writing), and that all such use is clearly acknowledged.

To Cait, James, Emmy.

Table of Contents

List of Tables	ix
List of Figures	x
Abstract	xiv
List of Symbols and Abbreviations Used	xv
Acknowledgements	xix
CHAPTER 1. Introduction.....	1
1.1. Lithium-ion Batteries	1
1.2. Positive Electrode Materials for Lithium-ion Batteries	3
1.3. LiCoO_2	10
1.4. LiNiO_2	12
1.5. LiMnO_2	13
1.6. LiFeO_2 , LiVO_2 , LiTiO_2 , and LiCrO_2	14
1.7. $\text{Li}[\text{Li}_{1/3}\text{Mn}_{2/3}]\text{O}_2$	15
1.8. Rules for Layered Oxides	18
1.9. Solid Solutions of Transition Metal Oxide Positive Electrode Materials.....	19
1.10. Lithium-Rich Transition Metal Oxides as Positive Electrode Materials for Lithium-ion Batteries	21
1.11. Solid Solution and Nanocomposite Models of the Lithium-Rich Oxides	30
1.12. Obstacles Surrounding the use of Lithium-rich Transition Metal Oxides.....	31
1.13. Synthesis of Dense and Spherical Transition Metal Oxides.....	34
1.14. Effect of Ammonia on Particle Growth	39
1.15. Scope of Thesis	40
CHAPTER 2. Experimental.....	41
2.1. X-ray Diffraction	41

2.1.1. Crystal Lattice.....	41
2.1.2. Bragg's Law.....	43
2.1.3. Geometrical Structure Factor.....	44
2.1.4. Bragg-Brentano Diffractometer.....	45
2.1.5. Rietica Refinement using Rietica.....	47
2.2. Electrochemical Cell Testing.....	48
2.3. Scanning Electron Microscopy.....	50
2.4. Thermogravimetric Analysis.....	52
2.5. Continuous-Stirred Tank Reactor.....	53
2.5.1. Typical CSTR Reaction.....	55
2.6. Tap-Density Measurements.....	56
2.7. Isothermal Microcalorimetry.....	57
2.8. Size-Distribution Analysis.....	59
CHAPTER 3. Investigation of $\text{Ni}_{1/3}\text{Mn}_{1/3}\text{Co}_{1/3}(\text{OH})_2$	60
3.1. Experimental.....	62
3.2. Results and Discussion.....	62
3.3. Summary.....	70
CHAPTER 4. Analysis of the Growth Mechanism of Coprecipitated Spherical and Dense Nickel, Manganese, and Cobalt Containing Hydroxides in the Presence of Aqueous Ammonia.....	72
4.1. Introduction.....	72
4.2. Experimental.....	73
4.3. Results and Discussion.....	73
CHAPTER 5. Determination of the Apparent Oxygen Diffusion Coefficients from Lithium-Rich Transition Metal Oxides $\text{Li}[\text{Li}_{1/9}\text{Ni}_{1/3}\text{Mn}_{5/9}]\text{O}_2$ and $\text{Li}[\text{Li}_{1/5}\text{Ni}_{1/5}\text{Mn}_{3/5}]\text{O}_2$ by the Atlung Method.....	87

5.1. The Diffusion Process During the Charge of Positive Electrode Materials in Lithium-ion Batteries	87
5.2. Oxygen Diffusion Through $\text{Li}[\text{Li}_{1/9}\text{Ni}_{1/3}\text{Mn}_{5/9}]\text{O}_2$ and $\text{Li}[\text{Li}_{1/5}\text{Ni}_{1/5}\text{Mn}_{3/5}]\text{O}_2$	93
5.3. Cycling of $\text{Li}[\text{Li}_{1/9}\text{Ni}_{1/3}\text{Mn}_{5/9}]\text{O}_2$	115
5.4. Summary	117
CHAPTER 6. Isothermal Microcalorimetry of $\text{Li}[\text{Li}_{1/5}\text{Ni}_{1/5}\text{Mn}_{3/5}]\text{O}_2$ and $\text{Li}[\text{Li}_{1/9}\text{Ni}_{1/3}\text{Mn}_{5/9}]\text{O}_2$	118
6.1. Stoichiometry Changes in Lithium-Rich Transition Metal Oxides During Charge and Discharge	118
6.2. Jahn-Teller Distortion in the MnO_6 Units in Lithium-rich Transition Metal Oxides	122
6.3. Meaning of the Heat Flow in Isothermal Battery Calorimetry	123
6.4. IMC Data of a $\text{Li}/\text{Li}[\text{Li}_{1/5}\text{Ni}_{1/5}\text{Mn}_{3/5}]\text{O}_2$ Cell Cycled Between 2.5 and 4.4 V	126
6.5. Model for the Configurational Entropy During Cycling of a $\text{Li}/\text{Li}[\text{Li}_{1/5}\text{Ni}_{1/5}\text{Mn}_{3/5}]\text{O}_2$ Cell Between 2.5 and 4.4 V	128
6.6. IMC data of $\text{Li}/\text{Li}[\text{Li}_{1/5}\text{Ni}_{1/5}\text{Mn}_{3/5}]\text{O}_2$ and $\text{Li}/\text{Li}[\text{Li}_{1/9}\text{Ni}_{1/3}\text{Mn}_{5/9}]\text{O}_2$ Cells	132
6.7. Summary	137
CHAPTER 7. Other Studies of Lithium-rich Oxide Materials	138
7.1. Stepwise Traverse of the Oxygen-Release Plateau	138
7.2. Irreversible Capacity During the Stepwise Traverse of the Oxygen-Release Plateau	142
7.3. High-Precision Charger Experiments on $\text{Li}/\text{Li}[\text{Li}_{1/9}\text{Ni}_{1/3}\text{Mn}_{5/9}]\text{O}_2$ and $\text{Li}/\text{Li}[\text{Li}_{1/5}\text{Ni}_{1/5}\text{Mn}_{3/5}]\text{O}_2$ Cells	144
CHAPTER 8. Conclusions	148
8.1. Synthesis of Spherical and Dense Hydroxide Precursors for Lithium Transition Metal Oxides	148
8.2. Studies on the Lithium-Rich Transition Metal Oxides	151
8.3. Suggested Future Studies on the Hydroxide Coprecipitation Reaction	155
8.4. Suggested Future Studies on the Lithium-Rich Transition Metal Oxides	155

References.....	159
Appendix.....	169
Copyright Information	169

List of Tables

Table 1.1. Advantages and disadvantages of lithium-ion battery positive electrodes.....	5
Table 1.2. Delmas notation for A_xMO_2 structures.....	9
Table 1.3. Techniques to improve the irreversible capacity and the rate-capability issues of lithium-rich TM oxides.....	33
Table 3.1. Lattice constants of hydroxides and oxyhydroxides.....	66
Table 4.1. The hexagonal lattice constants and z-position of the oxygen atom calculated for $Ni(OH)_2$, $Ni_{1/2}Mn_{1/2}(OH)_2$, and $Ni_{1/3}Mn_{1/3}Co_{1/3}(OH)_2$	75
Table 4.2. Equilibria and mass balances solved to determine the concentration of species present in the coprecipitation reaction at various pH-values.	82
Table 5.2. Errors in capacity measured during the charge of lithium-rich transition metal oxides.....	110
Table 5.3. Capacities in the oxygen-loss region and fractional capacities of $Li[Li_{1/9}Ni_{1/3}Mn_{5/9}]O_2$ with different particle sizes, charge rates, and temperatures.	110
Table 5.4. Capacities in the oxygen-loss region and fractional capacities of $Li[Li_{1/5}Ni_{1/5}Mn_{3/5}]O_2$ with different particle sizes, charge rates, and temperatures.	111
Table 6.1. Stoichiometry changes in $Li[Li_{1/5}Ni_{1/5}Mn_{3/5}]O_2$ during cycling, with the associated capacities shown.....	121

List of Figures

Figure 1.1. Schematic of a lithium-ion battery.	2
Figure 1.2. The structures of layered, spinel, and olivine positive electrode materials.	4
Figure 1.3. Structure of layered LiTiS_2	7
Figure 1.4. Discharge curves of $\text{Li}/\text{Li}_x\text{TiS}_2$ cells.	8
Figure 1.5. Structures with Delmas notations O3, T1, and P3.	10
Figure 1.6. Charge and discharge profiles of LiCoO_2	11
Figure 1.7. Charge and discharge curves of LiNiO_2	12
Figure 1.8. Charge curve of LiMnO_2	13
Figure 1.9. Charge and discharge profiles of LiFeO_2	14
Figure 1.10. Layered structure of $\text{Li}[\text{Li}_{1/3}\text{Mn}_{2/3}]\text{O}_2$	16
Figure 1.11. XRD patterns of Li_2MnO_3	16
Figure 1.12. Transition metal layer of $\text{Li}[\text{Li}_{1/3}\text{Mn}_{2/3}]\text{O}_2$	17
Figure 1.13. The charge and discharge curves for nanocrystalline $\text{Li}[\text{Li}_{1/3}\text{Mn}_{2/3}]\text{O}_2$	18
Figure 1.14. Composition triangle containing the lithium-rich transition metal oxides. ...	22
Figure 1.15. XRD patterns of $\text{Li}[\text{Ni}_x\text{Li}_{(1/3-2x/3)}\text{Mn}_{(2/3-x/3)}]\text{O}_2$	23
Figure 1.17. Charge and discharge curves for $\text{Li}[\text{Ni}_{5/12}\text{Li}_{1/18}\text{Mn}_{19/36}]\text{O}_2$	24
Figure 1.18. Charge and discharge curves for $\text{Li}/\text{Li}[\text{Ni}_x\text{Li}_{(1/3-2x/3)}\text{Mn}_{(2/3-x/3)}]\text{O}_2$	25
Figure 2.1. The unit cell parameters.	41
Figure 2.2. The (003) family of planes in $\text{Li}[\text{Ni}_{1/3}\text{Mn}_{1/3}\text{Co}_{1/3}]\text{O}_2$	42
Figure 2.3. Schematic of X-ray scattering in $\text{Li}[\text{Ni}_{1/3}\text{Mn}_{1/3}\text{Co}_{1/3}]\text{O}_2$	43
Figure 2.4. Schematic of the Bragg-Brentano diffractometer.	46
Figure 2.5. Picture of a Siemens D5000 diffractometer.	46
Figure 2.6. Exploded view of the electrochemical cell used for lithium battery testing. .	49

Figure 2.7. Schematic drawing of a scanning electron microscope (SEM).....	50
Figure 2.8. Picture of a Hitachi S4700 field-emission scanning electron microscope.	51
Figure 2.9. Top-view schematic of a dual-beam TGA instrument.	52
Figure 2.10. Picture of a TA Instruments SDT Q600.	53
Figure 2.11. Picture of the continuous-stirred tank reactor (CSTR).....	54
Figure 2.12. Schematic drawing of the continuous-stirred tank reactor (CSTR).	55
Figure 2.13. Picture of a VanKel tap density measuring device.....	57
Figure 2.14. Block diagram of the Calorimetry Sciences Corp. (CSC) 4400 isothermal microcalorimeter.	58
Figure 2.15. Schematic of the Microtrac standard range particle size analyzer.	59
Figure 3.1. XRD patterns of $\text{Ni}_{1/3}\text{Mn}_{1/3}\text{Co}_{1/3}(\text{OH})_2$	61
Figure 3.2. Rietveld refinement of the pure phase $\text{Ni}_{1/3}\text{Mn}_{1/3}\text{Co}_{1/3}(\text{OH})_2$	63
Figure 3.3. Structure of $\text{Ni}_{1/3}\text{Mn}_{1/3}\text{Co}_{1/3}(\text{OH})_2$	64
Figure 3.4. X-ray diffraction patterns during the heating of $\text{Ni}_{1/3}\text{Mn}_{1/3}\text{Co}_{1/3}(\text{OH})_2$	65
Figure 3.5. Thermogravimetric analysis in air of as-prepared $\text{Ni}_{1/3}\text{Mn}_{1/3}\text{Co}_{1/3}(\text{OH})_2$	67
Figure 3.6. XRD patterns of $\text{Ni}_{1/3}\text{Mn}_{1/3}\text{Co}_{1/3}(\text{OH})_2$ in this work and from commercial precursor material.	68
Figure 3.7. SEM images of the as-prepared $\text{Ni}_{1/3}\text{Mn}_{1/3}\text{Co}_{1/3}(\text{OH})_2$ particles at several magnifications.....	69
Figure 3.8. SEM images of the surface of the $\text{Ni}_{1/3}\text{Mn}_{1/3}\text{Co}_{1/3}(\text{OH})$ particles.	70
Figure 4.1. XRD patterns of $\text{Ni}(\text{OH})_2$, $\text{Ni}_{1/2}\text{Mn}_{1/2}(\text{OH})_2$, and $\text{Ni}_{1/3}\text{Mn}_{1/3}\text{Co}_{1/3}(\text{OH})_2$	74
Figure 4.2. XRD pattern of $\text{Ni}(\text{OH})_2$ with indicated Miller indices, showing selective broadening.....	76
Figure 4.3. Tap density of $\text{Ni}(\text{OH})_2$ as a function of reaction time.	77
Figure 4.4. SEM images of $\text{Ni}(\text{OH})_2$ a function of reaction time.	78
Figure 4.5. Dependence of tap density on reaction pH for various hydroxides.....	79
Figure 4.6. SEM images of $\text{Ni}(\text{OH})_2$ as different reaction pH-values.	80

Figure 4.7. Effect of pH on the concentration of relevant species in the nickel hydroxide coprecipitation reaction.	83
Figure 4.8. Effect of pH on the concentration of $[\text{Ni}(\text{NH}_3)_n]^{2+}$, $[\text{Mn}(\text{NH}_3)_n]^{2+}$, and $[\text{Co}(\text{NH}_3)_n]^{2+}$	84
Figure 5.1. Schematic of the diffusion process through a spherical positive and negative electrode during the charge process, with a higher charge rate for the bottom panel.	88
Figure 5.2. Characteristic Atlung graph for a material with a spherical geometry.	93
Figure 5.3. XRD patterns of $\text{Ni}_{3/8}\text{Mn}_{5/8}(\text{OH})_2$	95
Figure 5.4. XRD pattern of $\text{Ni}_{1/4}\text{Mn}_{3/4}(\text{OH})_2$	96
Figure 5.5. SEM images of $\text{Ni}_{3/8}\text{Mn}_{5/8}(\text{OH})_2$	97
Figure 5.6. XRD patterns of $\text{Li}[\text{Li}_{1/9}\text{Ni}_{1/3}\text{Mn}_{5/9}]\text{O}_2$	99
Figure 5.7. XRD patterns of $\text{Li}[\text{Li}_{1/5}\text{Ni}_{1/5}\text{Mn}_{3/5}]\text{O}_2$	99
Figure 5.8. Dependence of hexagonal lattice constants, a and c , on x in $\text{Li}[\text{Ni}_x\text{Li}_{(1/3-2x/3)}\text{Mn}_{(2/3-x/3)}]\text{O}_2$	100
Figure 5.9. Particle size distributions of $\text{Li}[\text{Li}_{1/9}\text{Ni}_{1/3}\text{Mn}_{5/9}]\text{O}_2$	101
Figure 5.10. SEM images of $\text{Li}[\text{Li}_{1/9}\text{Ni}_{1/3}\text{Mn}_{5/9}]\text{O}_2$	102
Figure 5.11. Particle size distributions of $\text{Li}[\text{Li}_{1/5}\text{Ni}_{1/5}\text{Mn}_{3/5}]\text{O}_2$	103
Figure 5.12. SEM images of $\text{Li}[\text{Li}_{1/5}\text{Ni}_{1/5}\text{Mn}_{3/5}]\text{O}_2$	104
Figure 5.13. Potential versus specific capacity during first charge of $\text{Li}/\text{Li}[\text{Li}_{1/9}\text{Ni}_{1/3}\text{Mn}_{5/9}]\text{O}_2$ cells.	105
Figure 5.14. dQ/dV versus voltage graphs during the first charge of $\text{Li}/\text{Li}[\text{Li}_{1/9}\text{Ni}_{1/3}\text{Mn}_{5/9}]\text{O}_2$ cells.	106
Figure 5.15. Potential versus specific capacity during the first charge of $\text{Li}/\text{Li}[\text{Li}_{1/5}\text{Ni}_{1/5}\text{Mn}_{3/5}]\text{O}_2$ cells.	107
Figure 5.16. dQ/dV versus voltage graphs during the first charge of $\text{Li}/\text{Li}[\text{Li}_{1/5}\text{Ni}_{1/5}\text{Mn}_{3/5}]\text{O}_2$ cells.	108
Figure 5.17. Atlung graphs used to determine the apparent diffusion coefficient of oxygen during the charge process in $\text{Li}[\text{Li}_{1/9}\text{Ni}_{1/3}\text{Mn}_{5/9}]\text{O}_2$ at 30°C and 55°C	113

Figure 5.18. Atlung graphs used to determine the apparent diffusion coefficient of oxygen during the charge process in $\text{Li}[\text{Li}_{1/5}\text{Ni}_{1/5}\text{Mn}_{3/5}]\text{O}_2$ at 30°C and 55°C.....	113
Figure 5.19. Cycling characteristics of 5.3, 6.9, and 7.6 μm $\text{Li}[\text{Li}_{1/9}\text{Ni}_{1/3}\text{Mn}_{5/9}]\text{O}_2$ at 55°C and at C/10 rate.....	116
Figure 6.1. Gibbs triangle of the Li-M-O system showing the stoichiometries of interest.....	118
Figure 6.2. Charge and discharge profile of a $\text{Li}/\text{Li}[\text{Li}_{1/5}\text{Ni}_{1/5}\text{Mn}_{3/5}]\text{O}_2$ cell.	122
Figure 6.3. Schematic of the possible crystal field splitting of the t_{2g} and e_g orbitals.	123
Figure 6.4. IMC data for a $\text{Li}/\text{Li}[\text{Li}_{1/5}\text{Ni}_{1/5}\text{Mn}_{3/5}]\text{O}_2$ cell cycled between 2.5 and 4.4 V.....	127
Figure 6.5. The second charge and discharge profiles of a $\text{Li}/\text{Li}[\text{Li}_{1/5}\text{Ni}_{1/5}\text{Mn}_{3/5}]\text{O}_2$ cell.....	131
Figure 6.6. IMC data for a $\text{Li}/\text{Li}[\text{Li}_{1/5}\text{Ni}_{1/5}\text{Mn}_{3/5}]\text{O}_2$ cell charged first to 4.8 V, with subsequent cycles between 2.5 and 4.6 V at a rate of C/40.	133
Figure 6.7. IMC data for a $\text{Li}/\text{Li}[\text{Li}_{1/5}\text{Ni}_{1/5}\text{Mn}_{3/5}]\text{O}_2$ cell charged first to 4.8 V, with subsequent cycles between 2.5 and 4.6 V at a rate of C/20.	134
Figure 6.8. IMC data for a $\text{Li}/\text{Li}[\text{Li}_{1/9}\text{Ni}_{1/3}\text{Mn}_{5/9}]\text{O}_2$ cell charged first to 4.8 V, with subsequent cycles between 2.5 and 4.6 V.....	136
Figure 7.1 Stepped cycling of $\text{Li}/\text{Li}[\text{Li}_{1/5}\text{Ni}_{1/5}\text{Mn}_{3/5}]\text{O}_2$ cells.	139
Figure 7.2. Differential capacity curves for each cycle associated with the cycling in the E panel of Figure 7.1.....	141
Figure 7.3. Stepwise traverse of the oxygen-release plateau in $\text{Li}/\text{Li}[\text{Li}_{1/5}\text{Ni}_{1/5}\text{Mn}_{3/5}]\text{O}_2$ cells.....	143
Figure 7.4. Cycling capacity versus cycle number of a $\text{Li}/\text{Li}[\text{Li}_{1/9}\text{Ni}_{1/3}\text{Mn}_{5/9}]\text{O}_2$ cell....	145
Figure 7.5. Coulombic efficiency versus cycle number of a $\text{Li}/\text{Li}[\text{Li}_{1/9}\text{Ni}_{1/3}\text{Mn}_{5/9}]\text{O}_2$ cell.....	146
Figure 7.6. Cycling capacity versus cycle number of a $\text{Li}/\text{Li}[\text{Li}_{1/9}\text{Ni}_{1/3}\text{Mn}_{5/9}]\text{O}_2$ cell....	147
Figure 7.1. Charge and discharge profile of a $\text{Li}/\text{Li}[\text{Li}_{1/5}\text{Ni}_{1/5}\text{Mn}_{3/5}]\text{O}_2$ cell also shown in Figure 6.2.....	158

Abstract

Lithium-ion batteries are used as power sources in portable devices. A strong candidate for the next generation layered oxide positive electrode material in lithium-ion batteries is the class of lithium-rich oxides. These have much higher first charge and low-rate cycling capacities compared to the non-lithium-rich transition metal oxides. Disadvantages of the lithium-rich system include relatively high irreversible capacity and low rate capability. A better knowledge of the lithium-rich system is needed.

Commercial-quality electrode material must have a high packing density to ensure a high volumetric energy density of the lithium-ion cell. In this thesis, the preparation of spherical and dense transition metal oxide was studied. The precursor to this material, a mixed-metal hydroxide, was made by the coprecipitation reaction in the presence of aqueous ammonia. It was found that the pure hydroxide phase could be made if the hydroxide was prepared with deaerated solutions and by bubbling nitrogen during the reaction. The conversion of the pure hydroxide phase to the oxyhydroxide phase was supported by colour change, XRD, and TGA measurements. The morphology and tap density of the hydroxide was found to be dependent on the reaction pH. This was studied by solving the relevant equilibria present during the reaction as a function of pH. It was found that a lower pH was needed to produce nickel- and manganese-containing hydroxides than for nickel hydroxide since nickel-ammonia coordination complexes form at higher pH. A hydroxide growth dissolution-recrystallization reaction mechanism was suggested.

The electrochemistry of lithium-rich oxides was studied as a function of particle size. It was found that, in the range of parameters studied, the normal lithium deintercalation region was unaffected by charge rate, temperature, or particle size. However, the capacity associated with the oxygen-release plateau was affected by these parameters, with the highest capacity in this region for the slowest charge rate, highest temperature, and smallest particle size. The diffusion in the oxygen release region was studied with the Atlung method and apparent oxygen diffusion coefficients were determined. These were found to be several orders of magnitude lower than diffusion coefficients in the normal lithium deintercalation region.

Isothermal microcalorimetry measurements were used to probe the heat flow change arising from changes in cells containing lithium-rich material. Heat flow changes were observed during the region where Mn^{4+} to Mn^{3+} reduction is expected. It was suggested that this was due to a local Jahn-Teller distortion in the MO_6 units of the lithium-rich structure. It was also suggested that this could lead the relatively poor rate-capability of the lithium-rich oxides.

Other studies of the lithium rich oxides were carried out. It was found that by traversing step-wise across the oxygen-release plateau, with discharge between each voltage step, higher cycling capacities could be obtained. As well, the irreversible capacity was obtained in the initial charging steps, which indicates that lithium is first removed from the transition metal layer during oxygen release. HPC measurements suggest that reactions with the electrolyte occur during cycling, especially at higher temperatures.

List of Symbols and Abbreviations Used

α, β, γ	interior angles
a, b, c	lattice constants
c	concentration
ccp	cubic closed-packed
C	C as in C-rate
CSTR	continuous-stirred tank reactor
d	plane spacing
D	diffusion coefficient
DEC	diethyl carbonate
e	electronic charge
E	energy
EC	ethylene carbonate
F	Faraday constant
F_{hkl}	geometric structure factor
f_o	atomic scattering factor
g	Gibbs free energy
\tilde{g}	partial Gibbs free energy
\tilde{g}_o	partial Gibbs free energy for one atom of Li in lithium metal
h	enthalpy
\tilde{h}	partial entropy
\tilde{h}_o	partial entropy for one atom of Li in lithium metal
(hkl)	Miller index

H	half-width of XRD peaks
I	intensity of a scattered X-ray
I_c	calculated intensity of diffracted X-ray peak
I_o	intensity of the incident X-ray beam
J	flux
j_o	flux density
λ	wavelength
K	equilibrium constant
k_b	Boltzmann's constant
K_{sp}	solubility product
K_w	dissociation constant of water
MW	Molecular weight
N	number of sites
η	overpotential
O	octahedral environment
P	prismatic environment
Q	ratio of stoichiometric charge time to time constant (Chapter 5)
Q	specific capacity
Q	heat (Chapter 6)
\dot{Q}	heat flow
r	distance from the electron to the XRD detector (Chapter 2)
r	radius of a particle (Chapter 5)
r_e	classical radius of an electron

R	least squares residual
s	entropy
\tilde{s}	partial entropy
S	configurational entropy
SEM	scanning electron microscopy
S_m	molar surface area
θ	scattering angle
τ	residence time
τ	fractional capacity (Chapter 5)
t	actual charge time
T	stoichiometric charge time (Chapter 5)
T	temperature
T	trigonal environment (Chapter 1)
TEM	transmission electron microscopy
U, V, W	adjustable XRD peak-fitting parameters (Chapter 2)
V	voltage
V_m	molar volume
W	number of possible configurations
X	number lithium atoms per mole positive electrode material
X^*	X at the electrode surface
X_d	average X before charge
XRD	X-ray diffraction
x,y,z	fractional coordinates of an atom in a unit cell

z_o	oxygen positional parameter
z	x/r for a spherical particle (Chapter 5)

Acknowledgements

I would like to thank so many people for helping me during my time here at Dalhousie University. This includes Gordie Hall for size-distribution analysis help, Juergen Mueller for fixing my glass reaction vessel when I dropped it, Patricia Scallion for scanning-electron microscopy help, Simon Trussler for so much machining and fixing help and letting me jump the queue, Ping Li for sputtering the SEM samples, and Larry Krause for running the IMC experiments.

As well, I want to thank several Dahn lab students. This includes Vincent Chevrier for Maple-solving the solution equilibria, Jing Li for teaching me coin-cell fabrication, Lee Moshurchsk and Hubert Fortier for getting me set-up in the lab, Andrew Todd for electronics help, and Fu Zhou and Xuemei Zhao for help and helpful discussions. I want to thank my friends here at Dal – especially Andrew Ritchie and Vincent Chevrier.

Thanks to NSERC and 3M for funding. I would like to thank Dalhousie University and the Chemistry Department for their support. Especially Giselle Andrews, who helped me on so many occasions. I'd like to thank my committee, Drs. White, Andreas, and Burford for their time and help during my PhD.

I want to thank Jeff Dahn. He is always busy, but I could always steal some time to talk about my project, my future, or just to chin-wag. He has a no hoo-haw approach to research and therefore is so well-revered by the battery community. I would like to thank Jeff for pushing me to be on-task and being the ideal supervisor for my PhD.

My wife, Cait, and kids, James and Emmy, have been so amazing though all of this. Their support is incredible. Cait is working on her PhD, gave birth to two kids, is a wonderful mother to these two kids, yet still finds energy to support me during my work. And James and Emmy are pretty cute and it is pretty amazing to come home to see their smiling faces.

CHAPTER 1. Introduction

1.1. Lithium-ion Batteries

There has been growing interest in using lithium-ion batteries as a power source in portable electronic devices. In a lithium-ion battery, a positive electrode provides the source of lithium ions which are transferred to a negative electrode through a liquid electrolyte. Lithium-ion batteries in use today are typically composed of a layered transition metal oxide as the positive electrode, a non-aqueous electrolyte, and a carbon-based negative electrode.

Figure 1.1 shows a schematic of a typical lithium-ion battery. In this example, graphite serves as the negative electrode and a transition metal oxide (such as LiCoO_2) as the positive electrode. Both materials are lithium insertion or intercalation materials - the combination of two lithium insertion materials, one of more positive potential, results in an electrochemical cell. In this cell, lithium ions are transferred from the positive electrode to the negative electrode* during charge, and from the negative electrode to the positive electrode during discharge. The thermodynamically favorable discharge reaction delivers electrical power via an external circuit. In order for the cell to act in this manner, an ionically-conducting, electrically-insulating electrolyte** is selected and the electrodes are separated by a plastic, permeable separator.¹⁻³

* Negative electrodes for lithium-ion batteries are not the focus of this thesis. Good reviews of negative electrode materials can be found in references 1-2.

** Non-aqueous electrolytes for lithium-ion batteries are not the focus of this thesis. A good electrolyte review can be found in reference 3.

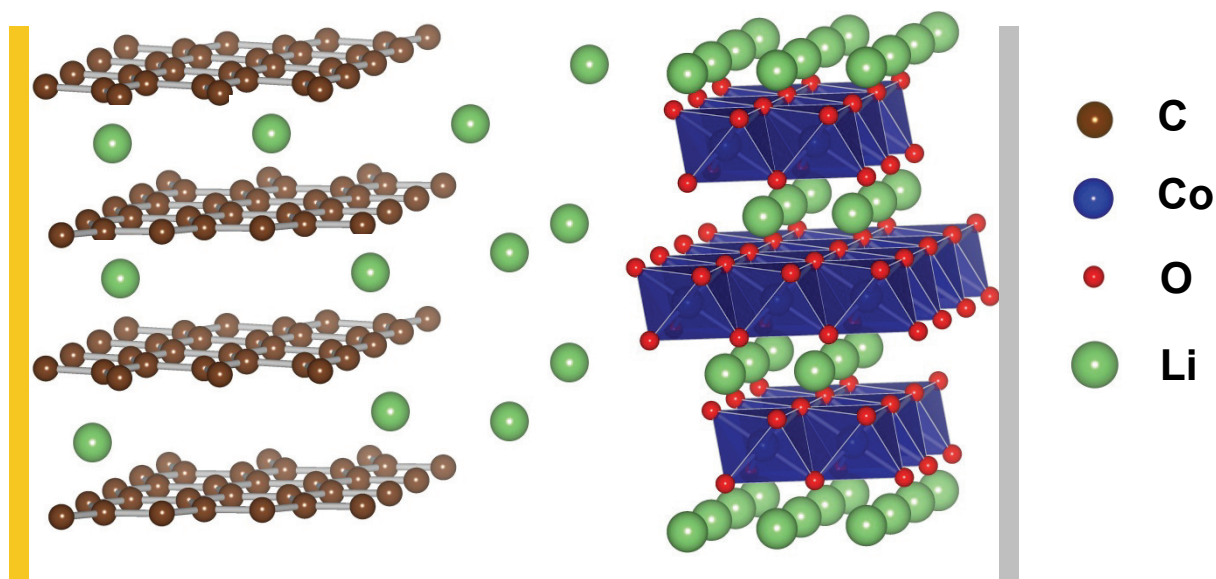


Figure 1.1. Schematic of a lithium-ion battery.

Graphite is the negative electrode (left side of figure) and the layered LiCoO₂ is the positive electrode (right side of figure).

The atoms are as labeled, with the CoO₆ units depicted as octahedra, with the cobalt atoms in the center and the oxygen atoms on the corners of the octahedra. The space in between the electrodes is filled with nonaqueous electrolyte. The oxygen atoms are drawn smaller than scale so that the positions of the lithium atoms are clear.

The role of the electrolyte in a lithium-ion battery is to act as the medium of charge transfer (via ions) between the two electrodes. In lithium-ion batteries, the electrolyte is most commonly a lithium salt dissolved in an aprotic, nonaqueous, organic solvent. Typical solvents used in lithium-ion battery electrolytes include ethylene carbonate (EC) and diethyl carbonate (DEC). Commonly used lithium salts for lithium-ion batteries include lithium hexafluorophosphate (LiPF₆) and lithium perchlorate (LiClO₄). The reactions of the electrolyte with the electrodes may or may not be desired – the formation of a passivation layer on the first cycle is of high importance in the cycling success of lithium-ion batteries.³⁻⁵

The negative electrode material of choice for lithium-ion batteries is often carbon, in the form of graphite. The structure of graphite is a hexagonal array of carbon atoms

forming a layer of the graphite material, and the layers are usually stacked in an ABAB sequence. As lithium ions are intercalated into the layers of graphite, the carbon layers adopt an AA stacking sequence. Alternatives to graphite negative electrodes include alloy-based structures such as lithium-aluminum⁶, lithium-silicon⁷, lithium-tin⁸, and tin-cobalt carbon.^{9,10}

1.2. Positive Electrode Materials for Lithium-ion Batteries

The next sections are devoted to the discussion of the layered materials as positive electrodes for lithium-ion batteries. It is worth noting that there are positive electrode materials other than the layered compounds. For instance, the spinel LiMn_2O_4 was discovered as an intercalation compound by Thackeray *et al.*¹¹ The spinel structure is closely related to the $\alpha\text{-NaFeO}_2$ layered structure, with cubic closed-packed (ccp) oxygen atoms. The difference is in the cations, which are located in various positions in tetrahedral and octahedral sites. Its high voltage lends itself well to high-power applications, such as in hybrid electric vehicles and its main advantages are lower cost and better safety than lithium cobalt oxide.¹²

As well, investigations have been carried out on the phosphates of iron and vanadium.¹² Iron phosphate has attracted particular attention. The electrochemical properties of LiFePO_4 were first studied by Padhi *et al.* and this material is currently involved in commercial applications due to its low cost and environmental safety.¹³

Figure 1.2 shows some common structures of lithium-ion battery positive electrode materials – layered, spinel, and olivine.

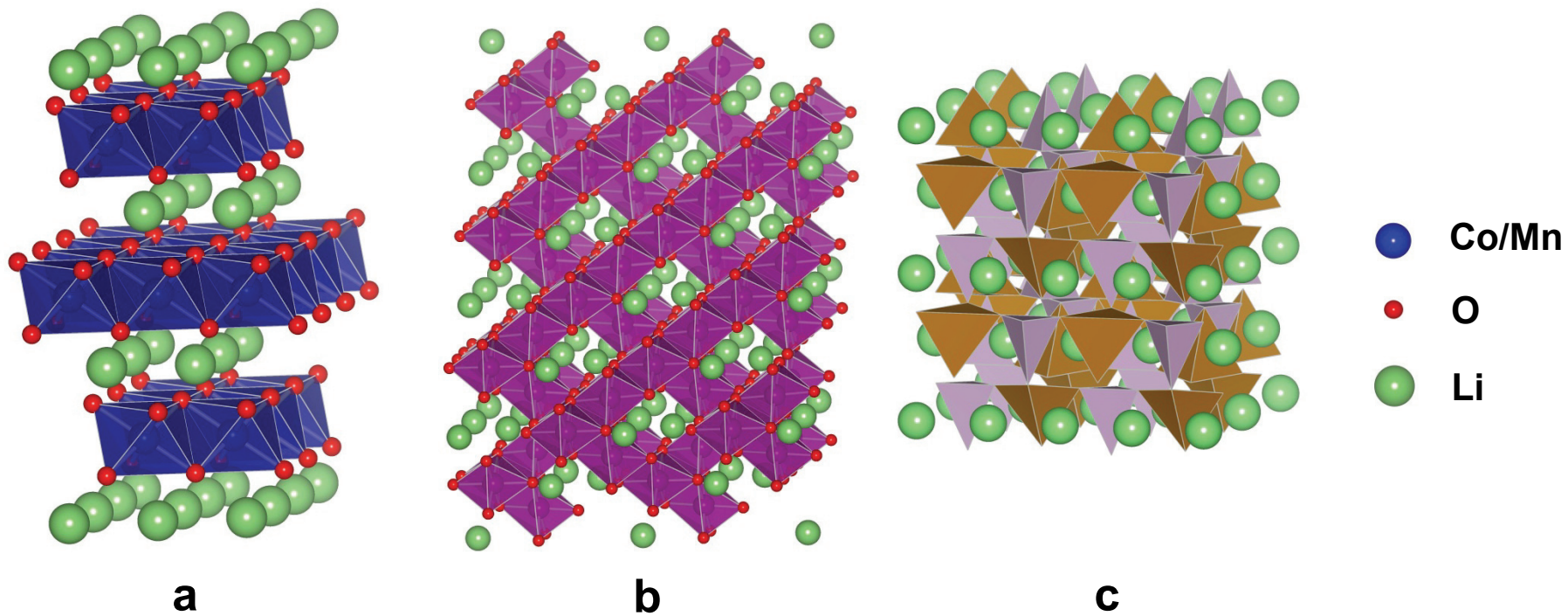


Figure 1.2. The structures of layered, spinel, and olivine positive electrode materials.

- a) Layered LiCoO_2 – the CoO_6 units are represented by blue octahedra with blue central Co atoms and red corner O atoms
- b) Spinel LiMn_2O_4 – the MnO_6 units are represented by purple octahedra with blue central Mn atoms and red corner O atoms
- c) Olivine LiFePO_4 – the FeO_4 units are represented by opaque brown tetrahedra and the PO_4 units are represented by grey opaque tetrahedra. The oxygen atoms are drawn smaller than scale so that the positions of the lithium atoms are clear.

Table 1.1 shows a comparison of positive electrode materials. The layered transition metal oxides generally show higher capacities and worse safety characteristics than LiFePO_4 or LiMn_2O_4 . The lithium-rich oxides have even larger capacities and they are outlined in Section 1.10.

Table 1.1. Advantages and disadvantages of lithium-ion battery positive electrodes.

Material	Specific capacity (mAh g⁻¹)	Advantages	Disadvantages
LiCoO_2	150 ¹⁴	Good capacity	Very expensive Poor safety
LiMn_2O_4	110 ¹¹	Excellent safety Inexpensive	Low capacity
LiFePO_4	160 ¹²	Excellent safety	Low volumetric capacity
$\text{Li}[\text{Ni}_{1/2}\text{Mn}_{1/2}]\text{O}_2$	150-180 ¹⁵	High capacity	Poor rate capability
$\text{Li}[\text{Ni}_{1/3}\text{Mn}_{1/3}\text{Co}_{1/3}]\text{O}_2$ (NMC)	150-200 ¹⁶	High capacity Less expensive than LiCoO_2	Moderately expensive
$x\text{Li}[\text{Mn}_{1/2}\text{Ni}_{1/2}]\text{O}_2 \cdot$ $y\text{LiCoO}_2 \cdot$ $z\text{Li}[\text{Li}_{1/3}\text{Mn}_{2/3}]\text{O}_2$ (Li-rich NMC)	180-250 ¹⁷	Very high capacity	Large irreversible capacity Poor rate capability

1.3. History of Layered Positive Electrode Materials

The history of positive electrode materials for lithium batteries began with studies of layered dichalcogenides. An early study of the intercalation of a wide range of electron-donating molecules and ions into layered dichalcogenides was carried out by Gamble *et al.*¹⁸ At that time, the interest was in the change in the superconducting properties of tantalum disulfide upon the introduction of Lewis bases. This initial study prompted the investigation of the insertion and removal of intercalates into and from layered dichalcogenides in an electrochemical cell by Whittingham *et al.*¹⁹

At that time, the strongest candidate for a dichalcogenide intercalating material was found to be titanium disulfide, the lightest of this series.²⁰ Lithium intercalation into TiS_2 was found to leave the structure in the same phase even to full lithium insertion, as in LiTiS_2 . The sulfur atoms in TiS_2 are arranged in a hexagonal closed-packed (hcp) structure. The sulfur sheets are stacked on top of each other, leading to an ABAB arrangement, with the titanium atoms residing in the octahedral sites. If the position of the transition metal is designated a, b, c and the position of the lithium ion a, b, c , then the full arrangement of LiTiS_2 can be described with the notation: $\dots(\text{AcB})c(\text{AcB})\dots$ ¹² Figure 1.3 shows the layered structure of LiTiS_2 , with the titanium atoms in the octahedral sites and the lithium atoms represented by spheres between the layers of octahedra. The corners of the octahedra are sulfur atoms.

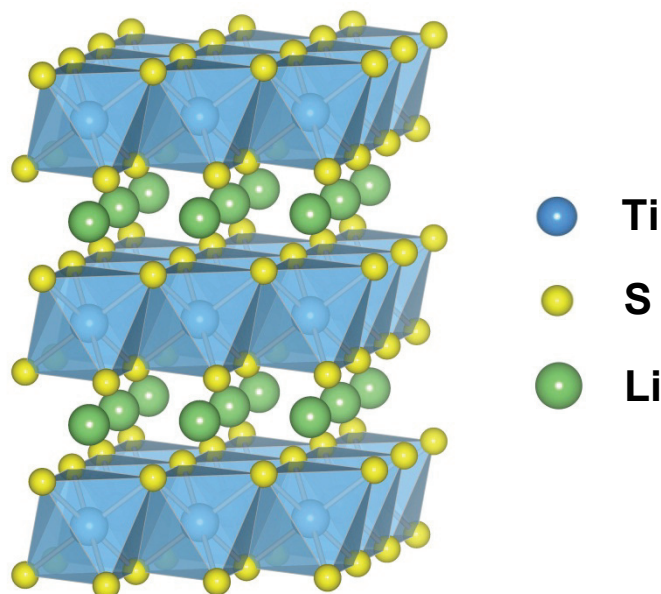


Figure 1.3. Structure of layered LiTiS_2 .

The MS_6 units are represented by blue octahedra with corner sulfur atoms and central titanium atoms. The sulfur atoms are drawn smaller than scale so that the positions of the lithium atoms are clear. Space group: $P\bar{3}m$, $a = 3.457 \text{ \AA}$, $c = 6.18 \text{ \AA}$.²¹

Other dichalcogenides have been found to be electrochemically active as lithium intercalation hosts, including the disulfides and diselenides of titanium, zirconium, hafnium, niobium, tantalum, molybdenum, and tungsten.²² Many of these materials exhibit single-phase behavior upon lithium intercalation, with the exception of vanadium diselenide.²³ In the two-phase $\text{LiVSe}_2/\text{Li}_2\text{VSe}_2$ system, lithium ions are located at octahedral sites in LiVSe_2 and subsequently at tetrahedral sites in Li_2VSe_2 . Chalcogenide-rich materials, such as niobium triselenide, have also been studied. Li_3NbSe_3 was found to extract and reinsert three lithium atoms while maintaining a single phase.²⁴

The layered dichalcogenides were limited in their operating voltage. Figure 1.4 shows the discharge curve for LiTiS_2 .¹⁹ The cell voltage is approximately 2 V against lithium. As well, it was found that Li/LiTiS_2 cells were not suitable for commercial use

due to dendritic growth of the lithium metal during cycling, potentially leading to short circuit and safety issues of the lithium batteries.¹² Therefore, other negative electrode materials would have to be selected, which would raise the voltage of the negative electrode and further decrease the voltage of the battery containing LiTiS_2 .

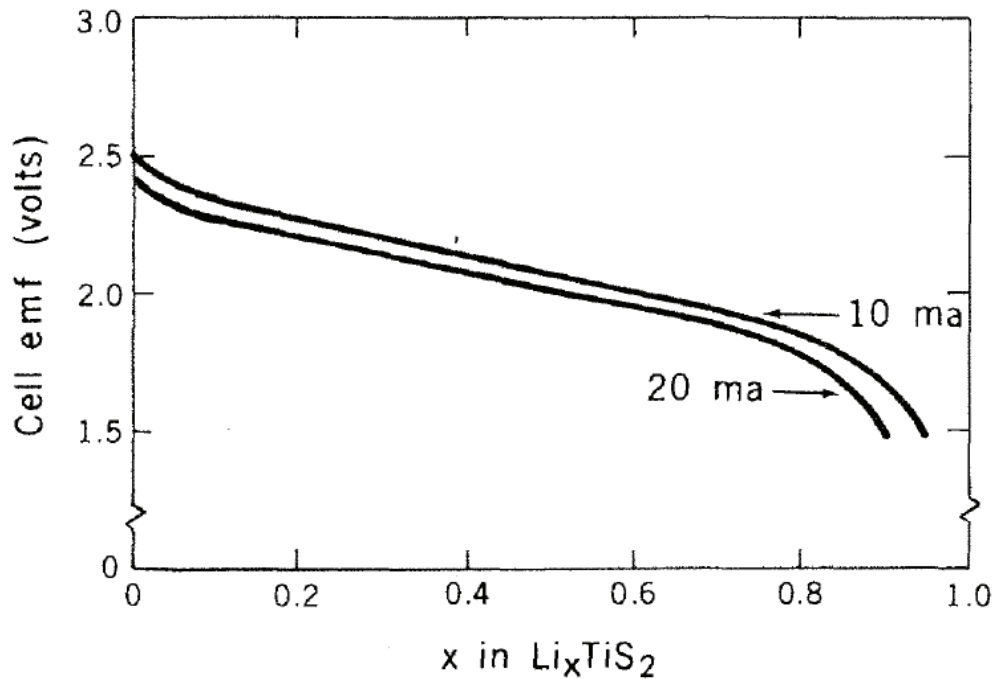


Figure 1.4. Discharge curves of $\text{Li}/\text{Li}_x\text{TiS}_2$ cells.

Two different discharge rates are shown.

From Whittingham, M. S. *Science* **1976**, *192*, 1126-1127.

Reprinted with permission from AAAS. Copyright 1976.

An understanding of the structures of oxide materials is important in material characterization and the study of lithium diffusion. The nomenclature for the structures of oxide materials of the type A_xMO_2 (where A is any alkali ion and M is a transition metal ion) was given by Delmas *et al.*^{25,26} Oxygen atoms are in a hexagonal environment and this leads to MO_6 edge-sharing octahedra forming $(\text{MO}_2)_n$ sheets. The first layer is

always designated (AcB) for the location of the oxygen atoms (A and B) and the metal ion (c). The relation of the next $(\text{MO}_2)_n$ sheet compared to the first is what determines the environment of the alkali metal ion between the slabs – octahedral, trigonal, or prismatic. This leads to the designations O, T, and P for these environments. This forms one to six layer (each layer a $(\text{MO}_2)_n$ sheet) building blocks. Table 1.2 shows examples of the Delmas notation for various positive electrode materials.

Table 1.2. Delmas notation for A_xMO_2 structures.

Delmas notation	ABC structure	Examples
O2	$(\text{AcB})_a(\text{CaB})_a(\text{AcB})$	Li_xCoO_2 $\text{Li}_{2/3}\text{Ni}_{1/3}\text{Mn}_{2/3}\text{O}_2$
O3	$(\text{AcB})_a(\text{CbA})_c(\text{BaC})_b(\text{AcB})$	Li_xCoO_2
O6	$(\text{AcB})_a(\text{CaB})_a(\text{CbA})_c(\text{BcA})_c(\text{BaC})_b(\text{AbC})_b(\text{AcB})$	Li_xCoO_2
T1	$(\text{AcB})_ab(\text{AcB})$	Li_2VO_2
T2	contains atom positions shifted from ABC locations	$\text{Li}_{2/3}\text{Ni}_{1/3}\text{Mn}_{2/3}\text{O}_2$
P2	$(\text{AcB})_a/c(\text{BcA})_b/c(\text{AcB})$	Na_xCoO_2
P3	$(\text{AcB})_a/c(\text{BaC})_a/b(\text{CbA})_b/c(\text{AcB})$	Na_xCoO_2

Figure 1.5 shows examples of the O3, T1, and P3 structures with octahedral layers and octahedral, trigonal, and prismatic lithium environments. The octahedra represent MO_6 units, with oxygen at the corners of the octahedra and metal atoms in the center of the octahedra. The lithium layer is between the octahedra layers.

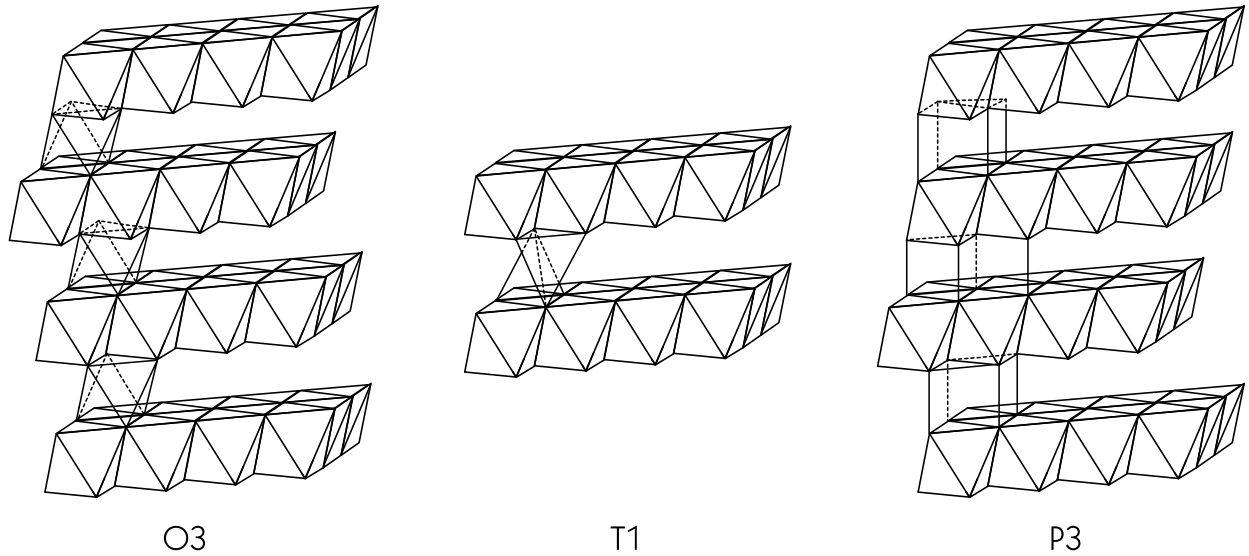


Figure 1.5. Structures with Delmas notations O3, T1, and P3.

The horizontal layers of octahedra represent MO_6 units. The octahedral, tetrahedral, and prismatic sites in between the layers of octahedra represent the lithium environment (with the lithium in the center of the polygon). Adapted from reference 25.

1.3. LiCoO_2

Gravimetric capacity is given in mAh g^{-1} , and it is related to the amount of lithium atoms able to be extracted (during charge) and reinserted (during discharge) from and into the positive electrode material. If one mole of lithium ions are transferred into or from one mole of material, the theoretical capacity is given by the equation

$$\text{Theoretical Capacity} = \frac{F}{MW} = \frac{26800 \text{ mAh mol}^{-1}}{MW}, \quad (1.1)$$

where F is the Faraday constant and MW is the molecular weight of the positive electrode material.

With a molecular weight of 97.87 g mol^{-1} , the theoretical specific capacity of LiCoO_2 is 274 mAh g^{-1} . LiCoO_2 has the $\alpha\text{-NaFeO}_2$ structure, also known as O3-type in the Delmas notation²⁵, with the oxygen atoms in a cubic-closed packed arrangement.

Mizushima *et al.* first reported the electrochemical removal of lithium from lithium cobalt oxide.²⁷ A phase transition exists in Li_xCoO_2 from trigonal to monoclinic symmetry at $x=0.5$.¹⁴ If that material undergoes charge such that $x < 0.5$ in Li_xCoO_2 , there is a large decrease in charge and discharge capacities with cycle life.¹⁴ This limits LiCoO_2 to a usable specific capacity of approximately $140\text{-}150 \text{ mAh g}^{-1}$. Figure 1.6 shows the charge and discharge curves for LiCoO_2 .¹⁴ Note the higher operating voltage than that of LiTiS_2 (Figure 1.4).

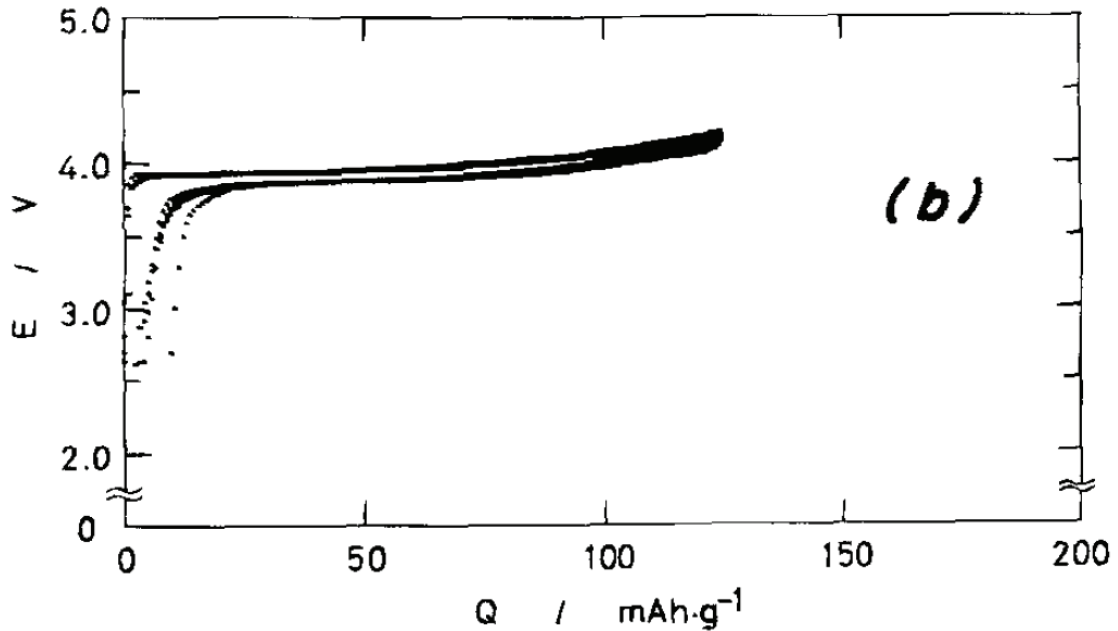


Figure 1.6. Charge and discharge profiles of LiCoO_2 .
From Ohzuku, T.; Ueda, A. *J. Electrochem. Soc.* **1994**, *141*, 2973-2977.
Reprinted with permission from The Electrochemical Society, Inc. Copyright 1994.

In June, 1991, Sony introduced the first commercial lithium-ion battery, with LiCoO_2 as the positive electrode and carbon as the negative electrode.²⁸ The main disadvantages in using LiCoO_2 as a positive electrode are a) its limited capacity, b) its relatively poor safety characteristics, and c) the high cost of cobalt.

1.4. LiNiO₂

LiNiO₂ has a theoretical capacity of 275 mAh g⁻¹. This material is often written as the composition Li_{1-y}Ni_{1+y}O₂. To maintain structural integrity of this material, its maximum state of delithiation is approximately Li_{0.5}NiO₂ and in some cases Li_{0.25}NiO₂.²⁹ This allows LiNiO₂ to have usable capacities of more than 130 mAh g⁻¹ and 200 mAh g⁻¹, respectively.

Figure 1.7 shows the charge and discharge profiles of LiNiO₂.²⁹

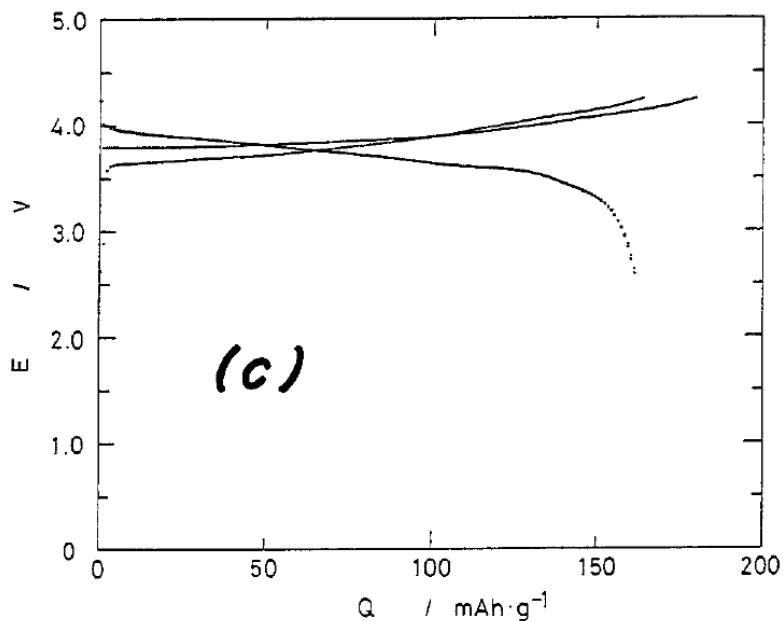


Figure 1.7. Charge and discharge curves of LiNiO₂.
Ohzuku, T; Ueda, A.; Nagayama, M. *J. Electrochem. Soc.* **1993**, *140*, 1862-1870.
Reprinted with permission from The Electrochemical Society, Inc. Copyright 1993.

Initially, LiNiO₂ was an extremely appealing positive electrode material. This is because LiNiO₂ a) shows higher specific capacities than LiCoO₂ and b) nickel is a much cheaper alternative to cobalt.

The death of LiNiO_2 as a commercially-applicable positive electrode material was its poor thermal stability. Although LiNiO_2 was stable when heated with an organic electrolyte, in its delithiated state, it showed highly exothermic reactions with the electrolyte.³⁰ At higher temperatures, the delithiated LiNiO_2 underwent loss of oxygen, forming NiO .³⁰ The released oxygen reacted (combusts) with the organic electrolyte releasing large amounts of heat.³⁰

1.5. LiMnO_2

The layered transition metal oxide LiMnO_2 converts to the spinel LiMn_2O_4 when heated and so LiMnO_2 was first synthesized by ion-exchange of NaMnO_2 .³¹ Figure 1.8 shows the charge profile of LiMnO_2 .³¹

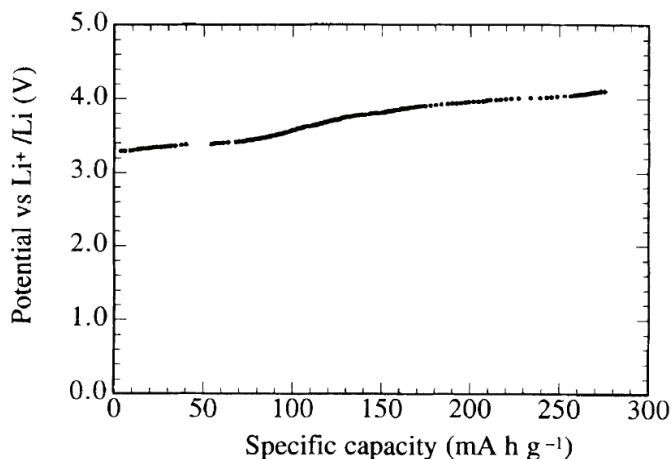


Figure 1.8. Charge curve of LiMnO_2 .

From Armstrong, A. R.; Bruce, P. B. *Nature* **1996**, 381, 499-500.

Reprinted by permission from Macmillan Publishers Ltd: Nature. Copyright 1996.

The voltage step at approximately $x = 0.5$ arises from the oxidation of Mn^{3+} to Mn^{4+} during delithiation. This is attributed to a structural change in the material because of the loss of Jahn-Teller distortion around the Mn^{3+} after oxidation.³¹ Although LiMnO_2

is an attractive positive electrode material, conversion to spinel occurs with insertion and removal of lithium and it therefore has a large loss of capacity with subsequent charge and discharge cycles.³⁰

1.6. LiFeO_2 , LiVO_2 , LiTiO_2 , and LiCrO_2

LiFeO_2 adopts an orthorhombic structure, which exists as corrugated layers of lithium and iron atoms.³² The charged LiFeO_2 positive electrode undergoes transformation to an amorphous phase and its rechargeable capacity is limited to about 80 mAh g^{-1} .³² Figure 1.9 shows the charge and discharge curves of LiFeO_2 .³²

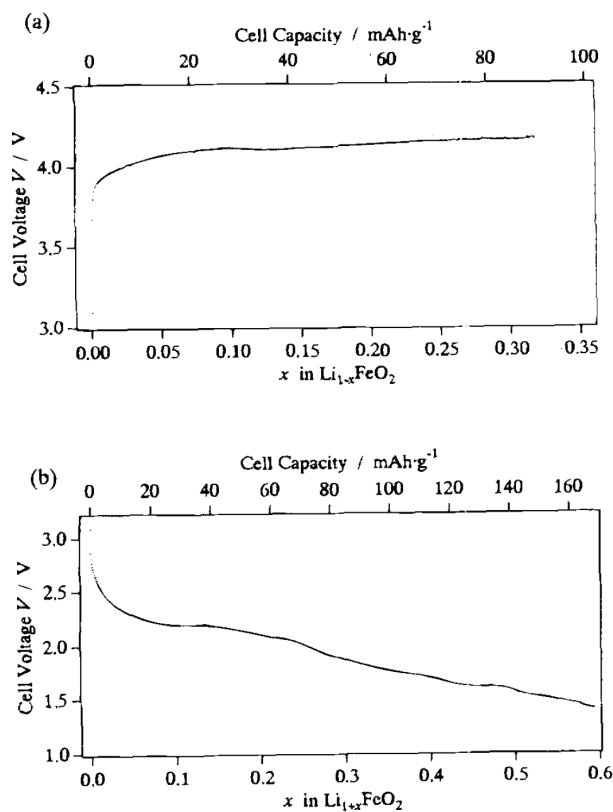


Figure 1.9. Charge and discharge profiles of LiFeO_2 .
Kanno, R.; Shirane, T.; Kawamoto, Y.; Takeda, Y.; Takano, M.; Ohashi, M.; Yamaguchi, Y. *J. Electrochem. Soc.* **1996**, *143*, 2435-2442.

Reprinted with permission from The Electrochemical Society. Copyright 1996.

LiVO_2 is isostructural to LiCoO_2 .³³ It was found to be unstable in its delithiated state as the vanadium ions diffused from their octahedral sites.^{33, 34} Other layered oxides of vanadium employed in lithium battery research include V_2O_5 ,³⁵ V_6O_{13} ³⁶ and LiV_3O_8 .³⁷ Three lithium atoms can be inserted into V_2O_5 , with five phases existing from $x = 0$ to $x = 3$ in $\text{Li}_x\text{V}_2\text{O}_5$.³⁵ More recent research in the area of vanadium oxides has been carried out in the field of xerogels³⁸ and nanotubes.³⁹ These materials both exhibit a change in their electrochemical behavior due to the double layers of vanadium oxide (as opposed to single layers found in conventional structures).³⁸

The layered structure of LiTiO_2 was computationally predicted to be stable by Ceder *et al.*⁴⁰ and was synthesized by Obrovac *et al.*⁴¹ Its electrochemical characteristics are poor – only a small amount of lithium can be deintercalated from LiTiO_2 .⁴¹

Layered LiCrO_2 can be synthesized but cannot be used in a lithium-ion battery. When Cr^{3+} is oxidized to Cr^{6+} during charge, the smaller chromium ions migrate to tetrahedral sites in the lithium layer.⁴²

1.7. $\text{Li}[\text{Li}_{1/3}\text{Mn}_{2/3}]\text{O}_2$

$\text{Li}[\text{Li}_{1/3}\text{Mn}_{2/3}]\text{O}_2$ is typically written as Li_2MnO_3 and has a layered structure. Figure 1.10 shows the structure of $\text{Li}[\text{Li}_{1/3}\text{Mn}_{2/3}]\text{O}_2$, with the lithium, oxygen, and transition metal layers. The structure is drawn based on the monoclinic system, with space group $C2/m$, $a = 4.9246 \text{ \AA}$, $b = 8.5216 \text{ \AA}$, $c = 5.0245 \text{ \AA}$, and $\beta = 109.398^\circ$.⁴³

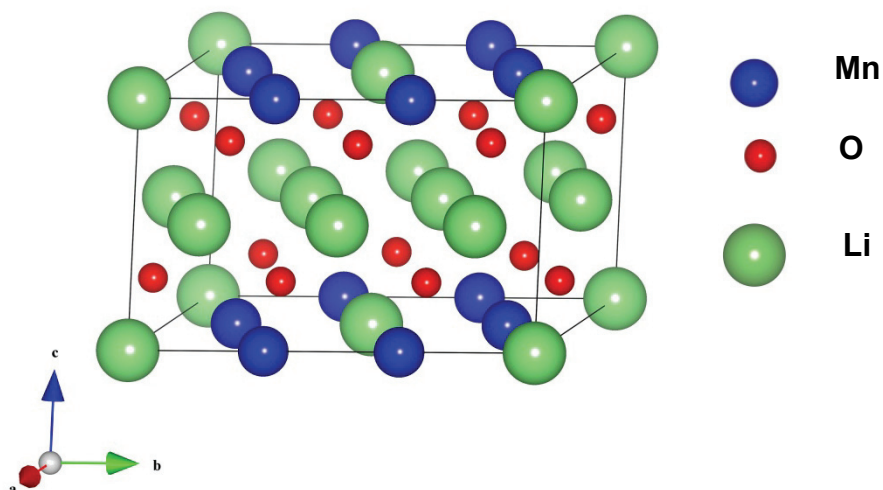


Figure 1.10. Layered structure of $\text{Li}[\text{Li}_{1/3}\text{Mn}_{2/3}]\text{O}_2$.

If the diffraction lines are calculated considering $\text{Li}[\text{Li}_{1/3}\text{Mn}_{2/3}]\text{O}_2$ to be isostructural to $\text{O}_3\text{-LiCoO}_2$, the calculation does not take into account the ordering of the manganese and lithium in the transition metal layer. Figure 1.11 shows this, with additional peaks as indicated.

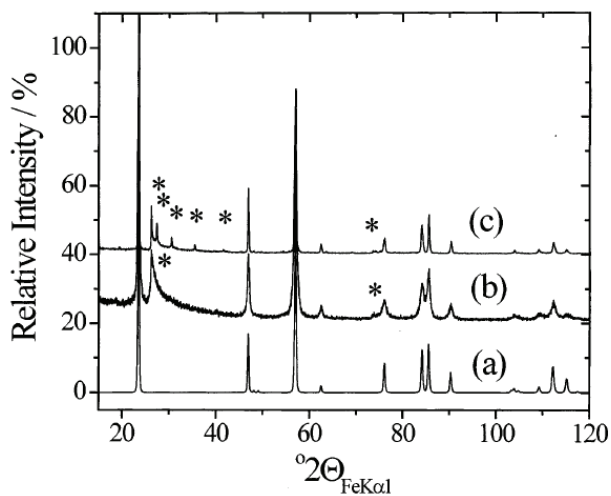


Figure 1.11. XRD patterns of Li_2MnO_3 .

a) Calculated pattern of Li_2MnO_3 based on a rhombohedral unit cell and XRD pattern of Li_2MnO_3 material heated b) 500°C and c) 800°C .⁴⁴

From Robertson, A. D.; Bruce, P. G. *Chem. Mater.* **2003**, *15*, 1984-1992.

Reprinted with permission from the American Chemical Society. Copyright 2003.

The additional diffraction lines in $\text{Li}[\text{Li}_{1/3}\text{Mn}_{2/3}]\text{O}_2$ (when compared to, for instance, $\text{O}_3\text{-LiCoO}_2$) arise from the superlattice ordering in the transition metal layer.

Figure 1.12 shows the transition metal layer in $\text{Li}[\text{Li}_{1/3}\text{Mn}_{2/3}]\text{O}_2$.

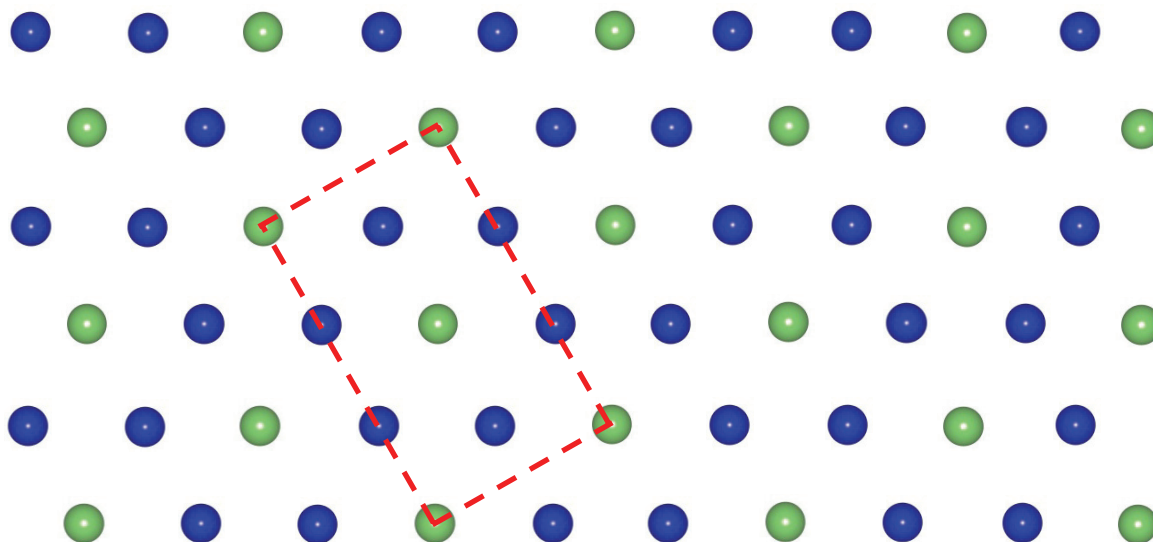


Figure 1.12. Transition metal layer of $\text{Li}[\text{Li}_{1/3}\text{Mn}_{2/3}]\text{O}_2$.
An outline of the monoclinic unit cell is shown in red.
The lithium atoms are green and the manganese atoms are blue.

No lithium removal should be expected for $\text{Li}[\text{Li}_{1/3}\text{Mn}_{2/3}]\text{O}_2$. Manganese has a maximum oxidation state of 4+ in its octahedral environment of oxygen atoms so there are no cations available for oxidation. The material is typically found to be electrochemically inactive in its microcrystalline form.⁴⁵ However, there is some electrochemical activity in its nanocrystalline form.⁴⁴ Figure 1.14 shows the charge and discharge curves for nanocrystalline $\text{Li}[\text{Li}_{1/3}\text{Mn}_{2/3}]\text{O}_2$.⁴⁴ It shows that this material does have electrochemical activity, along with a large irreversible capacity.

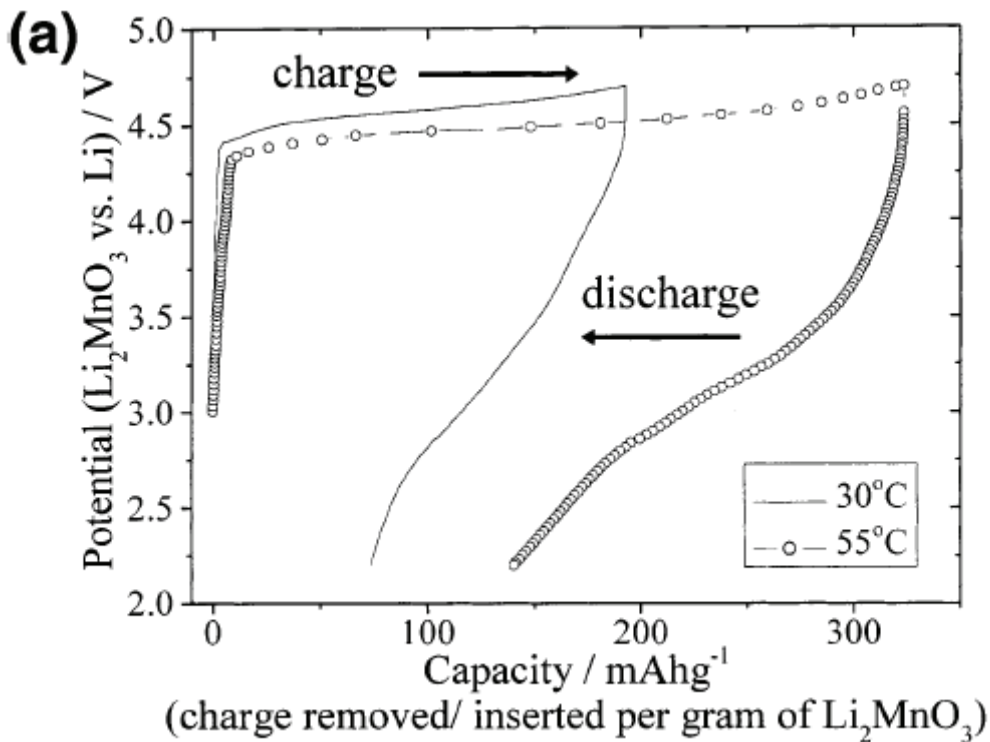


Figure 1.13. The charge and discharge curves for nanocrystalline $\text{Li}[\text{Li}_{1/3}\text{Mn}_{2/3}]\text{O}_2$.
 From Robertson, A. D.; Bruce, P. G. *Chem. Mater.* **2003**, *15*, 1984-1992.
 Reprinted with permission from the American Chemical Society. Copyright 2003.

1.8. Rules for Layered Oxides

The review of layered oxides in Sections 1.4 – 1.6 shows that various transition metals can be used in the synthesis of a layered oxide LiMO_2 (with one transition metal) as long as the metal has an available oxidation state of 3+. $\text{Li}[\text{Li}_{1/3}\text{Mn}_{2/3}]\text{O}_2$ reveals that multiple cations can be included in the transition metal layer.

Various stoichiometries can be written for the layered transition metal oxides. These materials can be written as $\text{Li}[\text{Li}_x\text{M}_y^1\text{M}_z^2]\text{O}_2$, where M is a transition metal and the square bracket encloses elements in the transition metal layer. The allowed

stoichiometries for lithium-ion battery positive electrode materials can be found by following this set of rules as given by Lu *et al.*:¹⁷

- The transition metal oxide layer sequence should be lithium-oxygen-transition metal-oxygen-lithium and the lithium planes should be full
- The sum of the cation occupations in the transition metal layer must equal one
- The sum of the cation oxidation states in the transition metal layer times their occupations must equal three
- The oxidation states of the cations must be those that they naturally adopt at normal synthesis temperatures in air in the presence of the other cations
- At least one of the metal cations should be able to be oxidized within the electrochemical window of the electrolyte

1.9. Solid Solutions of Transition Metal Oxide Positive Electrode Materials

Solid solutions of the $\text{Li}[\text{M}]\text{O}_2$ (one transition metal) oxides exist such that the metals in the transition metal layer are homogeneously distributed. In other words, there can be formation of the mixed transition metal oxides which are only one phase.

Mixed nickel-cobalt dioxide was formed by Rougier *et al.* by the heating of stoichiometric amounts of Li_2CoO_3 , NiO , and Co_3O_4 .⁴⁶ The material $\text{Li}_x[\text{Ni}_{1-y}\text{Co}_y]\text{O}_2$ was made with $y = 0, 0.1, 0.2,$ and 0.3 . It was found that the addition of cobalt into the LiNiO_2 structure provided stability for the structure, giving the $\text{Li}_x[\text{Ni}_{1-y}\text{Co}_y]\text{O}_2$ material better electrochemical characteristics upon removal and insertion of lithium ions compared to LiNiO_2 .

The ion exchange of sodium in NaMnO_2 by lithium and addition of cobalt led to the formation of $\text{LiMn}_{1-z}\text{Co}_z\text{O}_2$ by Armstrong *et al.*⁴⁷ The addition of cobalt in LiMnO_2 led to improved electrochemistry; however, the cobalt-containing material still converted to the spinel structure upon cycling. The improved electrochemical behavior was attributed both to the stabilization of the $\alpha\text{-NaFeO}_2$ structure and the increase in conductivity with the introduction of cobalt ions.

Rossen *et al.* studied the $\text{Li}_x\text{Mn}_y\text{Ni}_{1-y}\text{O}_2$ system for $0 < y < 0.6$.⁴⁸ It was found that the capacity of the $\text{Li} / \text{Li}_x\text{Mn}_y\text{Ni}_{1-y}\text{O}_2$ cells decreased with increasing values of y and it was concluded that these materials may not be useful in practical applications. However, Spahr *et al.* found the optimum electrochemical behaviour in this series with the material $\text{Li}[\text{Mn}_{0.5}\text{Ni}_{0.5}]\text{O}_2$ (where the transition metal ions are Mn^{4+} and Ni^{2+}).⁴⁹ As well, a novel coprecipitation method was developed to synthesize this material. Manganese and nickel nitrates were added to a Br_2/LiOH solution to form their hydroxides, which were heated with LiOH to form the lithium-containing mixed-metal oxide. Spahr *et al.* reported a capacity of 150 mAh g^{-1} for their $\text{Li}[\text{Mn}_{0.5}\text{Ni}_{0.5}]\text{O}_2$ positive electrode which fell to 125 mAh g^{-1} after 25 cycles.⁴⁹

The investigation of $\text{Li}[\text{Ni}_{1-y-z}\text{Mn}_y\text{Co}_z]\text{O}_2$ by the Ohzuku¹⁵ and Dahn¹⁷ groups led to considerable research in this system. Ohzuku *et al.* maintained a 150 mAh g^{-1} capacity for 30 cycles.¹⁵ Research carried out on increasing this capacity by the selection of optimum voltage window, heating temperature, and cycling rate has brought the capacity of $\text{Li}[\text{Mn}_{0.5}\text{Ni}_{0.5}]\text{O}_2$ to approximately 180 mAh/g .¹²

Layered oxides of the form $\text{Li}[\text{Ni}_{1-y-z}\text{Mn}_y\text{Co}_z]\text{O}_2$ containing all three transition metal ions were considered by Liu *et al.*⁵⁰ It was found that these materials could be

synthesized with the metals homogeneously distributed. However, the authors had difficulty in that they made lithium-deficient material and the electrochemistry was not ideal.

Makimura *et al.* refined the previous study by Liu *et al.*, focusing their investigation on the compound $\text{Li}[\text{Ni}_{0.33}\text{Mn}_{0.33}\text{Co}_{0.33}]\text{O}_2$ (where the transition metal ions were Ni^{2+} , Mn^{4+} , and Co^{3+}).¹⁶ This material was found to deliver a capacity of 150 mAh g^{-1} cycled between 2.5 and 4.2 V. This material also gave cycling capacities up to 200 mAh g^{-1} from 2.5-5.0 V.

Lu *et al.* studied the material $\text{Li}[\text{Ni}_x\text{Co}_{1-2x}\text{Mn}_x]\text{O}_2$, with $x = 1/4$ and $3/8$.⁵¹ It was found that the $\text{Li}[\text{Ni}_{1/4}\text{Co}_{1/2}\text{Mn}_{1/4}]\text{O}_2$ material gave a stable capacity of 160 mAh g^{-1} between 2.5 and 4.4 V. In this study, differential scanning calorimetry indicated that this nickel, manganese, and cobalt-containing (NMC) material has better safety characteristics than the conventional LiCoO_2 positive electrode material.

The $\text{Li}[\text{Ni}_{0.33}\text{Mn}_{0.33}\text{Co}_{0.33}]\text{O}_2$ positive electrode is currently being used a replacement for LiCoO_2 , with the former material having comparable electrochemical behavior (capacity and cycling), better safety, and being less expensive than the latter.¹²

1.10. Lithium-Rich Transition Metal Oxides as Positive Electrode Materials for Lithium-ion Batteries

Section 1.7 gave the rules to make layered transition metal oxide positive electrode materials for lithium-ion batteries. The rules indicated that lithium can be inserted into the transition metal layer. The next section describes the materials that are obtained with lithium in the transition metal layer.

The initial lithium-rich, or oxygen-release materials, can be located on the pseudoternary system $x\text{Li}[\text{Mn}_{1/2}\text{Ni}_{1/2}]\text{O}_2 \cdot y\text{LiCoO}_2 \cdot z\text{Li}[\text{Li}_{1/3}\text{Mn}_{2/3}]\text{O}_2$. Figure 1.14 shows the ternary phase diagram of this system. Materials located at the leftmost line of the phase triangle, i.e.: not containing cobalt, were the first lithium-rich materials to be introduced and the series of the materials located on this line can be written as $\text{Li}[\text{Ni}_x\text{Li}_{(1/3-2x/3)}\text{Mn}_{(2/3-x/3)}]\text{O}_2$.

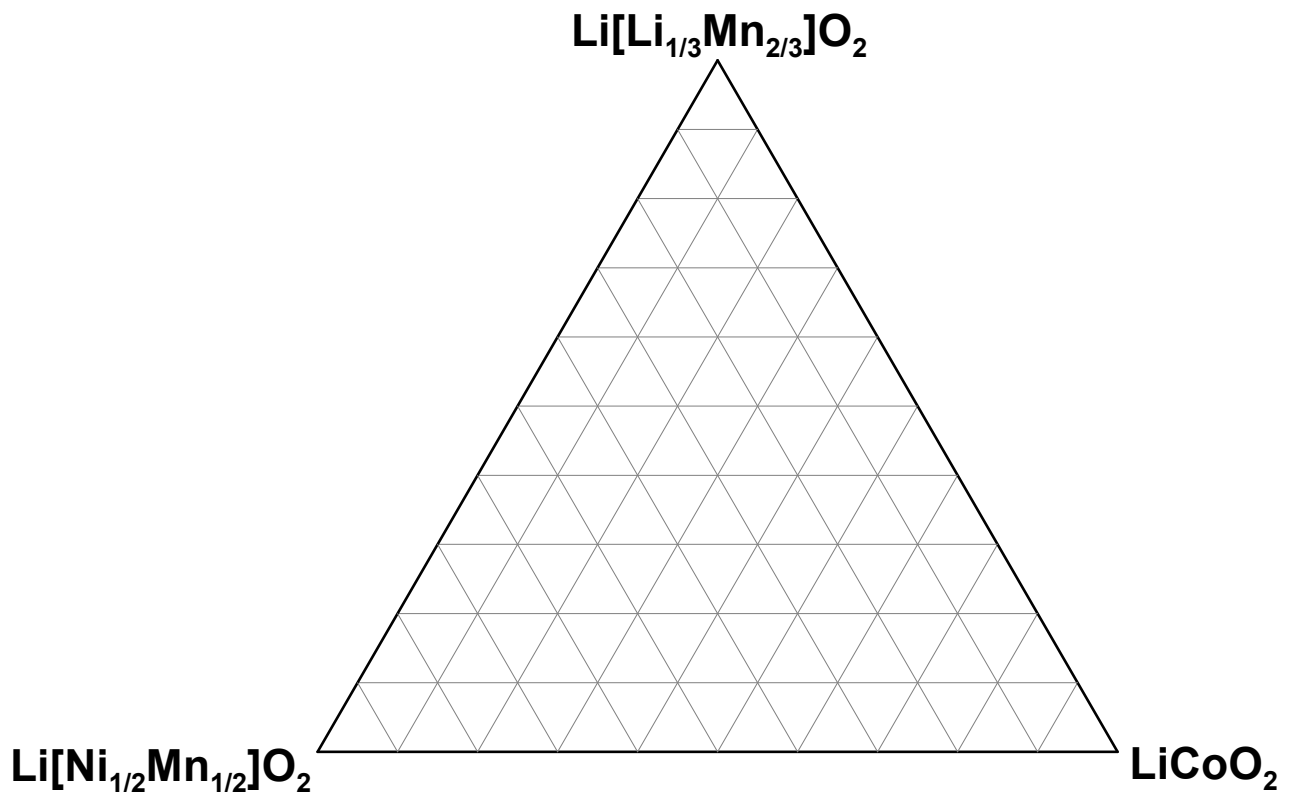


Figure 1.14. Composition triangle containing the lithium-rich transition metal oxides.

In 2001, Lu *et al.* published the first report of the synthesis, structure, and electrochemical behavior of the layered oxide, $\text{Li}[\text{Ni}_x\text{Li}_{(1/3-2x/3)}\text{Mn}_{(2/3-x/3)}]\text{O}_2$.¹⁷ This oxide can be viewed as a solid solution between $\text{Li}[\text{Ni}_{1/2}\text{Mn}_{1/2}]\text{O}_2$ and $\text{Li}[\text{Li}_{1/2}\text{Mn}_{2/3}]\text{O}_2$ – these materials are located at the left line of the composition triangle in Figure 1.14. Figure 1.15 shows the XRD patterns of $\text{Li}[\text{Ni}_x\text{Li}_{(1/3-2x/3)}\text{Mn}_{(2/3-x/3)}]\text{O}_2$ with $x = 1/2$, $x = 5/12$, and $x = 1/3$ from the work by Lu *et al.*¹⁷

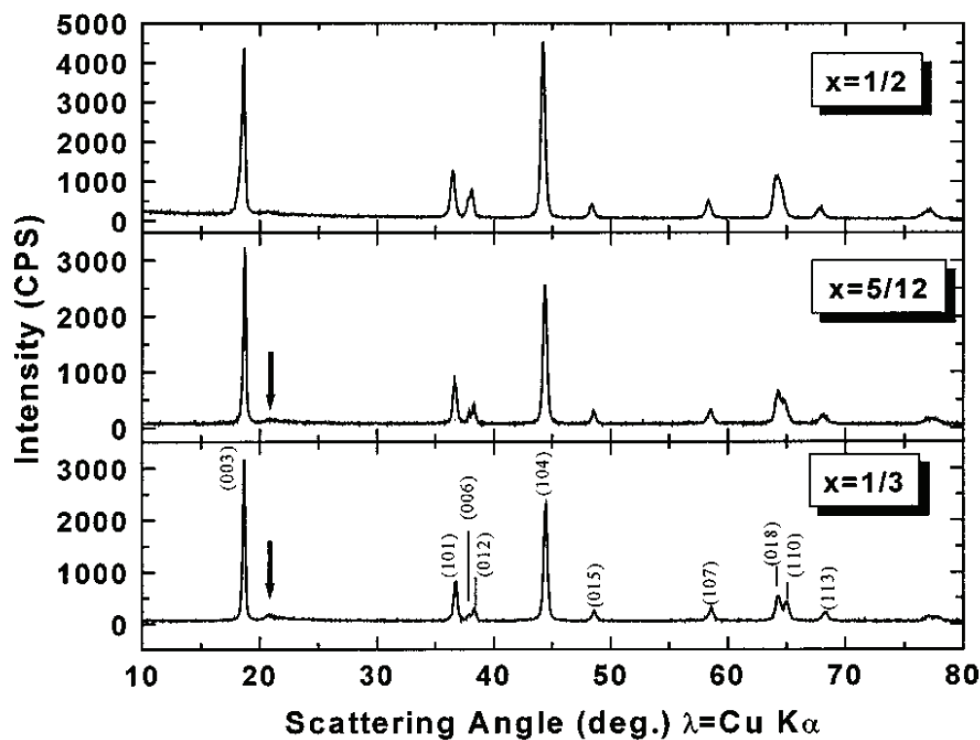


Figure 1.15. XRD patterns of $\text{Li}[\text{Ni}_x\text{Li}_{(1/3-2x/3)}\text{Mn}_{(2/3-x/3)}]\text{O}_2$.

The stoichiometries were $x = 1/2$, $x = 5/12$, and $x = 1/3$.

From Lu, Z.; Dahn, J. R. *Electrochem. Solid-State Lett.* **2001**, *4*, A191-A194.
Reprinted with permission from The Electrochemical Society. Copyright 2001.

The lithium-rich oxides, as other layered transition metal oxides, could be indexed by the $\alpha\text{-NaFeO}_2$ structure, except for powder X-ray diffraction peaks in the $20\text{-}35^\circ$

range. These peaks were attributed to the superlattice ordering of the lithium and manganese atoms in the transition metal layer.¹⁷ These were the same peaks that can be indexed to the monoclinic $\text{Li}[\text{Li}_{1/3}\text{Mn}_{2/3}]\text{O}_2$ material discussed in Section 1.6.

It would be expected that there would be a decrease in capacity by synthesizing materials in the system between the $\text{Li}[\text{Ni}_{1/2}\text{Mn}_{1/2}]\text{O}_2$ and $\text{Li}[\text{Li}_{1/3}\text{Mn}_{2/3}]\text{O}_2$ stoichiometries. After all, this means that there is drop in the fraction of nickel in the transition metal layer and only nickel, not manganese, is oxidized during the charge process in $\text{Li}[\text{Ni}_{1/2}\text{Mn}_{1/2}]\text{O}_2$.¹⁷ However, $\text{Li}/\text{Li}[\text{Ni}_x\text{Li}_{(1/3-2x/3)}\text{Mn}_{(2/3-x/3)}]\text{O}_2$ electrochemical cells were fabricated in the study by Lu *et al.*¹⁷ At a voltage range of 3.0-4.4 V, an expected capacity of approximately 150 mAh g^{-1} was obtained. Figure 1.17 shows the charge and discharge curves of $\text{Li}/\text{Li}[\text{Ni}_{5/12}\text{Li}_{1/18}\text{Mn}_{19/36}]\text{O}_2$ cells from 3.0-4.4 V. There is a decrease in capacity when compared to $\text{Li}[\text{Ni}_{1/2}\text{Mn}_{1/2}]\text{O}_2$ for this voltage range.

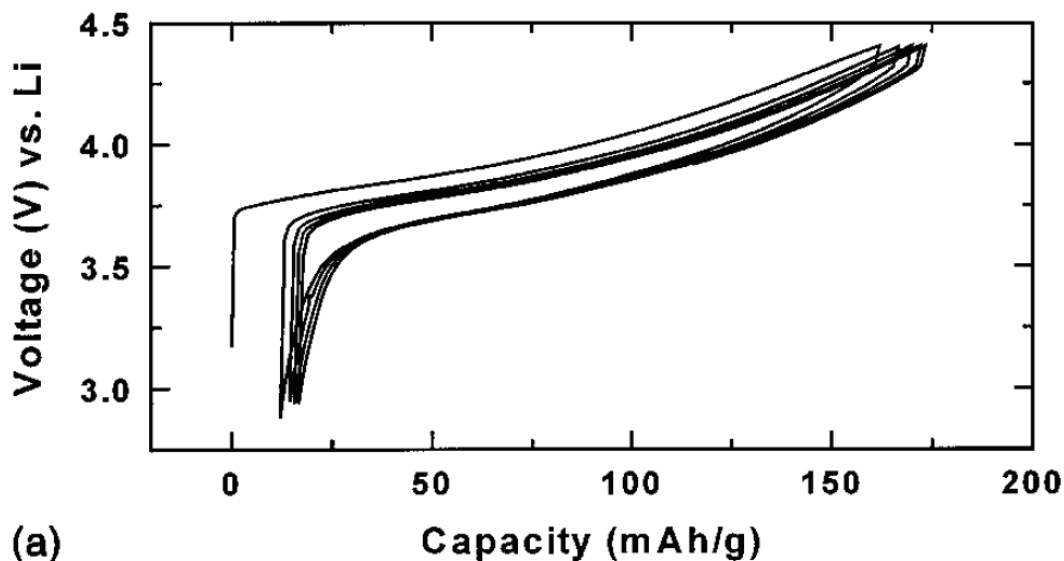


Figure 1.17. Charge and discharge curves for $\text{Li}[\text{Ni}_{5/12}\text{Li}_{1/18}\text{Mn}_{19/36}]\text{O}_2$.
The voltage range was 3.0-4.4 V.

From Lu, Z.; Dahn, J. R. *Electrochem. Solid-State Lett.* **2001**, *4*, A191-A194.
Reprinted with permission from The Electrochemical Society. Copyright 2001.

Lu *et al.* decided to vary the voltage range and see the effect on the electrochemistry.¹⁷ Figure 1.18 shows the charge discharge curves for Li/Li[Ni_xLi_(1/3-2x/3)Mn_(2/3-x/3)]O₂ cells with x = 1/2, x = 5/12, and x = 1/3 with a voltage range of 2.0 – 4.8 V for the first cycle and 2.0 – 4.6 V for subsequent cycles.

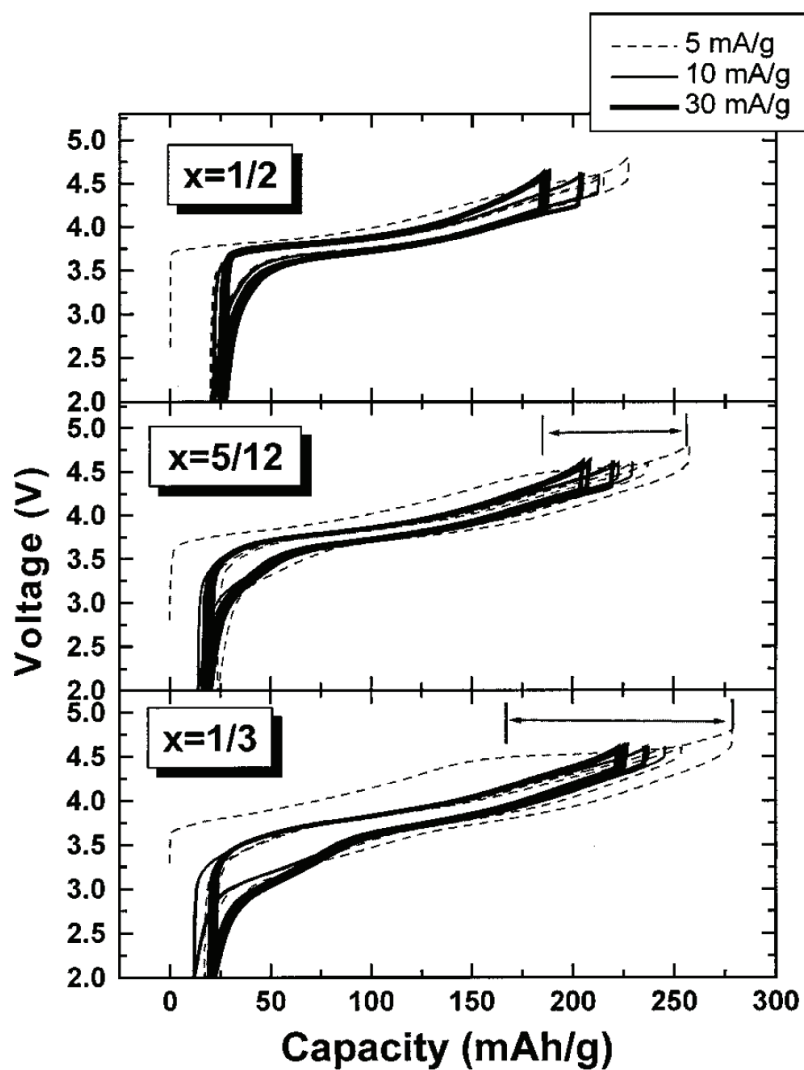


Figure 1.18. Charge and discharge curves for Li/Li[Ni_xLi_(1/3-2x/3)Mn_(2/3-x/3)]O₂. The first charge was to 4.8 V with subsequent cycles between 2.0 and 4.6 V. From Lu, Z.; Dahn, J. R. *Electrochem. Solid-State Lett.* **2001**, *4*, A191-A194. Reprinted with permission from The Electrochemical Society. Copyright 2001.

It must have come as a big surprise to obtain first charge capacities of up to 275 mAh g⁻¹ for this series of materials.¹⁷ This is a huge capacity when compared to the other positive electrode materials discussed so far. It was speculated that in the initial charge range (3.0-4.4 V), lithium is extracted from the layered oxide as Ni²⁺ is oxidized to Ni⁴⁺. In the case of an extended voltage range plateau, it was speculated that lithium and oxygen were simultaneously released from the layered oxide; O²⁻ was being oxidized to compensate for the Li⁺ extraction. When the lithium was reinserted during discharge, the authors assumed that Mn⁴⁺ reduced to Mn³⁺ and therefore the oxygen was not reinserted back into the structure. At a cycling voltage range of 2.0-4.6 V, capacities of 200 and 180 mAh g⁻¹ were obtained for x = 1/3 and 1/5, respectively. As a comparison, Li[Ni_{1/2}Mn_{1/2}]O₂ cycled at 160 mAh g⁻¹ in this voltage range.¹⁷

A larger series of materials in the Li/Li[Ni_xLi_(1/3-2x/3)Mn_(2/3-x/3)]O₂ series was investigated by Lu *et al.* in 2002.⁵² This included x = 0, 1/12, 1/6, 1/4, 1/3, 5/12, and 1/2. The preparation was the same as in the previous study.¹⁷ The structure of the materials was studied by X-ray and neutron diffraction and analyzed with Rietveld refinement. All samples showed diffraction lines corresponding to those of Li[Li_{1/3}Mn_{2/3}]O₂. Superlattice ordering lines, in the region between 20 and 35° were exhibited, especially with larger x-values. Neutron diffraction studies indicated that some nickel was in the lithium layer.⁵² Electrochemical measurements showed that Li/Li[Ni_xLi_(1/3-2x/3)Mn_(2/3-x/3)]O₂ cells delivered cycling capacities of 230 mAh g⁻¹ for x = 1/3, with a current density of 30 mA g⁻¹. The oxides were made at temperatures varying from 600-900°C, with a layered structure being obtained above 800°C.⁵²

Understanding the irreversible plateau was the focus of another study by Lu *et al.* in 2002.⁵³ The range of oxides included $1/6$, $1/4$, $1/3$, $5/12$, and $1/2$ in $\text{Li}[\text{Ni}_x\text{Li}_{(1/3-2x/3)}\text{Mn}_{(2/3-x/3)}]\text{O}_2$. In-situ XRD studies were carried out. These showed that the decrease in unit cell volume corresponded with the charge from 3.0 to 4.4 V and was reversible. When the material was charged to 4.8 V, the *c*-axis decreased rapidly as the cell approached 4.8 V as the last lithium ions were being extracted from the lattice. As well, there was loss of the superlattice ordering peaks during cycling.

It was not long before other groups began work on the lithium-rich transition metal oxides. In a study by Shin *et al.*, $\text{Li}[\text{Ni}_x\text{Li}_{(1/3-2x/3)}\text{Mn}_{(2/3-x/3)}]\text{O}_2$ was made with $x = 0.41$, 0.35 , 0.275 , and 0.2 using a sol-gel method.⁵⁴ For the stoichiometry $\text{Li}[\text{Li}_{1/5}\text{Ni}_{1/5}\text{Mn}_{3/5}]\text{O}_2$, cycling capacities of 200 and 240 mAh g^{-1} were obtained at 30°C and 55°C , respectively. The authors also identified the growth of peaks near 3.1 and 3.3 V during the charge and discharge processes during cycling in the differential capacity curves.

The first reports of lithium-rich transition metal oxides suggested that oxygen and lithium were simultaneously released to give an irreversible plateau during the first charge process.^{17, 52, 53} Other groups had different views on the mechanism of lithium extraction in the high voltage range. Robertson *et al.* suggested, in their paper investigating the electrochemical activity of Li_2MnO_3 , that lithium and oxygen are not simultaneously released from these types of materials.⁵⁵ It was proposed that lithium is being released and being exchanged with protons generated from the electrolyte. The authors concluded that the Mn^{4+} remains in the 4+ oxidation state and therefore there was no reduction of the manganese component during subsequent discharges of the cell.

Methods other than the coprecipitation process were reported as synthetic routes to produce the lithium-rich transition metal oxide. Kim *et al.* synthesized $\text{Li}[\text{Li}_{0.1}\text{Ni}_{0.35}\text{Mn}_{0.55}]\text{O}_2$ using a sol-gel method.⁵⁶ The material exhibited the expected α - NaFeO_2 structure with superlattice peaks at 20-25°. The material cycled well between 2.5 and 4.6 V when the oxide was produced at 1000°C. Differential capacity curves revealed a new peak during the 35th discharge cycle near 3.2 V and XRD analysis showed that there was disappearance of the superlattice peaks in the range of 20-25° at the 35th discharge.

In a study by Park *et al.*, $\text{Li}[\text{Ni}_x\text{Li}_{(1/3-2x/3)}\text{Mn}_{(2/3-x/3)}]\text{O}_2$ was made with $x = 0.17, 0.25, 0.33,$ and 0.5 using a solid state method heating acetate and nitrate metal salts.⁵⁷ It was found that the oxide materials exhibited the α - NaFeO_2 structure, the same structure as $\text{O}_3\text{-LiCoO}_2$ but with added superlattice peaks. Analysis of the materials showed that Ni^{2+} oxidizes to Ni^{3+} during charge, whereas Mn^{4+} stays in the 4+ state. During discharge, data indicated that the oxidation state of nickel was the 2+ state, but there was no indication of reduction of Mn^{4+} to Mn^{3+} . The materials cycled well at a capacity of approximately 200 mAh g^{-1} at a rate of 20 mA g^{-1} .

Kim *et al.* showed the first results on the $\text{Li}[\text{Li}_{0.1}\text{Ni}_{0.35-x/2}\text{Co}_x\text{Mn}_{0.55-x/2}]\text{O}_2$ series, synthesized by a sol-gel method.⁵⁸ The Co-containing system exhibited the crystal structure of α - NaFeO_2 with the existence of superlattice peaks. The authors suggested that cobalt addition allowed for improved rate capability of the lithium-rich oxide system, with 174 mAh g^{-1} at C-rate.

Park *et al.* made $\text{Li}[\text{Co}_x\text{Li}_{(1/3-x/3)}\text{Mn}_{(2/3-2x/3)}]\text{O}_2$ materials with $x = 0.1, 0.17, 0.20, 0.25, 0.33,$ and 0.5 by a solid state method with metal acetates and nitrate salts.⁵⁹ In the

layered oxide material, it was found that the manganese existed as Mn^{4+} and the cobalt as Co^{3+} . The first discharge of the materials was found to range from 150 mAh g^{-1} for $x = 0.1$ and 265 mAh g^{-1} for $x = 0.5$ at a specific current of 20 mA g^{-1} . The $\text{Li}[\text{Co}_{0.5}\text{Li}_{0.17}\text{Mn}_{0.33}]\text{O}_2$ material had a capacity of 220 mAh g^{-1} . It was suggested that the manganese existed as $\text{Mn}^{3.5+}$ after the 20th discharge.

Johnson *et al.* studied the material $0.3\text{Li}_2\text{MnO}_3 \cdot 0.7\text{LiMn}_{0.5}\text{Ni}_{0.5}\text{O}_2$.⁶⁰ The researchers viewed the capacity obtained in the normal lithium deintercalation region to be from $\text{Li}[\text{Mn}_{0.5}\text{Ni}_{0.5}]\text{O}_2$ and the capacity obtained in the oxygen loss region to be from the Li_2MnO_3 component – the theoretical capacities correlated well with those obtained from the first charge. Any capacity obtained above 4.8 V was attributed to electrolyte oxidation. The material $0.3\text{Li}_2\text{MnO}_3 \cdot 0.7\text{LiMn}_{0.5}\text{Ni}_{0.5}\text{O}_2$ was found to cycle at 250 mAh g^{-1} between 2.0 and 5.0 V . Acid treatment of the positive electrode decreased its irreversible capacity but reduced its overall rechargeable capacity.

Armstrong *et al.* showed, with mass spectrometry, that O_2 was evolved during the charge process of $\text{Li}/\text{Li}[\text{Li}_{1/5}\text{Ni}_{1/5}\text{Mn}_{3/5}]\text{O}_2$ cells.⁶¹ They also stated a hypothesis for lithium extraction: oxygen evolution happened as lithium ions diffused from the transition metal layer into the lithium layer. This leaves vacancies in the transition metal layer, which are filled as nickel and manganese transition metals rearrange by diffusion from the surface to the bulk. This gives a reason for the suppression of the superlattice peaks during cycling of the $\text{Li}/\text{Li}[\text{Li}_{1/5}\text{Ni}_{1/5}\text{Mn}_{3/5}]\text{O}_2$ cells. The earlier work that was presented by this group in reference 55 and 44 was, in effect, deemed incorrect by the more recent study, giving the general consensus that oxygen and lithium are

simultaneously released during the charge process at high voltages in the lithium-rich materials.⁶¹

1.11. Solid Solution and Nanocomposite Models of the Lithium-Rich Oxides

As previously mentioned, some researchers viewed the lithium-rich oxides as a solid solution of $\text{Li}[\text{M}]\text{O}_2$ and Li_2MnO_3 ⁵³ whereas others viewed the material as having both $\text{Li}[\text{M}]\text{O}_2$ regions and Li_2MnO_3 regions, of which the oxygen release only occurs from the Li_2MnO_3 regions.⁶⁰

Recent transmission electrode microscopy (TEM) images reveal that both $\text{Li}[\text{M}]\text{O}_2$ and the monoclinic Li_2MnO_3 regions exist in nanostructures on the 2 nm scale.⁶²⁻⁶⁴ In this case, when lithium was removed in the oxygen release region, it was being removed from the Li_2MnO_3 regions.

This thesis will discuss the materials as existing in a solid solution but as both the $\text{Li}[\text{M}]\text{O}_2$ and Li_2MnO_3 adopt the layered structures, which coexist together. Therefore this does not change the analysis in this thesis. For instance, the $\text{Li}[\text{Li}_{1/5}\text{Ni}_{1/5}\text{Mn}_{3/5}]\text{O}_2$ material will be described as a solid solution and written as such. In reality, it is likely that a nanocomposite exists and this material could also be written $3/5\text{Li}[\text{Li}_{1/3}\text{Mn}_{2/3}]\text{O}_2 \cdot 2/5\text{Li}[\text{Ni}_{1/2}\text{Mn}_{1/2}]\text{O}_2$. In the nanocomposite, all crystallographic planes are continuous and only the cations in the transition metal layer form into 2 nm clusters, driven by an order-disorder mechanism.

1.12. Obstacles Surrounding the use of Lithium-rich Transition Metal Oxides

The high first charge capacity of lithium-rich transition metal oxides sparked excitement in the lithium-ion battery field, as seen by the devotion of research of these materials by many research groups. Although many groups described the lithium-rich oxides as being very good electrochemical performers, the fact that there are currently no commercial lithium-ion batteries containing lithium-rich transition metal oxides clearly indicates that there are barriers to the use of lithium-rich transition metal oxides as industrially-relevant positive electrode materials.

The first charge capacity at low rates of lithium-rich transition metal oxides is excellent. However, irreversible capacity loss is relatively large, rate capability is relatively poor, and the materials produced in the initial reports of lithium-rich oxides were of small size, low tap-density⁵³, and therefore would make lithium-ion batteries with low volumetric capacities and possibly poor safety characteristics.

For the transition metal oxides in the series $\text{Li}[\text{Ni}_x\text{Li}_{(1/3-2x/3)}\text{Mn}_{(2/3-x/3)}]\text{O}_2$, the irreversible capacity can range from 20 mAh g⁻¹ for $x = 5/12$ to more than 100 mAh g⁻¹ for $x = 1/6$.⁵³ Similar results were shown for the series with cobalt doping, with Kim *et al.* showing materials in the series $\text{Li}[\text{Li}_{0.1}\text{Ni}_{0.35-x/2}\text{Co}_x\text{Mn}_{0.55-x/2}]\text{O}_2$ having irreversible capacities of greater than 60 mAh g⁻¹.⁵⁸ For materials without lithium in the transition metal layer, such as the $\text{Li}[\text{Ni}_x\text{Co}_{1-2x}\text{Mn}_x]\text{O}_2$ series, the irreversible capacity is much lower, usually less than 20 mAh g⁻¹.⁵¹ The origin of the large irreversible capacity in the case of oxygen release materials is not well understood – the origin of the irreversible capacity is hinted at by, for example, Armstrong *et al.* who include transition metal reorganization in their mechanism for oxygen release.⁶¹ That is, the irreversible capacity

could be due to the loss of lithium sites in the transition metal layer when the transition metals diffuse to the lithium vacancies after lithium extraction from this layer.

Next is the relatively poor rate-capability of these materials after the oxygen loss process. Many cycling tests of the lithium-rich oxides have previously been reported for rates of $C/10$ to $C/50$ ^{17, 52, 53} (C-rate is discussed in Section 2.2). These are relatively low rates and are not suitable in the testing of positive electrode materials for high power applications. For lithium-rich oxides, the cycling capacity can decrease up to 50% of theoretical capacity at C-rate.^{65, 66} By contrast, for $\text{Li}[\text{Ni}_{1/3}\text{Mn}_{1/3}\text{Co}_{1/3}]\text{O}_2$, which is not lithium-rich, the capacity at C-rate is approximately 90% of its theoretical capacity.^{67, 68}

There have been recent efforts in an attempt to reduce the irreversible capacity and improve the rate capability of lithium-rich transition metal oxides. For instance, several groups have focused on coating the lithium-rich transition metal oxide to decrease the irreversible capacity and improve the rate capability.⁶⁹⁻⁷⁸ It has been stated that the mechanism of decreasing the irreversible capacity is to retain part of the oxygen vacancies after oxygen release so that more number of lithium sites are available for lithium insertion during discharge.⁷⁵ Others have performed some electrochemical pretreatment on the material to decrease the capacity losses associated with the lithium-rich oxides.^{79, 80} Table 1.3 shows some techniques used to address the issues.

Table 1.3. Techniques to improve the irreversible capacity and the rate-capability issues of lithium-rich TM oxides.

The “5C rate” is equivalent to approximately 1500 mA g⁻¹.

Lithium-rich material	Modification	Effect	Reference
Li[Li _{1/5} Ni _{1/5} Mn _{3/5}]O ₂	0% Al(OH) ₃ +1.4% Al(OH) ₃ +2.8% Al(OH) ₃ +5.6% Al(OH) ₃	100 mAh g ⁻¹ at 5C rate 140 mAh g ⁻¹ at 5C rate 135 mAh g ⁻¹ at 5C rate 130 mAh g ⁻¹ at 5C rate	69
Li[Li _{0.2} Ni _{0.13} Mn _{0.54} Co _{0.13}]O ₂	no treatment 3% Al ₂ O ₃	IRC = 75 mAh g ⁻¹ IRC = 41 mAh g ⁻¹	70
Li[Li _{0.1} Ni _{0.23} Mn _{0.43} Co _{0.23}]O ₂	no treatment 3% Al ₂ O ₃	IRC = 63 mAh g ⁻¹ IRC = 38 mAh g ⁻¹	
Li[Li _{0.17} Ni _{0.25} Mn _{0.58}]O ₂	no treatment 3% Al ₂ O ₃	IRC = 60 mAh g ⁻¹ IRC = 30 mAh g ⁻¹	
Li[Li _{0.2} Ni _{0.17} Mn _{0.56} Co _{0.07}]O ₂	no treatment pre-cycling treatment	210 mAh g ⁻¹ at 20 mA g ⁻¹ 250 mAh g ⁻¹ at 20 mA g ⁻¹	79
Li[Li _{0.2} Ni _{0.13} Mn _{0.54} Co _{0.13}]O ₂	no treatment 0.75% AlPO ₄ 2% 3% 4%	IRC = 75 mAh g ⁻¹ IRC = 51 mAh g ⁻¹ IRC = 27 mAh g ⁻¹ IRC = 22 mAh g ⁻¹ IRC = 30 mAh g ⁻¹	72
Li[Li _{0.2} Ni _{0.13} Mn _{0.54} Co _{0.13}]O ₂	0% 2% AlPO ₄ 3% CoPO ₄ 3% Al ₂ O ₃ 2% AlPO ₄ + 3% Al ₂ O ₃ 2% CoPO ₄ + 3% Al ₂ O ₃	IRC = 75 mAh g ⁻¹ IRC = 27 mAh g ⁻¹ IRC = 47 mAh g ⁻¹ IRC = 41 mAh g ⁻¹ IRC = 26 mAh g ⁻¹ IRC = 40 mAh g ⁻¹	73
Li[Li _{0.2} Ni _{0.17} Mn _{0.56} Co _{0.07}]O ₂	no treatment pre-cycling treatment	210 mAh g ⁻¹ at 20 mA g ⁻¹ 250 mAh g ⁻¹ at 20 mA g ⁻¹	80
Li _{1.375} Ni _{0.25} Mn _{0.75} O _{2.4375}	material is a (nano) mixture of Li[Li _{0.2} Ni _{0.2} Mn _{0.6}]O ₂ and spinel Li(Ni _{0.5} Mn _{1.5})O ₄	200 mAh g ⁻¹ at 73 mA g ⁻¹	74
Li[Li _{0.2} Ni _{0.13} Mn _{0.54} Co _{0.13}]O ₂	no treatment 2% Al ₂ O ₃ 2% RuO ₂ 1% Al ₂ O ₃ + 1% RuO ₂	100 mAh g ⁻¹ at 5C rate 110 mAh g ⁻¹ at 5C rate 140 mAh g ⁻¹ at 5C rate 160 mAh g ⁻¹ at 5C rate	75

1.13. Synthesis of Dense and Spherical Transition Metal Oxides

As particle size and density control are important in the development of positive electrode materials for lithium-ion batteries, development of techniques for size-control will be reviewed below. Because of the direct commercial application for this research, most of the studies are found in the patent literature.

The commercially applicable metal hydroxide and oxide particles are usually characterized in terms of their tap-density, size distribution, surface area, and crystallographic structure. Commercially-applicable materials must have sufficiently high tap-densities. The tap-density is found by tapping a vial containing the material for a predetermined number of taps, and calculating the mass to volume ratio of the material in the compacted state.

Industrial-scale oxide synthesis in the rechargeable battery field relies on the coprecipitation reaction for the formation of hydroxide precursors. Generally, metal sulfates or nitrates are introduced to a basic solution at a controlled rate to form the mixed metal hydroxide. Aqueous ammonia is typically added to the reaction mixture as a coordinating agent which aids in the formation of spherical hydroxide particles. The mixed-metal hydroxide is then heated to form the oxide. The density and size of the oxide particles is directly related to the density and size of the metal hydroxide precursors.

Many studies focus on the preparation of dense and spherical nickel hydroxide as it is used as the positive electrode material in nickel metal hydride rechargeable batteries. The same preparation techniques can be applied to the formation of dense and spherical mixed metal hydroxide particles to be used as precursor to positive electrode materials

(for lithium-ion batteries) of the form $\text{Li}[(\text{Ni}_{1/2}\text{Mn}_{1/2})_x\text{Co}_y(\text{Li}_{1/3}\text{Mn}_{2/3})_z]\text{O}_2$ in lithium-ion batteries. To give an idea of the maximum attainable tap-density, the crystallographic density of $\text{Ni}(\text{OH})_2$ is 4.15 g cm^{-3} .⁸¹

Makimota *et al.* prepared nickel hydroxide by the concurrent addition of 0.5-3.5 M nickel sulfate, 0.5-20 M aqueous ammonia, and 2-18 M sodium hydroxide.⁸² The aqueous solution was withdrawn from a filtered tube as the reaction proceeded. The nickel hydroxide precipitate was then filtered and dried. The material obtained had a tap-density of $1.9\text{-}2.1 \text{ g cm}^{-3}$ and an average particle diameter of approximately 10-20 μm .

Konstantinov *et al.* reported a solution to the difficulty in controlling the reaction conditions of the nickel hydroxide precipitation reaction.⁸³ Formation of particles of irregular shapes and a wide range of sizes was attributed to even a small deviation in the synthetic conditions (reagent type and concentration, flow rate, pH, reaction temperature, and reaction time). The precipitation reaction was carried out in a similar manner as previous reports, with nickel nitrate, aqueous ammonia, and sodium hydroxide mixed to precipitate nickel hydroxide. In this case, the final suspension was spray dried resulting in spherical particles with a particle size of 2-5 μm .

Although the Konstantinov report claimed to have an easier preparation route, investigations continued without using the spray drying procedure. Shin *et al.* formed nickel hydroxide from 1.8-2.6 M nickel sulfate, 10-16 M aqueous ammonia, and 4-10 M sodium hydroxide at a pH of 11-11.5.⁸¹ Tap-densities obtained were 1.90 g cm^{-3} with particle sizes of 8-40 μm . Addition of boron to the material increased the tap-density to 2.15 g cm^{-3} . Boron was added by introducing boric acid during the reaction. The increase in the tap-density was attributed to the restriction of the formation of low-density

γ -NiOOH material by boron. In a separate report, Shin *et al.* obtained tap-densities of up to 2.27 g cm^{-3} by the addition of small amounts of cobalt, zinc, and cadmium sulfates.⁸⁴

Similarly, Ikoma *et al.* had positive results adding salts of cadmium, calcium, zinc, magnesium, iron, cobalt, and manganese to a nickel sulfate solution as the precipitation reaction was carried out.⁸⁵ This study also illustrates the sensitivity of the precipitation reaction. Nickel hydroxide (with added cobalt and zinc) was found to have a tap-density of 2.3 g cm^{-3} at pH = 11.0 and 1.8 g cm^{-3} at pH = 11.6.

Aladjov prepared nickel hydroxide with an altered surface morphology by the application of ultrasonic energy to the reaction mixture.⁸⁶ The nickel hydroxide particles synthesized with addition of ultrasonic energy were found to have approximately the same tap-density (2.0 g cm^{-3}) but with higher surface area leading to 14-18% higher capacities. Since increased surface area may also lead to increased contact with the electrolyte in lithium-ion batteries, it is unknown if the application of ultrasonic energy will be beneficial for commercial applications.

Wakao showed that ammonia solution can be substituted by the amino acids glycine, DL-aniline, β -aniline, and glyclglycine.⁸⁷ The benefit of replacing ammonia would be in eliminating odors and reducing possible corrosion in the reactors. This method was able to produce nickel hydroxide with tap-densities of 2.0 - 2.1 g cm^{-3} .

Investigations into the formation of spherical mixed-metal hydroxides and oxides have been carried out recently. The oxides are formed by heating the hydroxides in air at temperatures of 700 - $1100 \text{ }^\circ\text{C}$. The metal oxide typically has a higher tap-density than the non-heated hydroxide. Results given in the literature may discuss only the oxide, only the hydroxide, or both oxide and hydroxide.

Komatsu *et al.* reported the formation of a manganese-nickel hydroxide of the form $[\text{Ni}_{0.9}\text{Mn}_{0.1}](\text{OH})_2$ with a tap-density of 2.2 g cm^{-3} .⁸⁸ Cho *et al.* presented the electrochemical properties of dense and spherical $\text{LiNi}_{0.74}\text{Co}_{0.26-x}\text{Mg}_x\text{O}_2$ and $\text{LiNi}_{0.74}\text{Co}_{0.26}\text{O}_2$ ^{89, 90}. Ito *et al.* coprecipitated various compositions of a hydroxide of nickel, manganese, and cobalt.⁹¹ Tap-density of this material was as high as 1.9 g cm^{-3} . Ying *et al.* synthesized spherical $\text{LiNi}_{0.8}\text{Co}_{0.2}\text{O}_2$ with a tap-density of 3.2 g cm^{-3} (2.25 g cm^{-3} for the hydroxide) and a capacity of 170 mAh/g .⁹²

Following the relatively recent development of the $\text{Li}[\text{Ni}_{1/3}\text{Co}_{1/3}\text{Mn}_{1/3}]\text{O}_2$, studies have been carried out on increasing the tap-density of the material.⁹³⁻⁹⁵ Ohzuku *et al.* developed a novel reactor in which the precipitate is pumped and meets the incoming raw materials forming spherical $\text{Li}[\text{Ni}_{1/3}\text{Co}_{1/3}\text{Mn}_{1/3}]\text{O}_2$ with a large particle size.⁹³ Lee *et al.* studied the effect of stirring speed, ammonia concentration, and pH on $\text{Li}[\text{Ni}_{1/3}\text{Co}_{1/3}\text{Mn}_{1/3}](\text{OH})_2$.⁹⁴ It was found that high stirring speeds, high ammonia concentrations, and low pH-values result in high tap-density materials. He *et al.* synthesized $\text{Li}[\text{Ni}_{1/3}\text{Co}_{1/3}\text{Mn}_{1/3}]\text{O}_2$ with a tap-density of 2.2 g cm^{-3} and a capacity of 179 mAh/g .⁹⁵

Table 1.4 shows the synthetic conditions for the coprecipitation reaction to make spherical and dense hydroxides and oxides. The table gives pH, T_{rxn} (temperature), $[\text{NH}_3]$ (concentration of aqueous ammonia), $[\text{metal salt}]$ (concentration of metal salt), $[\text{NaOH}]$ (concentration of sodium hydroxide), t_{rxn} (overall reaction time), and τ (residence time = volume/total flow rate) for the coprecipitation reaction. The table also gives particle size, tap density, T_{oxide} (temperature to synthesize oxide), capacity, and voltage range for the mixed metal hydroxides or oxides, as indicated.

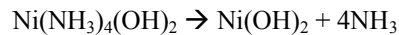
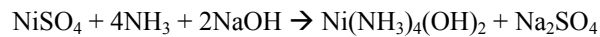
Table 1.4. Spherical metal hydroxide and oxide synthesis conditions

Material	pH	T_{rxn} (°C)	[NH ₃] (M)	[metal salt] (M)	[NaOH] (M)	t_{rxn} (h)	τ (h)	Particle size (μm)	Tap-density (g cm^{-3})	T_{oxide} (°C)	Capacity (mAh/g)	Voltage range (V)	Reference
Ni(OH) ₂			0.07	0.4	1.5				2.12				82
Ni(OH) ₂	12	65			6		2-4	2-5					83
Ni(OH) ₂ 1.2% B 3.8% Co 3.1% Zn	11	50	0.5:1 NH ₃ :Ni ²⁺	2.6	6.0		4	2-40	2.15				81
Ni(OH) ₂	11	50	0.5:1 NH ₃ :Ni ²⁺	2.3	6.0		4	2-50	2.14				84
Ni(OH) ₂ 3.7% Zn 0.5% Co	11.0	35							2.3				85
Ni(OH) ₂	11.0	50						2-30	2.24				96
Ni(OH) ₂	11-13	20-80						12	2.04				86
Ni(OH) ₂	11.0	60	1 (glycine)	2	6			10-30	2.05				87
Ni(OH) ₂	12.0	40	5	2	5			8	2.01				97
Ni(OH) ₂	12.3-12.8	47	29%	10%				12	1.93				98
Ni _{0.1} Mn _{0.9} (OH) ₂	12.5	30	6.5	1.75	6			30	2.2				88
LiNi _{0.74} Co _{0.26} O ₂	10							5 13 25		700	205 210 208	3.0-4.3	90
[Ni:Co:Mn](OH) ₂ 35:20:9	12.6			4.3	30%	120			1.91				91
Ni _{0.8} Co _{0.2} (OH) ₂ LiNi _{0.8} Co _{0.2} O ₂	11.5	60	0.6	2.0	5.0		10		2.25 3.25	750	172	3.0-4.3	92
LiNi _{1/3} Mn _{1/3} Co _{1/3} O ₂ LiNi _{1/2} Mn _{1/2} O ₂ LiNi _{1/4} Co _{3/4} O ₂			4.8	3.6	4.8					1000	165 154 129	3.0-4.3	93
LiNi _{0.79} Co _{0.19} Mg _{0.02} O ₂	11		1	2.5	6	6			2.4	750	160	2.8-4.1	99
Ni _{1/3} Mn _{1/3} Co _{1/3} (OH) ₂ LiNi _{1/3} Mn _{1/3} Co _{1/3} O ₂	11	60	0.36	2.0	2.0	12			1.79 2.39	1000	177	2.8-4.5	94
Ni _{0.8} Co _{0.2} (OH) ₂ LiNi _{0.8} Co _{0.2} O ₂	11-12	65-70	1	1	3.6-4.0	12		30	2.20	750	160	3.0-4.35	100
Ni _{1/3} Mn _{1/3} Co _{1/3} (OH) ₂ LiNi _{1/3} Mn _{1/3} Co _{1/3} O ₂		15-90	2.0	0.5		12			2.19	1000	179	2.8-4.5	95

1.14. Effect of Ammonia on Particle Growth

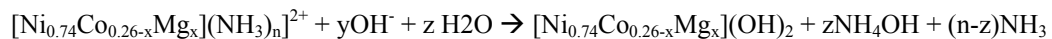
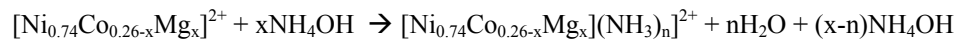
Ammonia first complexes with the metal ions (from the metal sulfate or nitrate entering the reaction), reducing the precipitation reaction rate as nickel ions are gradually added to the basic solution to form metal hydroxide.⁸¹ The metal sulfate and aqueous ammonia are either added simultaneously or premixed in a separate reaction vessel to form the amine complex $[M(\text{NH}_3)_6]^{2+}$.⁸⁶ A premix may provide more control in the kinetics of the overall reaction but can also result in the form of unwanted precipitates outside the reaction vessel.⁸⁶

Junichi *et al.* present the reaction of nickel sulfate with ammonia and sodium hydroxide as follows⁹⁷:



By following this reaction scheme, no more than four moles of ammonia are needed for each mole of nickel sulfate. Junichi *et al.* report that even 0.5 molar equivalents will suffice since aqueous ammonia is a product of the second reaction, the formation of $\text{Ni}(\text{OH})_2$.⁹⁷

Cho *et al.* describe the formation of spherical $[\text{Ni}_{0.74}\text{Co}_{0.26-x}\text{Mg}_x](\text{OH})_2$ and this is given below⁸⁹



This reaction scheme was also reported by Lee *et al.* in the formation of $\text{Ni}_{1/3}\text{Mn}_{1/3}\text{Co}_{1/3}(\text{OH})_2$.⁹⁴

1.15. Scope of Thesis

Chapter 2 describes the experimental techniques used in this thesis. Chapter 3 goes into the study of the mixed metal hydroxides made by the coprecipitation reaction and their conversion into oxyhydroxide. Chapter 4 details the preparation of spherical and dense mixed metal hydroxides via the coprecipitation reaction in the presence of ammonia, with analysis of the hydroxide growth mechanism. Chapter 5 gives insight into the diffusion during the first charge of lithium-rich transition metal oxides. Chapter 6 describes the investigation of lithium-rich transition metal oxides using isothermal microcalorimetry. Chapter 7 outlines further work that was carried out in the field of lithium-rich transition metal oxides. Conclusions and suggestions for future work are given in Chapter 8.

CHAPTER 2. Experimental

2.1. X-ray Diffraction

In X-ray diffraction studies, X-rays are produced in an X-ray tube: electrons hit a target in the X-ray tube as they are accelerated between two electrodes with a voltage in the magnitude of 10,000 V.¹⁰¹⁻¹⁰³ Diffraction of X-rays can occur once the X-rays hit a crystalline sample. Diffraction of X-rays can be used to indirectly resolve the atomic structure of materials. For instance, lattice constants can be resolved to 0.0001 Å. This section will give basic descriptions of the crystal lattice, Bragg's law, the geometric structure factor, and the Bragg-Brentano X-ray diffractometer.

2.1.1. Crystal Lattice

A crystal lattice is composed of atoms, molecules, or ions arranged in repetition with certain symmetry in the arrangement.¹⁰² If the actual constituents of a crystal (atoms, molecules, or ions) are ignored, the lattice can be represented by a three-dimensional array of points, called lattice points. A unit-cell can be found within these points, defined by three lattice vectors and three interior angles, shown in Figure 2.1.

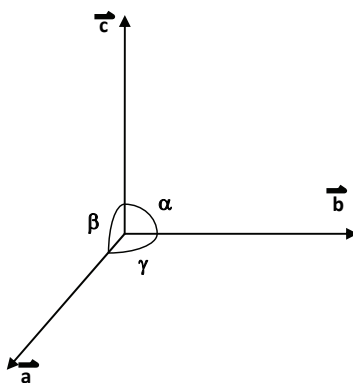


Figure 2.1. The unit cell parameters.

The schematic shows three lattice vectors (\vec{a} , \vec{b} , and \vec{c}) and three interior angles (α , β and γ).

The fractional atomic coordinates in the \vec{a} , \vec{b} , and \vec{c} directions are designated x , y , and z . The orientations of planes in a crystal lattice are designated using Miller indices. For the Miller index (hkl) , the planes intercept the unit cell at $x=1/h$, $y=1/k$, and $z=1/l$. This results in a family of planes for the entire crystal, with the Miller index (hkl) . Figure 2.2 shows the family of (003) planes in $\text{Li}[\text{Ni}_{1/3}\text{Mn}_{1/3}\text{Co}_{1/3}]\text{O}_2$.

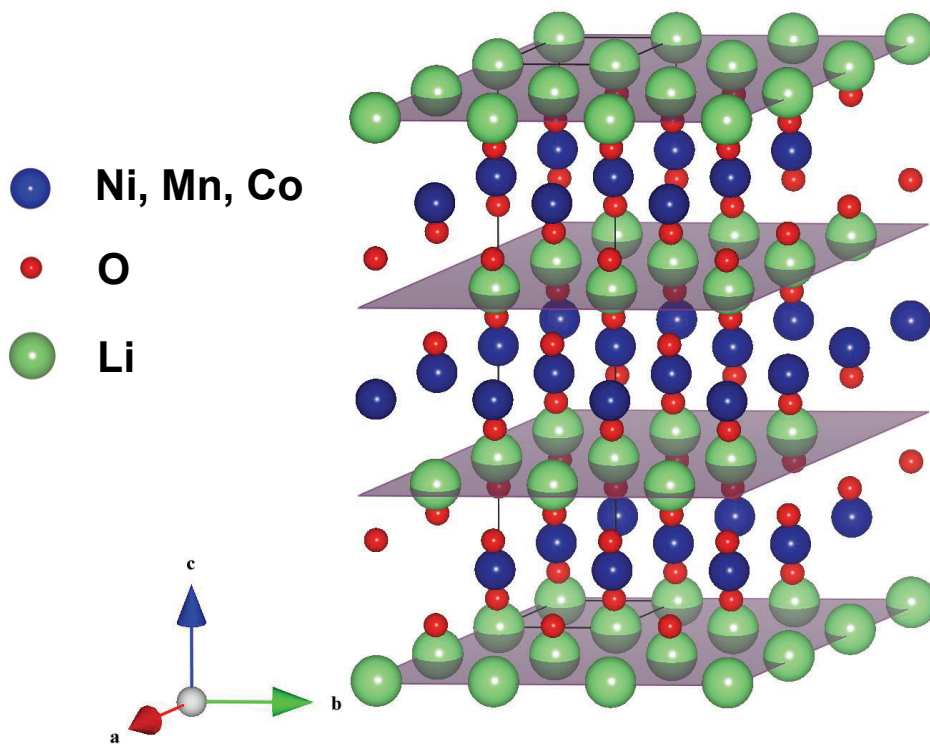


Figure 2.2. The (003) family of planes in $\text{Li}[\text{Ni}_{1/3}\text{Mn}_{1/3}\text{Co}_{1/3}]\text{O}_2$.
The planes are shown as grey slices.
The oxygen atoms are drawn smaller than scale so that the positions of the lithium atoms are clear.

2.1.2. Bragg's Law

Figure 2.3 shows a view of the (100) plane in $\text{Li}[\text{Ni}_{1/3}\text{Mn}_{1/3}\text{Co}_{1/3}]\text{O}_2$. The arrows indicate the X-ray scattering that exists from the (003) planes in this material.

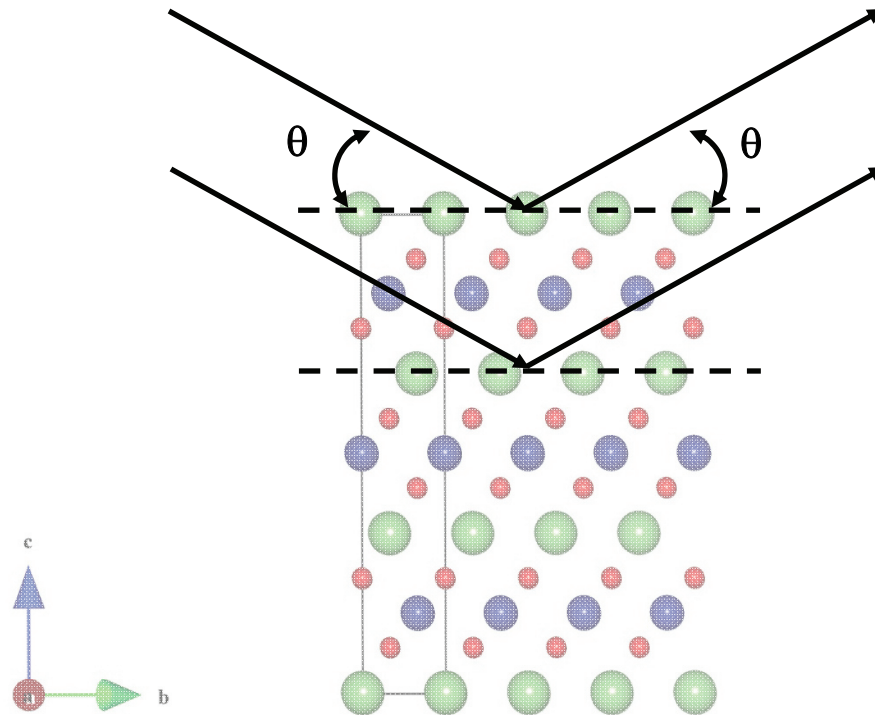


Figure 2.3. Schematic of X-ray scattering in $\text{Li}[\text{Ni}_{1/3}\text{Mn}_{1/3}\text{Co}_{1/3}]\text{O}_2$. The view is of the (100) plane in $\text{Li}[\text{Ni}_{1/3}\text{Mn}_{1/3}\text{Co}_{1/3}]\text{O}_2$ showing X-ray scattering from the (003) planes.

The identity of the atoms are the same as in Figure 2.2.

Constructive interference will occur if the X-rays scattered are in-phase.¹⁰²

Bragg's law dictates which scattered X-rays are in-phase and is written as

$$n\lambda = 2d \sin \theta, \quad (2.1)$$

where λ is the X-ray wavelength, d is the spacing between the relevant planes in the material, and θ is the incident angle of the X-rays with respect to the plane of the sample.

In the example of scattering from the (003) planes in $\text{Li}[\text{Ni}_{1/3}\text{Mn}_{1/3}\text{Co}_{1/3}]\text{O}_2$ shown in Figure 2.3, the scattering angle, 2θ , can be determined from the lattice parameters and Bragg's law. With $c = 14.25 \text{ \AA}$ for $\text{Li}[\text{Ni}_{1/3}\text{Mn}_{1/3}\text{Co}_{1/3}]\text{O}_2$ ¹⁶, $d_{(003)} = 4.75 \text{ \AA}$. Bragg's law (Equation 2.1) gives a scattering angle of 18.9° .

2.1.3. Geometrical Structure Factor

The intensity of an X-ray scattered by a single electron was determined by Thompson as

$$I = \frac{I_o r_e^2}{r^2} \left(\frac{1 + \cos^2(2\theta)}{2} \right), \quad (2.2)$$

where I_o is the intensity of the incident X-ray beam, r_e is the classical radius of an electron, r is the distance from the electron to the detector, and θ is the angle between the incident beam and the beam collected at the detector.¹⁰²

In an atom with more than one electron, the scattering of the X-ray beam results in constructive and destructive interference. If one considers two X-ray beams, scattered from two different electrons in the atom at $\theta = 0^\circ$, then the X-rays emerge from the atom in-phase. If viewed at a larger angle, the X-ray paths will be of different length. Since the atomic radii are on the order of the X-ray wavelength, destructive interference is likely to occur. This results in the atomic scattering factor, f_o . The atomic scattering factor depends on the atom, its charge, the X-ray wavelength, and the scattering angles. The atomic scattering factor is normalized to the scattering from one electron. Therefore,

when the X-ray beam emerges in-phase, the atomic scattering factor is equal to the number of electrons in an atom or ion. Thermal motions of the atom lead to a large effective size of the atom. This gives rise to more deconstructive interference, decreasing the atomic scattering factor.

To estimate the scattering intensity from a crystal, one must consider the interference effects of the atoms in the unit cell. The geometric structure factor takes this into account and is given as

$$F_{hkl} = \sum_{j=1}^m f_j \exp[2\pi i(hx_j + ky_j + lz_j)], \quad (2.3)$$

where f_j is the atomic scattering factor, h , k , and l are the Miller indices (hkl), and x , y , and z are the fractional coordinates of the atom in the unit cell.¹⁰² The observed intensity of a Bragg reflection in an XRD experiment is proportional to F_{hkl}^2 and the intensity can be further determined taking into account the experimental parameters.

2.1.4. Bragg-Brentano Diffractometer

In the investigations outlined in this thesis, a Siemens D5000 diffractometer equipped with a Cu-target X-ray tube and a diffracted beam monochromator was used to collect powder diffraction patterns of the synthesized materials. Figure 2.4 shows a schematic of a Bragg-Brentano X-ray diffractometer.¹⁰² The X-ray beam emerges from the point the electron beam hits the copper target, the focus point (F), where it passes through a divergence slit (DS) and a parallel plate collimator set (SS1) to the specimen (S). The diffracted X-rays leave the specimen at an angle of 2θ with respect to the incident beam. The X-ray beam goes through another parallel plate collimator set (SS2) and a receiving slit (RS) and then goes to a diffracted beam monochromator. The

diffracted beam monochromator consists of a crystal (C) and a detector slit (DS). The X-ray beam is finally detected at a detector (D). Figure 2.5 shows a picture of the Siemens D5000 diffractometer.

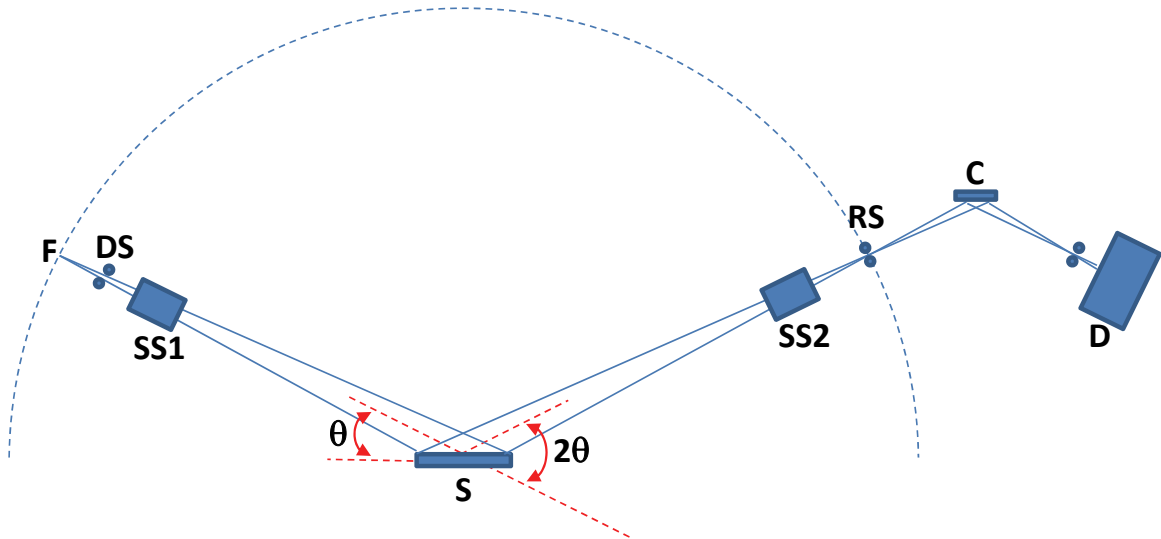


Figure 2.4. Schematic of the Bragg-Brentano diffractometer. It shows the line of focus of the X-ray tube (F), the divergence slit (DS), the first Soller slit (SS1), the specimen (S), the second Soller slit (SS2), a crystal for the divergent beam monochromator (C), a detector slit (DS), and the detector (D). Adapted from reference 102.



Figure 2.5. Picture of a Siemens D5000 diffractometer.

2.1.5. Rietica Refinement using Rietica

A diffraction pattern can be fit with a calculated diffraction pattern, which can be calculated from crystal structure data.¹⁰² The Rietveld method is a typical procedure that is carried out in quantitative phase analysis of an experimental XRD pattern. In the Rietveld method, refinement is carried out by minimizing the sum of the weighted, squared difference between the calculated and the experimental XRD patterns.

For each phase, the space group, identity of the atoms, approximate atom positions, and approximate lattice parameters must be known. With this information, the diffraction lines and the relative intensities can be estimated. In the Rietveld method, the least squares residual, R , is minimized:

$$R = \sum_j w_j |I_{j(o)} - I_{j(c)}|^2, \quad (2.4)$$

where the step j is that of the 2θ scale, w_j is the statistical weight, $I_{j(o)}$ is the experimental intensity, and $I_{j(c)}$ is the calculation intensity. The calculated intensity is initially based on calculations using the geometric structure factor as described in Section 2.1.3. Additional corrections such as background, preferred orientation, and peak shape functions can be carried out. A Rietveld scale factor, S , is applied to fit the calculated intensities to that of the measured sample. Details on the variables involved in the Rietveld analysis can be found in reference 102.

By fitting the experimental data (by varying the structural information used for the calculation), information about the sample can be determined. This includes refined lattice parameters, atom positions, sample purity, and preferred orientation. In this thesis, the computer software Rietica¹⁰⁴ was used for Rietveld refinement of the XRD patterns.

2.2. Electrochemical Cell Testing

Figure 2.6 shows a schematic of the electrochemical cell used for testing electrode materials. All cell assembly was carried out in an argon-filled glove box. The working electrodes were prepared by mixing the active material with a binder and conductive carbon in a solvent and spreading on aluminum foil. The working electrode was placed on the bottom casing. A separator was placed on the electrode and electrolyte was placed on the working electrode and separators. Lithium was placed on the separator. A spacer and spring were placed on the lithium. The casing top, fixed with a gasket, was placed on the rest of the cell. Two crimpers in the glove box seal the cell and the cells could be taken outside the glove box for testing. Before testing, stainless steel metal tabs were welded onto the positive and negative ends of the cell so they could be attached to the cell chargers.

For the electrochemical tests, cell chargers operated at a constant current mode, with the voltage of the cell being measured. In a typical electrochemical cell experiment, a current was selected depending on the rate of lithium deintercalation and intercalation desired. The rate can be given in terms of C-rate, which is the current applied such that the theoretical amount of lithium is deintercalated (or intercalated) in one hour. With a theoretical capacity of 274 mAh g^{-1} (see Section 1.3), the C-rate of LiCoO_2 corresponds to a current of 274 mA g^{-1} . Any fraction of this C-rate is a fraction of the C-rate current. As well, minimum and maximum cell voltages are chosen, at which the chargers change between the charge and discharge processes. In this way, the charge-discharge profiles (voltage versus time or specific capacity) can be obtained. Example of such profiles are shown in Chapter 1.

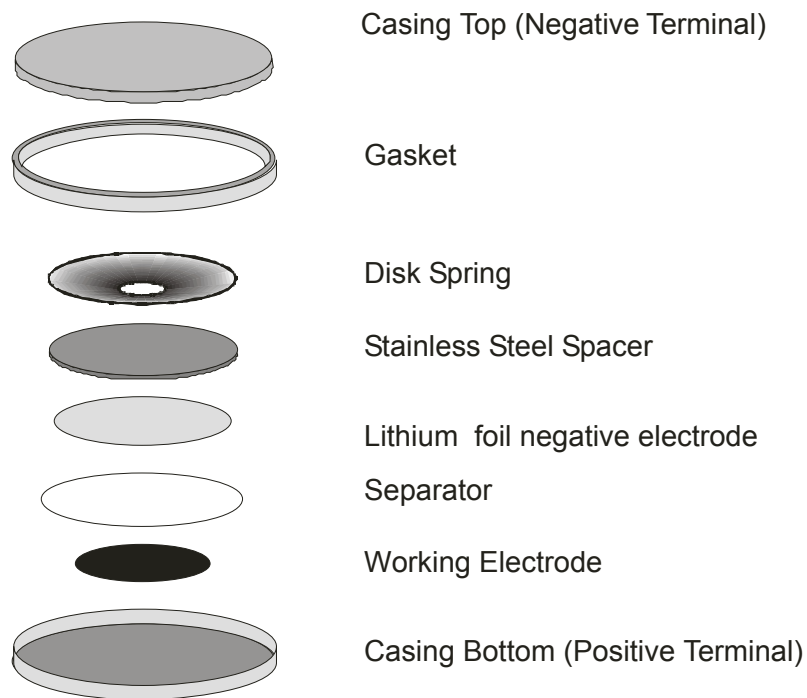


Figure 2.6. Exploded view of the electrochemical cell used for lithium battery testing.

In the investigations in this thesis, electrochemical tests were carried out using a standard 2325 cell with the positive electrode cycled versus lithium foil. The electrolyte used was 1 M LiPF_6 in 1:2 ethylene carbonate/diethyl carbonate (Novolyte Technologies). The active material electrodes contained 7% poly(vinylidene fluoride) binder (Kynar 301P, Elf Atochem) and 7% Super S carbon black (MMM Carbon).

2.3. Scanning Electron Microscopy

A scanning electron microscope (SEM) was used to image materials with micron and submicron-sized particles. Figure 2.7 shows a schematic drawing of a scanning electron microscope.

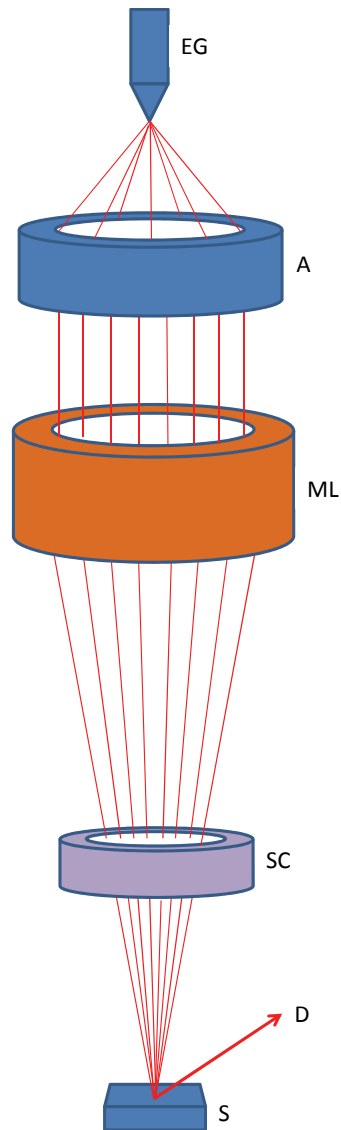


Figure 2.7. Schematic drawing of a scanning electron microscope (SEM). It shows the electron gun (EG), anode (A), magnetic lenses (ML), scanning coils (SC), sample stage (S), and the electron beam directed toward the detector (D). Adapted from reference 105.

An electron beam, with a typical energy from 1-40 keV, is produced by an electron gun and is directed towards the sample.¹⁰⁵ The electron beam diameter, or the spot size of the electron beam, dictates the resolution at which the SEM operates. The electron beam can be focused and narrowed with electron lenses, to a spot size of less than 10 nm. The electron beam scans the sample as it is directed by scan coils. A smaller raster size of the specimen results in a higher magnification. The electron beam interacts with the atoms of the sample and a range of radiation products are produced and detected (backscattered and secondary electrons). In this way, local topography can be probed.

All SEM images in this thesis were obtained with a Hitachi S4700 cold-field emission scanning electron microscope. Figure 2.8 shows a picture of this SEM. The SEM was operated with an electron beam energy of 15 keV and a current of 5 μ A.



Figure 2.8. Picture of a Hitachi S4700 field-emission scanning electron microscope.

2.4. Thermogravimetric Analysis

Thermogravimetric analysis measures the change in mass of a material as a function of temperature in a controlled atmosphere.¹⁰⁶ Figure 2.9 shows a top-view schematic of a TGA instrument with a dual-balance design. Before the TGA experiment, the masses of the reference (R) and sample (S) pans are zeroed. The sample is placed in the sample pan and the reference pan is empty. During the TGA experiment, gas (G) flows through the TGA instrument while it is heated with the furnace (F). The mass measured on the sample pan is determined in reference to the reference pan.

In this thesis, thermogravimetric analysis was carried out using a TA Instruments SDT Q600 dual-beam instrument. Figure 2.10 shows a picture of this instrument. The flowing gas was air, the temperature range was 30 – 300°C, and the temperature was increased at a rate of 1°C min⁻¹.

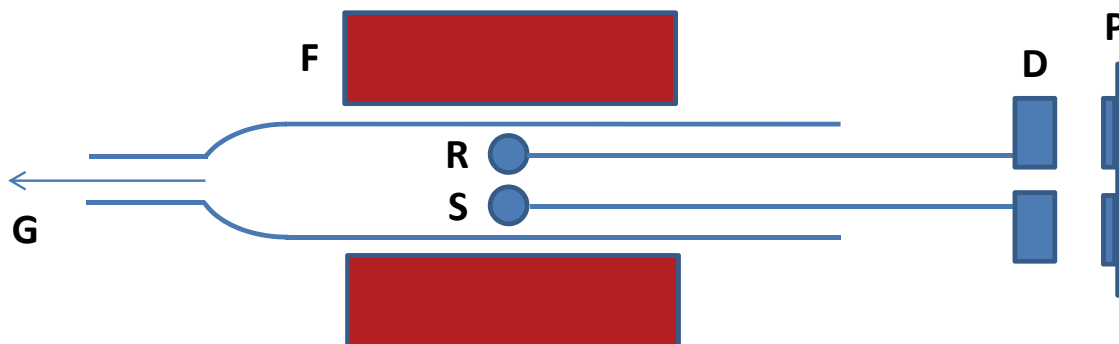


Figure 2.9. Top-view schematic of a dual-beam TGA instrument. It shows the reference pan (R), sample pan (S), furnace (F), gas flow (G), dual-balance mechanism (D), and photodiodes and sensors (P). Adapted from reference 106.

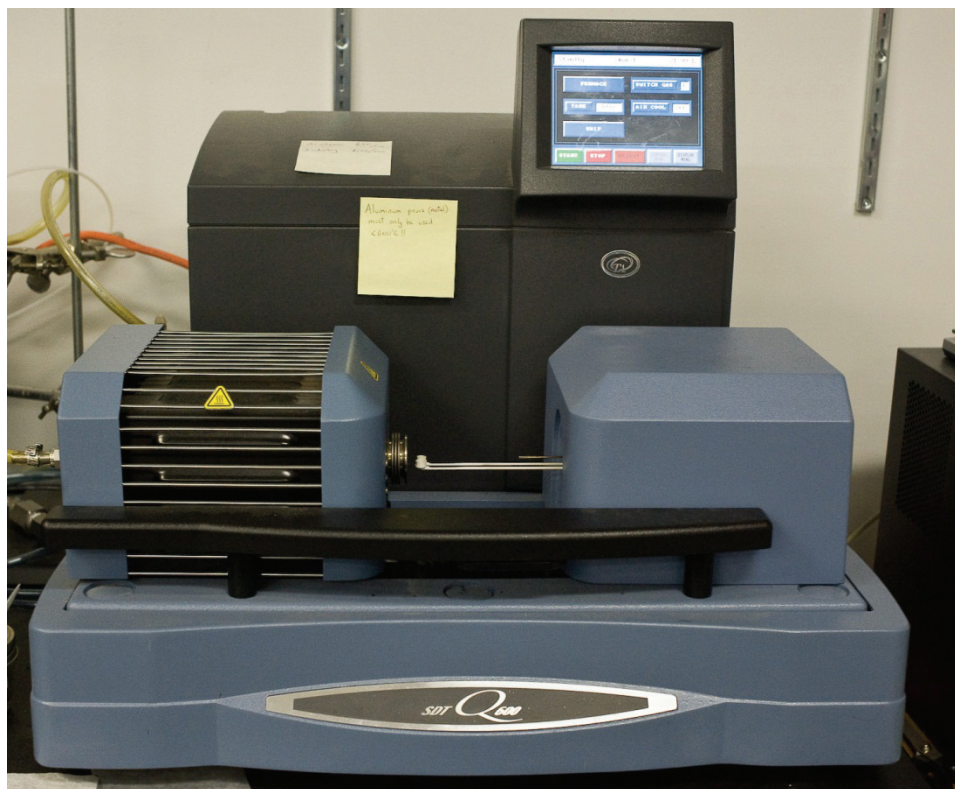


Figure 2.10. Picture of a TA Instruments SDT Q600.

2.5. Continuous-Stirred Tank Reactor

The synthesis of the metal hydroxides was carried out using a continuous-stirred tank reactor (CSTR). Figure 2.11 shows a picture of the CSTR and Figure 2.12 shows a schematic drawing of the reactor. The reactor consists of reagent pumps and controls for pH, temperature, and reaction atmosphere described in Section 2.5.1.

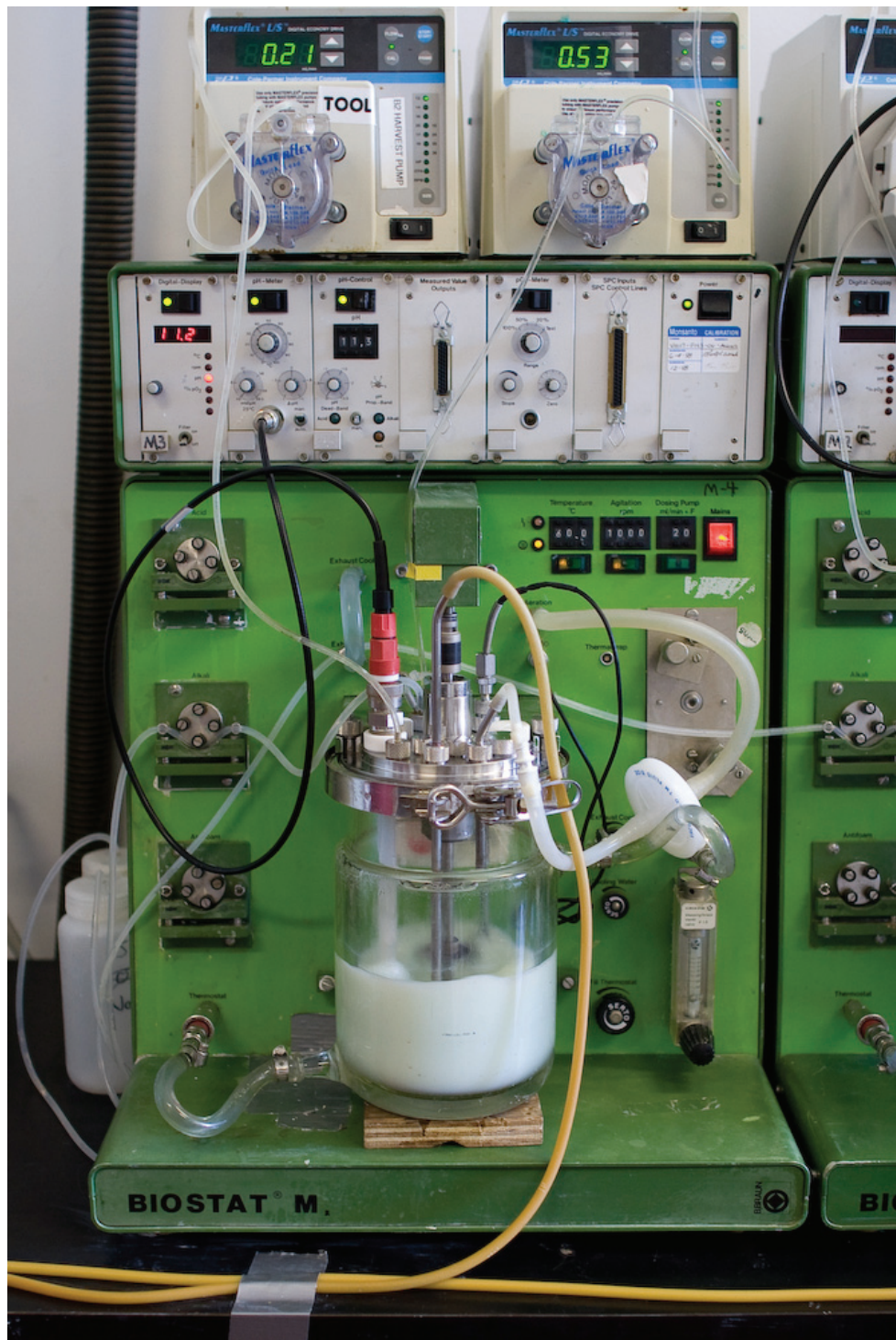


Figure 2.11. Picture of the continuous-stirred tank reactor (CSTR).

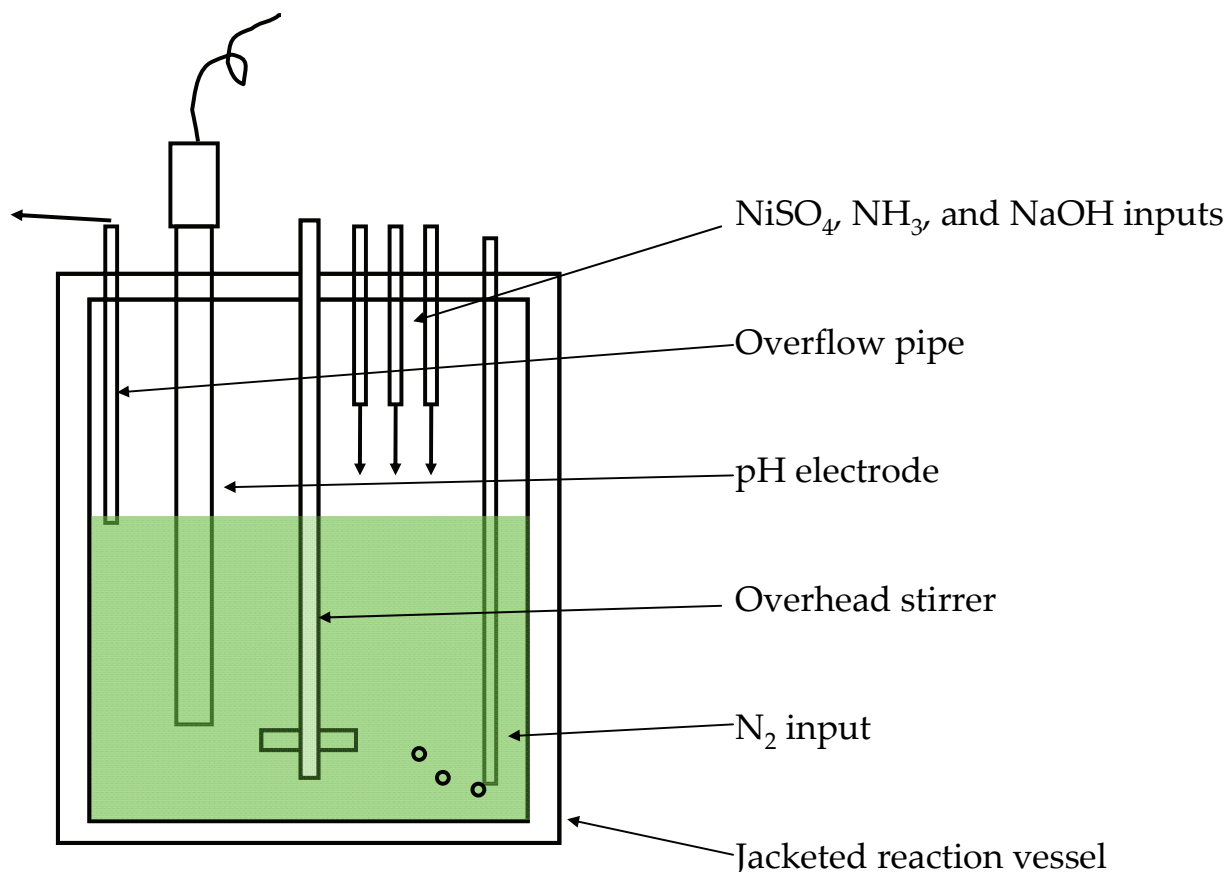


Figure 2.12. Schematic drawing of the continuous-stirred tank reactor (CSTR).

2.5.1. Typical CSTR Reaction

The reagents used in the investigations in this thesis included nickel (II) sulfate hexahydrate (98%, Alfa Aesar), manganese sulfate monohydrate (Alfa Aesar, 98%), cobalt sulfate heptahydrate (Alfa Aesar, 98%), sodium hydroxide (Alfa Aesar), and ammonium hydroxide in aqueous solution (28.0-30.0%, Sigma-Aldrich). All solutions were prepared with deionized water which was deaerated by boiling for 10 minutes.

A coprecipitation reactor with a 2 L jacketed reaction vessel equipped with pH and temperature controllers was used. Reagents were added using digital peristaltic pumps (Masterflex L/S 07524) and sodium hydroxide addition was automatically

controlled by the pH controller and added as required by a peristaltic pump on the reactor. Reaction contents were maintained at a temperature of 60°C and the contents of the reactor were stirred by an overhead stirrer at 1000 rpm. Nitrogen was bubbled (60 sccm) into the reactor throughout the reaction.

The pH meter and electrode (Mettler-Toledo InLab 424) were calibrated at 60°C using buffer solutions. The pH-values of the buffer solutions were 7.0 at 60°C (Fisher Scientific) and 11.1 at 60 °C (Fixanal, Riedel-de Haën).

A volume of 1 L of a 1 M NH₃(aq) solution made in de-aerated water was heated to 60°C. The reaction proceeded with the addition of 10.0 M NH₃(aq) at 0.005 L/h and 2.0 M MSO₄ (M = Ni, Co and/or Mn in equimolar ratios) at 0.025 L/h. A concentration of 5.0 M NaOH was automatically added to the reaction contents to maintain the desired pH. The rate of NaOH solution addition was near the predicted value of 0.02 L/h based on the expected co-precipitation reaction. The reaction vessel was fitted with an overflow pipe and the reaction contents were pressurized with nitrogen to ensure a constant volume during the reaction. The residence time, given by the total flow rate of the reagents and the reactor volume, was set to be 20 h. The total reaction time varied depending on the reaction. After reaction, the solid material was filtered and washed with 3 L deaerated deionized water in several rinses.

2.6. Tap-Density Measurements

The tap density of a material measures the ratio of mass to volume of the bulk material when tapped in a container. If an active material for a lithium ion battery has a

high tap density, more material can be added to the cell, giving the cell a higher volumetric energy density.

Figure 2.13 shows a picture of the tap density measuring device. A tap density measuring device taps a sample in a container (such as a graduated cylinder). In this thesis, tap densities were determined using a VanKel tap density measuring device. A 25 ml graduated cylinder and 1000 taps were used.



Figure 2.13. Picture of a VanKel tap density measuring device.

2.7. Isothermal Microcalorimetry

Isothermal microcalorimetry (IMC) is used to probe small changes in heat associated with chemical or physical changes in a material.¹⁰⁷ In an IMC experiment, the

net heat flow rate between a sample (placed in a sample well) and its surrounding is measured, at a constant temperature. A reference well can be used, with the heat flow to or from the test well being measured relative to the reference well.

In this thesis, a Calorimetry Sciences Corp. (CSC) 4400 isothermal microcalorimeter was used to investigate the heat change in $\text{Li/Li}[\text{Li}_{1/9}\text{Ni}_{1/3}\text{Mn}_{5/9}]\text{O}_2$ and $\text{Li/Li}[\text{Li}_{1/5}\text{Ni}_{1/5}\text{Mn}_{3/5}]\text{O}_2$ cells during charge and discharge. Figure 2.14 shows a block diagram of this calorimeter. A coin cell (section 2.2) was placed in the sample well and a dummy cell of equivalent size, shape, and mass was placed in the reference well. A review of heat conduction and microcalorimetry can be found in reference 107.

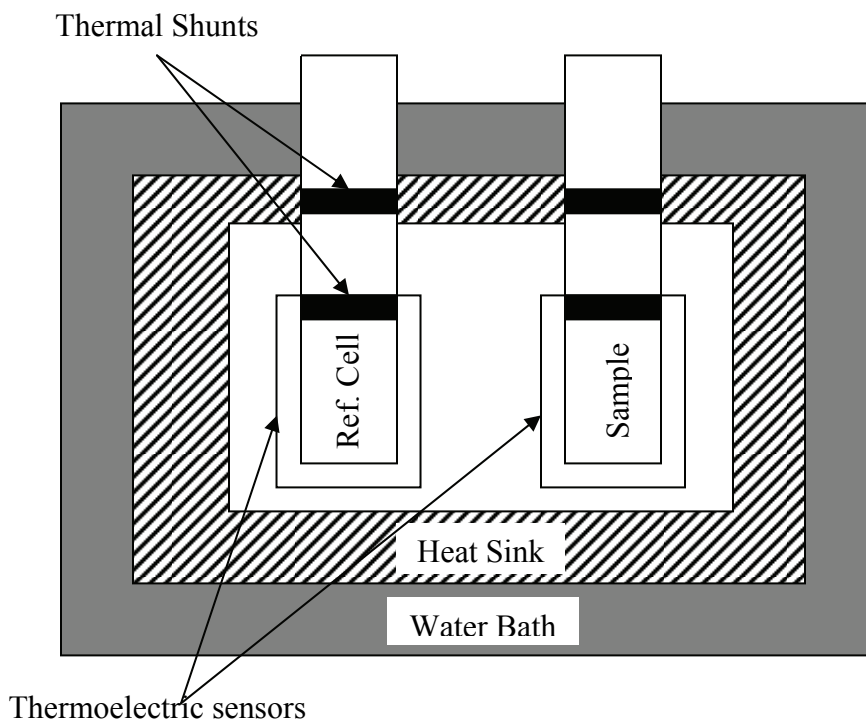


Figure 2.14. Block diagram of the Calorimetry Sciences Corp. (CSC) 4400 isothermal microcalorimeter. Adapted from reference 107.

2.8. Size-Distribution Analysis

The use of light scattering and diffraction measurements can determine the size of particles of a material from 0.1 to 1000 μm .^{108, 109} A special case of Mie theory, called Fraunhofer diffraction, explains that the scattering angle is inversely proportional to the size of the particle and the intensity of the scattered light is proportional to the fourth power of the particle diameter.¹⁰⁸

In this thesis, particle size analysis was carried out using a Leeds and Northrup Microtrac Standard Range Analyzer. The instrument measured particles from 1.9 – 176 μm with a helium-neon laser (0.63 μm). Figure 2.15 shows a schematic of the Microtrac standard range particle size analyzer.¹⁰⁸ The laser (L) path passed through a sample cell (S) in which the particles are suspended in a turbulent flow circulating system. The mask (M) separates the diffraction pattern into 13 separate zones. Light passes through each zone sequentially and its intensity is measured at a photodetector (D). This allows the 13 different sizes to be analyzed, with the amount of each size related to the detected intensity.

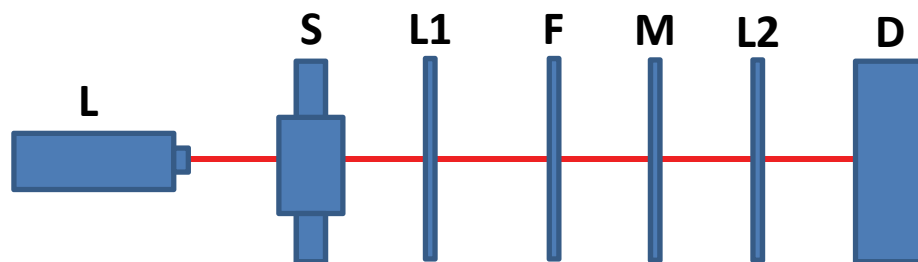


Figure 2.15. Schematic of the Microtrac standard range particle size analyzer. The components are He-Ne laser (L), sample and drain (S), first lens (L1), fixed sector disk (F), rotating disk with 13 masks (M), second lens (L2), and photo-detector (D). Adapted from reference 108.

CHAPTER 3. Investigation of $\text{Ni}_{1/3}\text{Mn}_{1/3}\text{Co}_{1/3}(\text{OH})_2$

The $\text{Ni}_{1/3}\text{Mn}_{1/3}\text{Co}_{1/3}(\text{OH})_2$ precursor in the production of $\text{Li}[\text{Ni}_{1/3}\text{Mn}_{1/3}\text{Co}_{1/3}]\text{O}_2$ (NMC) as a positive electrode material in lithium-ion batteries is typically synthesized via a co-precipitation reaction between aqueous metal salts and base.^{15-17, 50-53, 65, 110-118} The metal salts are sulfates or nitrates of nickel, manganese, and cobalt. The base used is typically sodium hydroxide or lithium hydroxide. Others have suggested instead that the precursor is the oxyhydroxide phase, $\text{Ni}_{1/3}\text{Mn}_{1/3}\text{Co}_{1/3}\text{OOH}$.^{49, 119} Recent research into the formation of dense and spherical NMC-oxide precursors using the coprecipitation reaction has labeled the heated $\text{Li}[\text{Ni}_{1/3}\text{Mn}_{1/3}\text{Co}_{1/3}]\text{O}_2$ precursors as hydroxides.⁹⁴

It is important to synthesize NMC oxides with high tap densities to allow the materials to be used in commercial applications. Dense NMC oxides are synthesized from spherical and dense NMC hydroxides. Dense and spherical NMC hydroxides are synthesized by adding a complexing agent to the reaction, typically aqueous ammonia.

Figure 3.1 shows the XRD patterns of a commercial sample of the NMC-oxide precursor, reported by Yabuuchi *et al.*¹¹⁹ and of the pattern of $\text{Ni}_{1/3}\text{Mn}_{1/3}\text{Co}_{1/3}(\text{OH})_2$ calculated using the Rietica software.¹⁰⁴ The difference between the two XRD patterns (peak positions and shapes) indicate that this commercial precursor to $\text{Li}[\text{Ni}_{1/3}\text{Mn}_{1/3}\text{Co}_{1/3}]\text{O}_2$ is not the pure hydroxide, $\text{Ni}_{1/3}\text{Mn}_{1/3}\text{Co}_{1/3}(\text{OH})_2$.

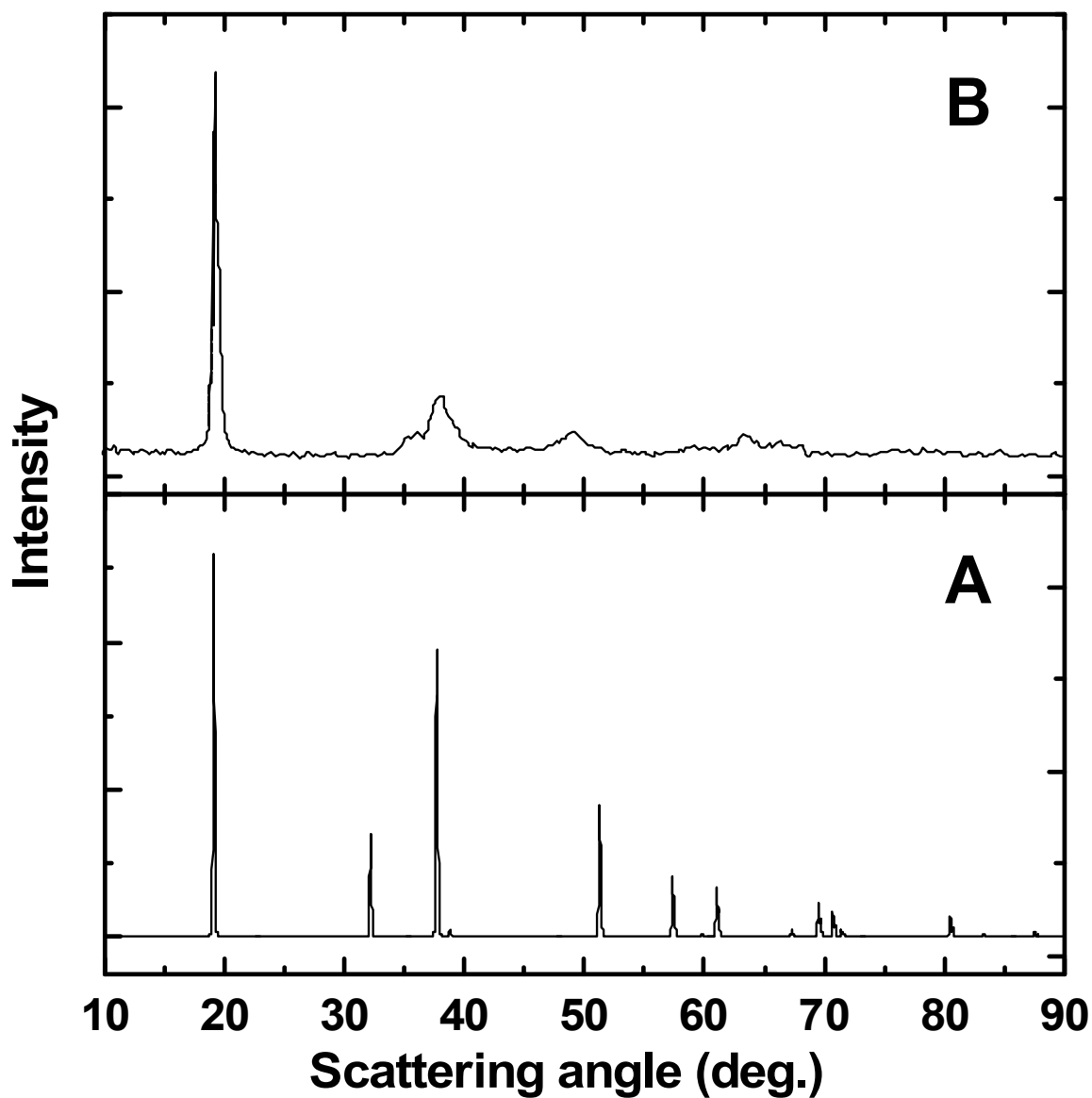


Figure 3.1. XRD patterns of $\text{Ni}_{1/3}\text{Mn}_{1/3}\text{Co}_{1/3}(\text{OH})_2$. Measured (B (Ref. 119)) and calculated (A) XRD patterns for $\text{Ni}_{1/3}\text{Mn}_{1/3}\text{Co}_{1/3}(\text{OH})_2$ are shown.

The calculations used space group $P_{\bar{3}m}$ with metal atoms randomly filling 1a sites and oxygen atoms in 2d sites with $z = 0.25$. The hydrogen atoms were not included. The lattice constants for the calculation were $a = 3.22$ and $c = 4.70 \text{ \AA}$.

From van Bommel, A; Dahn, J. R. *J. Electrochem. Soc.* **2009**, *156*, A362.
Reprinted with permission from The Electrochemical Society. Copyright 2009.

There has been little discussion in the literature on the structure of the precursor for NMC oxides. Here, spherical and dense $\text{Ni}_{1/3}\text{Mn}_{1/3}\text{Co}_{1/3}(\text{OH})_2$ has been synthesized with a pure hydroxide. XRD pattern and the transformation of the hydroxide to other phases upon air exposure and heating is discussed. Through this work, the complex experimental diffraction pattern in Figure 3.1 can be explained.

3.1. Experimental

The experimental procedure to make mixed metal hydroxides was outlined in Section 2.5.1. In this particular experiment, the total reaction time was 40 h and the pH-value was 10.0.

3.2. Results and Discussion

The $\text{Ni}_{1/3}\text{Mn}_{1/3}\text{Co}_{1/3}(\text{OH})_2$ co-precipitation product, which was light pink, was analyzed with X-ray diffraction soon after filtering. Figure 3.2 shows the experimental XRD pattern matched that calculated for $\text{Ni}_{1/3}\text{Mn}_{1/3}\text{Co}_{1/3}(\text{OH})_2$ using Rietveld refinement with the space group and atom positions as defined in the caption to Figure 3.1. The hexagonal lattice constants, a and c , were refined to 3.22 and 4.70 Å, respectively. The z -position of the oxygen atom in the unit cell was 0.25. The Bragg-R factor was 1.95 given as

$$R_B = \frac{1}{N} \sum_i \frac{|I_c^i - I_m^i|}{I_m^i} \times 100, \quad (3.1)$$

where N is the number of peaks, and I_c^i and I_m^i are the calculated and measured peak intensities, respectively.

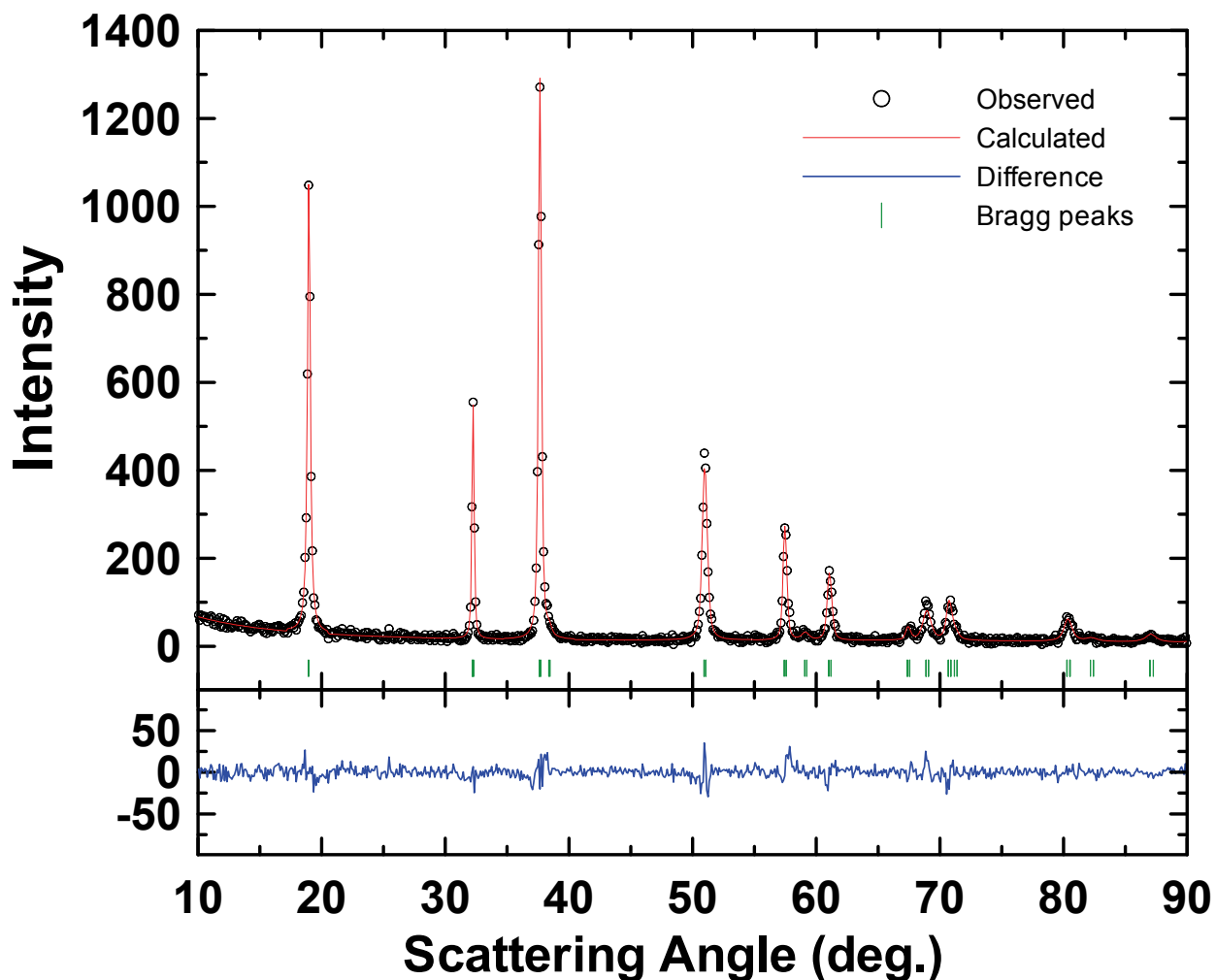


Figure 3.2. Rietveld refinement of the pure phase $\text{Ni}_{1/3}\text{Mn}_{1/3}\text{Co}_{1/3}(\text{OH})_2$. The calculation used the same parameters as described in the Figure 3.1 caption. From van Bommel, A; Dahn, J. R. *J. Electrochem. Soc.* **2009**, *156*, A362. Reprinted with permission from The Electrochemical Society. Copyright 2009.

Figure 3.3 shows the structure of $\text{Ni}_{1/3}\text{Mn}_{1/3}\text{Co}_{1/3}(\text{OH})_2$. The octahedra represent the $\text{M}(\text{OH})_6$ units, with the metal (nickel, manganese, or cobalt) atom in the center of the octahedra. The oxygen atoms are on the vertices of the octahedra and the hydrogen atoms are not drawn.

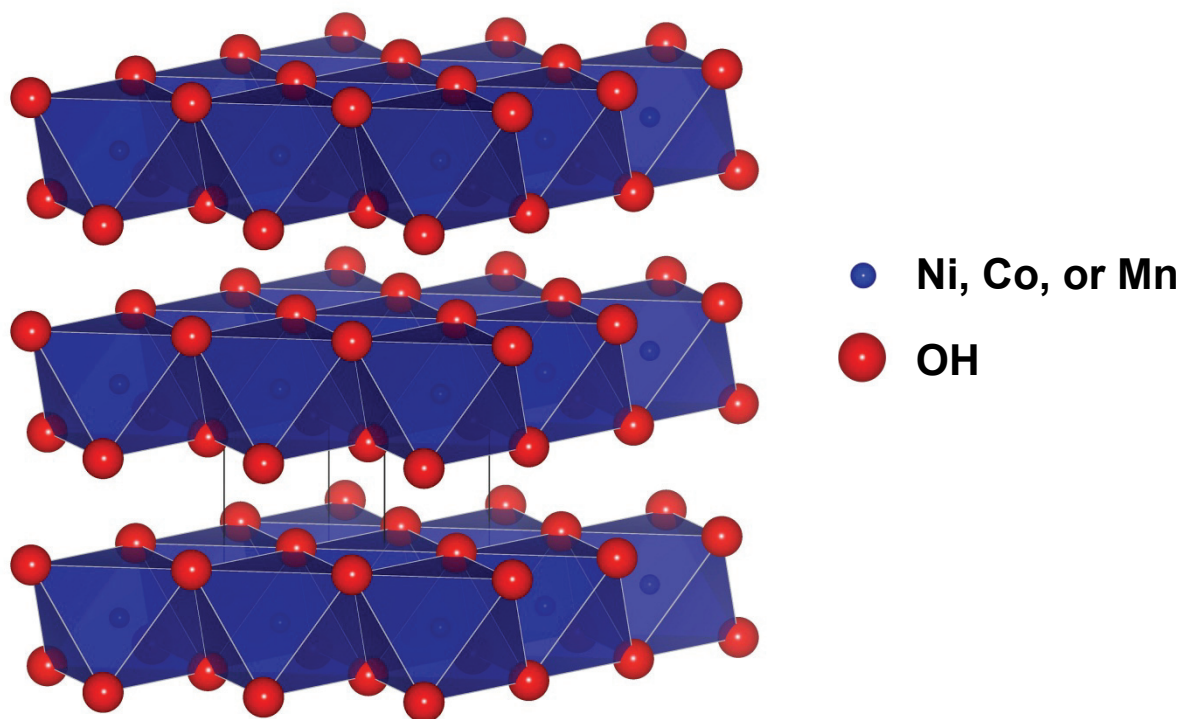


Figure 3.3. Structure of $\text{Ni}_{1/3}\text{Mn}_{1/3}\text{Co}_{1/3}(\text{OH})_2$. Space group P_{3m}^2 , $a = 3.22$, $c = 4.70$. The $\text{M}(\text{OH})_6$ units are represented by octahedra, with the metal atom at the center. The hydrogen atoms not drawn.

Oxidation of $\text{Ni}_{1/3}\text{Mn}_{1/3}\text{Co}_{1/3}(\text{OH})_2$ occurs upon exposure to air, especially at elevated temperatures. During the oxidation, the colour of the material changed from light pink to dark brown. The N_2 synthesis atmosphere, the use of deaerated water and the lack of elevated temperature drying allowed for preparation of the pure pink-colored NMC hydroxide. Typical synthesis conditions in air followed by elevated drying temperature results in oxidation and XRD patterns similar to that of the commercial material in Figure 3.1.

The oxidation of the pink-colored $\text{Ni}_{1/3}\text{Mn}_{1/3}\text{Co}_{1/3}(\text{OH})_2$ was studied by heating the material in air for 1 h at various temperatures. Figure 3.4 shows the effects of heating

on the XRD patterns of the material. As the heating temperature increases, a new set of Bragg peaks begins to appear. These are indicated by the arrows in the top panel of Figure 3.4. The red arrows define a set of Bragg peaks that appear to be similar to those of the unheated material, but shifted to progressively larger angles compared to the original peaks. This suggests that the sample has transformed to a related structure, but with contracted lattice constants.

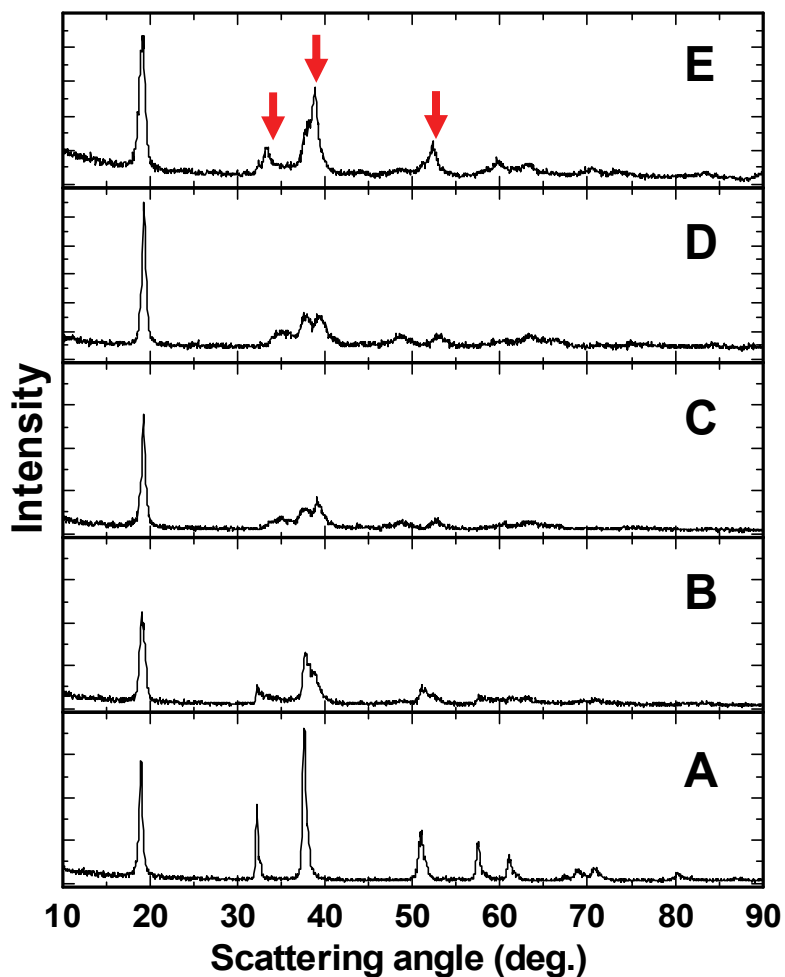


Figure 3.4. X-ray diffraction patterns during the heating of $\text{Ni}_{1/3}\text{Mn}_{1/3}\text{Co}_{1/3}(\text{OH})_2$. The heating temperatures are: A – as-prepared; B – 120°C ; C – 140°C ; D – 160°C ; E – 180°C . The red arrows in the top panel indicate the positions of the Bragg peaks of the $\text{Ni}_{1/3}\text{Mn}_{1/3}\text{Co}_{1/3}(\text{OOH})$ phase.

From van Bommel, A; Dahn, J. R. *J. Electrochem. Soc.* **2009**, *156*, A362.
Reprinted with permission from The Electrochemical Society. Copyright 2009.

It is believed the new phase is the oxyhydroxide phase. Table 3.1 shows the literature hexagonal lattice constants for Co(OH)_2 and CoOOH .¹²⁰ The decrease in lattice constants can be attributed to the decrease in size of the Co-ion upon oxidation from 2+ to 3+. Table 3.1 also gives the lattice constants of the $\text{Ni}_{1/3}\text{Mn}_{1/3}\text{Co}_{1/3}(\text{OH})_2$ phase from the Rietveld fit in Figure 3.2 and the smaller lattice constants derived from the peaks marked with the arrows in the top panel of Figure 3.3. The decrease in lattice constants supports the identification of the new set of Bragg peaks as coming from the oxyhydroxide phase.

Table 3.1. Lattice constants of hydroxides and oxyhydroxides. Lattice constants of Co(OH)_2 and CoOOH are from references 120 and 121. The lattice constants of $\text{Ni}_{1/3}\text{Mn}_{1/3}\text{Co}_{1/3}(\text{OH})_2$ and $\text{Ni}_{1/3}\text{Mn}_{1/3}\text{Co}_{1/3}\text{OOH}$ from this work are also given.

Material	a (Å)	c (Å)
Co(OH)_2	3.173	4.640
CoOOH	2.854	4.38
NMC-(OH) ₂	3.22	4.70
NMC-OOH	3.09	4.61

Oxidation of the hydroxide to oxyhydroxide would result in a mass loss of 1.1 % in the case of $\text{Ni}_{1/3}\text{Mn}_{1/3}\text{Co}_{1/3}(\text{OH})_2$. Figure 3.5 shows thermogravimetric analysis of the initially pink-colored $\text{Ni}_{1/3}\text{Mn}_{1/3}\text{Co}_{1/3}(\text{OH})_2$ sample during heating in air. There is

observed mass loss of about 1 % in the 140-160°C region, consistent with the changes to the XRD patterns.

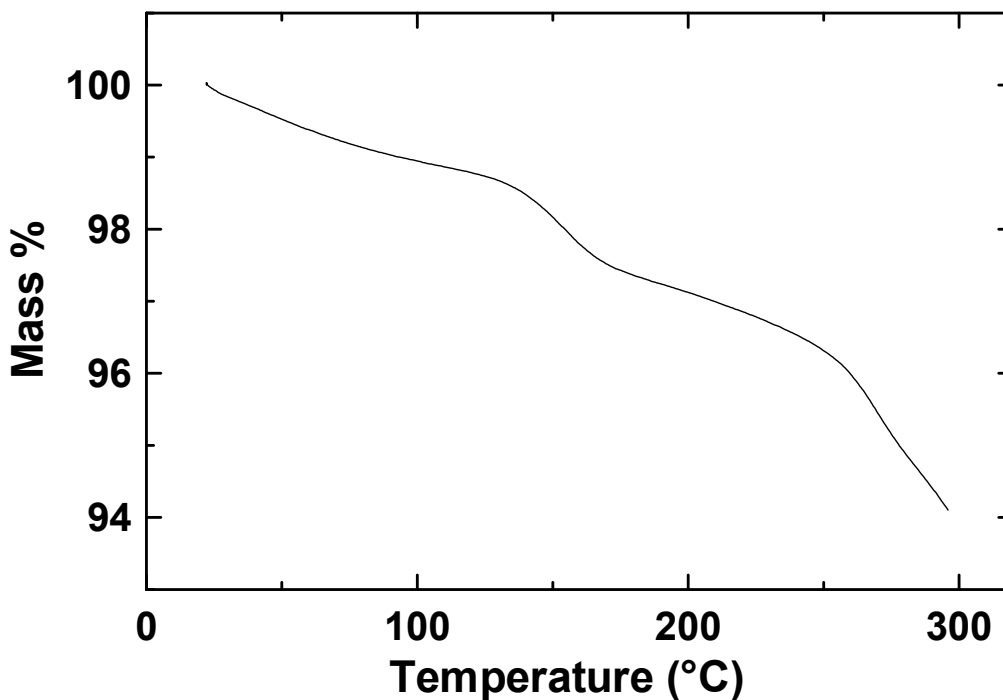
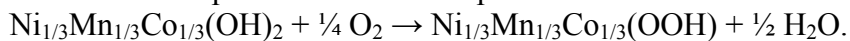


Figure 3.5. Thermogravimetric analysis in air of as-prepared $\text{Ni}_{1/3}\text{Mn}_{1/3}\text{Co}_{1/3}(\text{OH})_2$. The heat rate was 1°C min^{-1} .

The “step” near 150°C corresponds to the reaction:



From van Bommel, A; Dahn, J. R. *J. Electrochem. Soc.* **2009**, *156*, A362.

Reprinted with permission from The Electrochemical Society. Copyright 2009.

In order to understand the complexity of the diffraction pattern shown in Figure 3.1 for the commercial sample, $\text{Ni}_{1/3}\text{Mn}_{1/3}\text{Co}_{1/3}(\text{OH})_2$ was heated to various temperatures overnight. Figure 3.6 shows a comparison between as-prepared $\text{Ni}_{1/3}\text{Mn}_{1/3}\text{Co}_{1/3}(\text{OH})_2$, $\text{Ni}_{1/3}\text{Mn}_{1/3}\text{Co}_{1/3}(\text{OH})_2$ heated to 140°C , and the commercial sample.¹¹⁹

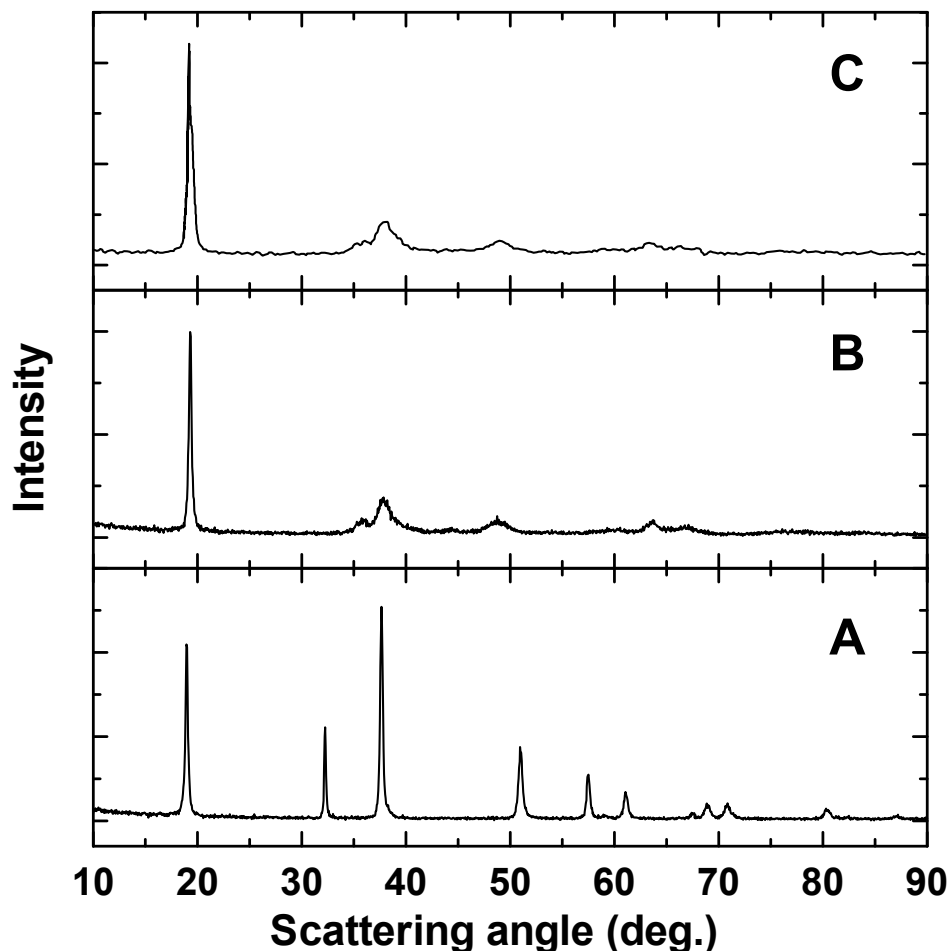


Figure 3.6. XRD patterns of $\text{Ni}_{1/3}\text{Mn}_{1/3}\text{Co}_{1/3}(\text{OH})_2$ in this work and from commercial precursor material. $\text{Ni}_{1/3}\text{Mn}_{1/3}\text{Co}_{1/3}(\text{OH})_2$ (A), $\text{Ni}_{1/3}\text{Mn}_{1/3}\text{Co}_{1/3}(\text{OH})_2$ heated to 140°C overnight (B) and the commercial “ $\text{Ni}_{1/3}\text{Mn}_{1/3}\text{Co}_{1/3}(\text{OH})_2$ ” sample (C)¹¹⁹.
 From van Bommel, A; Dahn, J. R. *J. Electrochem. Soc.* **2009**, 156, A362.
 Reprinted with permission from The Electrochemical Society. Copyright 2009.

$\text{Ni}_{1/3}\text{Mn}_{1/3}\text{Co}_{1/3}(\text{OH})_2$ heated to 140°C has a similar XRD pattern to the commercial sample. By comparison to the patterns shown in Figure 3.4 and the TGA in Figure 3.5, it is believed that $\text{Ni}_{1/3}\text{Mn}_{1/3}\text{Co}_{1/3}(\text{OH})_2$ heated to 140°C overnight and the commercial sample are both mixtures of hydroxide and oxyhydroxide phases.

Figure 3.7 shows the scanning electron micrographs of the as-prepared synthesized $\text{Ni}_{1/3}\text{Mn}_{1/3}\text{Co}_{1/3}(\text{OH})_2$. Using the synthesis conditions described in the

experimental section results in material that is spherical and dense, with particle sizes around 20 μm . The SEM images reveal that each particle is comprised of densely packed crystallites. The tap density of the NMC hydroxide was determined to be 1.7 g cm^{-3} . Once heated to 140°C, the tap density of the NMC oxyhydroxide was found to be 2.0 g cm^{-3} . Figure 3.8 shows the surface of the particle heated to 35°C and 140°C. The primary particles become fused when heated, leading to denser particles and a higher tap density. Changes to the synthesis conditions results in changes to the particle size, morphology and tap density.

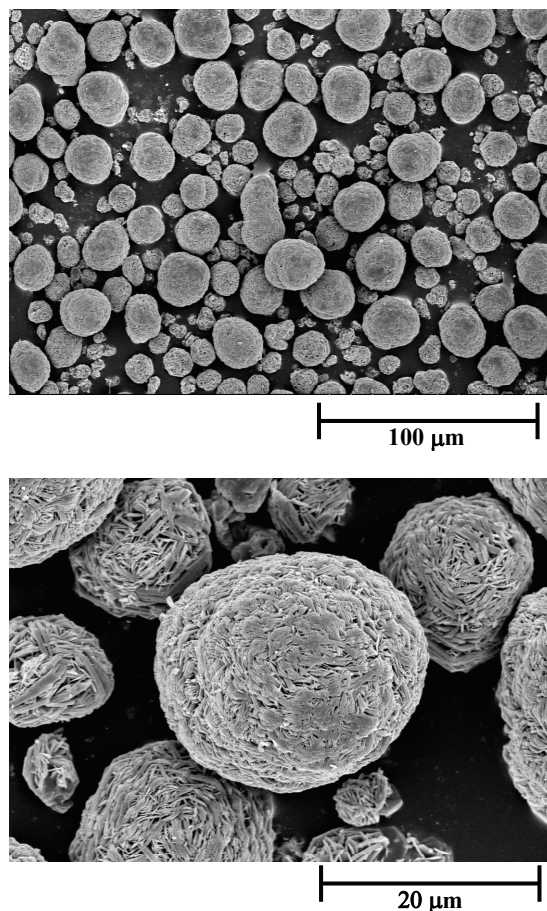


Figure 3.7. SEM images of the as-prepared $\text{Ni}_{1/3}\text{Mn}_{1/3}\text{Co}_{1/3}(\text{OH})_2$ particles at two magnifications.

From van Bommel, A; Dahn, J. R. *J. Electrochem. Soc.* **2009**, *156*, A362.
Reprinted with permission from The Electrochemical Society. Copyright 2009.

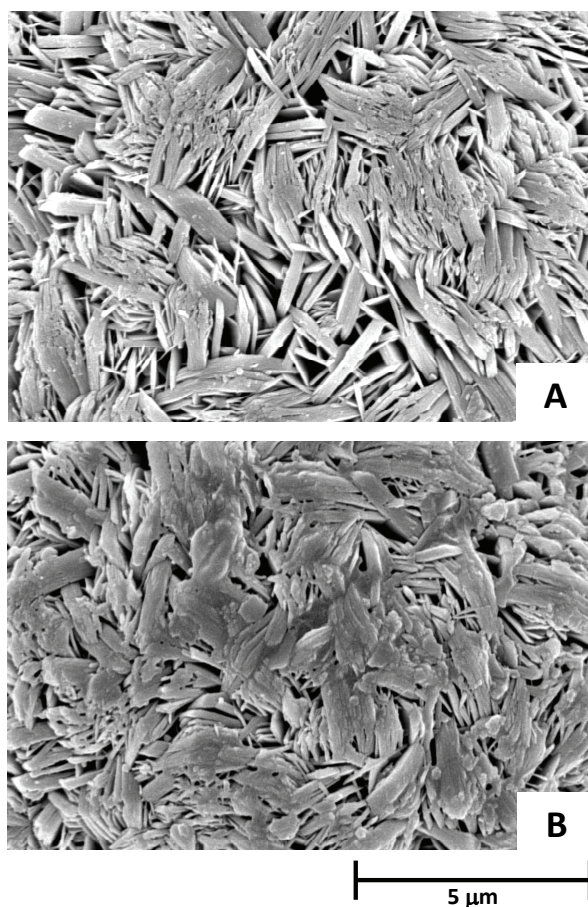


Figure 3.8. SEM images of the surface of the $\text{Ni}_{1/3}\text{Mn}_{1/3}\text{Co}_{1/3}(\text{OH})$ particles. The material was heated to 35 °C (A) and 140 °C (B).
From van Bommel, A; Dahn, J. R. *J. Electrochem. Soc.* **2009**, *156*, A362.
Reprinted with permission from The Electrochemical Society. Copyright 2009.

3.3. Summary

The $\text{Ni}_{1/3}\text{Mn}_{1/3}\text{Co}_{1/3}(\text{OH})_2$ precursor to $\text{Li}[\text{Ni}_{1/3}\text{Mn}_{1/3}\text{Co}_{1/3}]\text{O}_2$ can be synthesized by the co-precipitation reaction between metal salts and basic solution. The co-precipitation reaction allows for a homogeneous distribution of metal cations. By control of reaction conditions, oxidation of the hydroxide product can be prevented and pure $\text{Ni}_{1/3}\text{Mn}_{1/3}\text{Co}_{1/3}(\text{OH})_2$ can be synthesized. This material is pink in color. Reaction

atmosphere, drying temperature, and drying time are important factors in the synthesis of the pure hydroxide phase.

$\text{Ni}_{1/3}\text{Mn}_{1/3}\text{Co}_{1/3}(\text{OH})_2$ after synthesis is pink and turns brown upon exposure to air over several hours, suggesting that its surface is readily oxidized. X-ray diffraction shows that it is easily oxidized at elevated temperatures and converts to $\text{Ni}_{1/3}\text{Mn}_{1/3}\text{Co}_{1/3}(\text{OOH})$. The commercial product, as reported by Yabuuchi *et al.*¹¹⁹, is likely a mixture of the hydroxide and oxyhydroxide phases. Heating the pure $\text{Ni}_{1/3}\text{Mn}_{1/3}\text{Co}_{1/3}(\text{OH})_2$ to 140°C overnight gave a product with a XRD pattern similar to the commercial material.

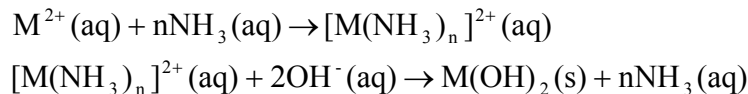
Pure $\text{Ni}_{1/3}\text{Mn}_{1/3}\text{Co}_{1/3}(\text{OH})_2$ has been synthesized in the presence of aqueous ammonia under anaerobic conditions, resulting in dense and spherical particles with a tap density of 1.7 g cm⁻³. Heating the material to 140°C increased the tap density to 2.0 g cm⁻³.

CHAPTER 4. Analysis of the Growth Mechanism of Coprecipitated Spherical and Dense Nickel, Manganese, and Cobalt Containing Hydroxides in the Presence of Aqueous Ammonia

4.1. Introduction

Many studies have been carried out on the synthesis of spherical and dense hydroxides by using a coprecipitation reaction in the presence of ammonia. These include the preparation of spherical and dense nickel hydroxide to be used in nickel metal hydride batteries.^{81-87, 96-98} Spherical and dense metal hydroxides have also been made with mixed metals, including nickel, manganese, and cobalt (NMC).^{88, 90-95, 99, 100} NMC hydroxides are precursors to lithium-NMC oxides, positive electrode materials for lithium-ion batteries.^{16, 51}

The typical growth mechanism for the synthesis of spherical and dense hydroxide particles in the presence of ammonia has been presented by several researchers.^{81, 86, 89, 94, 97} These researchers state that the metal ions from the incoming salt solution first coordinate to the ammonia present in solution, and then are slowly released to the basic solution to yield spherical and dense hydroxide particles. A general scheme of this reaction is given below.



In the present study, the growth of metal hydroxide particles, including $\text{Ni}(\text{OH})_2$, $\text{Ni}_{1/2}\text{Mn}_{1/2}(\text{OH})_2$ and $\text{Ni}_{1/3}\text{Mn}_{1/3}\text{Co}_{1/3}(\text{OH})_2$, in the presence of ammonia is studied. A different mechanism for spherical and dense hydroxide particle growth is presented.

4.2. Experimental

The experimental procedure to make mixed metal hydroxides was outlined in Section 2.5.1. In this particular experiment, the total reaction time and the reaction pH were varied.

4.3. Results and Discussion

Figure 4.1 shows examples of X-ray diffraction (XRD) patterns for $\text{Ni}(\text{OH})_2$, $\text{Ni}_{1/2}\text{Mn}_{1/2}(\text{OH})_2$, and $\text{Ni}_{1/3}\text{Mn}_{1/3}\text{Co}_{1/3}(\text{OH})_2$ as prepared in this study along with calculated patterns using Rietveld profile analysis with the Rietica software.¹⁰⁴ The calculations used space group $P\bar{3}m$ with metal atoms in 1a sites and oxygen atoms in 2d sites. The refined lattice constants and oxygen positional parameters are given in Table 4.1. Figure 4.1 shows that the Bragg peak positions match those of the calculated hydroxide pattern and that oxidation to oxyhydroxide has not yet occurred.

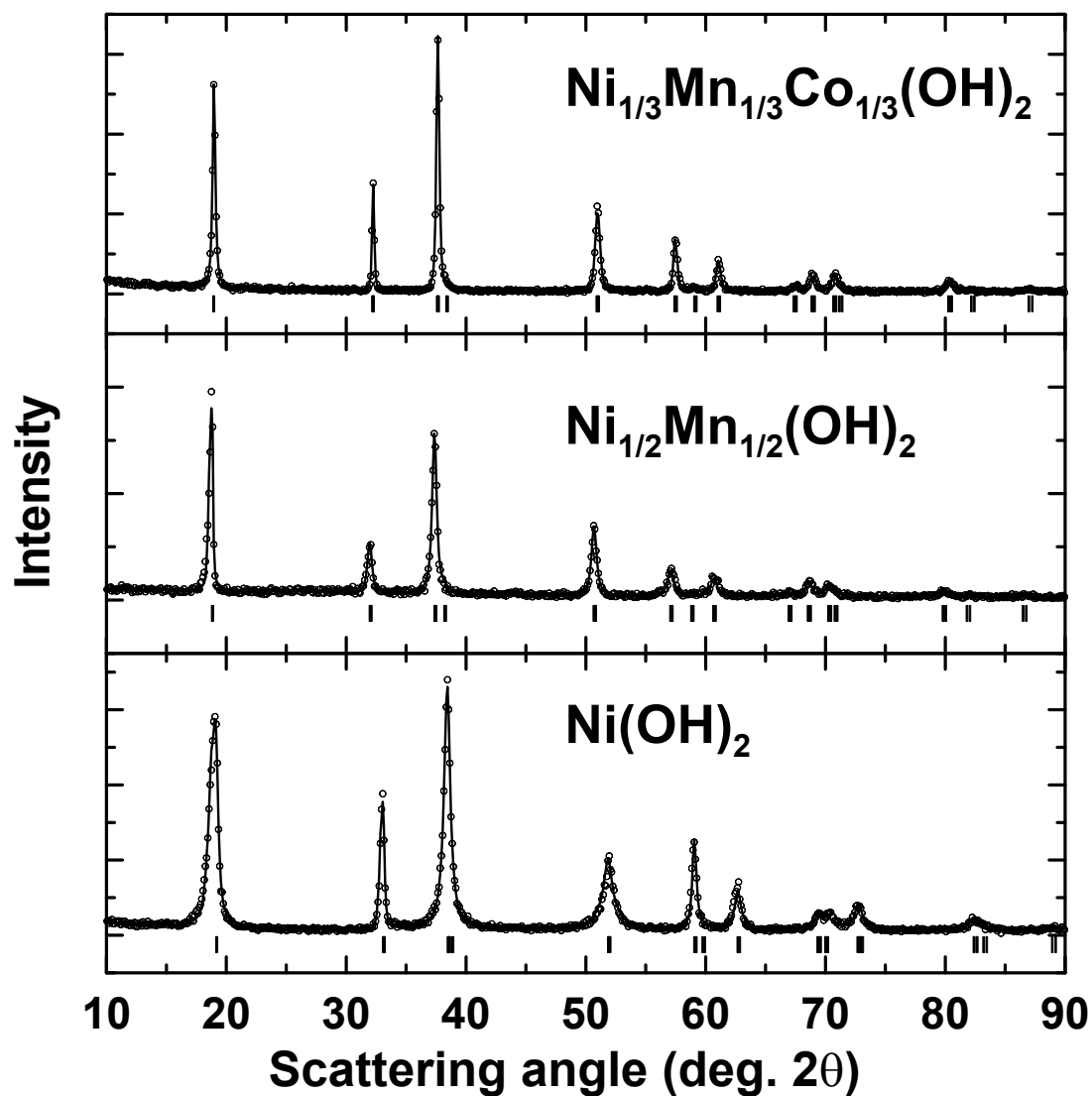


Figure 4.1. XRD patterns of $\text{Ni}(\text{OH})_2$, $\text{Ni}_{1/2}\text{Mn}_{1/2}(\text{OH})_2$, and $\text{Ni}_{1/3}\text{Mn}_{1/3}\text{Co}_{1/3}(\text{OH})_2$. The open circles are the experimental XRD patterns. The solid curve in each panel is the calculated pattern using Rietveld profile analysis and the parameters listed in Table 4.1.

The calculated Bragg lines are given under each XRD profile.

From van Bommel, A; Dahn, J. R. *Chem. Mater.* **2009**, *21*, 1500.

Reprinted with permission from the American Chemical Society. Copyright 2009.

Table 4.1. The hexagonal lattice constants and z-positions of the oxygen atom calculated for Ni(OH)₂, Ni_{1/2}Mn_{1/2}(OH)₂, and Ni_{1/3}Mn_{1/3}Co_{1/3}(OH)₂.

Material	z_o	a (Å)	c (Å)
Ni(OH) ₂	0.239	3.128	4.643
Ni _{1/2} Mn _{1/2} (OH) ₂	0.252	3.224	4.705
Ni _{1/3} Mn _{1/3} Co _{1/3} (OH) ₂	0.247	3.207	4.688

Figure 4.2 shows the XRD pattern of Ni(OH)₂ with indicated Miller indices. The anisotropic broadening capability of the Rietica software¹⁰⁴ was used in order to simulate the broad and narrow peaks most evident in the Ni(OH)₂ sample. The half width, H , of the peaks is represented by:

$$H_k = ((U + U_{anis}) \tan^2 \theta + V \tan \theta + W)^{1/2} \quad (4.1)$$

where U_{anis} is given by:

$$U_{anis} = U_a \cos 2\phi \quad (4.2)$$

and ϕ is the angle between the (001) reciprocal lattice vector and the (hkl) reciprocal lattice vector, and U , U_a , V and W are adjustable parameters.¹⁰⁴ This expression preferentially broadens the (001) peaks relative to the (hk0) peaks. Peaks with mixed in-plane and out-of-plane character are broadened to an intermediate extent. The (001) peaks may be preferentially broadened because of the plate-like shape of the primary particles.

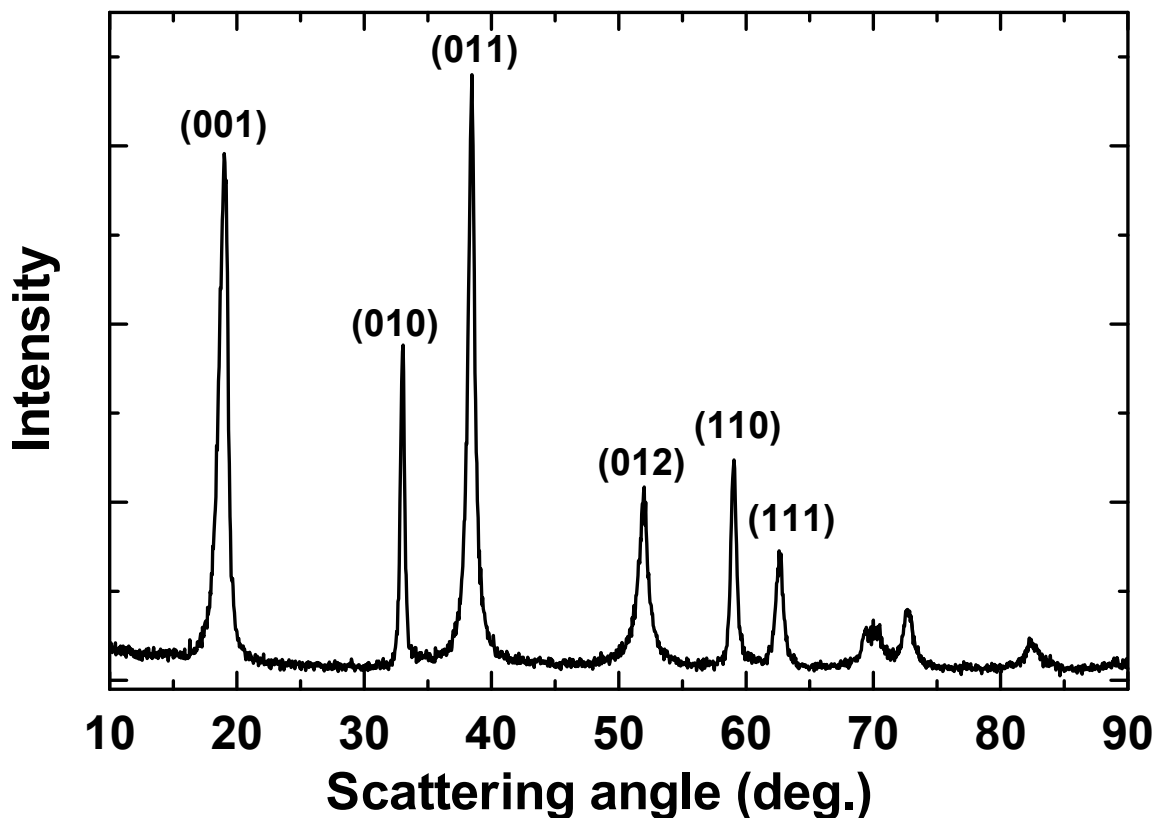


Figure 4.2. XRD pattern of Ni(OH)₂ with indicated Miller indices, showing selective broadening.

It is believed that the particles have homogeneous cation content: the lattice constants of the hydroxides depend strongly on Ni, Mn, and Co content¹²⁰ while the X-ray patterns show sharp (especially (010) and (110)) Bragg peaks suggesting homogeneous materials.

Nickel hydroxide was prepared in the presence of aqueous ammonia. Samples of the synthesized nickel hydroxide were extracted throughout the reaction. Figure 4.3 shows the dependence of the tap density of the sample on the reaction time. The tap density of the nickel hydroxide follows an asymptotic curve, increasing to 2.1 g cm⁻³ after 20 h.

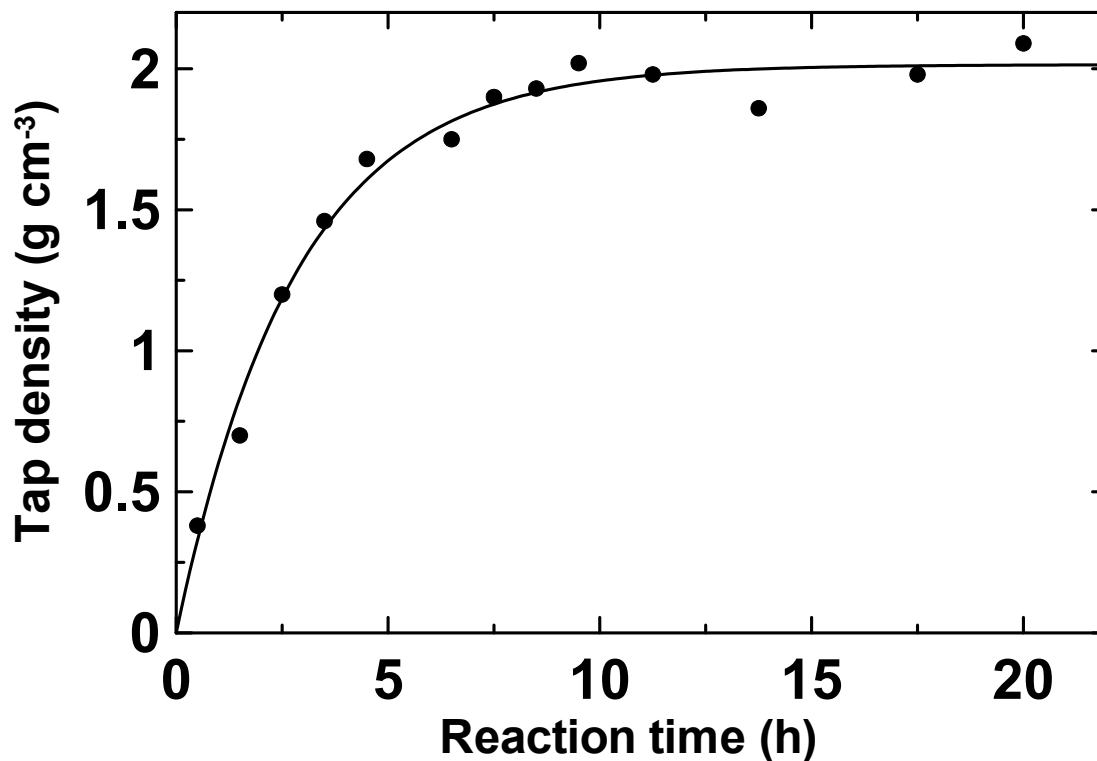


Figure 4.3. Tap density of Ni(OH)₂ as a function of reaction time.

The pH of the coprecipitation reaction was 11.0.

From van Bommel, A; Dahn, J. R. *Chem. Mater.* **2009**, *21*, 1500.

Reprinted with permission from the American Chemical Society. Copyright 2009.

Figure 4.4 shows the dependence of particle morphology on the reaction time. The nickel hydroxide secondary particle grows during the reaction. As well, there are smoother surfaces of the secondary particles at higher reaction times. The increase in tap density with reaction time can be attributed to 1) smoother surfaces at higher reaction times; 2) thickening of the plate-like primary particles, decreasing the porosity of the secondary particles and 3) the decrease in irregular-shaped particles which would lead to effects such as bridge formation, lowering the overall tap density of the sample.

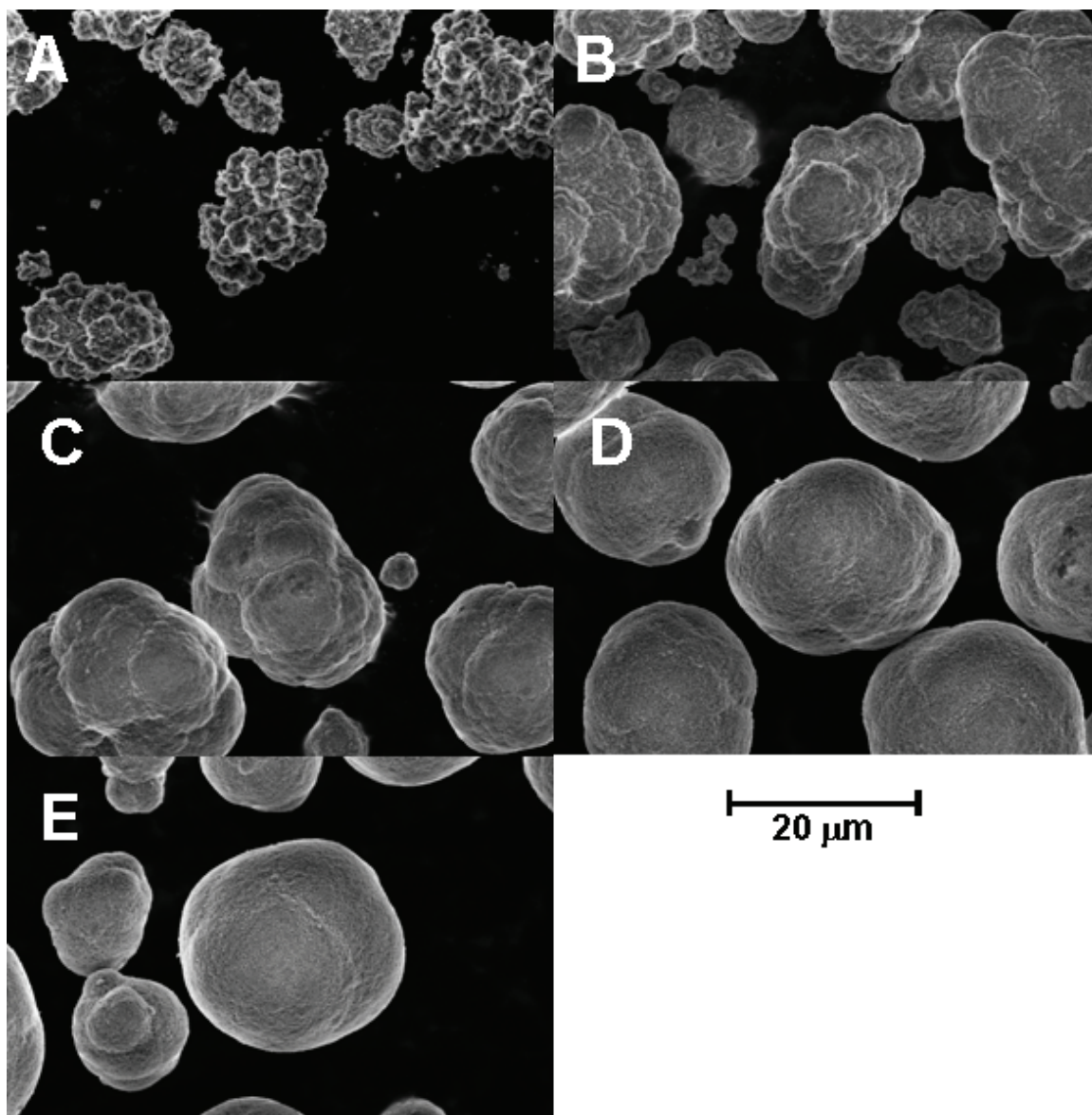


Figure 4.4. SEM images of Ni(OH)_2 a function of reaction time.
 A) $t = 2$ h; B) $t = 5$ h; C) $t = 10$ h; D) $t = 15$ h; E) $t = 20$ h (pH = 11.0)
 From van Bommel, A; Dahn, J. R. *Chem. Mater.* **2009**, *21*, 1500.
 Reprinted with permission from the American Chemical Society. Copyright 2009.

Figure 4.5 shows the effect of pH on the tap density of Ni(OH)_2 , $\text{Ni}_{1/2}\text{Mn}_{1/2}(\text{OH})_2$, and $\text{Ni}_{1/3}\text{Mn}_{1/3}\text{Co}_{1/3}(\text{OH})_2$. A relatively short reaction time of 5 h was used, which gave relatively low tap densities for the hydroxide samples. In the case of Ni(OH)_2 , high tap density materials can be made at a pH of 11.4 or less. At a pH greater than 11.4, there is

a large decrease in tap density, which indicates that dense, spherical particles cannot be synthesized at these pH-values. For $\text{Ni}_{1/2}\text{Mn}_{1/2}(\text{OH})_2$ and $\text{Ni}_{1/3}\text{Mn}_{1/3}\text{Co}_{1/3}(\text{OH})_2$, dense, spherical particle growth occurs at a pH of less than 10.2. The pH that is required for dense, spherical particle growth in the presence of aqueous ammonia is lower for manganese and cobalt hydroxides than for nickel hydroxide.

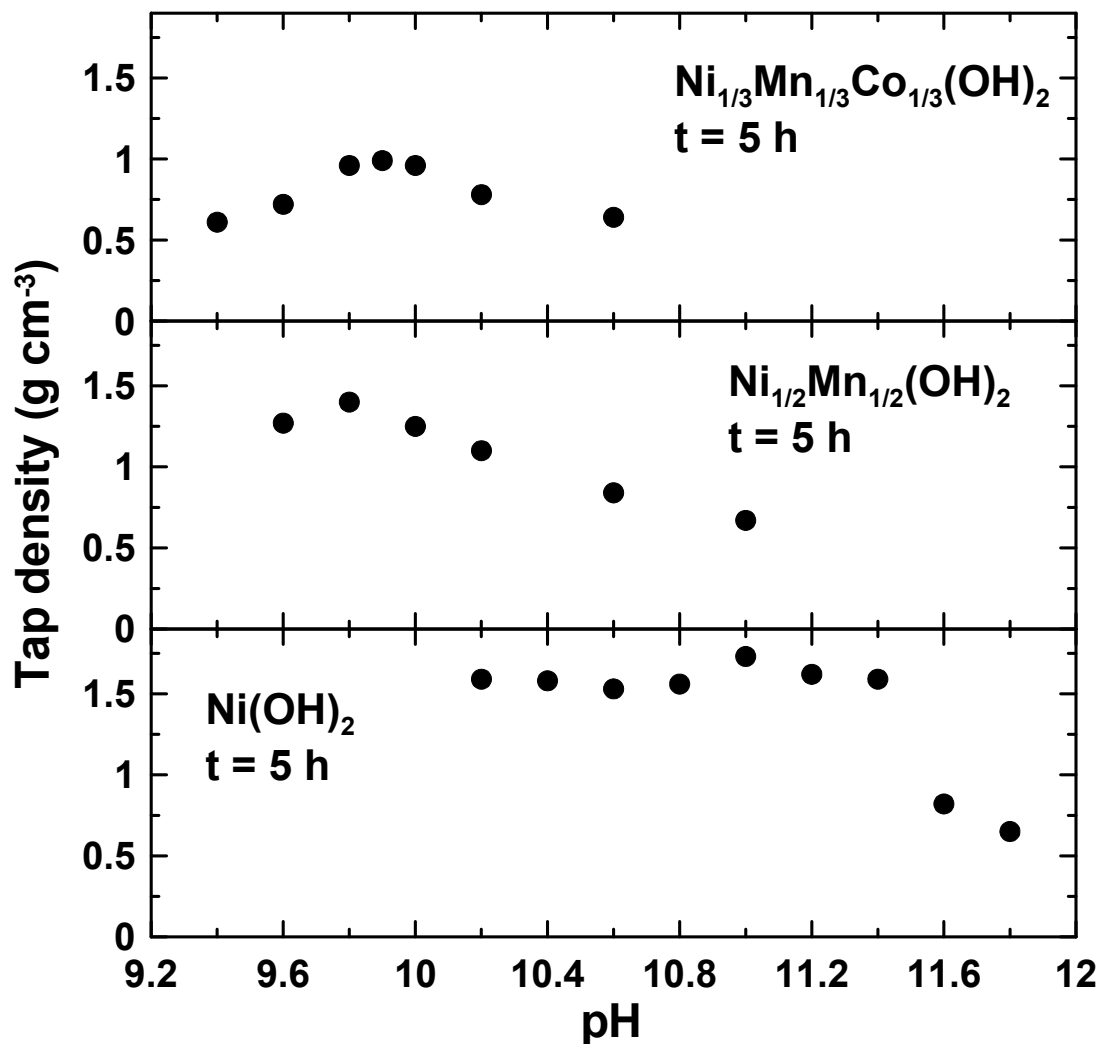


Figure 4.5. Dependence of tap density on reaction pH for various hydroxides.

$\text{Ni}(\text{OH})_2$, $\text{Ni}_{1/2}\text{Mn}_{1/2}(\text{OH})_2$, and $\text{Ni}_{1/3}\text{Mn}_{1/3}\text{Co}_{1/3}(\text{OH})_2$ data are shown.

From van Bommel, A; Dahn, J. R. *Chem. Mater.* **2009**, *21*, 1500.

Reprinted with permission from the American Chemical Society. Copyright 2009.

Figure 4.6 shows the SEM images of $\text{Ni}(\text{OH})_2$ prepared at various pH-values. All morphologies of samples prepared at a pH of 11.4 and lower indicated dense, spherical particle growth. The $\text{Ni}(\text{OH})_2$ sample prepared at a pH-value of 11.8 shows that spherical particle growth is not taking place.

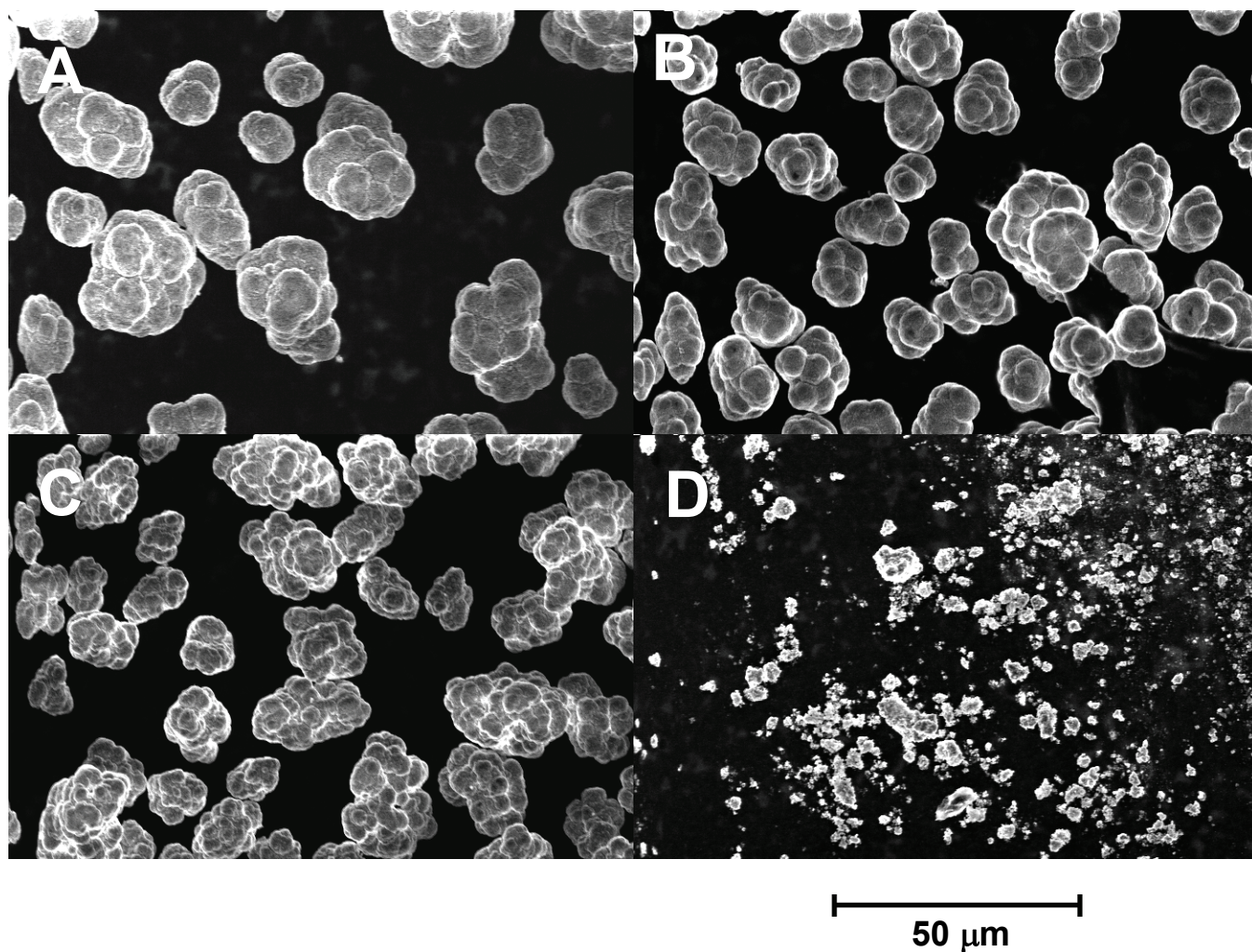


Figure 4.6. SEM images of $\text{Ni}(\text{OH})_2$ as different reaction pH-values. The material was synthesized for $t = 5$ h with a pH-value of A) 10.6 B) 11.0, C) 11.4, and D) 11.8.

From van Bommel, A; Dahn, J. R. *Chem. Mater.* **2009**, *21*, 1500.
Reprinted with permission from the American Chemical Society. Copyright 2009.

The dependence of the required pH for hydroxide particle growth on the metal(s) was studied by investigating the chemical equilibria present during the reaction. The equilibrium constants used were the equilibrium constants for coordination of ammonia to the metal ions, the base dissociation constant of aqueous ammonia, the solubility product of the metal hydroxide, and the water dissociation constant.¹²² Table 4.2 shows the relevant equilibria and the mass balances for Ni(OH)₂, Mn(OH)₂, and Co(OH)₂. For clarity, the coordinating water molecules (as in [M(H₂O)₆]²⁺) are not indicated. These equilibria were solved for various pH-values with the total metal concentration ($C_{M^{2+}}$) and total ammonia concentration (C_{NH_3}) as 2 M and 1 M, respectively. The equilibrium constants were all for 25°C, while the reaction temperature in the experimental study was 60°C.

Table 4.2. Equilibria and mass balances solved to determine the concentration of species present in the coprecipitation reaction at various pH-values.

equilibrium reaction	K	$\log K^{122}$		
		Ni	Mn	Co
$M^{2+} + NH_3 \rightleftharpoons [M(NH_3)]^{2+}$	K_1	2.81	1.00	2.10
$M^{2+} + 2NH_3 \rightleftharpoons [M(NH_3)_2]^{2+}$	K_2	5.08	1.54	3.67
$M^{2+} + 3NH_3 \rightleftharpoons [M(NH_3)_3]^{2+}$	K_3	6.85	1.70	4.78
$M^{2+} + 4NH_3 \rightleftharpoons [M(NH_3)_4]^{2+}$	K_4	8.12	1.3	5.53
$M^{2+} + 5NH_3 \rightleftharpoons [M(NH_3)_5]^{2+}$	K_5	8.93	-	5.75
$M^{2+} + 6NH_3 \rightleftharpoons [M(NH_3)_6]^{2+}$	K_6	9.08	-	5.14
$NH_3 + H_2O \rightleftharpoons NH_4^+ + OH^-$	K_b	-4.80	-4.80	-4.80
$M(OH)_2 \rightleftharpoons M^{2+} + 2OH^-$	K_{sp}	-15.22	-12.70	-14.89
$H_2O \rightleftharpoons H^+ + OH^-$	K_w	-14	-14	-14
mass balances				
$C_{M^{2+}} = [M^{2+}] + [Ni(OH)_2] + [M(NH_3)_2]^{2+} + [M(NH_3)_3]^{2+} + [M(NH_3)_4]^{2+} \\ + [M(NH_3)_5]^{2+} + [M(NH_3)_6]^{2+}$				
$C_{NH_3} = [NH_3] + [NH_4^+] + [M(NH_3)]^{2+} + 2[M(NH_3)_2]^{2+} + 3[M(NH_3)_3]^{2+} + 4[M(NH_3)_4]^{2+} \\ + 5[M(NH_3)_5]^{2+} + 6[M(NH_3)_6]^{2+}$				

Figure 4.7 shows the solutions for the concentration of the relevant species for the nickel hydroxide coprecipitation reaction. The results are as expected – nickel hydroxide is formed in basic conditions, aqueous ammonia exists in basic conditions, and the concentration of Ni^{2+} and NH_4^+ is highest in acidic conditions. The coordination of ammonia to nickel occurs over a range of pH, depending on the coordination number.

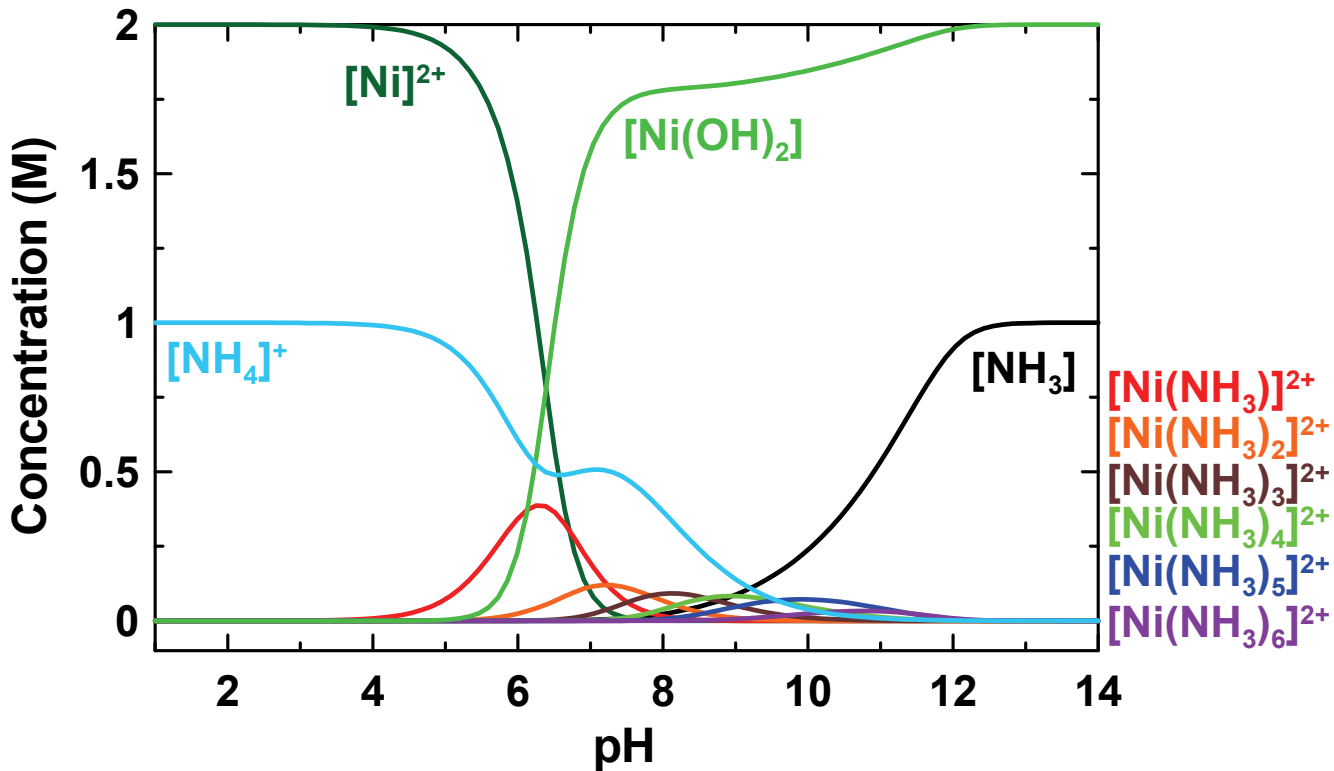


Figure 4.7. Effect of pH on the concentration of relevant species in the nickel hydroxide coprecipitation reaction.

The concentrations of all relevant species for manganese and cobalt hydroxides were also determined as a function of pH. Figure 4.8 shows the effect of pH on the concentration of the sum of all metal-ammonia complexes ($[\text{M}(\text{NH}_3)_n]^{2+}$) for nickel, manganese, and cobalt. Nickel shows coordination with ammonia at pH = 4 - 12,

whereas manganese and cobalt coordinate with ammonia in a smaller pH range: pH = 6 - 10. This is in agreement with the experimental data: Figure 4.5 shows that manganese and cobalt-containing hydroxides form materials with higher tap densities at a lower pH than the pH needed to synthesize spherical and dense Ni(OH)₂. Considering that spherical particle growth only occurs with interaction of metal and ammonia, manganese and cobalt-containing hydroxides require a lower pH-value than nickel-containing hydroxides for ammonia coordination, and, therefore, for the conditions for spherical particle growth.

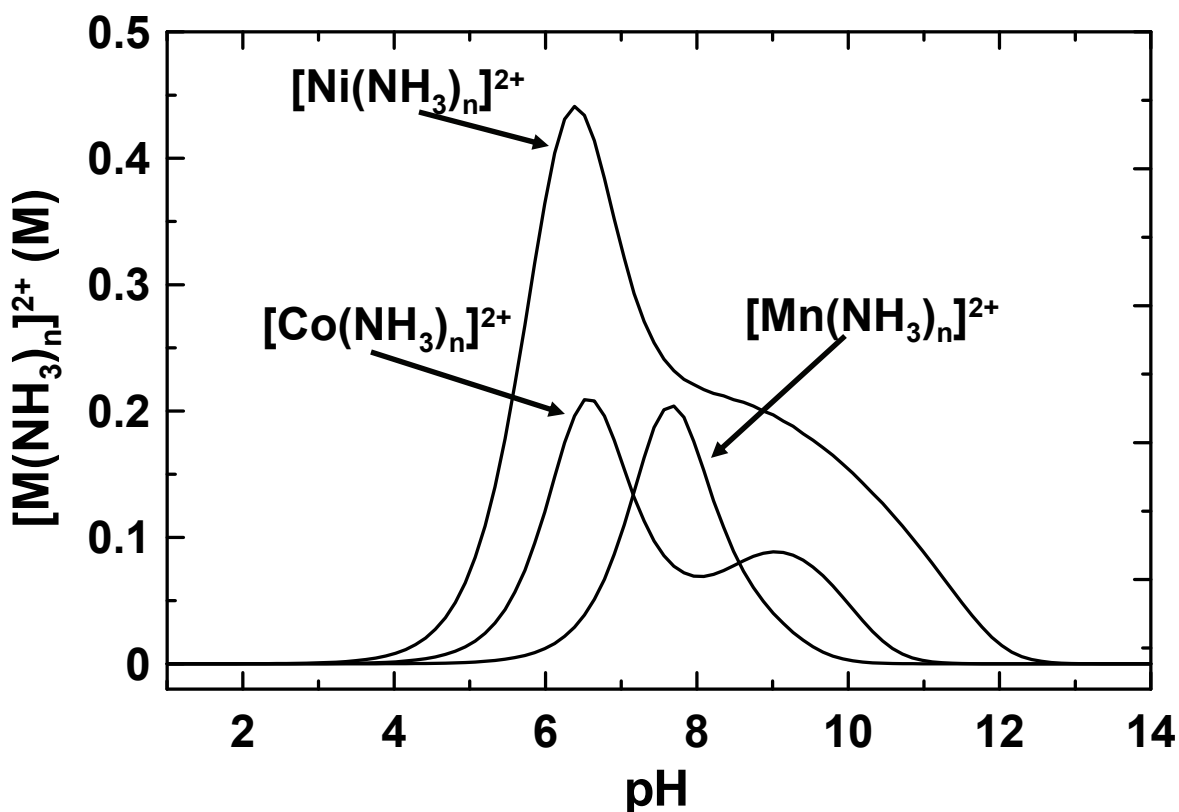


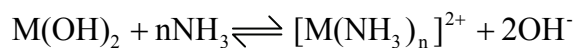
Figure 4.8. Effect of pH on the concentration of $[\text{Ni}(\text{NH}_3)_n]^{2+}$, $[\text{Mn}(\text{NH}_3)_n]^{2+}$, and $[\text{Co}(\text{NH}_3)_n]^{2+}$.

The curve is the sum of the concentrations for complexes with $1 \leq n \leq 6$.

From van Bommel, A; Dahn, J. R. *Chem. Mater.* **2009**, *21*, 1500.

Reprinted with permission from the American Chemical Society. Copyright 2009.

In view of the growth of hydroxide particles with time, the dependence of particle morphology on pH, and analysis of the relevant equilibria present in the coprecipitation reaction, this work suggested an alternate growth mechanism for spherical hydroxide growth in the presence of aqueous ammonia. Rather than a metal ion first coordinating with ammonia and then being slowly released to the basic solution, the growth of hydroxide particles is due to the equilibrium between metal hydroxide particles and aqueous ammonia solution. In this mechanism, the metal hydroxide has an effective increased solubility in the presence of aqueous ammonia. This is shown in the equilibrium below.



The strength of dissolution of metal hydroxide has been shown to be dependent on the pH of the reaction, which varies depending on the metal involved. Spherical hydroxide particle growth in the presence of aqueous ammonia therefore is due to a dissolution-recrystallization mechanism. In such a mechanism, small particles will be consumed in favor of larger particles to minimize surface free energy.

4.4. Summary

Spherical and dense nickel, manganese, and cobalt-containing hydroxides can be prepared in the presence of aqueous ammonia. The growth of the metal hydroxide occurs throughout the reaction time, which results in higher tap-density material. The conditions for particle growth depend on the pH of the reaction, which varies for different metal hydroxides. The pH required for spherical hydroxide growth varies since the pH-range at which coordination to ammonia occurs is different for nickel, manganese, and cobalt.

The spherical particle growth is due to the increase in solubility of the metal hydroxide in the presence of aqueous ammonia. Spherical particle growth in the presence of ammonia takes place by a dissolution-recrystallization mechanism.

The analysis of chemical equilibria present during the coprecipitation reaction can be used as a prediction of the materials obtained. For example, spherical particle growth is unlikely to occur with salts that have metal cations that do not coordinate with ammonia. For the case where the metal does coordinate with ammonia, the pH at which the concentration of metal-ammonia coordinated complexes can be calculated. If chemical equilibria calculations are carried out at a variety of temperatures and reagent concentrations, this could be a powerful tool in the prediction of the characteristics of the hydroxide material.

CHAPTER 5. Determination of the Apparent Oxygen Diffusion Coefficients from Lithium-Rich Transition Metal Oxides $\text{Li}[\text{Li}_{1/9}\text{Ni}_{1/3}\text{Mn}_{5/9}]\text{O}_2$ and $\text{Li}[\text{Li}_{1/5}\text{Ni}_{1/5}\text{Mn}_{3/5}]\text{O}_2$ by the Atlung Method

5.1. The Diffusion Process During the Charge of Positive Electrode Materials in Lithium-ion Batteries

Diffusion is due to the random motions of atoms or molecules in a material.¹²³

When a concentration gradient exists, there will be a net flux (the amount that flows through a unit area per unit time). The flux, J , is proportional to the gradient of concentration. For the one-dimensional case, Fick's first law¹²³ is written as

$$J = -D \frac{\partial c}{\partial x}, \quad (5.1)$$

where D is the diffusion coefficient and c is the concentration. For the 3D case,

$$\vec{J} = -D \vec{\nabla}(c). \quad (5.2)$$

In the previous equation,

$$\vec{\nabla}(c) = \frac{\partial c}{\partial x} \hat{x} + \frac{\partial c}{\partial y} \hat{y} + \frac{\partial c}{\partial z} \hat{z}. \quad (5.3)$$

For the one dimensional case, the conservation of mass gives

$$\frac{\partial c}{\partial t} = -\frac{\partial J}{\partial x}, \quad (5.4)$$

so Fick's second law of diffusion for the one-dimensional case is

$$\frac{\partial c}{\partial t} = D \frac{\partial^2 c}{\partial x^2}. \quad (5.5)$$

For the three-dimensional case, Fick's second law of diffusion is

$$\frac{\partial c}{\partial t} = D \nabla^2(c). \quad (5.6)$$

A diffusion model of alkali cations into and from insertion materials has been previously presented by Atlung *et al.*¹²⁴ Figure 5.1 shows a schematic of diffusion through a positive electrode and a negative electrode of spherical geometry.

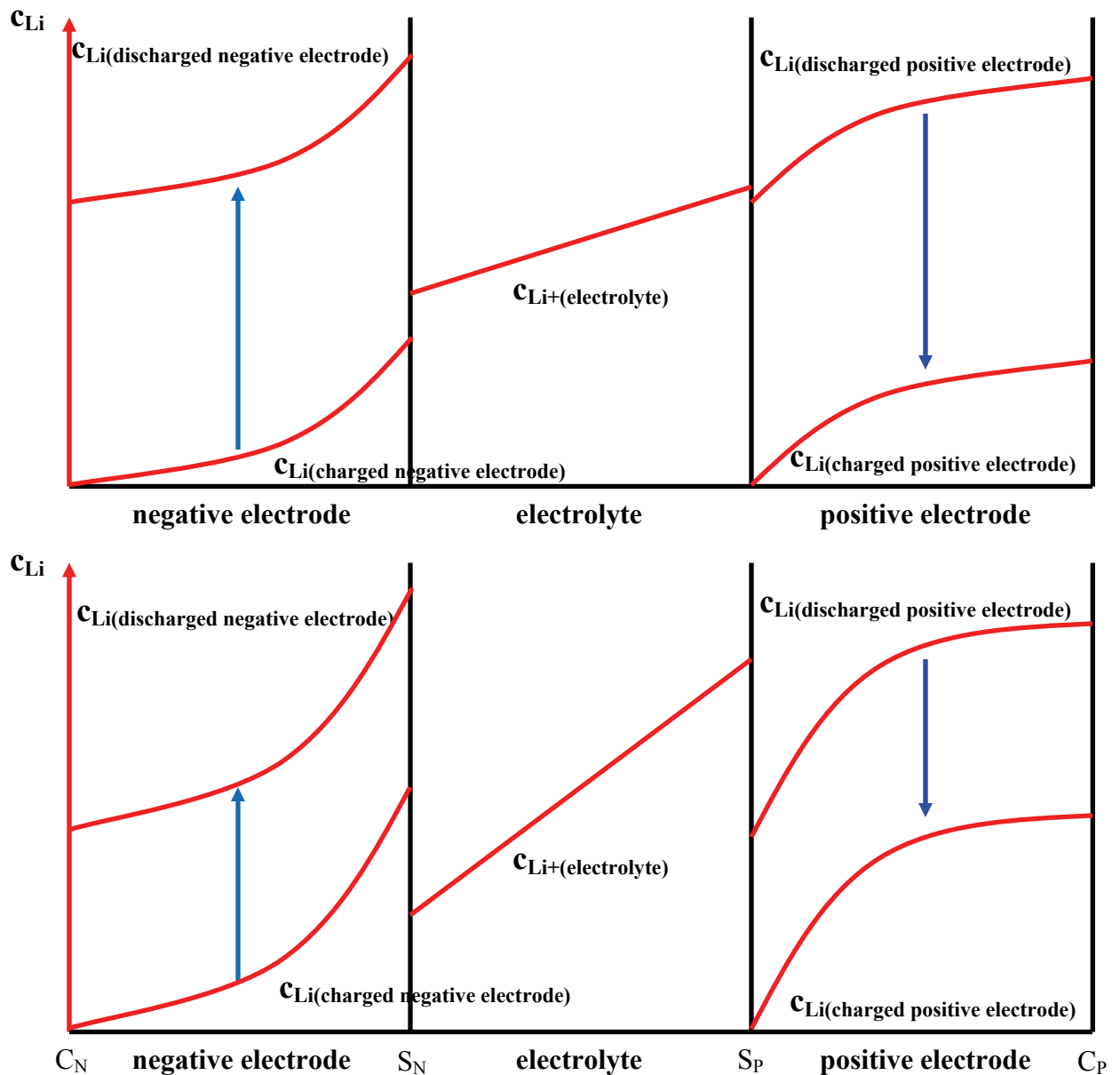


Figure 5.1. Schematic of the diffusion process through a spherical positive and negative electrode during the charge process, with a higher charge rate for the bottom panel. The center (C_N) and surface (S_N) of the negative electrode and center (C_P) and surface (C_S) of the positive electrode are indicated. Adapted from reference 124.

Figure 5.1 illustrates the diffusion process in a single positive electrode material particle and a single negative electrode material particle surrounded by electrolyte. In the actual bulk electrode, there are many particles of the electrode material. The electrolyte penetrates the bulk electrode so that the diffusion process occurs within single particles.

In the discussion of diffusion of lithium in the positive electrode and electrolyte, the lithium species will be referred to a “lithium ion” in the electrolyte and “lithium atom” in the positive electrode material. This is because in the electrolyte, lithium ions transfer with their associated counter-anion. However, in the positive electrode, an electron associated with the lithium moves as the lithium moves. If there is a gradient of lithium with some ionic character in the positive electrode material, there will also be a gradient of electron density associated with the lithium species. Therefore, the lithium species in the positive electrode will be referred to as “lithium atoms”.

In order for diffusion of lithium ions to occur from the positive electrode to the negative electrode, through the electrolyte, there must be a concentration gradient of lithium ions, with the lithium-ion concentration in the electrolyte increasing from the negative electrode to the positive electrode. The top panel of Figure 5.1 shows this concentration gradient in the electrolyte portion. For lithium diffusion to occur within the positive electrode there must be a lithium-atom concentration gradient in the positive electrode material. The top panel of Figure 5.1 shows this, with the lithium-atom concentration increasing from the surface to the center of the electrode, represented by the right-most portion of the schematic. As lithium is depleted from the positive electrode material, the lithium-atom concentration gradient moves down, as indicated in the top panel of Figure 5.1. At the end of the charge process, there is a certain number of

lithium atoms that are not removed from the material, represented by the area under the curve of the lithium-atom concentration gradient for the charged positive electrode material.

If the charge rate is increased, the concentration gradients in both the electrolyte and the positive electrode material become larger, as shown in the bottom panel of Figure 5.1. When the positive electrode material becomes completely charged, there are more lithium atoms not accessed for the material charged at higher rate. This is represented by the area under the lithium atom concentration versus position curve for the positive electrode material in the bottom panel of Figure 5.1.

The ratio of the lithium atoms removed during the charge process to the available lithium atoms in the positive electrode material is termed the “fractional capacity”. The fractional capacity of the positive electrode decreases if the charge rate is increased.

The stoichiometric charge time, T , is defined as the time required to access all of the lithium during charge. This time depends on the rate of discharge or charge – e.g.: a C/10 rate gives a stoichiometric charge time of 10 h.

The actual charge time (since all of the lithium is not removed due to diffusion limitations) is called t . The fraction of attained charge time to the stoichiometric charge time is given as

$$\tau = \frac{t}{T}. \quad (5.7)$$

For a spherical geometry, the first and second Fick’s laws can be solved using the relevant initial and boundary conditions for the charge process. For this discussion, the positive electrodes have a spherical geometry with radius, r .

The concentration, c , of lithium atoms in the positive electrode varies from 0 to 1 (with $c = 1$ at full lithiation). Before the charge process occurs (no gradient of lithium atoms), $c = 1$, or the initial condition can be written as

$$t = 0 \quad \text{all } x \quad c = 1, \quad (5.8)$$

where $-r < x < r$ is the radial space coordinate within the positive electrode particle.

As the charge process starts,

$$t > 0 \quad x = r \quad \frac{dc}{dx} = -\frac{j_o}{D}, \quad (5.9)$$

where j_o is the flux density of the transported lithium atoms in $\text{mol cm}^{-2} \text{ s}^{-1}$. For a sphere,

$$j_o = \frac{n}{S_m T} = \frac{nr}{3TV_m}, \quad (5.10)$$

where n is the number of moles of lithium atoms, S_m is the molar surface area (in $\text{cm}^2 \text{ mol}^{-1}$), and V_m is the molar volume of the positive electrode (in $\text{cm}^3 \text{ mol}^{-1}$).

The final boundary condition is

$$t > 0 \quad x \rightarrow 0 \quad 4\pi x^2 \frac{dc}{dx} = 0. \quad (5.11)$$

Solutions of equations 5.2 and 5.6, using the initial and boundary conditions in equations 5.8, 5.9, and 5.11 were determined by Carslaw and Jaeger¹²⁵ for the case of heat conduction in a sphere and can be written as:

$$1 - c(t, x) = -\frac{j_o r}{D} \left\{ \frac{3Dt}{r^2} + \frac{z^2}{2} - \frac{3}{10} - 2 \sum^i \left(\frac{e^{-\frac{\alpha_i^2 Dt}{r^2}} \sin \alpha_i z}{\alpha_i^2 \sin \alpha_i} \right) \right\}, \quad (5.12)$$

where $z = x/r$. For a spherical geometry, the first three α_i values are $\alpha_1 = 4.4934$, $\alpha_2 = 7.7253$, and $\alpha_3 = 10.9041$.¹²⁵

At the surface of the spherical particle, $z = 1$. In the case of charge of the positive electrode material, the number of removed lithium atoms at the surface has been determined by Atlung *et al.*¹²⁴ and can be expressed as

$$X^* = X_d - \left\{ \tau + \frac{1}{3Q} \left[\frac{1}{5} - 2 \sum_i \frac{e^{-\frac{\alpha_i^2 Dt}{r^2}}}{\alpha_i^2} \right] \right\}, \quad (5.13)$$

where the number of removed lithium atoms per mole of positive electrode material can be written as

$$X = \frac{cV_m}{n} \quad (5.14)$$

and the ratio of the stoichiometric charge time to the time constant for diffusion in a particle can be expressed as

$$Q = \left(\frac{T}{r^2/D} \right). \quad (5.15)$$

X^* is X at the positive electrode surface, and X_d is the average X in the positive electrode before charge. For a fresh positive electrode, $X_d = 1$. When the battery reaches the top of charge at fixed current, the surface concentration of lithium is zero and equation 5.13 becomes

$$1 = \tau + \frac{1}{3Q} \left\{ \frac{1}{5} - 2 \sum_i \frac{e^{-\frac{\alpha_i^2 Dt}{r^2}} \sin \alpha_i z}{\alpha_i^2 \sin \alpha_i} \right\}. \quad (5.16)$$

Figure 5.2 shows the dependence of the fractional capacity, τ , on $\log Q$ for a material with a spherical geometry. At smaller particle radii and lower rates (larger stoichiometric charge time, t), higher values of fractional capacity are obtained. Figure 5.2 is the characteristic “Atlung graph” for a material with a spherical geometry.

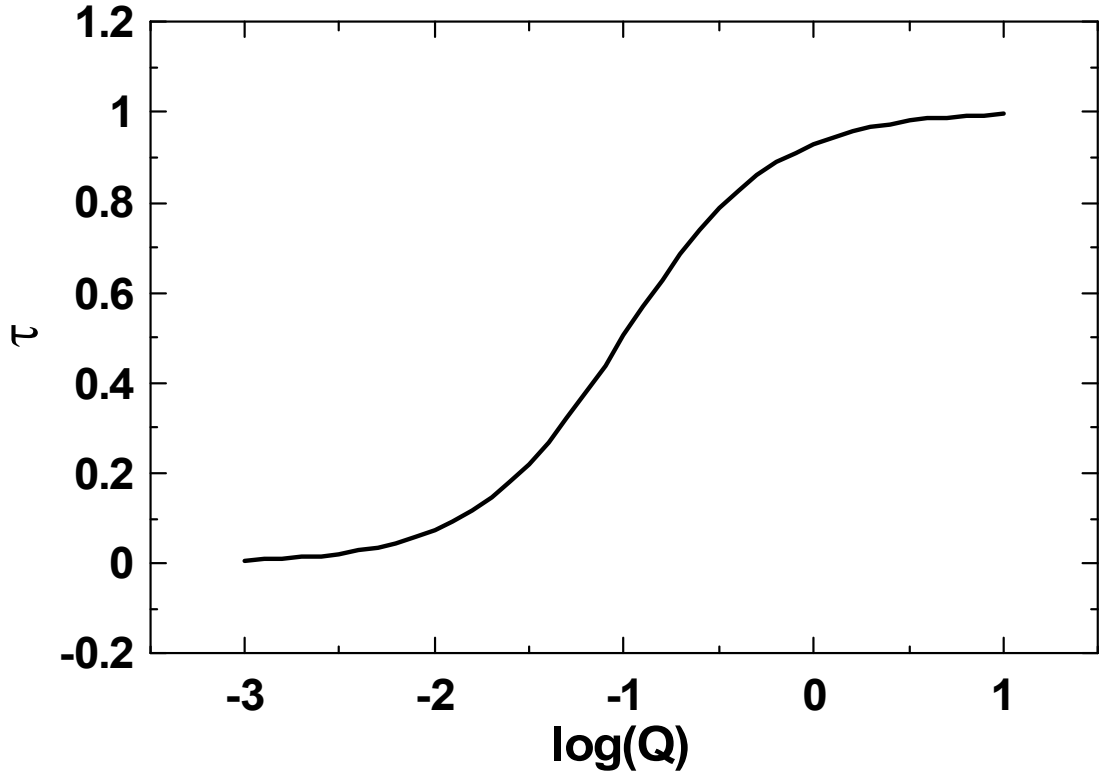


Figure 5.2. Characteristic Atlung graph for a material with a spherical geometry.

5.2. Oxygen Diffusion Through $\text{Li}[\text{Li}_{1/9}\text{Ni}_{1/3}\text{Mn}_{5/9}]\text{O}_2$ and $\text{Li}[\text{Li}_{1/5}\text{Ni}_{1/5}\text{Mn}_{3/5}]\text{O}_2$

Section 5.1 showed that, for diffusion in a single phase, the fractional capacity, τ , depends on the ratio of the characteristic diffusion time, r^2/D , to the charge or discharge time, T . The removal of lithium in the oxygen loss region has been determined to occur in a single phase process by Lu *et al.*⁵³ Therefore, the Atlung graph in Figure 5.2 can be used to determine information about the diffusion processes that exist in lithium-rich

transition metal oxide positive electrode materials. This Atlung method will be the foundation of the analysis of the lithium-rich positive electrode materials $\text{Li}[\text{Li}_{1/9}\text{Ni}_{1/3}\text{Mn}_{5/9}]\text{O}_2$ and $\text{Li}[\text{Li}_{1/5}\text{Ni}_{1/5}\text{Mn}_{3/5}]\text{O}_2$, to be carried out in this section. The Atlung method has been selected over other methods such as galvanostatic intermittent titration (GITT). The Atlung method involves simple measurements (measuring the amount of capacity in the oxygen-loss region at different rates, particle sizes, and temperatures) and the analysis is mathematically compact (using the known solutions of Fick's laws in the case of diffusion through a spherical particle). Methods such as GITT should be done to give a comparison between determined diffusion coefficients and to gain more insight into the lithium removal from the lithium-rich oxides.

Chapter 4 showed that, for the coprecipitation reaction in aqueous ammonia, the particle size of transition-metal oxides increases with the reaction time of the hydroxide precursor. The precursor hydroxides to $\text{Li}[\text{Li}_{1/9}\text{Ni}_{1/3}\text{Mn}_{5/9}]\text{O}_2$ and $\text{Li}[\text{Li}_{1/5}\text{Ni}_{1/5}\text{Mn}_{3/5}]\text{O}_2$ are $\text{Ni}_{3/8}\text{Mn}_{5/8}(\text{OH})_2$ and $\text{Ni}_{1/4}\text{Mn}_{3/4}(\text{OH})_2$, respectively.

$\text{Ni}_{3/8}\text{Mn}_{5/8}(\text{OH})_2$ was made with coprecipitation reaction times of 5, 10, and 20 h. Figure 5.3 shows the XRD patterns of these materials. The samples showed expected diffraction peaks with slight oxidation to MOOH, especially for the 5 h coprecipitation reaction time sample. The tap densities of $\text{Ni}_{3/8}\text{Mn}_{5/8}(\text{OH})_2$, made with coprecipitation reaction times of 5, 10, and 20 h, were 0.8, 1.3, and 1.6 g cm^{-3} , respectively. The values of a and c lattice parameters were as follows: for the $\text{Ni}_{3/8}\text{Mn}_{5/8}(\text{OH})_2$ coprecipitation reaction time of 5 h: $a = 3.2420 \pm 0.0005 \text{ \AA}$, $c = 4.709 \pm 0.002 \text{ \AA}$; 10 h: $a = 3.2393 \pm 0.0003 \text{ \AA}$, $c = 4.701 \pm 0.001 \text{ \AA}$; 20 h: $a = 3.2442 \pm 0.0002 \text{ \AA}$, $c = 4.7100 \pm 0.0007 \text{ \AA}$. The similar lattice constant values indicate that the materials vary in size, not structure.

$\text{Ni}_{1/4}\text{Mn}_{3/4}(\text{OH})_2$ was made with coprecipitation reaction times of 10, 20, and 40 h. Figure 5.4 shows the XRD pattern of $\text{Ni}_{1/4}\text{Mn}_{3/4}(\text{OH})_2$ made with a coprecipitation reaction time of 10 h. The samples with reaction times of 20 h and 40 h oxidized as they were not immediately taken for XRD analysis. The XRD pattern for the sample with a reaction time of 10 h also showed the expected diffraction peaks, with slight oxidation to MOOH . The tap densities of $\text{Ni}_{1/4}\text{Mn}_{3/4}(\text{OH})_2$, made with coprecipitation reaction times of 10, 20, and 40 h, were 0.8, 1.2, and 1.4 g cm^{-3} , respectively.

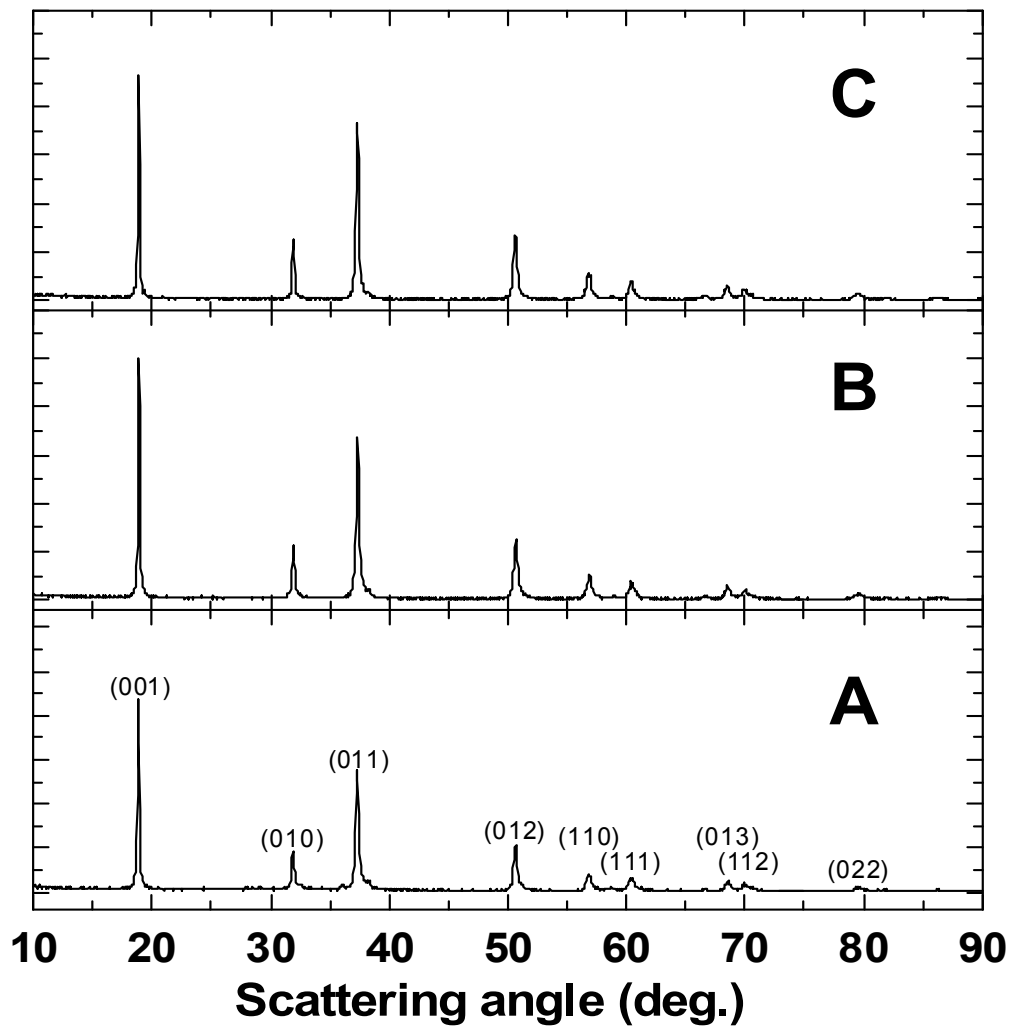


Figure 5.3. XRD patterns of $\text{Ni}_{3/8}\text{Mn}_{5/8}(\text{OH})_2$. The coprecipitation reaction times were 5 h (A), 10 h (B), and 20 h (C).

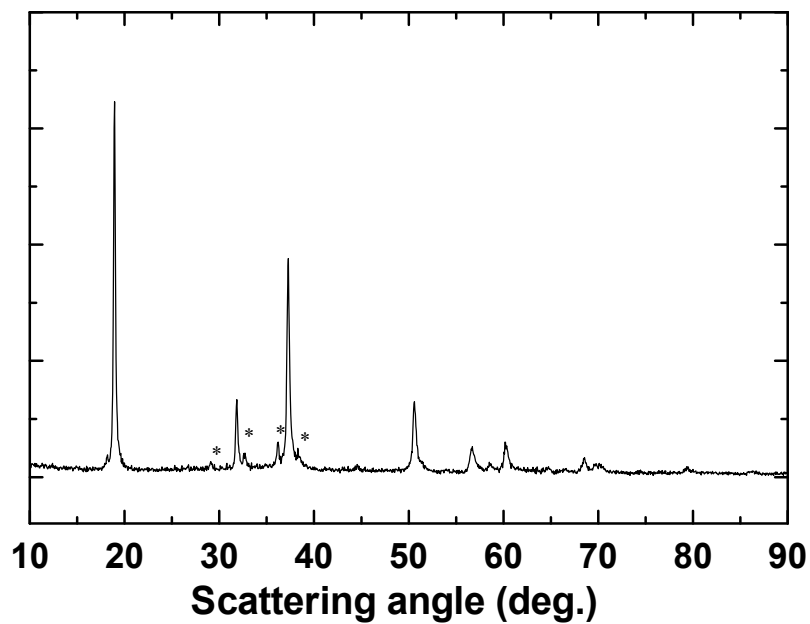


Figure 5.4. XRD pattern of $\text{Ni}_{1/4}\text{Mn}_{3/4}(\text{OH})_2$. The coprecipitation reaction time was 10 h. *Peaks from oxidation of pure hydroxide material (described in Chapter 3).

Figure 5.5 shows the SEM images of $\text{Ni}_{3/8}\text{Mn}_{5/8}(\text{OH})_2$ made with coprecipitation reaction times of 5, 10, and 20 h. As expected and described in Chapter 4, there is an increase in particle size with an increase in coprecipitation reaction time.

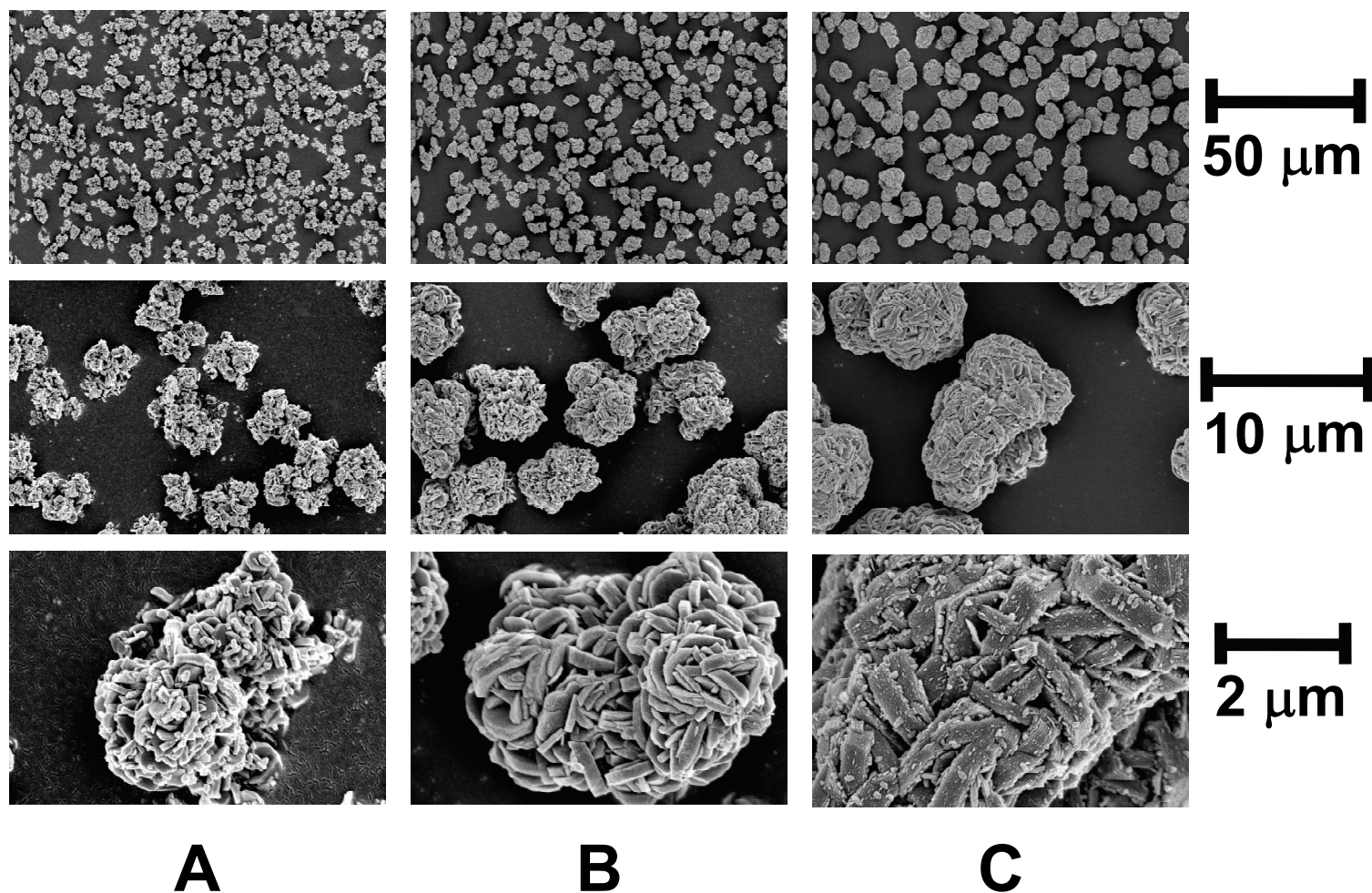


Figure 5.5. SEM images of $\text{Ni}_{3/8}\text{Mn}_{5/8}(\text{OH})_2$.
The coprecipitation reaction times were 5 h (A), 10 h (B), and 20 h (C).

$\text{Ni}_{3/8}\text{Mn}_{5/8}(\text{OH})_2$ and $\text{Ni}_{1/4}\text{Mn}_{3/4}(\text{OH})_2$ materials made at various coprecipitation reaction times were mixed with Li_2CO_3 and heated to 950°C to form the lithium-rich transition metal oxides $\text{Li}[\text{Li}_{1/9}\text{Ni}_{1/3}\text{Mn}_{5/9}]\text{O}_2$ and $\text{Li}[\text{Li}_{1/5}\text{Ni}_{1/5}\text{Mn}_{3/5}]\text{O}_2$, respectively.

Figure 5.6 shows the XRD patterns of $\text{Li}[\text{Li}_{1/9}\text{Ni}_{1/3}\text{Mn}_{5/9}]\text{O}_2$ from $\text{Ni}_{3/8}\text{Mn}_{5/8}(\text{OH})_2$ made with coprecipitation reaction times of 5 h, 10 h, and 20 h. As expected, there were superlattice peaks in the range of $20\text{-}25^\circ$. The XRD lines were indexed in the hexagonal system for the reduced lattice, neglecting the superlattice peaks.⁵³ The values of a and c lattice parameters were as follows: for the $\text{Ni}_{3/8}\text{Mn}_{5/8}(\text{OH})_2$ coprecipitation reaction time of 5 h: $a = 2.871 \pm 0.0002 \text{ \AA}$, $c = 14.276 \pm 0.002 \text{ \AA}$; 10 h: $a = 2.8707 \pm 0.0003 \text{ \AA}$, $c = 14.275 \pm 0.003 \text{ \AA}$; 20 h: $a = 2.8683 \pm 0.0004 \text{ \AA}$, $c = 14.274 \pm 0.004 \text{ \AA}$. The importance of the lattice parameter values is described below.

Figure 5.7 shows the XRD patterns of $\text{Li}[\text{Li}_{1/5}\text{Ni}_{1/5}\text{Mn}_{3/5}]\text{O}_2$ from $\text{Ni}_{1/4}\text{Mn}_{3/4}(\text{OH})_2$ made with coprecipitation reaction times of 10 h, 20 h, and 40 h. The values of a and c lattice parameters were also determined for $\text{Li}[\text{Li}_{1/5}\text{Ni}_{1/5}\text{Mn}_{3/5}]\text{O}_2$ and were as follows: for the $\text{Ni}_{1/4}\text{Mn}_{3/4}(\text{OH})_2$ coprecipitation reaction time of 10 h: $a = 2.860 \pm 0.001 \text{ \AA}$, $c = 14.246 \pm 0.002 \text{ \AA}$; 20 h: $a = 2.860 \pm 0.001 \text{ \AA}$, $c = 14.238 \pm 0.008 \text{ \AA}$; 40 h: $a = 2.860 \pm 0.001 \text{ \AA}$, $c = 14.242 \pm 0.004 \text{ \AA}$. The importance of the lattice parameter values is described below.

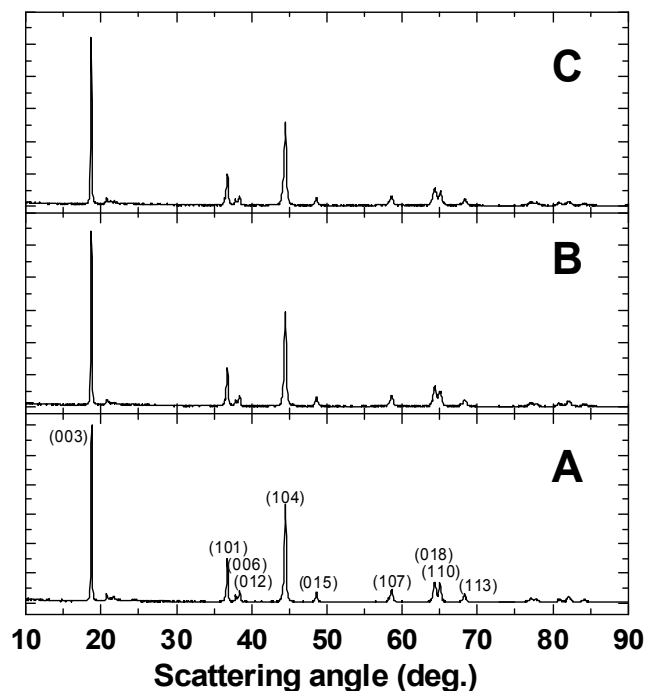


Figure 5.6. XRD patterns of $\text{Li}[\text{Li}_{1/9}\text{Ni}_{1/3}\text{Mn}_{5/9}]\text{O}_2$. The oxide was from $\text{Ni}_{3/8}\text{Mn}_{5/8}(\text{OH})_2$ made with coprecipitation reaction times of 5 h (A), 10 h (B), and 20 h (C).

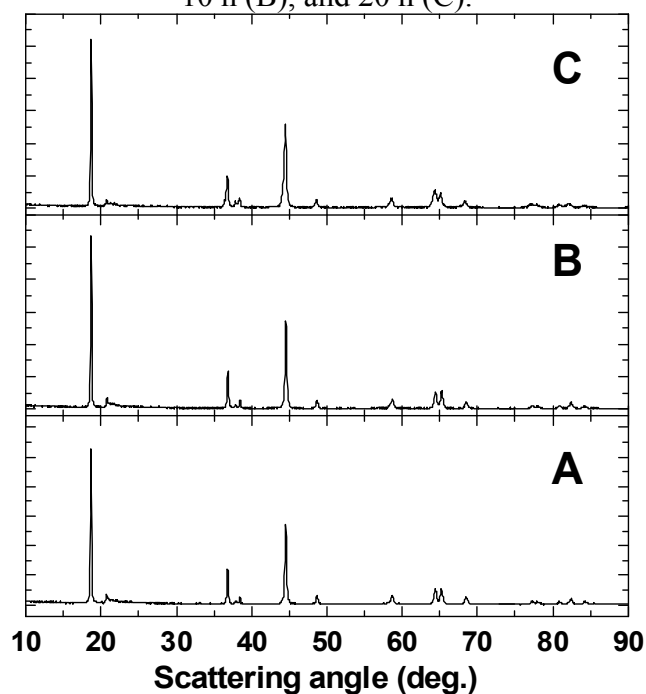


Figure 5.7. XRD patterns of $\text{Li}[\text{Li}_{1/5}\text{Ni}_{1/5}\text{Mn}_{3/5}]\text{O}_2$. The oxide was from $\text{Ni}_{1/4}\text{Mn}_{3/4}(\text{OH})_2$ made with a coprecipitation reaction time of 10 h (A), 20 h (B), and 40 h (C).

Figure 5.8 shows the lattice parameters of various stoichiometries of $\text{Li}[\text{Ni}_x\text{Li}_{(1/3-2x/3)}\text{Mn}_{(2/3-x/3)}]\text{O}_2$ as determined by Lu *et al.*¹¹², with comparison to those found in this work. The lattice parameters of the lithium rich oxides $\text{Li}[\text{Li}_{1/9}\text{Ni}_{1/3}\text{Mn}_{5/9}]\text{O}_2$ and $\text{Li}[\text{Li}_{1/5}\text{Ni}_{1/5}\text{Mn}_{3/5}]\text{O}_2$ made are consistent with those reported by Lu *et al.* This indicates that the stoichiometries intended are close to those synthesized. As well, the lattice parameters of the samples made at different coprecipitation reaction times are similar. Since the lattice parameters vary with composition (Figure 5.8), this indicates that the stoichiometries are comparable for samples made at different coprecipitation reaction times. This suggests that, for each stoichiometry, the samples differ only in particle size, not composition or structure.

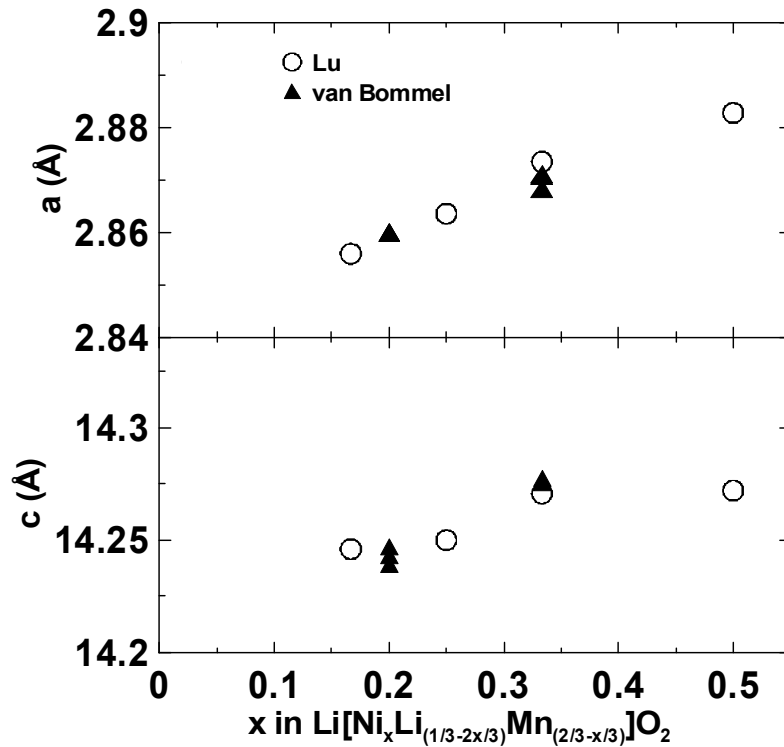


Figure 5.8. Dependence of hexagonal lattice constants, a and c , on x in $\text{Li}[\text{Ni}_x\text{Li}_{(1/3-2x/3)}\text{Mn}_{(2/3-x/3)}]\text{O}_2$. Comparison is made between the values in this work and those of Lu *et al.*¹¹²

Figure 5.9 shows the particle size distribution and Figure 5.10 shows the SEM images of $\text{Li}[\text{Li}_{1/9}\text{Ni}_{1/3}\text{Mn}_{5/9}]\text{O}_2$ synthesized from $\text{Ni}_{3/8}\text{Mn}_{5/8}(\text{OH})_2$ with coprecipitation reaction times of 5, 10, and 20 h. The particle size distribution has the number (N) normalized by the particle size interval (D_p). The tap densities of $\text{Li}[\text{Li}_{1/9}\text{Ni}_{1/3}\text{Mn}_{5/9}]\text{O}_2$ made from $\text{Ni}_{3/8}\text{Mn}_{5/8}(\text{OH})_2$ with coprecipitation reaction times of 5, 10, and 20 h were 0.8, 1.3, and 1.6 g cm^{-3} , respectively. These are the same tap density values as for the precursor hydroxide. Comparing the SEM images from the oxide, $\text{Li}[\text{Li}_{1/9}\text{Ni}_{1/3}\text{Mn}_{5/9}]\text{O}_2$, (Figure 5.10) with the precursor hydroxide, $\text{Ni}_{3/8}\text{Mn}_{5/8}(\text{OH})_2$, (Figure 5.5) reveals that the spherical morphology of the particles remain.

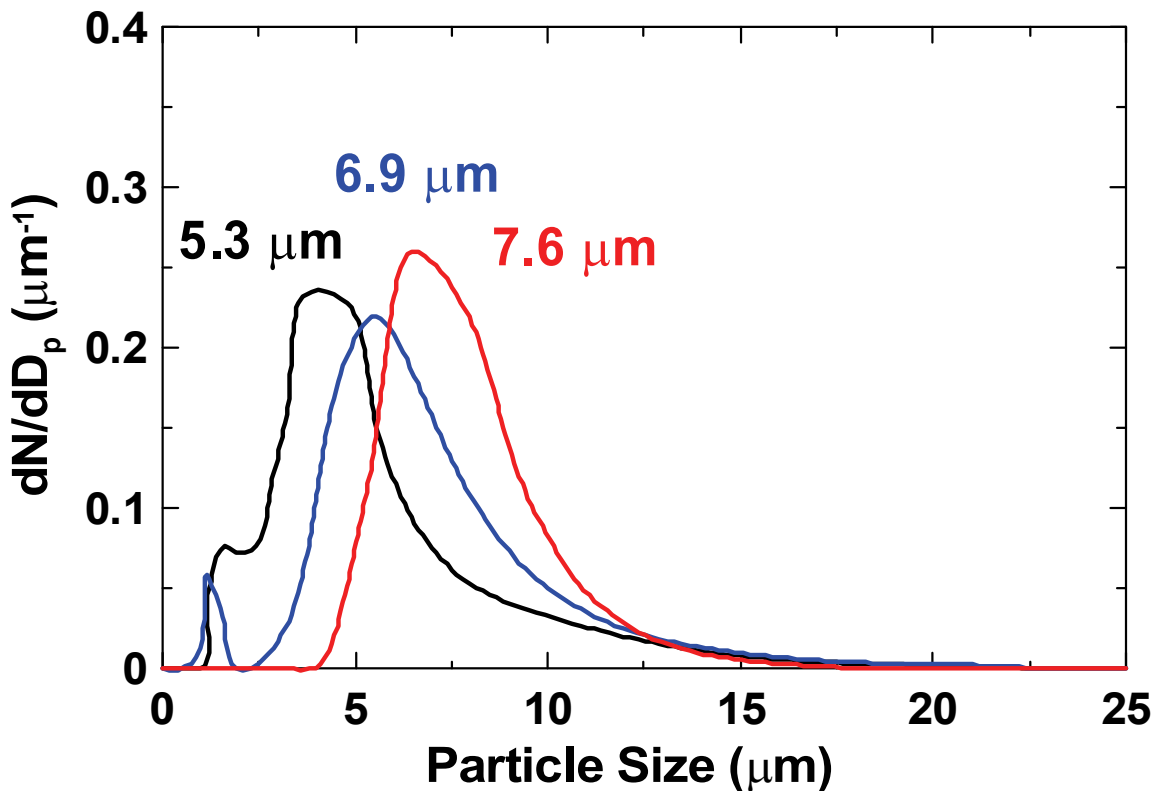


Figure 5.9. Particle size distributions of $\text{Li}[\text{Li}_{1/9}\text{Ni}_{1/3}\text{Mn}_{5/9}]\text{O}_2$. The y-axis is normalized by the size of the particle size interval and the total number.

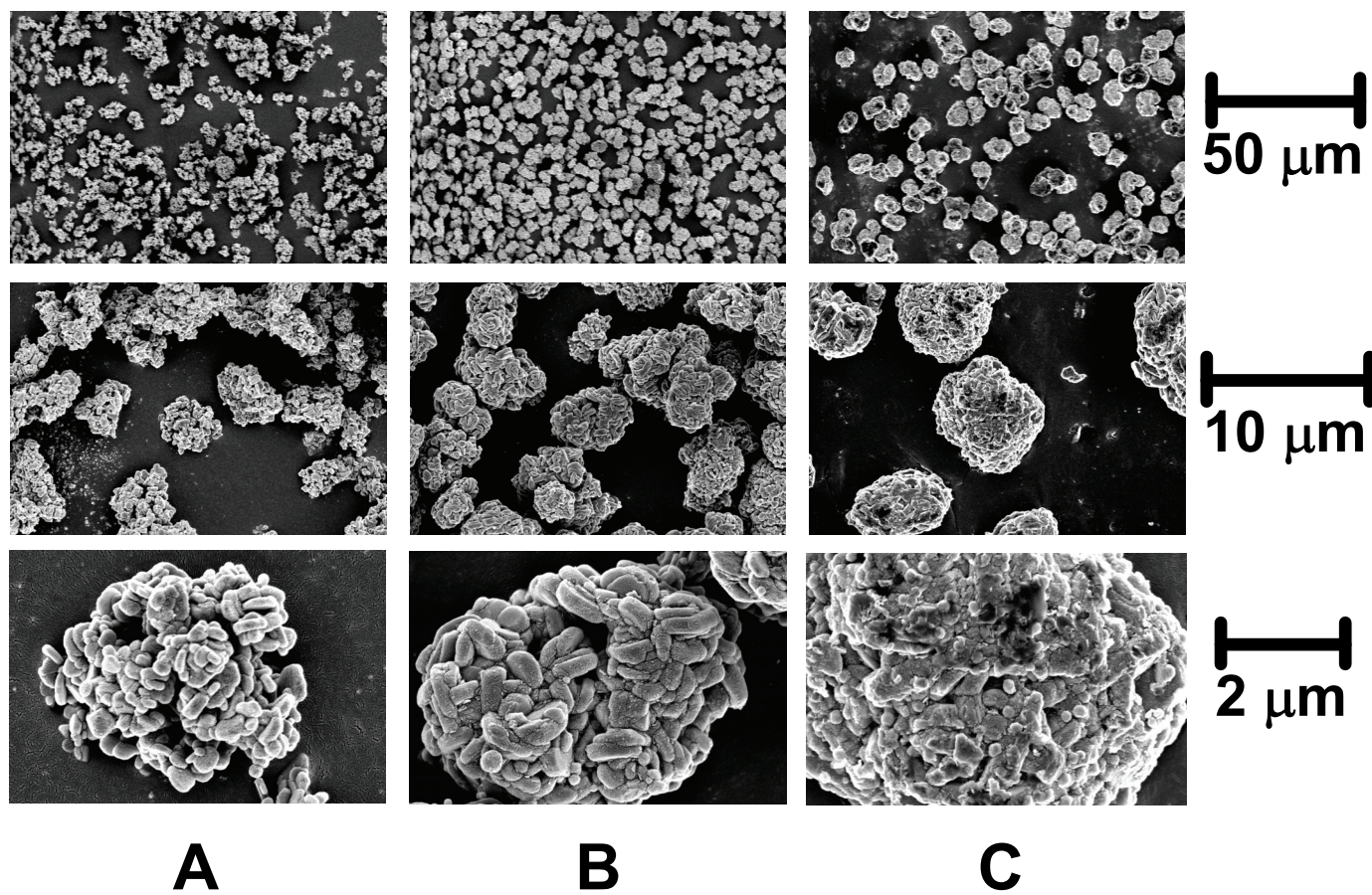


Figure 5.10. SEM images of $\text{Li}[\text{Li}_{1/9}\text{Ni}_{1/3}\text{Mn}_{5/9}]\text{O}_2$. The oxide was made from $\text{Ni}_{3/8}\text{Mn}_{5/8}(\text{OH})_2$ made with coprecipitation reaction times of 5 h (A), 10 h (B), and 20 h (C). From van Bommel, A; Dahn, J. R. *Electrochem. Solid-State Lett.* **2010**, *13*, A62. Reprinted with permission from the American Chemical Society. Copyright 2010.

Figure 5.11 shows the particle size distributions and Figure 5.12 shows the SEM images of $\text{Li}[\text{Li}_{1/5}\text{Ni}_{1/5}\text{Mn}_{3/5}]\text{O}_2$ synthesized from $\text{Ni}_{1/4}\text{Mn}_{3/4}(\text{OH})_2$ with coprecipitation reaction times of 10, 20, and 40 h. The tap densities of $\text{Li}[\text{Li}_{1/5}\text{Ni}_{1/5}\text{Mn}_{3/5}]\text{O}_2$ made from $\text{Ni}_{1/4}\text{Mn}_{3/4}(\text{OH})_2$ with coprecipitation reaction times of 5, 10, and 20 h were 1.0, 1.4, and 1.6 g cm^{-3} , respectively. These tap densities are slightly higher than those of the precursor hydroxide.

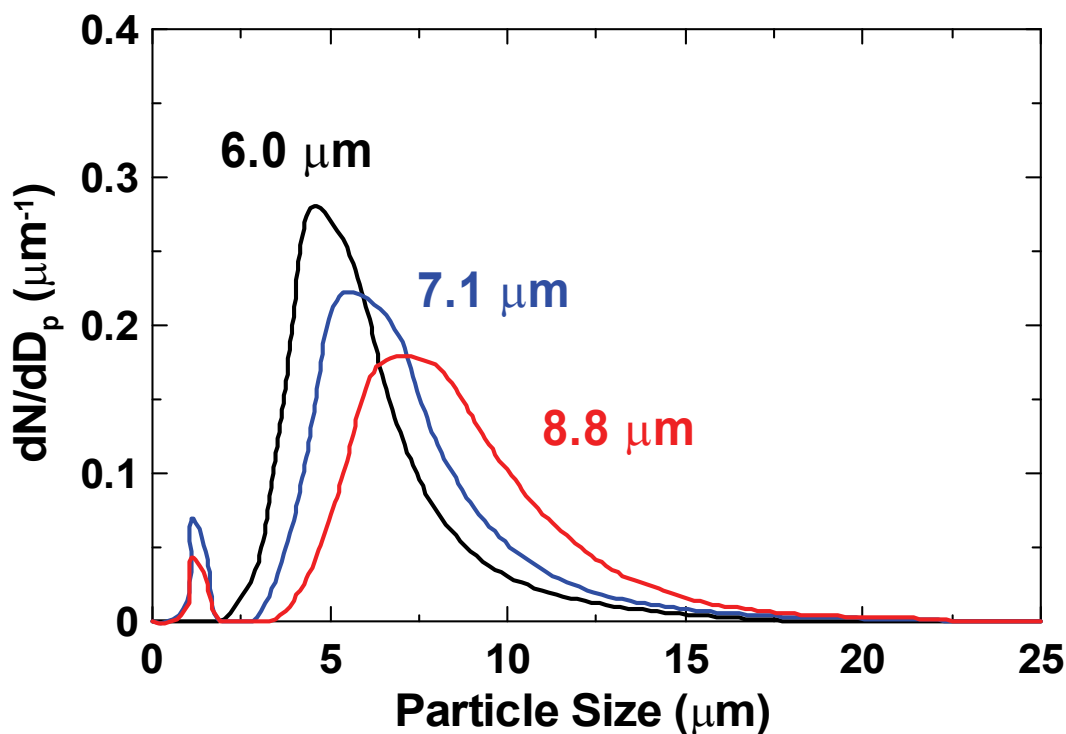


Figure 5.11. Particle size distributions of $\text{Li}[\text{Li}_{1/5}\text{Ni}_{1/5}\text{Mn}_{3/5}]\text{O}_2$. The y-axis is normalized by the size of the particle size interval and the total number

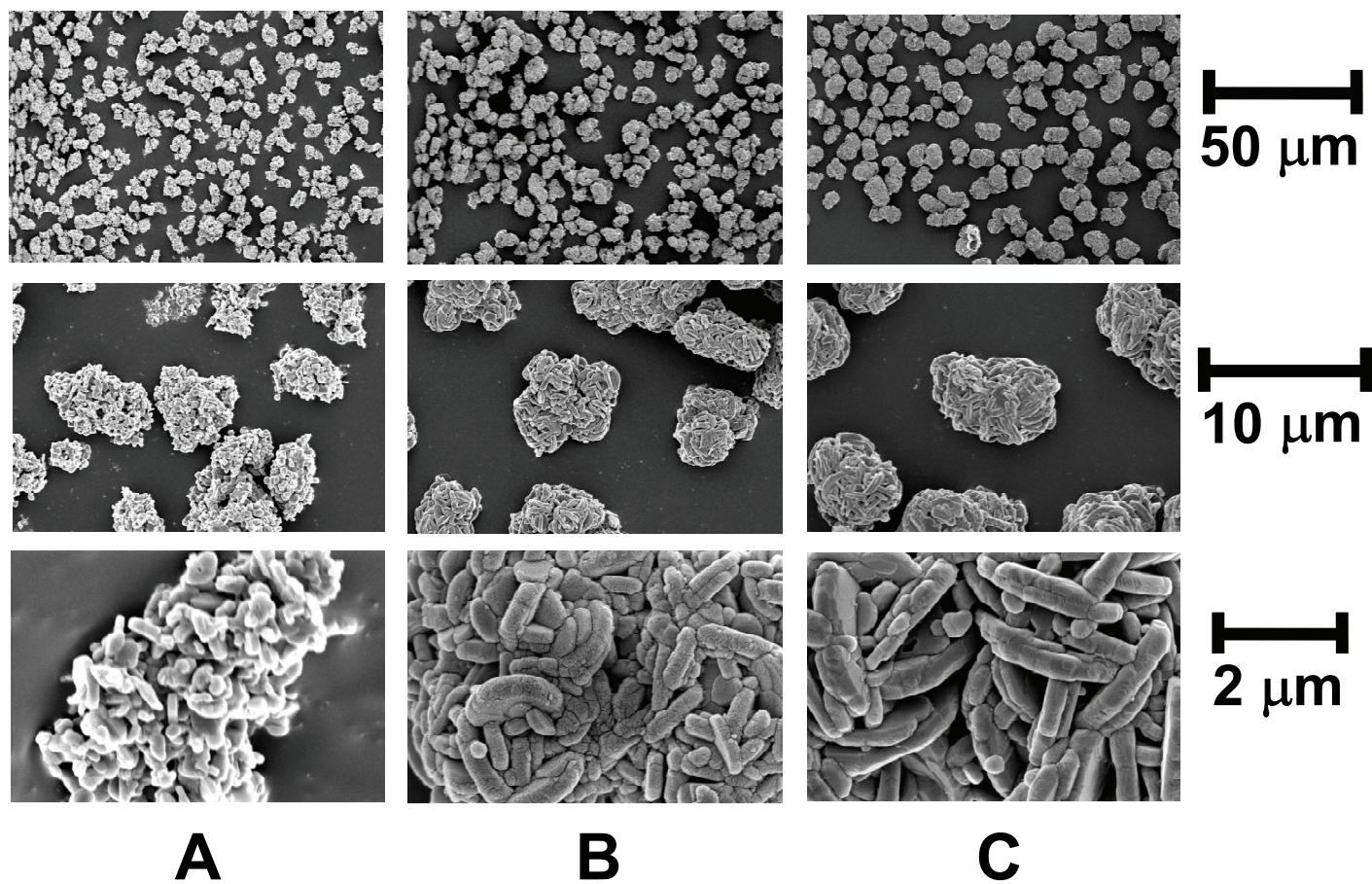


Figure 5.12. SEM images of $\text{Li}[\text{Li}_{1/5}\text{Ni}_{1/5}\text{Mn}_{3/5}]\text{O}_2$. The oxide was from $\text{Ni}_{1/4}\text{Mn}_{3/4}(\text{OH})_2$ made with coprecipitation reaction times of 10 h (A), 20 h (B), and 40 h (C).

Figure 5.13 shows the first charge to 4.8 V for Li/Li[Li_{1/9}Ni_{1/3}Mn_{5/9}]O₂ cells having positive electrodes with particles sizes of 5.3, 6.9, and 7.6 μm and at rates from C/5 to C/100 at both 30 and 55°C. For the selected parameters, there is virtually no change in the ‘normal’ lithium deintercalation region, as indicated by the portion of the potential-capacity curve to the left of the dashed vertical line. However, there is a dependence of both rate and particle size on the length of the oxygen-release plateau: lower charge rates and smaller particle sizes delivered higher oxygen-release capacity.

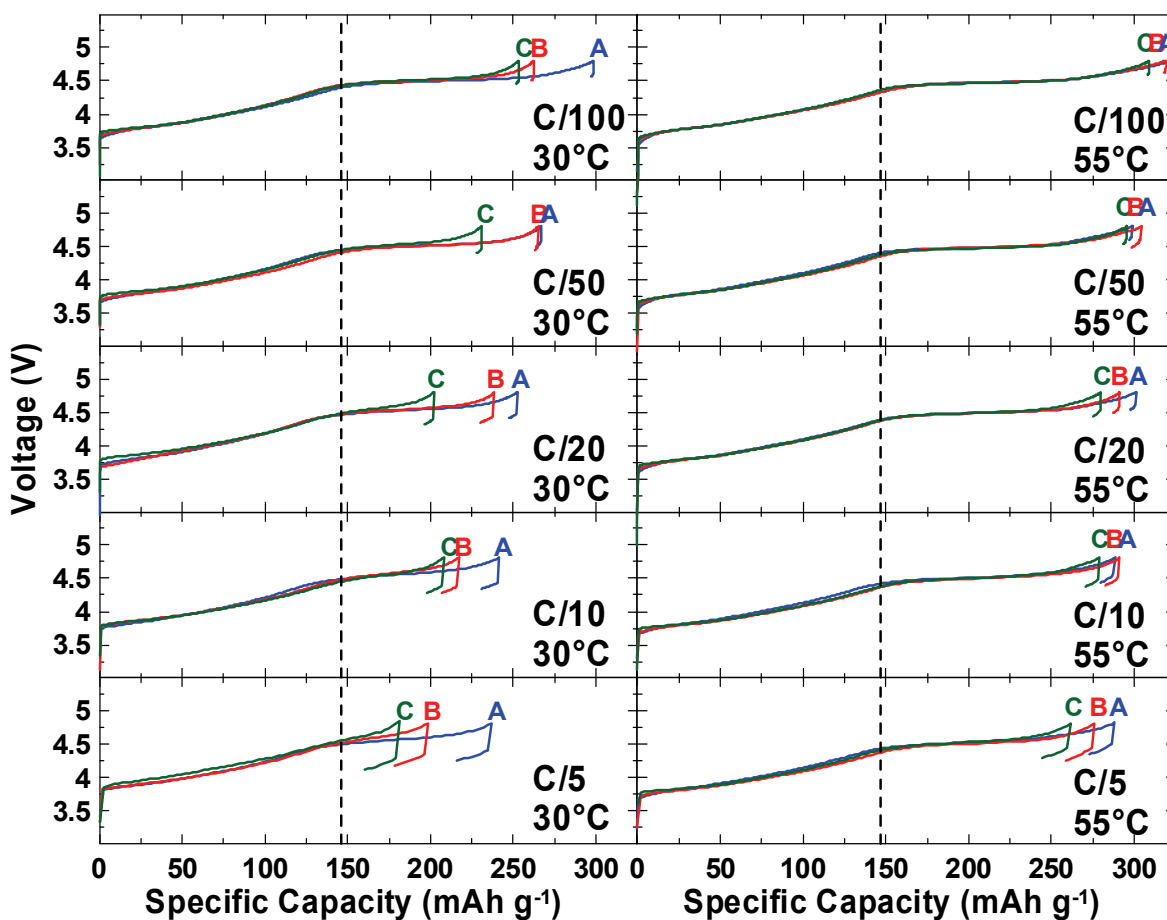


Figure 5.13. Potential versus specific capacity during first charge of Li/Li[Li_{1/9}Ni_{1/3}Mn_{5/9}]O₂ cells. The particle sizes were 5.3 μm (A), 6.9 μm (B), and 7.6 μm (C) and different charge rates and temperatures are shown.

From van Bommel, A; Dahn, J. R. *Electrochem. Solid-State Lett.* **2010**, *13*, A62. Reprinted with permission from the American Chemical Society. Copyright 2010.

Figure 5.14 shows the dQ/dV graphs of the first charge to 4.8 V for Li/Li[Li_{1/9}Ni_{1/3}Mn_{5/9}]O₂ cells having positive electrodes with particles sizes of 5.3, 6.9, and 7.6 μm and at rates from C/5 to C/100 at both 30 and 55°C. The lower voltage peak is that of normal lithium deintercalation and the higher voltage peak is for lithium deintercalation during the oxygen release process. Again, this shows that for the selected parameters, there is virtually no change in the ‘normal’ lithium deintercalation region, but there is an increase in the capacity of the oxygen-release region with decreased rate.

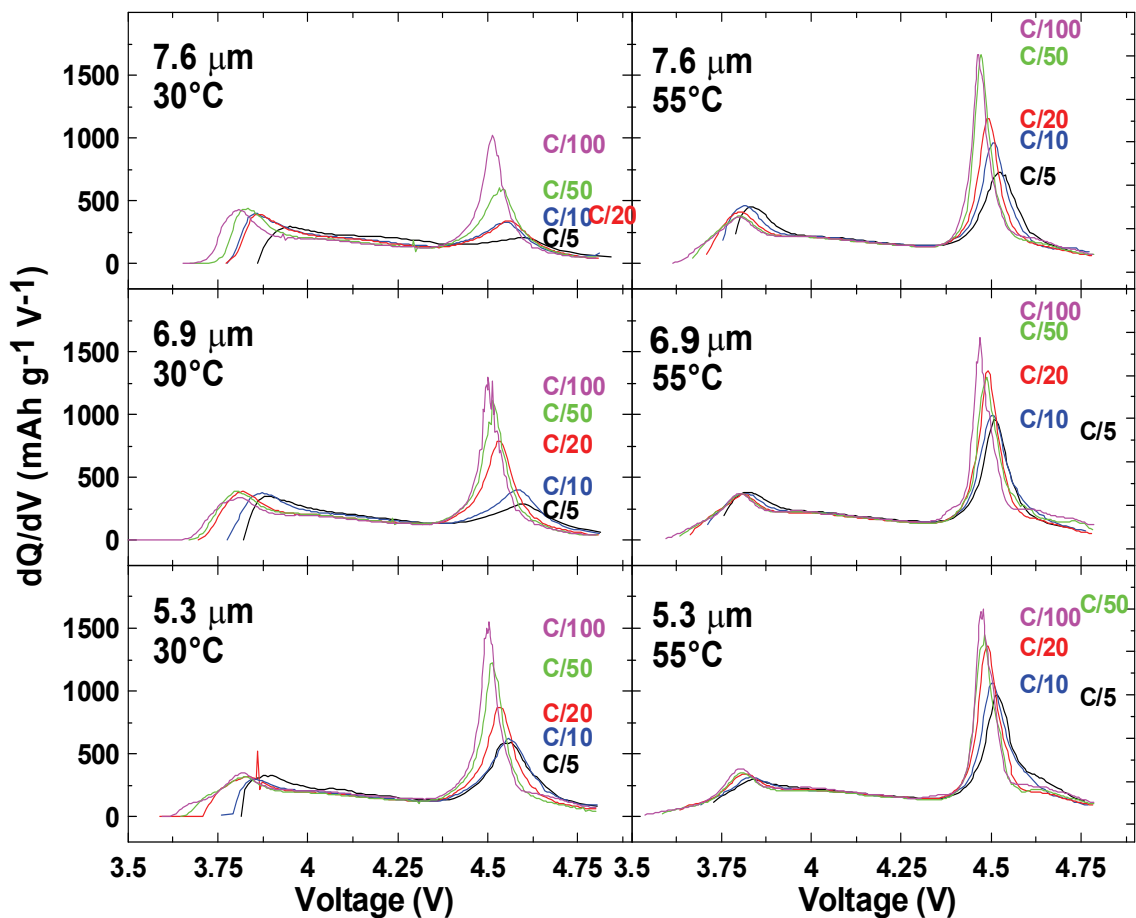


Figure 5.14. dQ/dV versus voltage graphs during the first charge of Li/Li[Li_{1/9}Ni_{1/3}Mn_{5/9}]O₂ cells.

The particle sizes were 5.3 μm , 6.9 μm , and 7.6 μm and different charge rates and temperatures are shown.

From van Bommel, A; Dahn, J. R. *Electrochem. Solid-State Lett.* **2010**, *13*, A62. Reprinted with permission from the American Chemical Society. Copyright 2010.

Figure 5.15 shows the first charge to 4.8 V for Li/Li[Li_{1/5}Ni_{1/5}Mn_{3/5}]O₂ cells having positive electrodes with particles sizes of 6.0, 7.1, and 8.8 μm and at rates from C to C/50 at both 30 and 55°C. For the most part, the normal lithium deintercalation region is unaffected by the rates, particle sizes, and temperatures selected. However, at fast charge rates and low temperatures (e.g. C-rate at 30°C), the initial normal deintercalation region is affected.

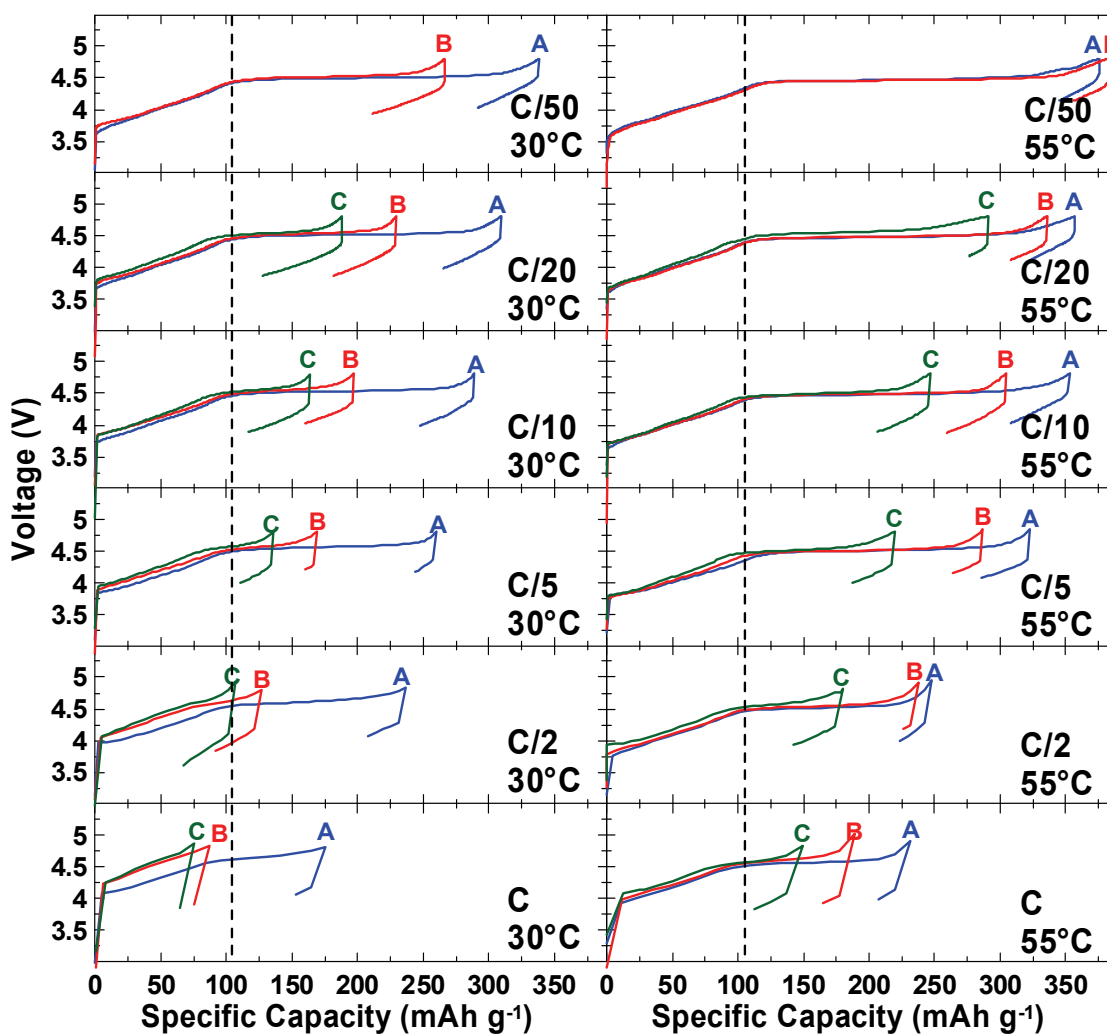


Figure 5.15. Potential versus specific capacity during the first charge of Li/Li[Li_{1/5}Ni_{1/5}Mn_{3/5}]O₂ cells. The particle sizes were 6.0 μm (A), 7.1 μm (B), and 8.8 μm (C) and different charge rates and temperatures are shown.

Figure 5.16 shows the dQ/dV graphs of the first charge to 4.8 V for Li/Li[Li_{1/5}Ni_{1/5}Mn_{3/5}]O₂ cells having positive electrodes with particles sizes of 6.0, 7.1, and 8.8 μm and at rates from C to C/50 at both 30 and 55°C.

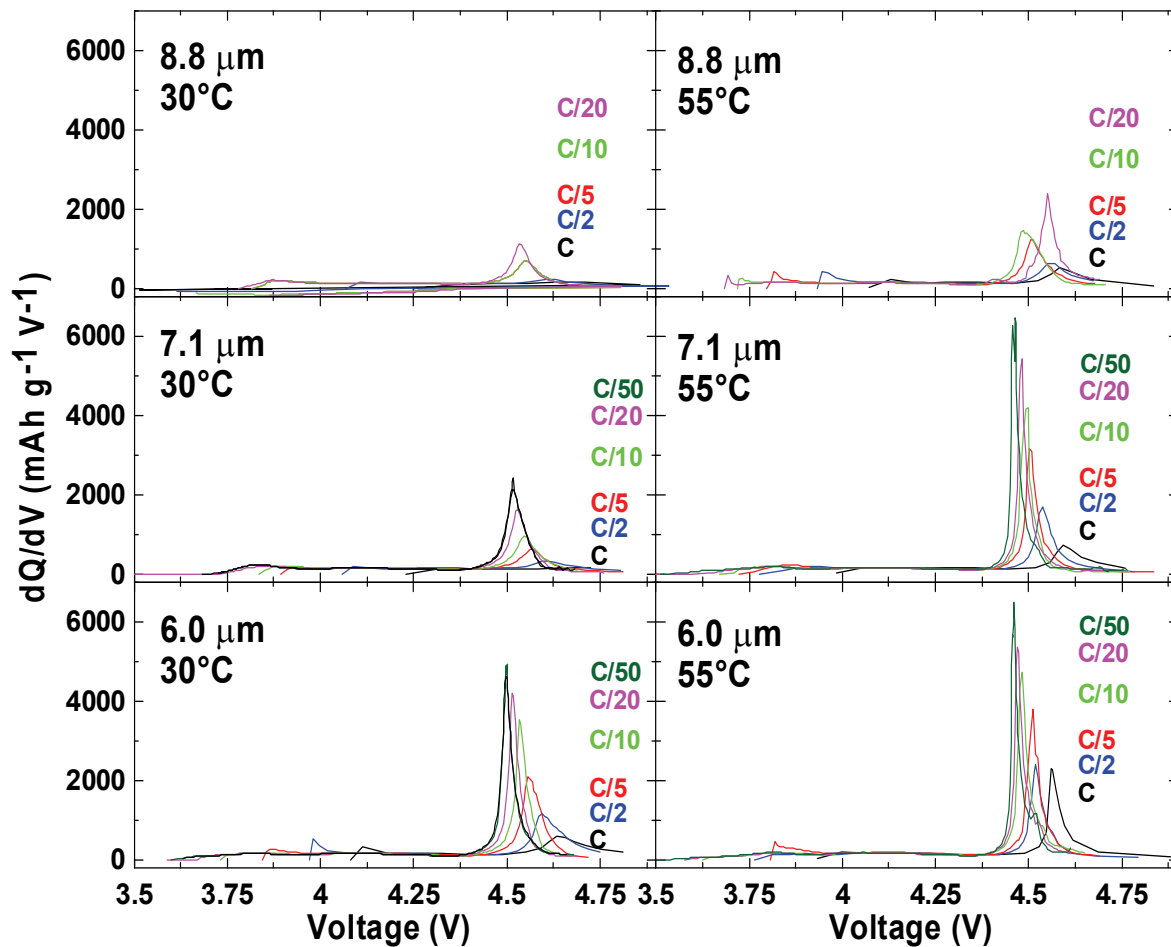


Figure 5.16. dQ/dV versus voltage graphs during the first charge of Li/Li[Li_{1/5}Ni_{1/5}Mn_{3/5}]O₂ cells. The particle sizes were 6.0 μm , 7.1 μm , and 8.8 μm and different charge rates and temperatures are shown.

The analysis of the variation of the specific capacity with charge rate, particle size, and temperature in the oxygen-loss region will now be discussed. In-situ XRD

measurements by Lu *et al.*⁵³ showed that the Bragg diffraction peaks shifted but remained sharp during the oxygen loss plateau, suggesting that the same amount of oxygen (and accompanying lithium) is lost throughout the particles. Thus, the electrochemical measurements during the first charge of $\text{Li}[\text{Li}_{1/9}\text{Ni}_{1/3}\text{Mn}_{5/9}]\text{O}_2$ and $\text{Li}[\text{Li}_{1/5}\text{Ni}_{1/5}\text{Mn}_{3/5}]\text{O}_2$ can be used to learn about the combined kinetics of the coupled processes of oxygen diffusion to the surface of the particle, transition metal motion (to fill vacancies) and corresponding removal of lithium.

Table 5.2 shows the approximate errors in the capacity measurements derived from the errors in the electrode mass, current delivered, and voltage cut-off. For the low rate cells, the error in current delivered is higher since the current delivered is smaller. For the high rate cells, the error in the voltage cut-off is higher since there is a greater chance for the upper cut-off voltage to exceed 4.8 V since the charging system scans the cells and measures the voltage of the cell only once every 2 minutes.

Table 5.3 shows the oxygen-release plateau capacity for particles of different sizes, rates, and temperatures of $\text{Li}/\text{Li}[\text{Li}_{1/9}\text{Ni}_{1/9}\text{Mn}_{5/9}]\text{O}_2$ cells. The fractional capacity is the ratio of the obtained capacity to the highest capacity obtained in the oxygen loss region (usually for the highest temperature, lowest rate, and smallest particle size). Table 5.3 includes the fractional capacity, τ .

Table 5.2. Errors in capacity measured during the charge of lithium-rich transition metal oxides.

approximate error in measurement (approximate error in capacity)							
Rate							
measurement	C	C/2	C/5	C/10	C/20	C/50	C/100
mass electrode	3% (3%)						
current delivered	0.05% (0.01%)	0.1% (0.02%)	0.2% (0.05%)	0.5% (0.1%)	1% (0.2%)	2% (0.5%)	5% (1%)
voltage cut-off	10% (10%)	5% (5%)	2% (2%)	1% (1%)	0.5% (0.5%)	0.2% (0.2%)	0.1% (0.1%)
total capacity error	10.4%	5.8%	3.6%	3.2%	3.1%	3.1%	3.2%

Table 5.3. Capacities in the oxygen-loss region and fractional capacities of $\text{Li}[\text{Li}_{1/9}\text{Ni}_{1/3}\text{Mn}_{5/9}]\text{O}_2$ with different particle sizes, charge rates, and temperatures.

Capacity in oxygen-loss region (mAh g^{-1})						
(τ)						
	5.3 μm		6.9 μm		7.6 μm	
	30°C	55°C	30°C	55°C	30°C	55°C
C/5	65 ± 3 (0.56 ± 0.02)	102 ± 4 (0.88 ± 0.04)	34 ± 2 (0.29 ± 0.02)	86 ± 4 (0.74 ± 0.03)	17 ± 1 (0.15 ± 0.01)	76 ± 3 (0.66 ± 0.03)
C/10	73 ± 3 (0.63 ± 0.03)	103 ± 4 (0.89 ± 0.03)	48 ± 2 (0.41 ± 0.02)	102 ± 4 (0.88 ± 0.03)	36 ± 2 (0.31 ± 0.01)	78 ± 3 (0.67 ± 0.03)
C/20	88 ± 3 (0.76 ± 0.03)	111 ± 4 (0.96 ± 0.03)	82 ± 3 (0.71 ± 0.03)	109 ± 4 (0.94 ± 0.03)	39 ± 2 (0.34 ± 0.02)	91 ± 3 (0.78 ± 0.03)
C/50	106 ± 4 (0.91 ± 0.03)	111 ± 4 (0.96 ± 0.03)	93 ± 3 (0.80 ± 0.03)	115 ± 4 (0.99 ± 0.04)	62 ± 2 (0.53 ± 0.02)	107 ± 4 (0.92 ± 0.03)
C/100	115 ± 4 (0.99 ± 0.04)	113 ± 4 (0.97 ± 0.04)	95 ± 4 (0.82 ± 0.03)	111 ± 4 (0.96 ± 0.04)	88 ± 3 (0.76 ± 0.03)	116 ± 4 (1.00 ± 0.04)

Table 5.4 shows the oxygen-release plateau capacity for particles of different sizes, rates, and temperatures of Li/Li[Li_{1/5}Ni_{1/5}Mn_{3/5}]O₂ cells. The fractional capacity is the ratio of the obtained capacity to the highest capacity obtained in the oxygen loss region (usually for the highest temperature, lowest rate, and smallest particle size). Table 5.4 includes the fractional capacity, τ .

Table 5.4. Capacities in the oxygen-loss region and fractional capacities of Li[Li_{1/5}Ni_{1/5}Mn_{3/5}]O₂ with different particle sizes, charge rates, and temperatures.

	Capacity in oxygen-loss region (mAh g ⁻¹)					
	(τ)					
	6.0 μm		7.1 μm		8.8 μm	
	30°C	55°C	30°C	55°C	30°C	55°C
C	-	115 ± 15	-	66 ± 7	-	42 ± 5
	-	(0.5 ± 0.06)	-	(0.3 ± 0.03)	-	(0.2 ± 0.02)
C/2	110 ± 7	120 ± 7	34 ± 2	112 ± 7	20 ± 2	64 ± 4
	(0.5 ± 0.03)	(0.5 ± 0.04)	(0.2 ± 0.09)	(0.48 ± 0.03)	(0.09 ± 0.01)	(0.3 ± 0.02)
C/5	148 ± 6	169 ± 7	51 ± 2	150 ± 6	36 ± 2	82 ± 3
	(0.64 ± 0.03)	(0.73 ± 0.03)	(0.22 ± 0.01)	(0.65 ± 0.03)	(0.15 ± 0.01)	(0.35 ± 0.02)
C/10	160 ± 6	208 ± 7	72 ± 3	174 ± 6	54 ± 2	120 ± 4
	(0.69 ± 0.03)	(0.90 ± 0.03)	(0.31 ± 0.01)	(0.75 ± 0.03)	(0.23 ± 0.01)	(0.52 ± 0.02)
C/20	176 ± 6	213 ± 7	115 ± 4	203 ± 7	78 ± 3	142 ± 5
	(0.76 ± 0.03)	(0.92 ± 0.03)	(0.50 ± 0.02)	(0.88 ± 0.03)	(0.34 ± 0.02)	(0.61 ± 0.02)
C/50	202 ± 7	230 ± 8	145 ± 5	231 ± 8	-	-
	(0.87 ± 0.03)	(1.00 ± 0.04)	(0.63 ± 0.02)	(1.00 ± 0.03)	-	-

In order to calculate the apparent diffusion coefficient of oxygen in the lithium-rich positive electrode materials, the average particle size (D50) was used. Figures 5.9 and 5.11 show that the particle sizes have an approximately symmetrical distribution.

The determination of Atlung curves across the particle size distribution for a sample can also be carried out, but this showed negligible differences with using the average particle size.

Figures 5.17 and 5.18 show the τ versus $\log(t/r^2)$ plots for the first charge process of $\text{Li}[\text{Li}_{1/9}\text{Ni}_{1/3}\text{Mn}_{5/9}]\text{O}_2$ and $\text{Li}[\text{Li}_{1/5}\text{Ni}_{1/5}\text{Mn}_{3/5}]\text{O}_2$ at the different charge rates, particle sizes, and temperatures. The Atlung curve was fitted to the data and the diffusion coefficient associated with the oxygen loss region was determined. For $\text{Li}[\text{Li}_{1/9}\text{Ni}_{1/3}\text{Mn}_{5/9}]\text{O}_2$, $\log D = -12.4 \pm 0.2$ at 30°C and -11.6 ± 0.4 at 55°C . And for $\text{Li}[\text{Li}_{1/5}\text{Ni}_{1/5}\text{Mn}_{3/5}]\text{O}_2$, $\log D = -12.5 \pm 0.4$ at 30°C and -11.9 ± 0.3 at 55°C . The errors were determined from the degree that the Atlung curve could be fitted to the experimental data within the error bars. Within experimental error, there is no difference between the apparent diffusion coefficients of oxygen in $\text{Li}[\text{Li}_{1/9}\text{Ni}_{1/3}\text{Mn}_{5/9}]\text{O}_2$ and $\text{Li}[\text{Li}_{1/5}\text{Ni}_{1/5}\text{Mn}_{3/5}]\text{O}_2$.

For comparison, Cho *et al.* determined the diffusion coefficient (for ‘normal’ lithium deintercalation) of LiCoO_2 to be $5 \times 10^{-10} \text{ cm}^2 \text{ s}^{-1}$ at 30°C .¹²⁶ Similar values of the diffusion coefficient for Li in Li_xCoO_2 were determined in a study by Jang *et al.*¹²⁷ The fact that, for the most part, the fractional capacity in the “normal” lithium deintercalation region is unchanged as the particle size, rate and temperature are changed (over the range of parameters studied) while the fractional capacity in the oxygen loss region changes significantly suggests that the kinetics of the oxygen loss process are much slower than simple lithium deintercalation, as might be expected. This agrees with the diffusion coefficient estimates.

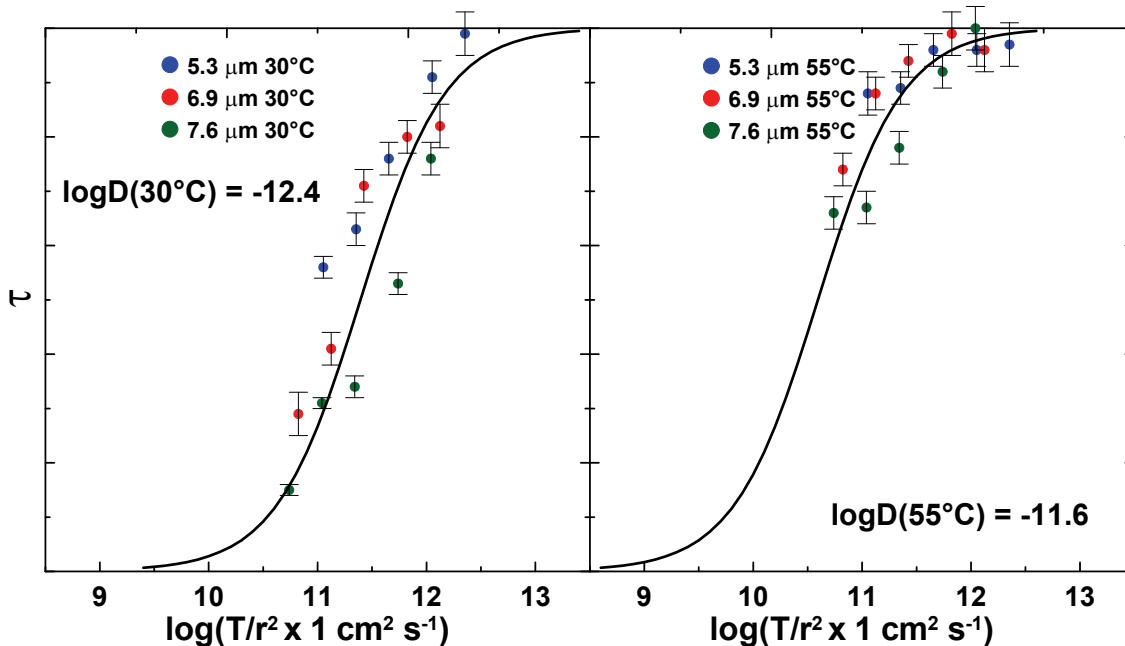


Figure 5.17. Atlung graphs used to determine the apparent diffusion coefficient of oxygen during the charge process in $\text{Li}[\text{Li}_{1/9}\text{Ni}_{1/3}\text{Mn}_{5/9}]\text{O}_2$ at 30°C and 55°C.

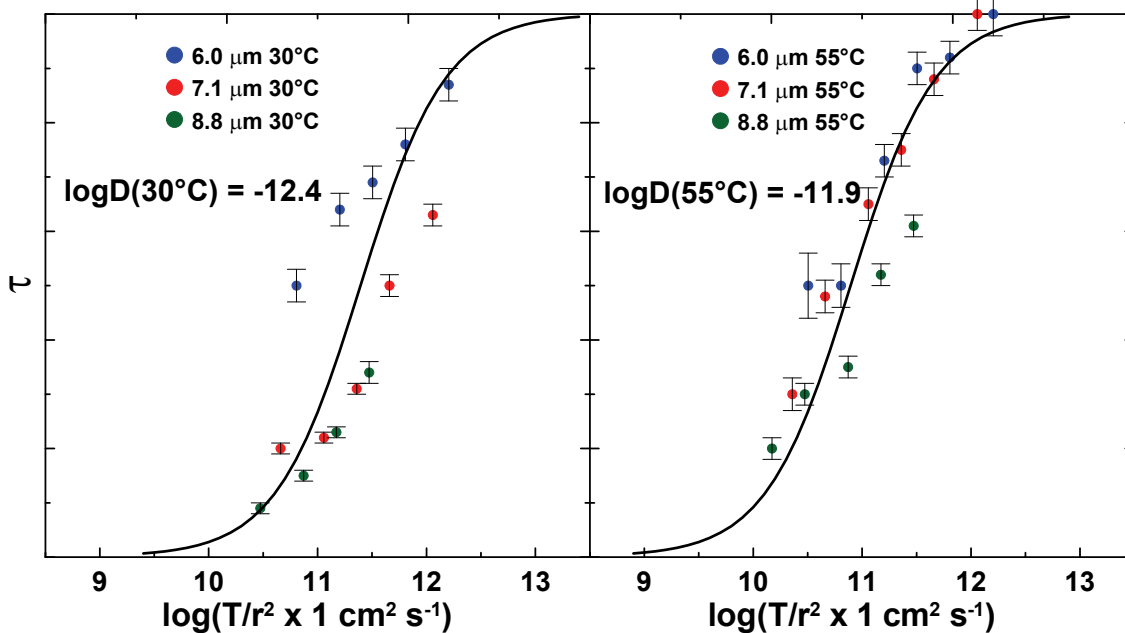


Figure 5.18. Atlung graphs used to determine the apparent diffusion coefficient of oxygen during the charge process in $\text{Li}[\text{Li}_{1/5}\text{Ni}_{1/5}\text{Mn}_{3/5}]\text{O}_2$ at 30°C and 55°C.

In the calculations to determine the apparent diffusion coefficient of oxygen in the lithium-rich positive electrode materials, the secondary particle size was used. If the

“normal” lithium deintercalation diffusion coefficients can be assumed to be on the order of magnitude of those determined for LiCoO_2 (since these materials have the same layered structure), one can determine the rate at which “normal” lithium deintercalation is affected (i.e.: there is a decrease in capacity associated with the normal lithium deintercalation region).

Figure 5.2 shows that there starts to be a decrease in the fractional capacity at $Q = 1$. For a $8.8 \mu\text{m}$ particle size and a diffusion coefficient of $10^{-10} \text{ cm}^2 \text{ s}^{-1}$ at 30°C , the stoichiometric charge time can be calculated from Equation 5.15:

$$T = \frac{Qr^2}{D} = \frac{(1)(0.00044 \text{ cm})^2}{10^{-10} \text{ cm}^2 \text{ s}^{-1}} = 2000 \text{ s} \quad (5.19)$$

A stoichiometric charge time of 2000 s approximately corresponds to a 2C-rate charge for the lithium-rich transition metal oxides. Figure 5.15 shows the normal lithium deintercalation region being affected at C-rate, which agrees approximately with equation 5.19. If the primary particle size of $0.5 \mu\text{m}$ is selected in the calculation, the rate would have to be approximately 25C in order to affect the area of normal lithium deintercalation. This suggests that the secondary particle size should be used or that the diffusion coefficient for normal lithium deintercalation is much smaller than $10^{-10} \text{ cm}^2 \text{ s}^{-1}$, and the diffusion coefficients in the oxygen release region would be several orders of magnitude lower than calculated.

5.3. Cycling of $\text{Li}[\text{Li}_{1/9}\text{Ni}_{1/3}\text{Mn}_{5/9}]\text{O}_2$

Figure 5.19 shows the charge–discharge cycling characteristics of 5.3, 6.9, and 7.6 μm $\text{Li}[\text{Li}_{1/9}\text{Ni}_{1/3}\text{Mn}_{5/9}]\text{O}_2$ at 55°C and C/10 rate. The first two cycles were made over a potential range of 2.5–4.8 V, with subsequent cycles between 2.5 and 4.6 V. There were several interesting features seen during cycling. In the center panel, there was an evolution of a peak near 3.1–3.5 V in the differential capacity curve going from the 3rd to the 33rd cycle. This peak probably corresponds to the reduction of manganese from Mn^{4+} to Mn^{3+} during discharge.¹⁷ The left panel shows that the length of the reversible $\text{Mn}^{4+}/\text{Mn}^{3+}$ portion of the charge–discharge profile is dependent on the particle size of the lithium-rich oxide. The smaller particles have a higher reversible capacity in that potential region. The right panel shows the cycling over 50 cycles of 5.3, 6.9, and 7.6 μm $\text{Li}[\text{Li}_{1/9}\text{Ni}_{1/3}\text{Mn}_{5/9}]\text{O}_2$ at 55°C and C/10 rate. The 5.3 μm particles of $\text{Li}[\text{Li}_{1/9}\text{Ni}_{1/3}\text{Mn}_{5/9}]\text{O}_2$ delivered a reversible capacity of 240 mAh g^{-1} at C/10 rate.

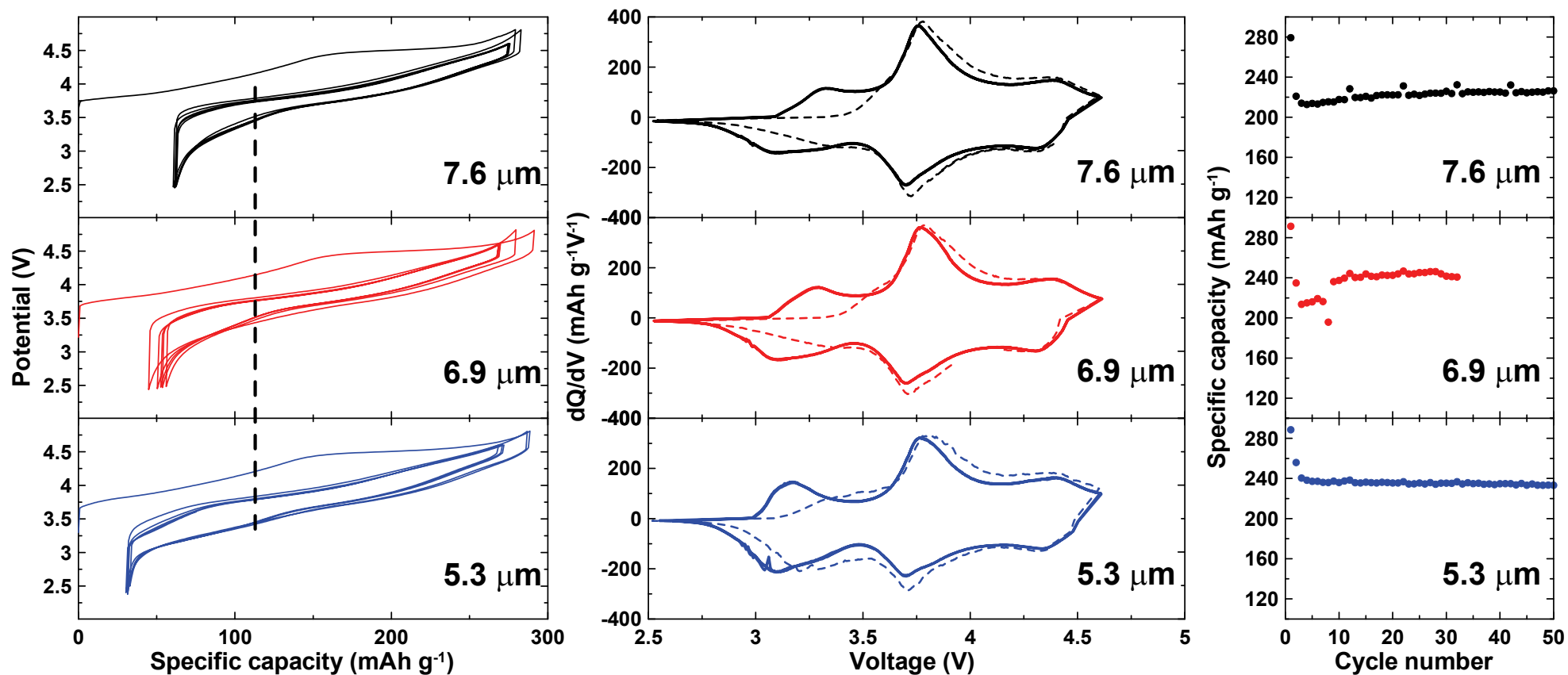


Figure 5.19. Cycling characteristics of 5.3, 6.9, and 7.6 μm $\text{Li}[\text{Li}_{1/9}\text{Ni}_{1/3}\text{Mn}_{5/9}]\text{O}_2$ at 55°C and at $C/10$ rate.

Left panel: potential versus specific capacity for the first five cycles.

Center panel: differential capacity versus potential of the 3rd (dashed) and 33rd cycles.

Right panel: specific capacity versus cycle number for the $\text{Li}/\text{Li}[\text{Li}_{1/9}\text{Ni}_{1/3}\text{Mn}_{5/9}]\text{O}_2$ cells.

From van Bommel, A; Dahn, J. R. *Electrochem. Solid-State Lett.* **2010**, *13*, A62.

Reprinted with permission from the American Chemical Society. Copyright 2010.

5.4. Summary

The characteristics of the oxygen release process in the lithium-rich transition metal oxides $\text{Li}[\text{Li}_{1/9}\text{Ni}_{1/3}\text{Mn}_{5/9}]\text{O}_2$ and $\text{Li}[\text{Li}_{1/5}\text{Ni}_{1/5}\text{Mn}_{3/5}]\text{O}_2$ were studied. It was found that varying charge rate, temperature, and particle size did not affect the amount of lithium that was deintercalated in the “normal” lithium deintercalation region (associated with the oxidation of nickel during charge), for the parameters studied. However, the size of the oxygen-release plateau depended on these parameters. Using the Atlung-graph method, the apparent diffusion coefficients of oxygen in lithium-rich transition metal oxides were estimated. For $\text{Li}[\text{Li}_{1/9}\text{Ni}_{1/3}\text{Mn}_{5/9}]\text{O}_2$, $\log D = -12.4 \pm 0.2$ at 30°C and -11.6 ± 0.4 at 55°C . And for $\text{Li}[\text{Li}_{1/5}\text{Ni}_{1/5}\text{Mn}_{3/5}]\text{O}_2$, $\log D = -12.5 \pm 0.4$ at 30°C and -11.9 ± 0.3 at 55°C , with D in $\text{cm}^2 \text{s}^{-1}$.

CHAPTER 6. Isothermal Microcalorimetry of $\text{Li}[\text{Li}_{1/5}\text{Ni}_{1/5}\text{Mn}_{3/5}]\text{O}_2$ and $\text{Li}[\text{Li}_{1/9}\text{Ni}_{1/3}\text{Mn}_{5/9}]\text{O}_2$

6.1. Stoichiometry Changes in Lithium-Rich Transition Metal Oxides During Charge and Discharge

Figure 6.1 shows the Gibbs triangle for the Li-M-O system. It was previously shown by Lu *et al.*⁵³ The two closed circles indicate the Li_2MO_3 (A) and LiMO_2 (B) stoichiometries. The stoichiometries along a line drawn from point A to B are the lithium-rich oxides with the general formula $\text{Li}[\text{Ni}_x\text{Li}_{(1/3-2x/3)}\text{Mn}_{(2/3-x/3)}]\text{O}_2$ if A is Li_2MnO_3 and B is $\text{Li}[\text{Ni}_{1/2}\text{Mn}_{1/2}]\text{O}_2$.

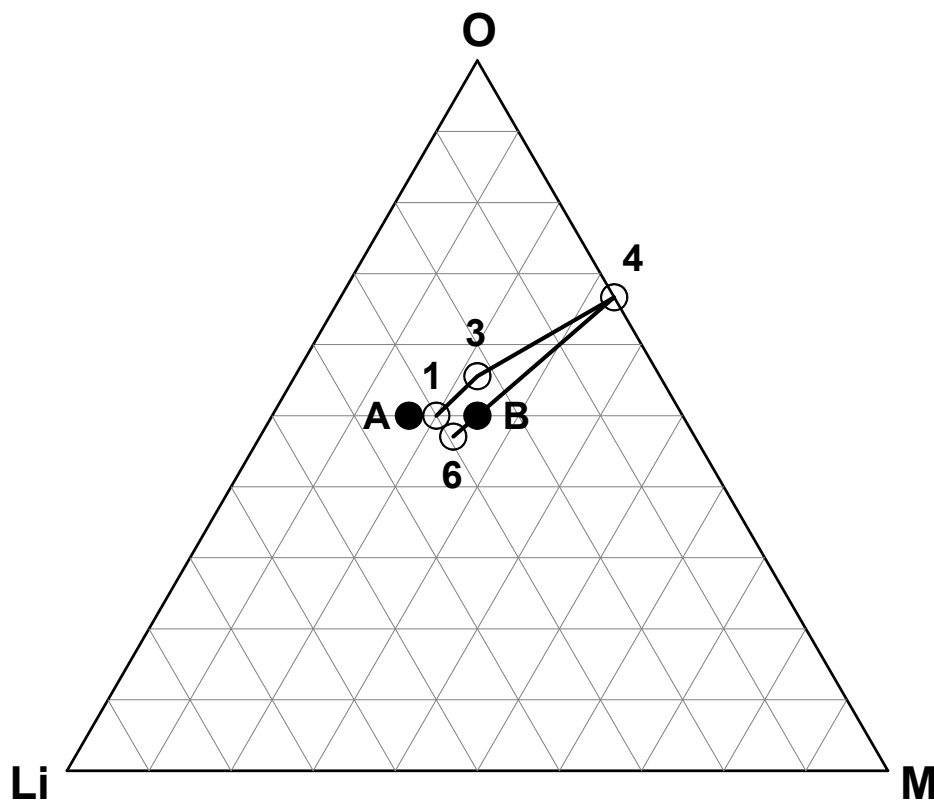


Figure 6.1. Gibbs triangle of the Li-M-O system showing the stoichiometries of interest.

It is for the lithium-rich oxides with the general formula $\text{Li}[\text{Ni}_x\text{Li}_{(1/3-2x/3)}\text{Mn}_{(2/3-x/3)}]\text{O}_2$. The points are Li_2MO_3 (A), LiMO_2 (B), $\text{Li}[\text{Li}_{1/5}\text{M}_{4/5}]\text{O}_2$ (1), $\text{Li}_{4/5}[\text{M}_{4/5}]\text{O}_2$ (3), $[\text{M}_{4/5}]\text{O}_{8/5}$ (4), and $\text{Li}[\text{M}_{4/5}]\text{O}_{8/5}$ (6).

The stoichiometry of interest in this chapter is $\text{Li}[\text{Li}_{1/5}\text{Ni}_{1/5}\text{Mn}_{3/5}]\text{O}_2$. The following discussion will investigate the stoichiometries that exist in the charge and discharge curves of this material. In the current study, there is no structural data to support the existence of the stoichiometries that will be mentioned. However, the set of stoichiometries are consistent with the data. As well, numerous studies have provided information that supports the existence of these stoichiometries.^{17, 52, 53, 56, 59, 61, 69-75}

Table 6.1 shows the various steps that the lithium-rich oxide $\text{Li}[\text{Li}_{1/5}\text{Ni}_{1/5}\text{Mn}_{3/5}]\text{O}_2$ goes through during the first charge and discharge process. Figure 6.2 shows the charge-discharge profile of a $\text{Li}/\text{Li}[\text{Li}_{1/5}\text{Ni}_{1/5}\text{Mn}_{3/5}]\text{O}_2$ cell. The secondary particle size of the $\text{Li}[\text{Li}_{1/5}\text{Ni}_{1/5}\text{Mn}_{3/5}]\text{O}_2$ sample was 6.0 μm . Charge and discharge were carried out at a C/50 rate and the cell temperature was 55°C. These conditions were selected to ensure that all oxygen was being released in the first cycle to illustrate the steps in Table 6.1. The numbers of each step in Table 6.1 correspond to the numbers on the Gibbs triangle in Figure 6.1 and the charge-discharge profile in Figure 6.2.

Step 1 to step 2 shows the deintercalation of lithium with oxidation of Ni^{2+} to an average oxidation state of 3+. It is assumed that the deintercalation of lithium occurs first from the lithium layer. At step 3, there is complete oxidation to Ni^{4+} , which would give a theoretical capacity of 126 mAh g^{-1} , also shown in Figure 6.1.

The rest of the lithium atoms were simultaneously removed along with 2/5 oxygen in step 4. This corresponded to a theoretical capacity of 378 mAh g^{-1} , which was in good agreement to that obtained in the first charge in Figure 6.1. The oxygen release phenomenon has been described by many groups and has been reviewed in Chapter 1.^{17, 53-60, 65, 66, 68, 111, 112, 115, 128-131}

During the re-intercalation of lithium, nickel was reduced from 4+ to 2+ oxidation states (step 5). Thereafter, evolved oxygen was not reinserted into the material. However, manganese was reduced from Mn⁴⁺ to Mn³⁺. The 3+ Mn oxidation state was seen in the XANES data presented by Park *et al.*⁵⁹ Since there were no more available species for reduction, an irreversible capacity of 70 mAh g⁻¹ was shown, which is close to the theoretical value of 63 mAh g⁻¹.

Table 1 shows the stoichiometries with the vacancies remaining after lithium removal and insertion. The materials are presented this way to illustrate where the lithium atoms are removed and the materials may not stay this way. In fact, Armstrong *et al.* believe that after the first charge, the vacancies are removed as transition metals diffuse from the surface of the bulk.⁶¹ On the other hand, Liu *et al.* presented a model in which the vacancies are partially filled, thereby allowing for higher capacities than calculated in the case where the vacancies disappear.⁷⁵ In several studies, a larger number of remaining vacancies can account for the increased cycling capacity when a coating is applied to a lithium-rich oxide.⁶⁹⁻⁷⁵

#	5 unit schematic	stoichiometry	average oxidation state		number in single unit		th'l capacity mAh g ⁻¹
			Ni	Mn	Li	O	
1	Li Li Li Li Li ○ ○ ○ ○ ○ Li Ni Mn Mn Mn ○ ○ ○ ○ ○	Li[Li _{1/5} Ni _{1/5} Mn _{3/5}]O ₂	2+	4+	6/5	10/5	0
2	□ Li Li Li Li ○ ○ ○ ○ ○ Li Ni Mn Mn Mn ○ ○ ○ ○ ○	Li _{4/5} □ _{1/5} [Li _{1/5} Ni _{1/5} Mn _{3/5}]O ₂	3+	4+	5/5	10/5	63
3	□ □ Li Li Li ○ ○ ○ ○ ○ Li Ni Mn Mn Mn ○ ○ ○ ○ ○	Li _{3/5} □ _{2/5} [Li _{1/5} Ni _{1/5} Mn _{3/5}]O ₂	4+	4+	4/5	10/5	126
4	□ □ □ □ □ □ ○ ○ ○ ○ □ Ni Mn Mn Mn □ ○ ○ ○ ○	□[□ _{1/5} Ni _{1/5} Mn _{3/5}] □ _{2/5} O _{8/5}	4+	4+	0	8/5	378
5	□ □ □ Li Li □ ○ ○ ○ ○ □ Ni Mn Mn Mn □ ○ ○ ○ ○	□ _{3/5} Li _{2/5} [□ _{1/5} Ni _{1/5} Mn _{3/5}] □ _{2/5} O _{8/5}	2+	4+	2/5	8/5	252
6	□ □ □ Li Li □ ○ ○ ○ ○ □ Ni Mn Mn Mn □ ○ ○ ○ ○	Li[□ _{1/5} Ni _{1/5} Mn _{3/5}] □ _{2/5} O _{8/5}	2+	3+	5/5	8/5	63

Table 6.1. Stoichiometry changes in Li[Li_{1/5}Ni_{1/5}Mn_{3/5}]O₂ during cycling, with the associated capacities shown. Numbers correspond to charge-discharge profile in Figure 6.1. The squares represent vacancies.

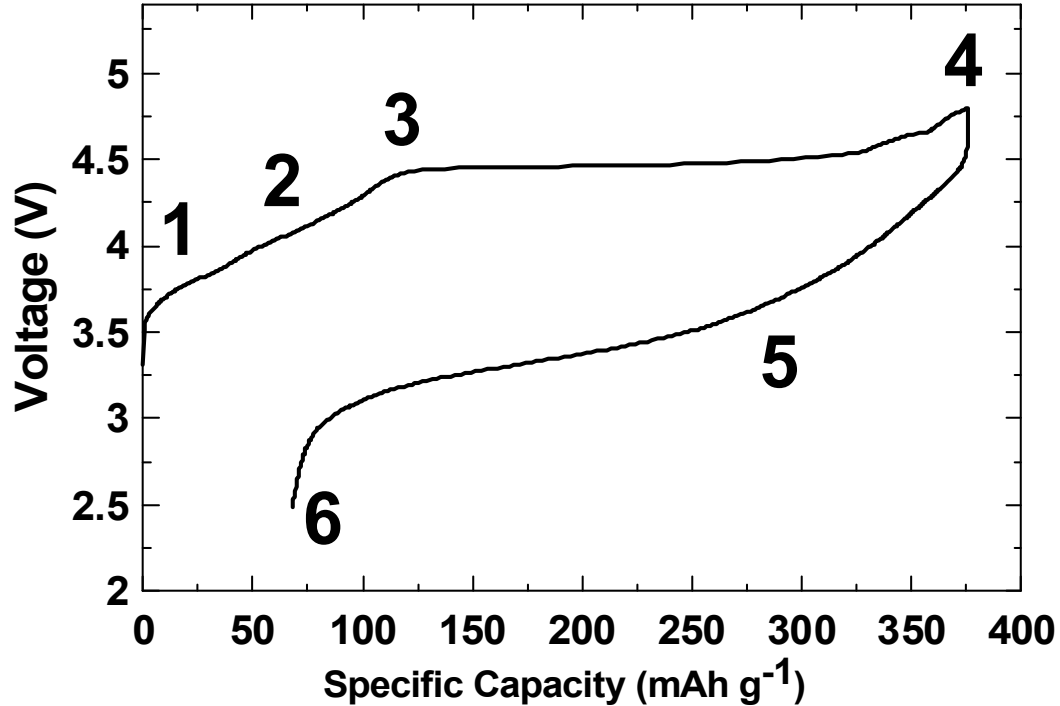


Figure 6.2. Charge and discharge profile of a $\text{Li}/\text{Li}[\text{Li}_{1/5}\text{Ni}_{1/5}\text{Mn}_{3/5}]\text{O}_2$ cell. The rate was $C/50$ rate and temperature was 55°C . The secondary particle size of $\text{Li}[\text{Li}_{1/5}\text{Ni}_{1/5}\text{Mn}_{3/5}]\text{O}_2$ is $6.0\ \mu\text{m}$. Numbers indicated correspond to the numbers in Figure 6.1 and Table 6.1.

6.2. Jahn-Teller Distortion in the MnO_6 Units in Lithium-rich Transition Metal Oxides

The reduction of manganese during the discharge of lithium-rich oxides is of particular interest in the discussion in this chapter. It has been described by several groups as the mechanism of lithium-ion insertion after nickel reduction to $2+$.^{53, 58, 60}

In an octahedral environment, reduction of manganese from $4+$ to $3+$ brings with it a Jahn-Teller distortion of the octahedral geometry. Manganese, with a $[\text{Ar}]4s^23d^5$ electron configuration, is d^3 and d^4 when at oxidation states of $4+$ and $3+$, respectively. Octahedral complexes of d^9 and d^4 high spin often have Jahn-Teller distortions, with the

axial bonds having different lengths than the equatorial ones. The Jahn-Teller distortion arises from the splitting of the d-states with respect to orbital energies. The t_{2g} orbitals (d_{yz} , d_{xz} , and d_{xy}) point away from the ligands and the e_g orbitals ($d_{x^2-y^2}$ and d_{z^2}) point towards the ligands. Elongation of the octahedral geometry stabilizes the structure.

Figure 6.2 shows the crystal field splitting for an octahedral environment.

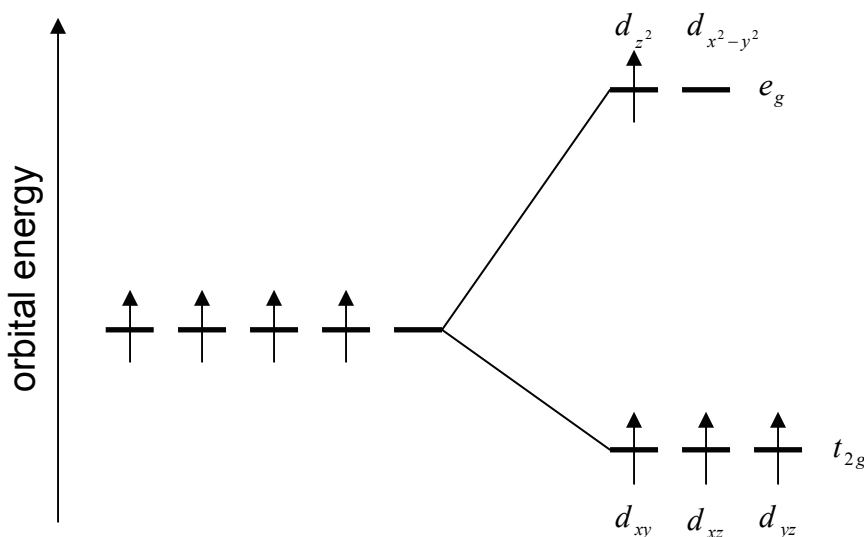


Figure 6.3. Schematic of the possible crystal field splitting of the t_{2g} and e_g orbitals. This arises from an octahedral distortion of the $[\text{MnO}_6]^{3+}$ units in $\text{Li}[\text{Li}_{1/5}\text{Ni}_{1/5}\text{Mn}_{3/5}]\text{O}_2$ during discharge.

6.3. Meaning of the Heat Flow in Isothermal Battery Calorimetry

Isothermal microcalorimetry, IMC, can be used to probe the heat evolved or absorbed during the charge and discharge of lithium-ion batteries.¹³²⁻¹³⁴ It is of interest to probe the heat evolution of lithium-rich oxides during charge and discharge to investigate the interesting changes in stoichiometry and oxidation state of these materials. Of

particular interest are the heat signatures during the first charge when oxygen is released and the subsequent discharge when manganese is reduced to a 3+ oxidation state.

Of importance in the IMC experiment are the thermodynamic quantities Gibbs free energy (g), enthalpy (h), and entropy (s).¹³²⁻¹³⁴ The partial quantities of Gibbs free energy (\tilde{g}), enthalpy (\tilde{h}), and entropy (\tilde{s}) are defined as

$$\tilde{g} = \frac{\partial g}{\partial x}, \quad (6.1)$$

$$\tilde{h} = \frac{\partial h}{\partial x}, \quad (6.2)$$

and

$$\tilde{s} = \frac{\partial s}{\partial x}, \quad (6.3)$$

where x is the amount of lithium in one formula unit of $\text{Li}_x\text{Ni}_{1/5}\text{Mn}_{3/5}\text{O}_2$. The values of \tilde{g} , \tilde{h} , and \tilde{s} for one atom of Li in lithium metal are denoted as \tilde{g}_o , \tilde{h}_o , and \tilde{s}_o , respectively.

Without a cell overpotential, the thermodynamic cell potential is

$$v_g = -\frac{1}{e} \left(\frac{\Delta g}{\Delta x} - \tilde{g}_o \right), \quad (6.4)$$

where e is the magnitude of the electron charge. The enthalpic contribution to the thermodynamic cell potential, given in volts, is

$$v_h = -\frac{1}{e} \left(\frac{\Delta h}{\Delta x} - \tilde{h}_o \right). \quad (6.5)$$

The entropic contribution to the thermodynamic cell potential, given in volts, is

$$v_s = -\frac{1}{e} \left(\frac{T\Delta s}{\Delta x} - T\tilde{s}_o \right), \quad (6.6)$$

where T is the temperature of the lithium ion cell.

The potentials in equations 6.5 and 6.6 are defined such that

$$v_g = v_h + v_s. \quad (6.7)$$

In the IMC experiment, the calorimeter chamber (containing the lithium-ion cell) is kept at a fixed temperature and heat can flow into and out of the calorimeter chamber.

The rate at which heat flows into or out of the calorimeter chamber is

$$\dot{Q} = \frac{dQ}{dt}. \quad (6.8)$$

In order to evaluate \dot{Q} in terms of the thermodynamic potential quantities, conservation of energy is considered, in which

$$\Delta E = Q + W, \quad (6.9)$$

where ΔE is the internal energy of the cell and W is the work done on the cell. The work done on the cell is

$$W = -eV\Delta n - P\Delta\Omega, \quad (6.10)$$

where V is the cell voltage, $e\Delta n$ is the total charge passed through the external circuit, P is the pressure in the cell, and $\Delta\Omega$ is the volume change of the cell.

The heat can now be written as

$$Q = \Delta E + eV\Delta n + P\Delta\Omega. \quad (6.11)$$

And since

$$\Delta H = \Delta E + P\Delta\Omega, \quad (6.12)$$

$$Q = \Delta H + eV\Delta n. \quad (6.13)$$

Using the enthalpic contribution to the thermodynamic cell potential in equation 6.5,

$$\dot{Q} = -e\nu_h\Delta n + eV\Delta n . \quad (6.14)$$

Since the cell voltage can be also written as the

$$V = \nu_g - \eta , \quad (6.15)$$

where η is the cell overpotential, \dot{Q} can be given in terms of the entropic contribution to the thermodynamic cell potential (Equation 6.6):

$$\dot{Q} = I\nu_s - I\eta , \quad (6.16)$$

where I is the cell current.

Equation 6.16 shows that the rate of heat flow into or out of the calorimeter, \dot{Q} , has both thermodynamic and overvoltage terms.

6.4. IMC Data of a Li/Li[Li_{1/5}Ni_{1/5}Mn_{3/5}]O₂ Cell Cycled Between 2.5 and 4.4 V

Figure 6.4 shows the charge-discharge profiles for the first three cycles of Li/Li[Li_{1/5}Ni_{1/5}Mn_{3/5}]O₂ cells between 2.5 and 4.4 V, along with the associated heat flows. If the overvoltage is the same for the charge and discharge processes, the overvoltage is half the difference between the charge and discharge voltage. This is not expected to be the case for some processes (e.g. oxygen release), but can estimate the overvoltage in other cases (e.g. the end of discharge). The values of half the differences between the charge and discharge voltages are also shown.

As expected, charging Li[Li_{1/5}Ni_{1/5}Mn_{3/5}]O₂ to 4.4 V results in no oxygen-release plateau. In this case, the lithium extraction during charge is only due to the oxidation of Ni²⁺ to Ni⁴⁺, corresponding to the change from steps 1 to 3 in Figures 6.1 and 6.2 and Table 6.1.

At the beginning of the first charge, there is some heat evolved. This is thought to be due to the reactions on the surface of the lithium to make a clean lithium surface. The heat evolved at the end of charge will be discussed in the next section. The heat evolved at the end of the discharges is due to iR heating, as indicated by the increase in the difference between the charge and discharge voltages. This is not a true value of overvoltage but gives an indication of the origin of the heat flow at the end of discharge.

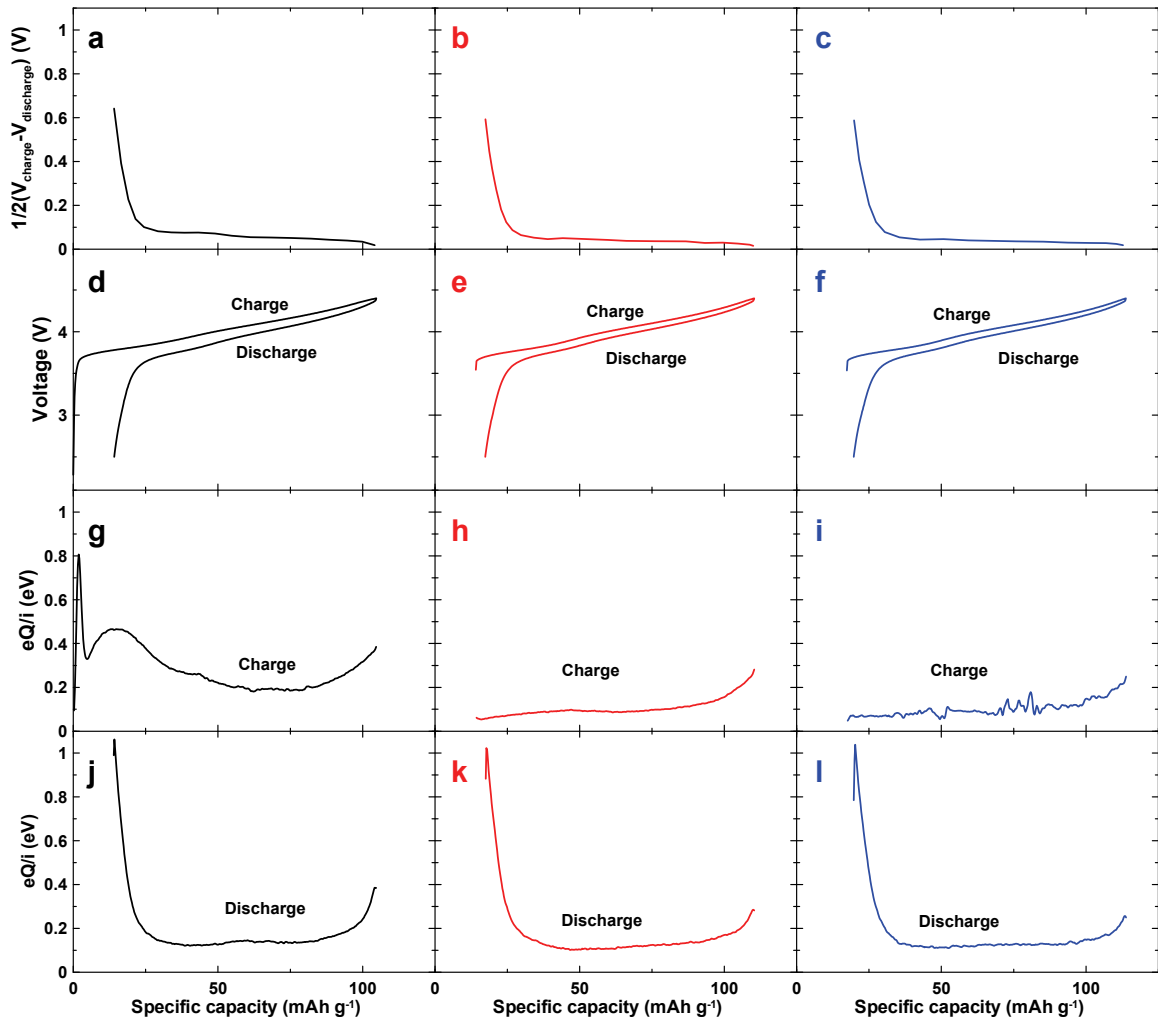


Figure 6.4. IMC data for a $\text{Li}/\text{Li}[\text{Li}_{1/5}\text{Ni}_{1/5}\text{Mn}_{3/5}]\text{O}_2$ cell cycled between 2.5 and 4.4 V.

The rates of charge and discharge were $C/40$.

$1/2(V_{\text{charge}} - V_{\text{discharge}})$ for the first (a), second (b), and third cycles (c).

Charge-discharge voltage profiles for the first (d), second (e), and third (f) cycles.

Heat profile during charge for the first (g), second (h), and third (i) cycles.

Heat profile during discharge for the first (j), second (k), and third (l) cycles.

6.5. Model for the Configurational Entropy During Cycling of a Li/Li[Li_{1/5}Ni_{1/5}Mn_{3/5}]O₂ Cell Between 2.5 and 4.4 V

Figure 6.4 also shows that there is some heat flow at the end of each charge. This can be rationalized by looking at the entropy changes at the end of the charge process for Li[Li_{1/5}Ni_{1/5}Mn_{3/5}]O₂. By calculating the configurational entropy with respect to the amount of lithiation, one can account for the heat changes in the material.

The configurational entropy of a material, S , is physically related to the number of ways or arranging atoms in the material. The configurational entropy is given as Boltzmann's entropy formula:

$$S = k_B \ln W, \quad (6.17)$$

where k_B is the Boltzmann constant, $86.2 \mu\text{eV K}^{-1}$ and W is the number of possible configurations.

In the case of Li[Li_{1/5}Ni_{1/5}Mn_{3/5}]O₂, the entropy varies as it is delithiated. If there are n lithium atoms that can be organized on N lithium sites, the degree of charge can be defined as

$$x = \frac{n}{N}, \quad (6.18)$$

where x is its value in Li _{x} [Li_{1/5}Ni_{1/5}Mn_{3/5}]O₂. From combinatorial mathematics, the number of ways of organizing n lithium atoms on N sites is

$$\binom{N}{n} = W = \frac{N!}{n!(N-n)!}. \quad (6.19)$$

By substituting $n = xN$,

$$W = \frac{N!}{(xN)!(N-xN)!}, \quad (6.20)$$

and the entropy can be written as

$$S = k_b \ln \left(\frac{N!}{(xN)!(N-xN)!} \right) \quad (6.21)$$

Stirling's approximation is $\ln x! = x \ln x - x$ and from equation 6.1 and rearrangement,

$$S = -Nk_b \ln(x \ln x + (1-x) \ln(1-x)). \quad (6.22)$$

The value dS/dx is therefore

$$\frac{dS}{dx} = -Nk_b \ln \left(\frac{x}{1-x} \right). \quad (6.23)$$

During the "normal deintercalation" charge process, only nickel is oxidized. The number of nickel ions oxidized can be related to the value, x , in $\text{Li}_x[\text{Li}_{1/5}\text{Ni}_{1/5}\text{Mn}_{3/5}]\text{O}_2$ as

$$y = 0.2 - \frac{(1-x)}{2}, \quad (6.24)$$

where y is the number of oxidized nickel ions in $\text{Li}_x[\text{Li}_{1/5}\text{Ni}_{1/5}\text{Mn}_{3/5}]\text{O}_2$. Equation 6.24 is relevant for stoichiometries $1 \leq x \leq 0.6$. The number of ways of organizing $m \text{ Ni}^{2+}$ on M nickel sites is

$$\binom{M}{m} = \frac{M!}{m!(M-m)!}. \quad (6.25)$$

In this case, $M = 0.2 N$. With consideration of the configurational entropy of both lithium in the lithium sites and nickel in the nickel sites, the entropy can be written as

$$S = k_b \ln \left(\frac{N!}{(xN)!(N-xN)!} \cdot \frac{0.2N!}{(0.2yN)!(0.2N-0.2yN)!} \right) \quad (6.26)$$

Similar to the lithium-only case, the value of dS/dx can be determined and is

$$\frac{dS}{dx} = -Nk_b \left[\ln \left(\frac{x}{1-x} \right) + 0.5 \ln \left(\frac{1 - \frac{5}{2}(1-x)}{\frac{5}{2}(1-x)} \right) \right]. \quad (6.27)$$

The entropy per formula unit can be found by:

$$\frac{ds}{dx} = \frac{dS}{dn} = \frac{1}{N} \frac{dS}{dx}, \quad (6.28)$$

therefore

$$\frac{ds}{dx} = -k_b \left[\ln\left(\frac{x}{1-x}\right) + 0.5 \ln\left(\frac{1 - \frac{5}{2}(1-x)}{\frac{5}{2}(1-x)}\right) \right]. \quad (6.29)$$

In Figure 6.4, the $e\dot{Q}/I$ is plotted versus specific capacity. From equation 6.16,

$$\frac{e\dot{Q}}{I} = e\nu_s - e\eta. \quad (6.30)$$

By inserting ν_s from equation 6.6,

$$\frac{e\dot{Q}}{I} = -T \frac{ds}{dx} + T\tilde{s}_o - e\eta. \quad (6.31)$$

By inserting ds/dx from equation 6.29,

$$\frac{e\dot{Q}}{I} = k_b T \left[\ln\left(\frac{x}{1-x}\right) + 0.5 \ln\left(\frac{1 - \frac{5}{2}(1-x)}{\frac{5}{2}(1-x)}\right) \right] + T\tilde{s}_o - e\eta, \quad (6.32)$$

which can be expressed as

$$\frac{e\dot{Q}}{I} = k_b T \left[\ln\left(\frac{x}{1-x}\right) + 0.5 \ln\left(\frac{1 - \frac{5}{2}(1-x)}{\frac{5}{2}(1-x)}\right) \right] + const., \quad (6.33)$$

where $const. = T\tilde{s}_o - e\eta$. In equation 6.33, $k_b T = 0.0261$ eV at a cell temperature of 30°C. Figure 6.5 shows ds/dx versus x with $const. = 0.15$. Since

$\tilde{s}_o = 0.000290 \text{ eV K}^{-1}$ (from reference 133), $T\tilde{s}_o = 0.088 \text{ eV K}^{-1}$. In this case, the overpotential, $\eta = 0.06 \text{ eV}$. The difference between the experimental and calculated heat curves at the end of discharge may be due to excess lithium in the transition metal layer or deficient nickel which would cause the heat flow to rise earlier than expected.

The heat flow and the charge-discharge curves are also shown. It shows that there was a large change in entropy as lithium was removed from $\text{Li}_x[\text{Li}_{1/5}\text{Ni}_{1/5}\text{Mn}_{3/5}]\text{O}_2$ from $x = 1$ to $x = 0.6$.

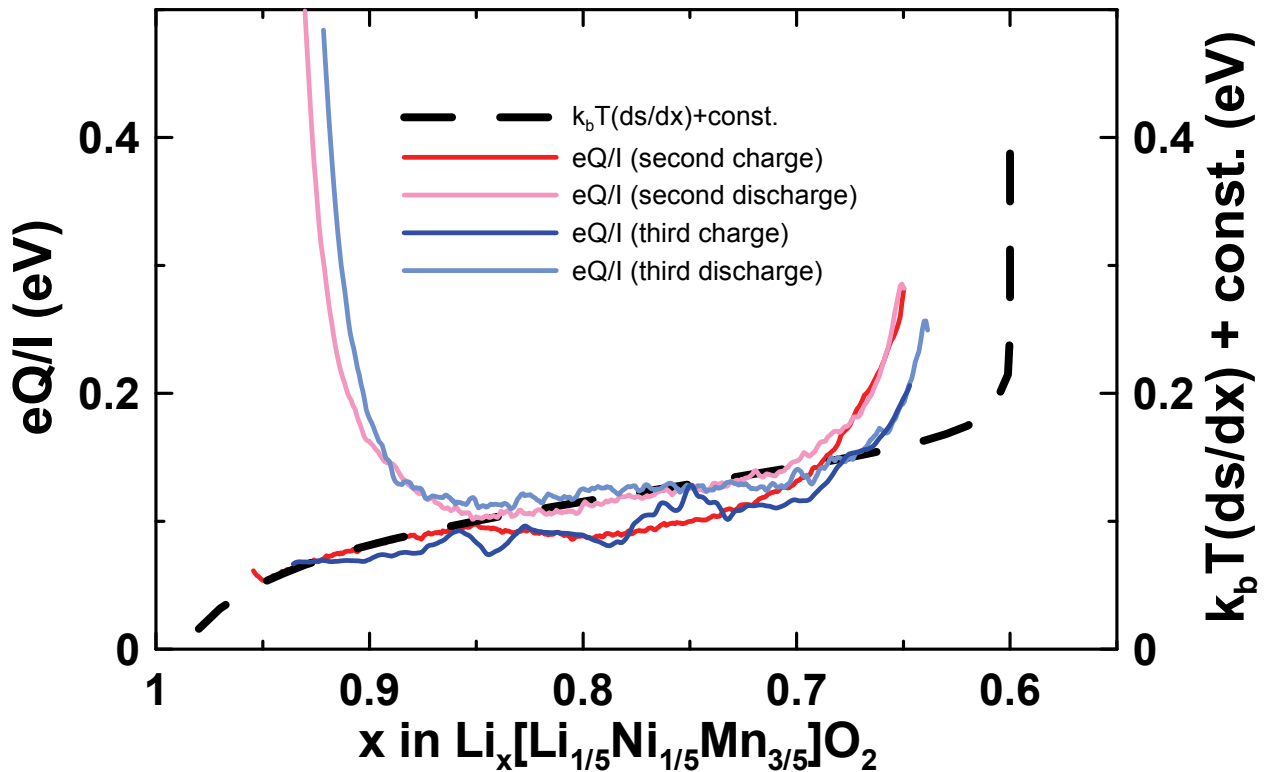


Figure 6.5. The second charge and discharge profiles of a $\text{Li}/\text{Li}[\text{Li}_{1/5}\text{Ni}_{1/5}\text{Mn}_{3/5}]\text{O}_2$ cell. The cell was charged between 2.5 and 4.4 V. The associated heat flow for the charge process and the values of dS/dx are also shown with respect to x in $\text{Li}_x[\text{Li}_{1/5}\text{Ni}_{1/5}\text{Mn}_{3/5}]\text{O}_2$.

6.6. IMC data of Li/Li[Li_{1/5}Ni_{1/5}Mn_{3/5}]O₂ and Li/Li[Li_{1/5}Ni_{1/5}Mn_{3/5}]O₂ Cells

Figures 6.6 and 6.7 show the charge-discharge profiles for the first three cycles of Li/Li[Li_{1/5}Ni_{1/5}Mn_{3/5}]O₂ cells, along with the associated heat flows. In these cases, the first charge was to 4.8 V and the subsequent cycling was from 2.5 – 4.6 V. The values of half the differences between the charge and discharge voltages are also shown. For Figures 6.6 and 6.7, cycling was carried out at C/40 and C/20 rates, respectively.

Figure 6.6 shows that for the first charge of Li/Li[Li_{1/5}Ni_{1/5}Mn_{3/5}]O₂ cells to 4.8 V, there was an expected oxygen-release plateau. There was a corresponding increase in heat flow during the oxygen release. This can be attributed to the formation of O₂ gas due to the oxidation of O²⁻ (in the form of Li₂O) from Li[Li_{1/5}Ni_{1/5}Mn_{3/5}]O₂. The formation of O₂ gas has been confirmed by Armstrong *et al.* with mass spectrometry during the first charge.⁶¹ The formation of O₂ gas has a high degree of entropy. Equation 6.31 shows that for a positive value of entropy and a negative value of dx , there is a positive heat flow.

During discharge, Figure 6.6 shows that there is step in the heat flow in the region where manganese is thought to be reduced from Mn⁴⁺ to Mn³⁺. This step is not shown in Figure 6.4, since there was no reduction of manganese when the cell is only charged to 4.4 V.

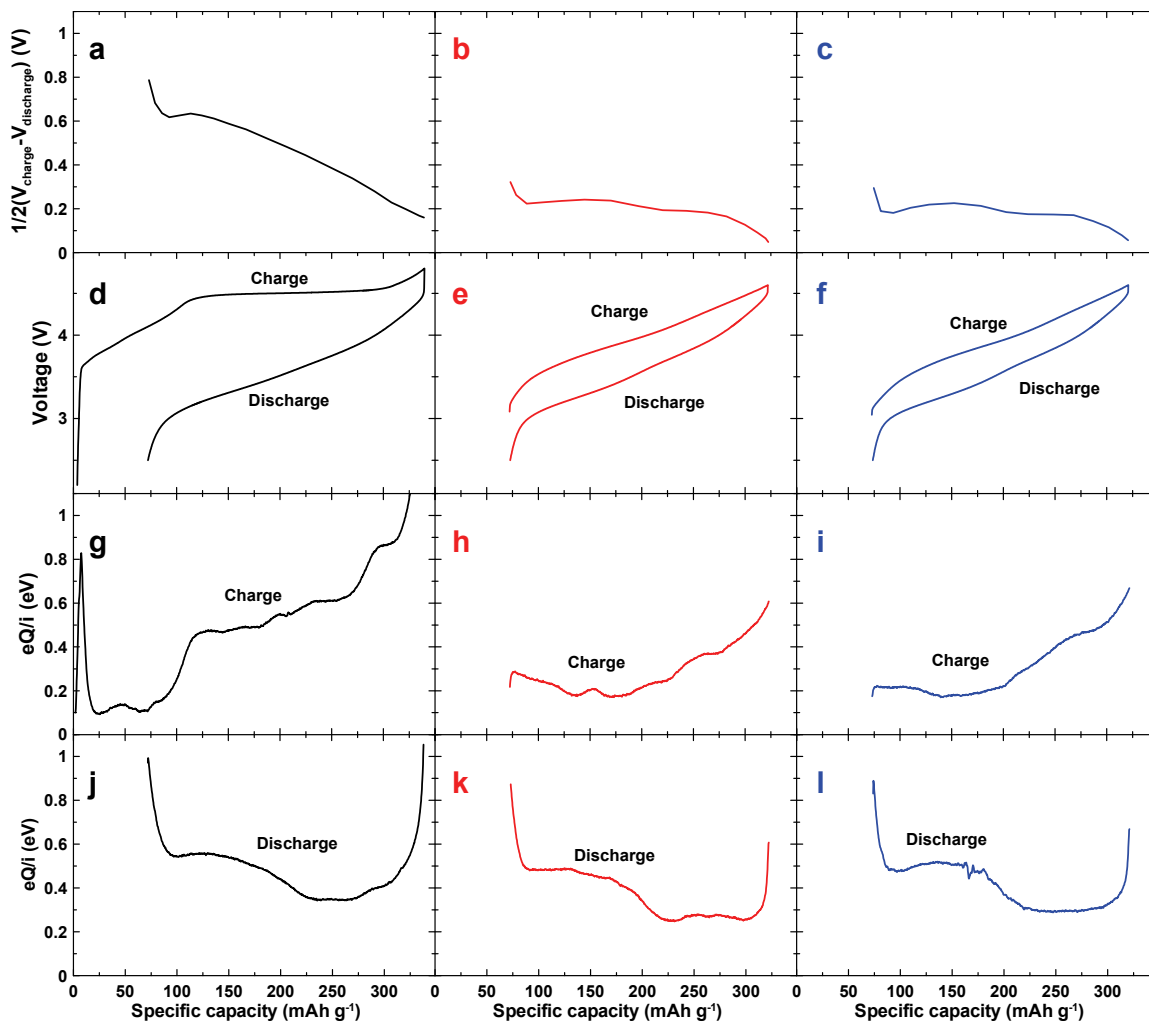


Figure 6.6. IMC data for a $\text{Li}/\text{Li}[\text{Li}_{1/5}\text{Ni}_{1/5}\text{Mn}_{3/5}]\text{O}_2$ cell charged first to 4.8 V, with subsequent cycles between 2.5 and 4.6 V at a rate of C/40.

$1/2(V_{\text{charge}} - V_{\text{discharge}})$ for the first (a), second (b), and third cycles (c).

Charge-discharge voltage profiles for the first (d), second (e), and third (f) cycles.

Heat profile during charge for the first (g), second (h), and third (i) cycles.

Heat profile during discharge for the first (j), second (k), and third (l) cycles.

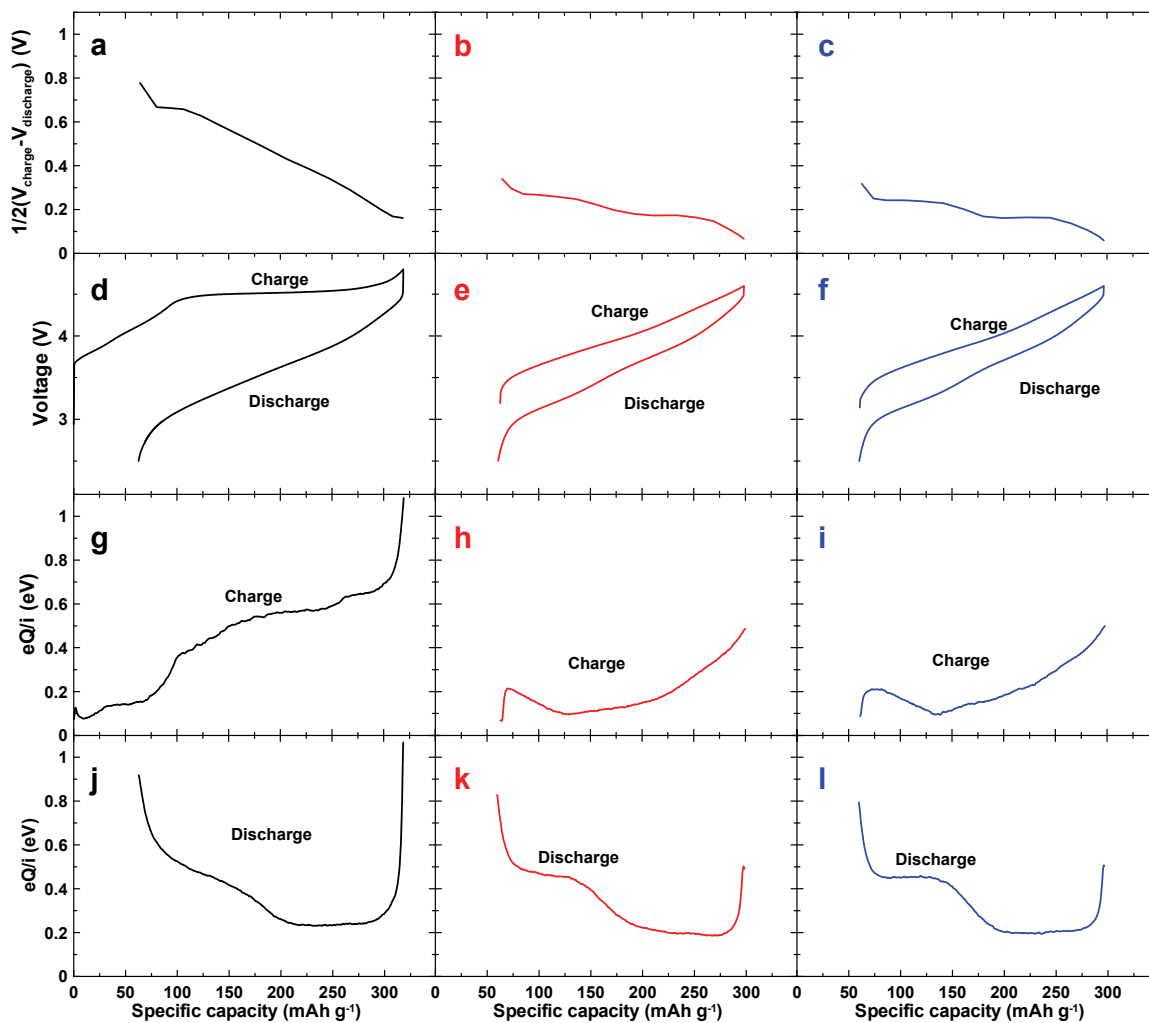


Figure 6.7. IMC data for a $\text{Li}/\text{Li}[\text{Li}_{1/5}\text{Ni}_{1/5}\text{Mn}_{3/5}]\text{O}_2$ cell charged first to 4.8 V, with subsequent cycles between 2.5 and 4.6 V at a rate of C/20.

$1/2(V_{\text{charge}} - V_{\text{discharge}})$ for the first (a), second (b), and third cycles (c).

Charge-discharge voltage profiles for the first (d), second (e), and third (f) cycles.

Heat profile during charge for the first (g), second (h), and third (i) cycles.

Heat profile during discharge for the first (j), second (k), and third (l) cycles.

Figure 6.8 shows the charge-discharge profiles for the first three cycles of Li/Li[Li_{1/9}Ni_{1/3}Mn_{5/9}]O₂ cells, along with the associated heat flows. In these cases, the first charge was to 4.8 V and the subsequent cycling was from 2.5 – 4.6 V (C/40 rate). The values of half the differences between the charge and discharge voltages are also shown. In the case of Li[Li_{1/9}Ni_{1/3}Mn_{5/9}]O₂, only 0.4 Mn⁴⁺ is expected to be reduced during discharge as compared to 0.6 Mn⁴⁺ in the case of Li[Li_{1/5}Ni_{1/5}Mn_{3/5}]O₂. The step during discharge, which is attributed to the reduction of manganese, was smaller for Li[Li_{1/9}Ni_{1/3}Mn_{5/9}]O₂ than for Li[Li_{1/5}Ni_{1/5}Mn_{3/5}]O₂. The step during discharge can be attributed to the Jahn-Teller distortion of the MnO₆ units in Li[Li_{1/5}Ni_{1/5}Mn_{3/5}]O₂ during discharge.

The oxidation of Mn³⁺ to Mn⁴⁺ during the second and third charge process should also result in some heat flow changes. Figure 5.16 shows a peak in the dQ/dV curves during the charge process at 3.2 – 3.4 V in Li[Li_{1/9}Ni_{1/3}Mn_{5/9}]O₂. Figure 6.8 shows a heat flow change in the low voltage regions for the second and third charge processes in Li/Li[Li_{1/9}Ni_{1/3}Mn_{5/9}]O₂ cells.

The heat flow data for the second and third charge processes in Li/Li[Li_{1/5}Ni_{1/5}Mn_{3/5}]O₂ cells is less clear, with heat flow changes arising in the low-voltage region (3.2 – 3.4 V) for the C/20-rate data in Figure 6.7, but the heat flow changes are less obvious in this region of the C/40-rate data in Figure 6.6. Looking forward to the dQ/dV curves for Li/Li[Li_{1/5}Ni_{1/5}Mn_{3/5}]O₂ cells, in Figure 7.2, it is difficult to find the region where manganese is oxidized during charge.

Figures 6.6-6.8 show an increase in heat flow at the end of discharge and the end of charge. This can be attributed to the change in configurational entropy as the lithium sites are either completely filled or emptied, respectively.

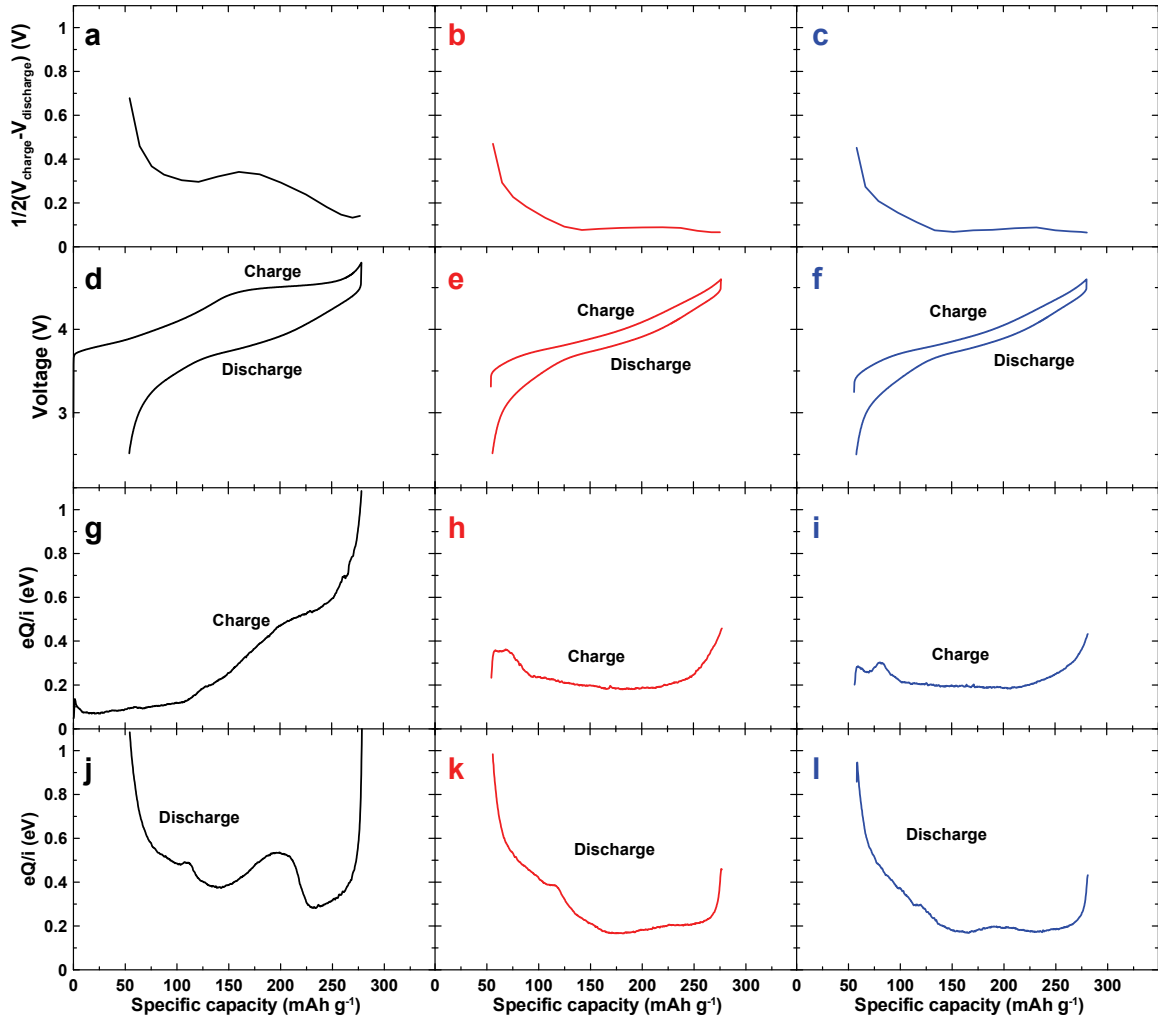


Figure 6.8. IMC data for a Li/Li[Li_{1/9}Ni_{1/3}Mn_{5/9}]O₂ cell charged first to 4.8 V, with subsequent cycles between 2.5 and 4.6 V.

The rates of charge and discharge were C/40.

$1/2(V_{charge} - V_{discharge})$ for the first (a), second (b), and third cycles (c).

Charge-discharge voltage profiles for the first (d), second (e), and third (f) cycles.

Heat profile during charge for the first (g), second (h), and third (i) cycles.

Heat profile during discharge for the first (j), second (k), and third (l) cycles.

6.7. Summary

The data gained from isothermal microcalorimetry measurements of $\text{Li}[\text{Li}_{1/5}\text{Ni}_{1/5}\text{Mn}_{3/5}]\text{O}_2$ and $\text{Li}[\text{Li}_{1/9}\text{Ni}_{1/3}\text{Mn}_{5/9}]\text{O}_2$ can be summarized by the following:

- At the end of charge to 4.4 V, there is an increase in heat flow due to the entropy changes as all the nickel is oxidized from 2+ to 4+. Likewise, an increase in heat flow is seen as the lithium sites are completely filled during discharge.
- Charging the cells to 4.8 V results in a relatively large heat flow increase, likely due to the formation of O_2 gas as oxygen is released from the lithium-rich oxide.
- Second and third charge-discharge curves show an increase in heat flow which corresponds to the $\text{Mn}^{3+/4+}$ redox couple. This has been attributed to the Jahn-Teller distortion which arises in the MnO_6 units when manganese is reduced to Mn^{3+} .
- Increase in heat flow at the end of charge and discharge for the cells which were initially charged to 4.8 V was attributed to entropy effects as the lithium sites were completely emptied or filled, respectively.

CHAPTER 7. Other Studies of Lithium-rich Oxide Materials

Other studies of lithium-rich transition metal oxides have been carried out and they will be described in this chapter. The preliminary results shown in this chapter suggest that more in-depth investigations of the lithium-rich transition metal oxides are required.

7.1. Stepwise Traverse of the Oxygen-Release Plateau

As shown in Table 1.3, Ito *et al.* increased the cycling capacity of $\text{Li}[\text{Li}_{0.2}\text{Ni}_{0.13}\text{Mn}_{0.54}\text{Co}_{0.13}]\text{O}_2$ with a pre-cycling treatment.^{79, 80} An example of the pre-cycling treatment of Ito *et al.* consisted of cycling to an upper voltage of 4.5 V for 5 cycles, and then cycling between 2.5 and 4.6 V.⁸⁰ This resulted in an increase cycling capacity from 200 to 240 mAh g⁻¹.

The pre-cycling treatment of Ito *et al.* was, in effect, doing a stepwise lithium extraction of the lithium-rich oxide, i.e. the complete charge was not carried out in the first step. It was of interest to study the effect of varying the amount of lithium accessed in the first charges, and studying the effect on the cycling and irreversible capacity.

Figure 7.1 shows different pre-cycling of $\text{Li}/\text{Li}[\text{Li}_{1/5}\text{Ni}_{1/5}\text{Mn}_{3/5}]\text{O}_2$ cells and the observed cycling capacities of the cells. The $\text{Li}[\text{Li}_{1/5}\text{Ni}_{1/5}\text{Mn}_{3/5}]\text{O}_2$ material had a particle size of 6.0 μm and the synthesis of the material was described in Chapter 5. Figure 5.7 (A) shows the XRD pattern, Figure 5.10 (A) shows the SEM images, and Figure 5.11 shows the particle size distribution of the $\text{Li}[\text{Li}_{1/5}\text{Ni}_{1/5}\text{Mn}_{3/5}]\text{O}_2$ material of interest.

Table 7.1 shows the cycling conditions of the cells in Figure 7.1. The oxygen release plateau was traversed in one whole step or divided into several steps, as indicated

in Table 7.1. It was found that if the oxygen release plateau was traversed in a stepwise fashion, the cycling capacity was higher than if the first charge was carried out in one step to 4.8 V. This is consistent with the results found by Ito *et al.*^{79, 80}

More studies would be useful to investigate the effect of pre-cycling conditions on the cycling capacity of lithium-rich transition metal oxides. The stepwise traverse corresponds to a stepped, simultaneous release of oxygen and lithium from the positive electrode. One could suggest that the stepped oxygen release could contribute to less adverse reactions at the positive electrode surface, but more studies would have to be carried out to investigate these effects.

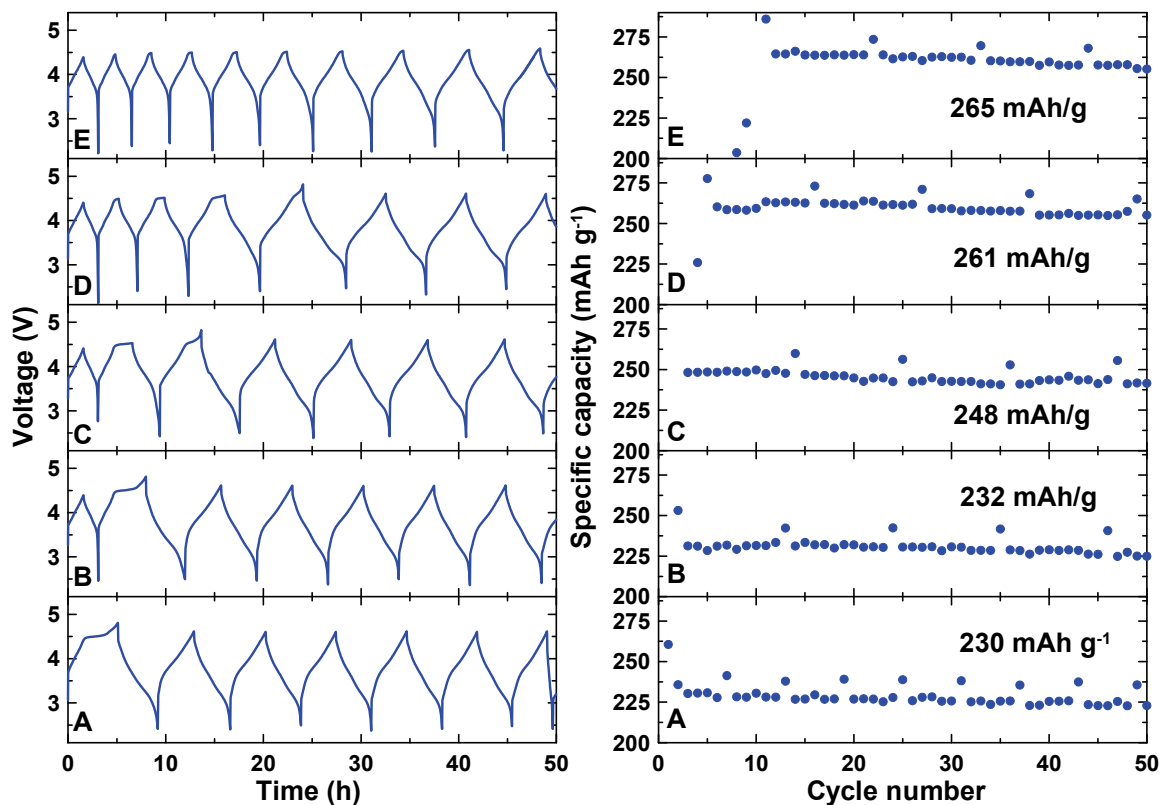


Figure 7.1 Stepped cycling of Li/Li[Li_{1/5}Ni_{1/5}Mn_{3/5}]O₂ cells. The pre-cycling conditions are shown in Table 7.1.

Cell	First charge stopped before O-release plateau?	Divisions of the oxygen release plateau	Cycling capacity (mAh g ⁻¹)
A	no	1	230
B	yes	1	232
C	yes	2	248
D	yes	4	261
E	yes	10	265

Table 7.1 The pre-cycling conditions of the stepped cycling of Li/Li[Li_{1/5}Ni_{1/5}Mn_{3/5}]O₂. The relevant cells are shown in Figure 7.1.

Figure 7.2 shows the differential capacity curves for Cell E in Figure 7.1 and Table 7.1 for the first 11 cycles. The increase of capacity with cycle number in Figure 7.1 for Cell E corresponds to an increase in the size of the peak around 3.2 V, associated with the reduction of Mn⁴⁺ to Mn³⁺. As more oxygen was released from the positive electrode during charge, more of the manganese reduction was accessed during discharge. This gave rise to a higher cycling capacity from cycle 1 to cycle 11 in Figure 7.2 (E).

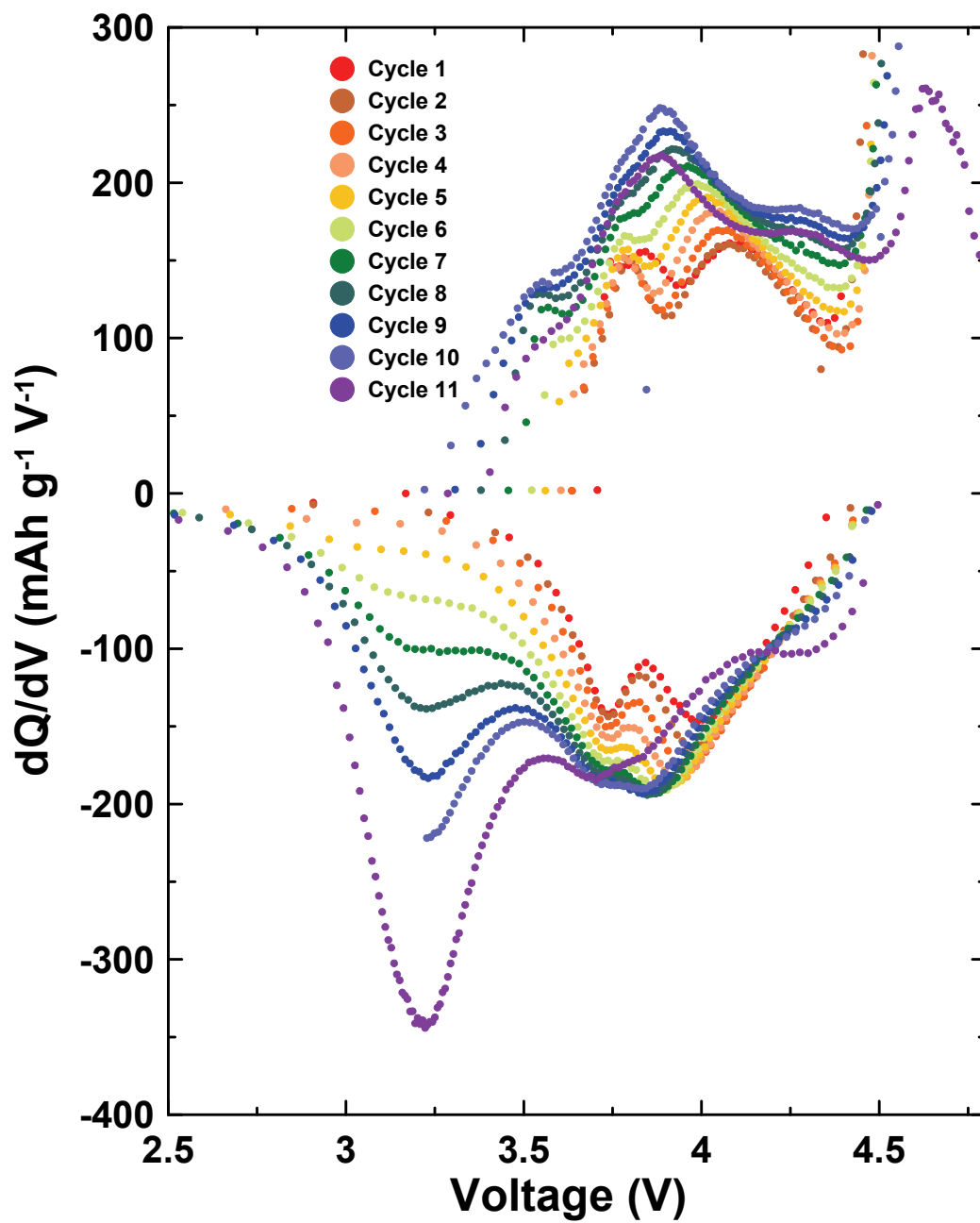


Figure 7.2. Differential capacity curves for each cycle associated with the cycling in the E panel of Figure 7.1.

7.2. Irreversible Capacity During the Stepwise Traverse of the Oxygen-Release Plateau

Figure 7.3 shows the stepwise traverse of the oxygen-release plateau in Li/Li[Li_{1/5}Ni_{1/5}Mn_{3/5}]O₂ cells. The traverse was carried out by increasing the charge time with each charge for a fixed current (C/5 rate). It can be seen that steps 1 and 2 make up the majority of the irreversible capacity. There is still oxygen release in the subsequent steps, but there is little added to the irreversible capacity loss. Thus the irreversible capacity comes mostly from the initial part of oxygen release.

It has been suggested that after complete charge (and removal of lithium from the transition metal layer), transition metals can diffuse from the surface to the bulk of the lithium-rich material.⁶¹ This would lead to an irreversible capacity loss, as lithium cannot be reinserted into the material during discharge.

Figure 7.3 suggests that lithium is first removed from the transition metal layer in the oxygen-release region. In the nanocrystalline model of the lithium-rich oxides, the mechanism of lithium-removal could be as follows: during normal lithium deintercalation (corresponding to the oxidation of nickel), lithium is removed from the Li[Ni_{1/2}Mn_{1/2}]O₂ regions. When the oxygen-release plateau is traversed, lithium is first removed from the transition metal layer in Li[Li_{1/3}Mn_{2/3}]O₂. The rest of the lithium is removed from the lithium layer after it is removed from the transition metal layer. After charge, diffusion of transition metals may occur from surface to bulk filling the lithium vacancies remaining in Li[Li_{1/3}Mn_{2/3}]O₂. The lithium cannot be reinserted into the transition metal layer, leading to the irreversible capacity loss.

This is also supported by Lei *et al.*, who observed weaker ordering of lithium in the transition metal planes for the charge and discharged lithium-rich material than for the as-prepared lithium-rich oxide.⁶⁴

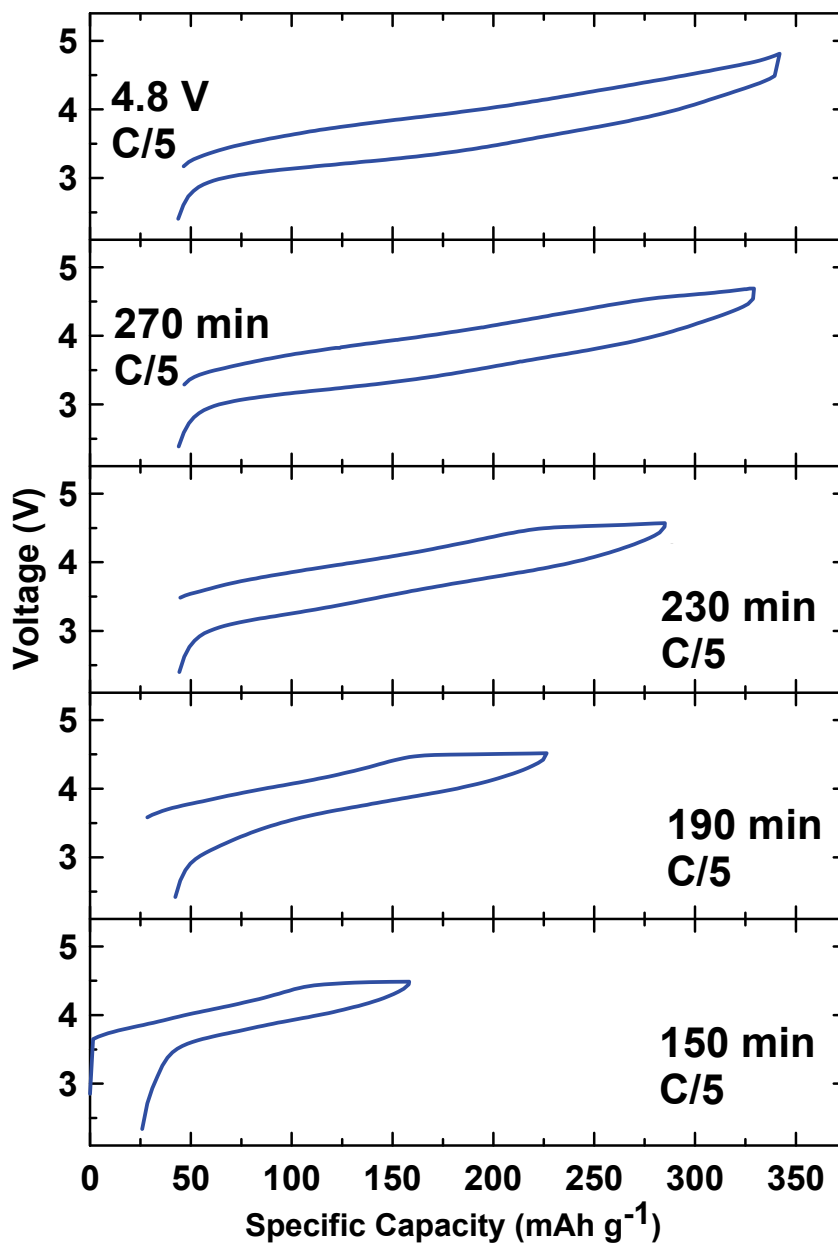


Figure 7.3. Stepwise traverse of the oxygen-release plateau in $\text{Li}/\text{Li}[\text{Li}_{1/5}\text{Ni}_{1/5}\text{Mn}_{3/5}]\text{O}_2$ cells.

C/5 rate, 55°C , and the lower voltage was 2.5 V.

7.3. High-Precision Charger Experiments on $\text{Li/Li}[\text{Li}_{1/9}\text{Ni}_{1/3}\text{Mn}_{5/9}]\text{O}_2$ and $\text{Li/Li}[\text{Li}_{1/5}\text{Ni}_{1/5}\text{Mn}_{3/5}]\text{O}_2$ Cells

There are several reasons why lithium-ion batteries have a limited cycle life, as seen by capacity fade during the cycling of lithium-ion batteries. For the negative electrode, as the solid-electrolyte interphase (SEI) grows, there is consumption of lithium to form the SEI layer, leading to capacity loss. In the case of the positive electrode, oxidation of the electrolyte at the positive electrode surface requires charge transfer and results in a reduced amount of lithium intercalated into the positive electrode material.

The requirements of lithium-ion batteries for automotive applications are different than the conventional uses of lithium-ion batteries, in portable electronic devices. A major difference is that the cycle life for lithium-ion batteries in automotive applications needs to be very large, 3000 or preferably 10000 cycles.¹³⁵ In order to study cycle life to 3000 cycles, the time required is too long.

An alternative method of studying whether the battery will have a long cycle life is to measure its coulombic efficiency to a high-degree of precision. The coulombic efficiency is the ratio of charge capacity to discharge capacity of the battery. The expected cycle life can be estimated if the coulombic efficiency of a battery is precisely measured. For example, if the coulombic efficiency is measured to a precision of $\pm 0.01\%$, the expected cycle life to 1000 or 2000 cycles can be estimated.¹³⁵ A description of the high precision charger (HPC) used in this investigation is given in reference 135.

The $\text{Li}[\text{Li}_{1/9}\text{Ni}_{1/3}\text{Mn}_{5/9}]\text{O}_2$ stoichiometry was selected to investigate its electrochemistry with the HPC. The $\text{Li}[\text{Li}_{1/9}\text{Ni}_{1/3}\text{Mn}_{5/9}]\text{O}_2$ material had a particle size of

5.3 μm and the synthesis of the material was described in Chapter 5. Figure 5.6 (A) shows the XRD pattern, Figure 5.8 (A) shows the SEM images, and Figure 5.9 shows the particle size distribution of the $\text{Li}[\text{Li}_{1/9}\text{Ni}_{1/3}\text{Mn}_{5/9}]\text{O}_2$ material of interest. A $\text{Li}/\text{Li}[\text{Li}_{1/9}\text{Ni}_{1/3}\text{Mn}_{5/9}]\text{O}_2$ cell was first charged to 4.8 V at C/10 rate, following by cycling at C/5 rate between 2.5 and 4.6 V for 40 cycles. Figure 7.4 shows the cycling characteristics of this cell.

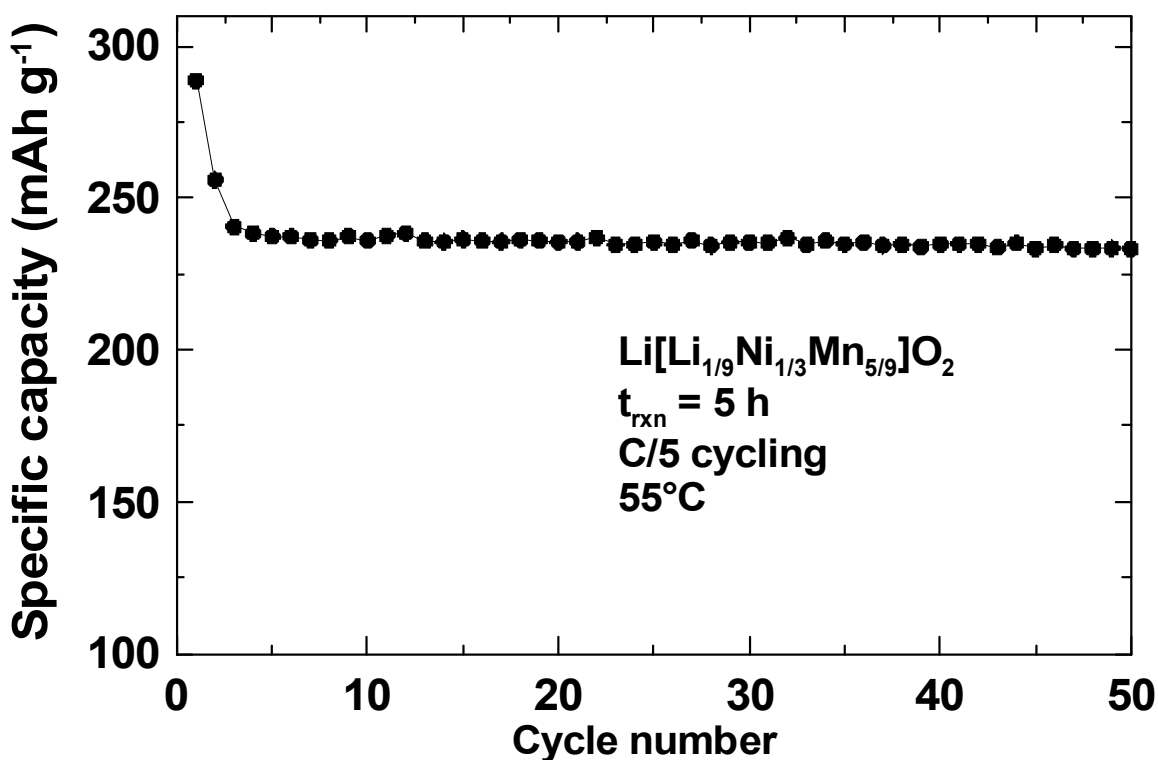


Figure 7.4. Cycling capacity versus cycle number of a $\text{Li}/\text{Li}[\text{Li}_{1/9}\text{Ni}_{1/3}\text{Mn}_{5/9}]\text{O}_2$ cell. The material had a 5.3 micron-sized positive electrode material. The first charge was to 4.8 V at C/10 rate. Subsequent cycles were between 2.5 and 4.6 V at C/5 rate. Temperature is 55°C.

The cell was removed from the traditional charger and placed in the HPC for further tests. The HPC cycles were carried out at 30°C, 40°C, 50°C, and 60°C. Figure

7.5 shows the coulombic efficiency of the $\text{Li}/\text{Li}[\text{Li}_{1/9}\text{Ni}_{1/3}\text{Mn}_{5/9}]\text{O}_2$ cell at various temperatures. The rate of cycling was $C/5$ at each temperature.

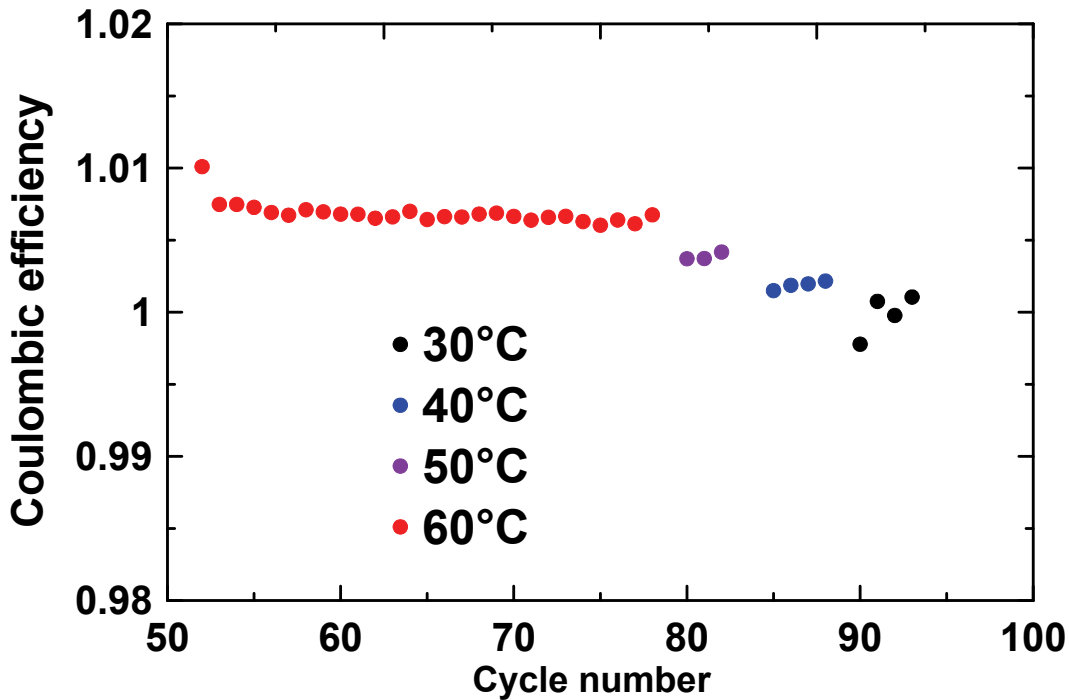


Figure 7.5. Coulombic efficiency versus cycle number of a $\text{Li}/\text{Li}[\text{Li}_{1/9}\text{Ni}_{1/3}\text{Mn}_{5/9}]\text{O}_2$ cell. The temperatures were 30°C , 40°C , 50°C , and 60°C . The $\text{Li}[\text{Li}_{1/9}\text{Ni}_{1/3}\text{Mn}_{5/9}]\text{O}_2$ particle size was $5.3\ \mu\text{m}$, the voltage range of the cell was 2.5 to 4.6 V, and the cycling rate was $C/5$.

Figure 7.5 shows that at low temperature cycle, the $\text{Li}/\text{Li}[\text{Li}_{1/9}\text{Ni}_{1/3}\text{Mn}_{5/9}]\text{O}_2$ cell had a coulombic efficiency of approximately 1.002. When the cell temperature was increased to 60°C , the coulombic efficiency was approximately 1.007. This can be attributed to possible oxidation at the positive electrode surface, leading to consumption of charge carriers and limiting the lithium uptake into the material.

Figure 7.6 shows the cycling of the $\text{Li}/\text{Li}[\text{Li}_{1/9}\text{Ni}_{1/3}\text{Mn}_{5/9}]\text{O}_2$ cell at 30°C , 40°C , 50°C , and 60°C . Lower temperature cycling is at a lower capacity than cycling at 60°C .

As discussed in Chapter 6, lithium-rich oxides have relatively poor rate capability, when compared to the non-lithium rich layered transition metal oxides.

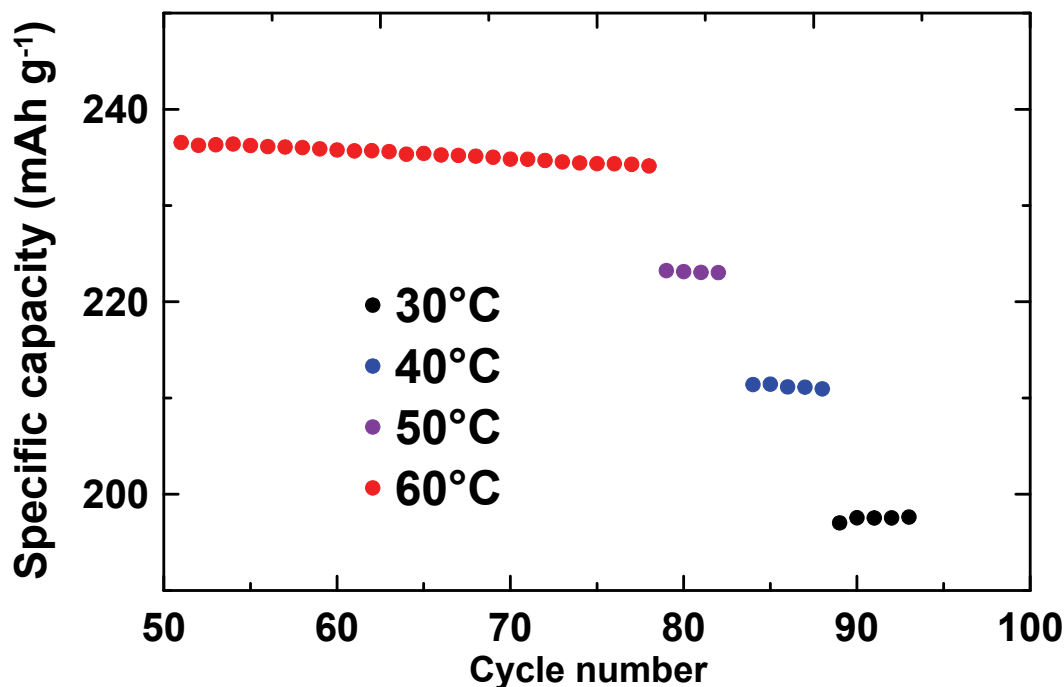


Figure 7.6. Cycling capacity versus cycle number of a Li/Li[Li_{1/9}Ni_{1/3}Mn_{5/9}]O₂ cell. The temperatures were 30°C, 40°C, 50°C, and 60°C. The Li[Li_{1/9}Ni_{1/3}Mn_{5/9}]O₂ particle size was 5.3 μm, the voltage range of the cell was 2.5 to 4.6 V, and the cycling rate was C/5.

If the increase in coulombic efficiency is due to oxidation at the positive electrode surface, methods that decrease the electrolyte oxidation should be studied. Methods that may affect the amount of electrolyte oxidation include changing the electrolyte, addition of electrolyte additives, and coating of the positive electrolyte material to decrease electrolyte-electrode surface interactions. Future work could be carried out to evaluate the effect of these methods using the HPC.

CHAPTER 8. Conclusions

Positive electrodes for lithium and lithium-ion batteries have gone through several generations. In lithium batteries, the positive electrode field was once dominated by the layered dichalcogenides, for example LiTiS_2 .²⁰ The higher voltage oxides eventually replaced the dichalcogenides.²⁷ Lithium batteries are desired for applications such as automobile and grid-storage. The requirements of these systems include lower cost, longer cycle life, longer calendar life, higher capacity, better rate capability, and better safety than the current technology.

Lithium-rich oxides provide a higher capacity than traditional transition metal oxides¹⁷ and therefore deserve study as possible electrodes in current and future lithium-ion batteries.

8.1. Synthesis of Spherical and Dense Hydroxide Precursors for Lithium Transition Metal Oxides

One important characteristic of a lithium-ion battery material is its density within the cell. Material that does not pack well will unnecessarily take up space in the cell, decreasing volumetric capacity. It is therefore of importance to learn how to make positive electrode material that packs well and to study the electrochemistry of the high tap-density material.

The density of a material is often characterized by its “tap density”, the density of the material in a container after it is tapped a number of times. For layered transition metal hydroxides and oxides, high tap density material is $2.0\text{-}2.5 \text{ g cm}^{-3}$.^{94, 98}

In this thesis, the preparation of spherical and dense transition metal oxides was studied. To prepare transition metal oxides for lithium-ion batteries, the coprecipitation

reaction was selected (over the solid-state reaction which results in inhomogeneous distribution of the transition metals in the transition metal layer). The coprecipitation reaction involves adding a metal salt (such as a nitrate or sulfate) to a basic solution (such as LiOH or NaOH) to precipitate out the transition metal hydroxide precursor. The transition metal hydroxide is heated with a lithium salt to form the lithium transition metal oxide.

The structure of the mixed metal hydroxide precursor was studied. It was found that the literature XRD patterns of mixed metal hydroxide did not match those of the calculated pure hydroxide phase.¹¹⁹ The pure hydroxide precursor was prepared by carrying out the coprecipitation synthesis in non-oxidizing conditions – using solutions made with deaerated water and bubbling nitrogen throughout the reaction. In this way, the pure hydroxides $\text{Ni}(\text{OH})_2$, $\text{Ni}_{1/2}\text{Mn}_{1/2}(\text{OH})_2$, and $\text{Ni}_{1/3}\text{Mn}_{1/3}\text{Co}_{1/3}(\text{OH})_2$ were made.

The oxidation of $\text{Ni}_{1/3}\text{Mn}_{1/3}\text{Co}_{1/3}(\text{OH})_2$ was observed by heating it in air in increments to 140°C. XRD patterns showed a shift of the Bragg peaks to higher scattering angles, corresponding to a decrease in the hexagonal lattice constants a and c . This was attributed to a conversion from the pure hydroxide phase to an oxyhydroxide phase: the decrease in lattice constants was consistent with literature values for the lattice constants of the hydroxide and oxyhydroxide phases. As well, TGA analysis revealed a step at approximately 140°C, which corresponded to the calculated mass loss in the conversion of a hydroxide to an oxyhydroxide.

Dense and spherical metal hydroxides are typically produced with the addition of aqueous ammonia to the coprecipitation reaction.⁹⁴ By selecting proper reaction parameters (as discussed later), spherical and dense $\text{Ni}_{1/3}\text{Mn}_{1/3}\text{Co}_{1/3}(\text{OH})_2$ was made with

a tap density of 1.7 g cm^{-3} and a pure hydroxide XRD pattern. By heating to 140°C , the tap density of the material increased to 2.0 g cm^{-3} . As well, the resulting XRD pattern matched that of the commercial NMC precursor XRD pattern found in the literature.¹¹⁹

The addition of aqueous ammonia to the coprecipitation reaction was studied. It was found that spherical and dense Ni(OH)_2 could be synthesized at a pH of 11.0. The Ni(OH)_2 material was obtained from the reactor as a function of reaction time. SEM analysis revealed that there was an increase in particle size with reaction time and the particle surface was smoother as the reaction proceeded. The final tap density of the Ni(OH)_2 was 2.1 g cm^{-3} .

However, the hydroxides containing manganese and cobalt, $\text{Ni}_{1/2}\text{Mn}_{1/2}(\text{OH})_2$ and $\text{Ni}_{1/3}\text{Mn}_{1/3}\text{Co}_{1/3}(\text{OH})_2$ could not be made spherical and dense at a pH of 11.0. The effect of pH on the tap density and morphology of the hydroxides was studied.

It was found that Ni(OH)_2 formed spherical particles up to a pH of 11.4. At a pH above 11.4, the tap density of the Ni(OH)_2 was low and the morphology of the particles was non-spherical. In the cases of $\text{Ni}_{1/2}\text{Mn}_{1/3}(\text{OH})_2$ and $\text{Ni}_{1/3}\text{Mn}_{1/3}\text{Co}_{1/3}(\text{OH})_2$, lower pH values had to be selected to make these materials spherical and dense. In both cases, the pH value had to be approximately 10.0 to make spherical and dense hydroxide.

The differences in the synthetic conditions required to make the precursor hydroxides were investigated by analyzing the relevant equilibria present during the coprecipitation reaction. The equilibria included the stepwise coordination of ammonia to transition metal, the solubility of hydroxide, the base dissociation of ammonia, the autodissociation of water, and the mass balances of ammonia and metal. Obtaining

literature equilibrium constants resulted in a system of equations, in which the concentrations of the relevant species could be determined as a function of pH.

The analysis of the relevant equilibria present during the coprecipitation reaction was carried out separately for nickel, manganese, and cobalt transition metals. It was found that there was a broader pH range at which ammonia complexes were formed for the nickel case than for the manganese and cobalt cases. As well, the pH required to form metal-ammonia coordination complexes was higher for nickel than for manganese and cobalt.

It was determined that the pH required to produce spherical and dense transition metal hydroxides has to fall within the range at which ammonia is coordinated to the transition metal. It was suggested that in the coprecipitation reaction in the presence of aqueous ammonia, particle growth occurs via a dissolution-precipitation mechanism. The addition of aqueous ammonia to the coprecipitation reaction effectively increases the solubility of the formed hydroxide, allowing for spherical particle growth.

8.2. Studies on the Lithium-Rich Transition Metal Oxides

The synthetic parameters determined to produce spherical and dense material allowed for the study of the effect of particle size on the electrochemical characteristics of lithium-rich transition metal oxides. Previously, the lithium-rich transition metal oxides were studied using a material that had a small particle size and low tap density.¹⁷ It was of interest to study the materials with particle sizes and tap densities that are commercially applicable.

The lithium-rich oxides that were selected to study were $\text{Li}[\text{Li}_{1/9}\text{Ni}_{1/3}\text{Mn}_{5/9}]\text{O}_2$ and $\text{Li}[\text{Li}_{1/5}\text{Ni}_{1/5}\text{Mn}_{3/5}]\text{O}_2$. The precursor hydroxides were $\text{Ni}_{3/8}\text{Mn}_{5/8}(\text{OH})_2$ and

$\text{Ni}_{1/4}\text{Mn}_{3/4}(\text{OH})_2$, respectively. $\text{Ni}_{3/8}\text{Mn}_{5/8}(\text{OH})_2$ was synthesized with a coprecipitation reaction in the presence of aqueous ammonia with reaction times of 5, 10, and 20 h. $\text{Ni}_{1/4}\text{Mn}_{3/4}(\text{OH})_2$ was likewise synthesized but with reaction times of 10, 20, and 40 h. As expected, the precursor hydroxides had varying particle size and tap density. Heating the hydroxides with a lithium salt produced lithium-rich transition metal oxides with various particle sizes.

The first charge of the lithium-rich transition metal oxides $\text{Li}[\text{Li}_{1/9}\text{Ni}_{1/3}\text{Mn}_{5/9}]\text{O}_2$ and $\text{Li}[\text{Li}_{1/5}\text{Ni}_{1/5}\text{Mn}_{3/5}]\text{O}_2$ was studied. In this investigation, the first charge was studied as a function of particle size, charge rate, and temperature. It was found that, for the most part, within the parameters studied, the ‘normal’ lithium deintercalation region was unaffected by particle size, charge rate, and temperature. However, for both lithium-rich oxide stoichiometries, the length of the oxygen release plateau varied for different particle sizes, charge rates, and temperatures. The smallest particle size, highest cell temperature, and lowest charge rate was found to result in the highest capacity in the oxygen release region.

The effect of various parameters on the length of the oxygen release plateau suggested that the oxygen release process is diffusion limited. The apparent diffusion coefficients of oxygen at 30°C and 55°C in $\text{Li}[\text{Li}_{1/9}\text{Ni}_{1/3}\text{Mn}_{5/9}]\text{O}_2$ and $\text{Li}[\text{Li}_{1/5}\text{Ni}_{1/5}\text{Mn}_{3/5}]\text{O}_2$ was determined using the Atlung method.¹²⁴ In the Atlung method, the fractional capacity (the fraction of theoretical oxygen release capacity obtained) can be related to the charge rate, diffusion coefficient, and particle radius for a spherical geometry.

The apparent oxygen diffusion coefficients for $\text{Li}[\text{Li}_{1/9}\text{Ni}_{1/3}\text{Mn}_{5/9}]\text{O}_2$ were found to be $4.0 \times 10^{-13} \text{ cm}^2 \text{ s}^{-1}$ at 30°C and $2.5 \times 10^{-12} \text{ cm}^2 \text{ s}^{-1}$ at 55°C . The apparent oxygen diffusion coefficients for $\text{Li}[\text{Li}_{1/5}\text{Ni}_{1/5}\text{Mn}_{3/5}]\text{O}_2$ were found to be $3.2 \times 10^{-13} \text{ cm}^2 \text{ s}^{-1}$ at 30°C and $1.3 \times 10^{-12} \text{ cm}^2 \text{ s}^{-1}$ at 55°C . These apparent oxygen diffusion coefficient values revealed that the diffusion in the oxygen release range was several orders of magnitude slower than diffusion in the normal lithium deintercalation region.^{126, 127}

The charge and discharge of the lithium-rich transition metal oxides $\text{Li}[\text{Li}_{1/9}\text{Ni}_{1/3}\text{Mn}_{5/9}]\text{O}_2$ and $\text{Li}[\text{Li}_{1/5}\text{Ni}_{1/5}\text{Mn}_{3/5}]\text{O}_2$ was studied using isothermal microcalorimetry (IMC). IMC measurements were used to probe the heat changes in the cell that correspond to structural changes in the electrode during charge and discharge.

IMC measurements were carried out on $\text{Li}[\text{Li}_{1/5}\text{Ni}_{1/5}\text{Mn}_{3/5}]\text{O}_2$ on three charge-discharge cycles between 2.5 and 4.4 V. There was an increase in heat flow as the material approached the stoichiometry $x = 0.6$ in $\text{Li}_x[\text{Li}_{1/5}\text{Ni}_{1/5}\text{Mn}_{3/5}]\text{O}_2$. The configurational entropy of the material was calculated as a function of x in $\text{Li}_x[\text{Li}_{1/5}\text{Ni}_{1/5}\text{Mn}_{3/5}]\text{O}_2$ and related to the heat flow change during charge.

IMC measurements were carried out on $\text{Li}[\text{Li}_{1/5}\text{Ni}_{1/5}\text{Mn}_{3/5}]\text{O}_2$ and $\text{Li}[\text{Li}_{1/9}\text{Ni}_{1/3}\text{Mn}_{5/9}]\text{O}_2$ with the first charge to 4.8 V and subsequent cycling between 2.5 and 4.6 V. There was a relatively large increase in heat flow as the oxygen release plateau was traversed.

As well, there was an increase in heat flow during the first discharge in the region where manganese is expected to be reduced from Mn^{4+} to Mn^{3+} . There also was an increase in heat flow on subsequent discharges in this region and in the region where manganese is expected to be oxidized from Mn^{3+} to Mn^{4+} during the second and third

charge processes. This was attributed to a Jahn-Teller distortion that occurs in the MO_6 units going from $d^5 \text{Mn}^{4+}$ to the $d^4 \text{Mn}^{3+}$. It was suggested that the Jahn-Teller elongation of the MO_6 units leads to a local structural change that leads to an increase in heat flow during discharge.

Other studies were carried out on the lithium-rich transition metal oxides. It was previously found by Ito *et al.* that following a specific precycling condition increased the cycling capacity of the lithium-rich transition metal oxides.^{79, 80} In the current work, the precycling was done such that the oxygen release plateau was traversed stepwise, with a discharge after each charge step. By traversing the oxygen release plateau in several steps, the cycling capacity was increased from 230 to 265 mAh g^{-1} .

The stepwise traverse of the oxygen release plateau also revealed that the irreversible capacity was obtained in the first portion of oxygen release. It was suggested that in the oxygen release region, lithium is first removed from the transition metal layer. After this, transition metal rearrangement (as described in reference 61) means the lithium cannot be reinserted into the transition metal layer, leading to the irreversible capacity.

High precision charger (HPC) measurements were carried out to investigate the cycling life of the lithium-rich transition metal oxide $\text{Li}[\text{Li}_{1/9}\text{Ni}_{1/3}\text{Mn}_{5/9}]\text{O}_2$. The coulombic efficiency of the cells increased from a cell temperature of 30°C to 60°C . This suggested that there were more reactions with the electrolyte at higher cell temperatures, which would lead to a loss in capacity and more fade.

8.3. Suggested Future Studies on the Hydroxide Coprecipitation Reaction

The coprecipitation reaction in the presence of ammonia was studied by looking at the relevant equilibria present during the coprecipitation reaction. In this work, the equilibria taken from the literature were room-temperature equilibria. However, many coprecipitation reactions occur at elevated temperatures. It would be useful to determine the concentration of relevant species at higher temperatures. This would involve determination of the equilibrium constants at different temperatures. One way of doing this is to determine the equilibrium constant at a different temperature using the enthalpy of the equilibrium and the van't Hoff equation. If this was carried out for each reaction, more insight into the effect of varying pH on the tap density and morphology could be obtained.

8.4. Suggested Future Studies on the Lithium-Rich Transition Metal Oxides

Diffusion information about the lithium-rich transition metal oxides was found using one method, the Atlung method. It would be of interest to study the rate of lithium deintercalation in the oxygen release region using other methods, such as potentiostatic and galvanostatic intermittent titration techniques (PITT and GITT). By doing this, a comparison could be made between the diffusion coefficients obtained from multiple techniques. This would give more insight into the diffusion process in lithium-rich transition metal oxides.

It has been suggested that the Mn^{4+} reduction and subsequent Mn^{3+} oxidation is sluggish and may be responsible for the relatively poor rate capability of the lithium-rich transition metal oxides. To test this idea, more studies have to be carried out on the rate capability of these materials. For example, $\text{Li}[\text{Li}_{1/5}\text{Ni}_{1/5}\text{Mn}_{3/5}]\text{O}_2$ could be synthesized

and its rate capability studied as a function of voltage window. In all cases, the oxygen release plateau would be completely traversed. In one instance, the cycling would occur in a relatively small voltage window such that the Mn^{4+} to $^{3+}$ reduction would not be accessed. And in the other case, the normal 2.5-4.6 V voltage window would be used. If the manganese reduction and oxidation is the reason for the poor rate capability, the cell in the reduced voltage window would have a much better rate capability.

More IMC studies should be carried out on the lithium-rich transition metal oxides. This would include IMC investigations of more lithium-rich stoichiometries. It would also be of interest to further study the heat flow changes as the oxygen release plateau is traversed. The heat in the second discharge was attributed to the manganese reduction. If this is the case, this $\text{Mn}^{4+/3+}$ heat flow change would not be present until the manganese portion is accessed. This would provide more evidence to support the structural changes that may occur when the manganese redox couple is accessed.

The studies in Chapter 7 all warrant future investigation of the lithium-rich transition metal oxides. This includes studies on the effect of the stepwise traverse of the oxygen release plateau on the cycling capacity and HPC tests on the material. Both these studies would benefit from investigating a wider range of lithium-rich stoichiometries. In the case of HPC tests, the introduction of electrolyte additives should be carried out to see the effect on the coulombic efficiency, especially at higher cell temperatures. The coating of lithium-rich transition metal oxides has been done by several other groups. The effect of the coating would benefit from HPC studies. This could investigate if the coating can decrease the amount of reaction with the electrolyte.

Safety studies of the lithium-rich oxides should also be carried out. The safety of the positive electrode material in lithium-ion batteries is of high importance. The effect of additives, coatings, and dopants, such as aluminum, should also be studied in terms of the effect on the safety of the material.

The fate of the evolved oxygen from the lithium-rich oxides is still relatively unknown. More measurements should be carried out to determine the amount and composition of the evolved materials from the cell. For instance, a measurement of volume expansion of an expandable cell (at fixed pressure) could give information on how much gases are evolved during the process. This experiment could also give insight into how much gas is not evolved, and may dissolve or react with the electrodes or electrolyte. This fate of the evolved oxygen in these materials is important and may affect the electrochemical performance of the lithium-rich materials.

The irreversible capacity needs to be studied, including investigating why the irreversible capacity occurs mostly in the initial part of oxygen release. An extremely careful structural study (in-situ or ex-situ XRD) would be ideal to probe the effect of traversing the plateau on structural changes in the lithium-rich material.

Chapter 6 discusses the possibility of vacancies being present in the lithium-rich transition metal oxides after charge and discharge. It is important to identify if oxygen vacancies exist in the oxygen layer and if lithium vacancies exist in the transition metal layer after charge. The existence of vacancies may give rise to larger cycling capacities. The vacancies could be probed, for example, with high-precision He-pycnometry. The experiment would be carried out by measuring the crystallographic density of the delithiated lithium-rich transition metal oxide by XRD. The ratio of true density to the

crystallographic density will be much less than unity if many vacancies exist in the material.

Figure 7.1 shows the first charge and discharge of the lithium rich material $\text{Li}[\text{Li}_{1/5}\text{Ni}_{1/5}\text{Mn}_{3/5}]\text{O}_2$. It would be of interest to make the composition at number 6, which was suggested to be $\text{Li}[\square_{1/5}\text{Ni}_{1/5}\text{Mn}_{3/5}]\square_{2/5}\text{O}_{8/5}$ in this work. This nomenclature is for a solid solution, and the material may not form a solid solution, as described in Section 1.11. Also, it is unknown what vacancies still exist, if any, at the bottom of discharge. If this material could be made, it would have no irreversible capacity and would be a great positive electrode material for lithium-ion batteries.

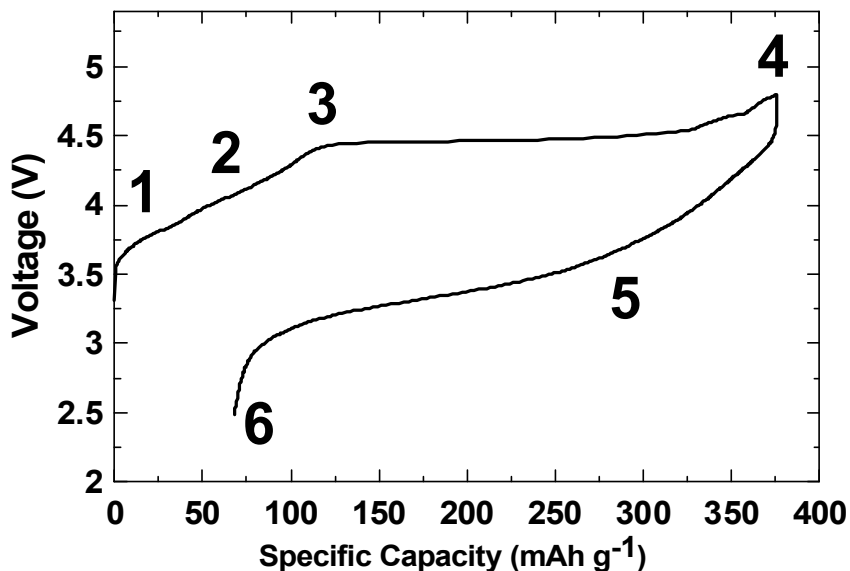


Figure 7.1. Charge and discharge profile of a $\text{Li}/\text{Li}[\text{Li}_{1/5}\text{Ni}_{1/5}\text{Mn}_{3/5}]\text{O}_2$ cell also shown in Figure 6.2.

References

- (1) Winter, M.; Besenhard, J. O.; Spahr, M. E.; Novák, P. *Adv. Mater.* **1998**, *10*, 725-763.
- (2) Winter, M.; Brodd, R. J. *Chem. Rev.* **2004**, *104*, 4245-4270.
- (3) Xu, K. *Chem. Rev.* **2004**, *104*, 4303-4418.
- (4) Fong, R.; Sacken, U. v.; Dahn, J. R. *J. Electrochem. Soc.* **1990**, *137*, 2009-2013.
- (5) Peled, E. *J. Electrochem. Soc.* **1979**, *126*, 2047-2051.
- (6) Wen, C. J.; Boukamp, B. A.; Huggins, R. A.; Weppner, W. *J. Electrochem. Soc.* **1979**, *126*, 2258-2266.
- (7) Lai, S. *J. Electrochem. Soc.* **1976**, *123*, 1196-1197.
- (8) Wen, C. J.; Huggins, R. A. *J. Electrochem. Soc.* **1981**, *128*, 1181-1187.
- (9) Dahn, J. R.; Mar, R. E.; Abouzeid, A. *J. Electrochem. Soc.* **2006**, *153*, A361-A365.
- (10) Tian, Y.; Timmons, A.; Dahn, J. R. *J. Electrochem. Soc.* **2009**, *156*, A187-A191.
- (11) Thackeray, M. M.; David, W. I. F.; Bruce, P. G.; Goodenough, J. B. *Mater. Res. Bull.* **1983**, *18*, 461-472.
- (12) Whittingham, M. S. *Chem. Rev.* **2004**, *104*, 4271-4302.
- (13) Padhi, A. K.; Nanjundaswamy, K. S.; Goodenough, J. B. *J. Electrochem. Soc.* **1997**, *144*, 1188-1194.
- (14) Ohzuku, T.; Ueda, A. *J. Electrochem. Soc.* **1994**, *141*, 2972-2977.
- (15) Ohzuku, T.; Makimura, Y. *Chem. Lett.* **2001**, 744-745.
- (16) Ohzuku, T.; Makimura, Y. *Chem. Lett.* **2001**, 642-643.
- (17) Lu, Z.; MacNeil, D. D.; Dahn, J. R. *Electrochem. Solid-State Lett.* **2001**, *4*, A191-A194.

- (18) Gamble, F. R.; Osiecki, J. H.; Cais, M.; Pisharody, R.; DiSalvo, F. J.; Geballe, T. H. *Science* **1971**, *174*, 493-497.
- (19) Whittingham, M. S. *Science* **1976**, *192*, 1126-1127.
- (20) Whittingham, M. S. *J. Electrochem. Soc.* **1976**, *123*, 315-320.
- (21) Dahn, J. R.; Haering, R. R. *Solid State Commun.* **1981**, *40*, 245-248.
- (22) Whittingham, M. S. *Prog. Solid State Chem.* **1978**, *12*, 41-99.
- (23) Whittingham, M. S. *Mater. Res. Bull.* **1978**, *13*, 959-965.
- (24) Murphy, D. W.; Trumbore, F. A. *J. Electrochem. Soc.* **1976**, *123*, 960-964.
- (25) Mendiboure, A.; Delmas, C.; Hagenmuller, P. *Mater. Res. Bull.* **1984**, *19*, 1383-1392.
- (26) Delmas, C.; Fouassier, C.; Hagenmuller, P. *Physica B* **1980**, *99*, 81-85.
- (27) Mizushima, K.; Jones, P. C.; Wiseman, P. J.; Goodenough, J. B. *Mater. Res. Bull.* **1980**, *15*, 783-789.
- (28) Ozawa, K. *Solid State Ionics* **1994**, *69*, 212-221.
- (29) Ohzuku, T.; Ueda, A.; Nagayama, M. *J. Electrochem. Soc.* **1993**, *140*, 1862-1870.
- (30) Ohzuku, T. In *Overcharge-Protected Oxide Cathodes*; Besenhard, J. O., Ed.; Handbook of Battery Materials; Wiley-VCH: Weinheim, 1999; pp 323-337.
- (31) Armstrong, A. R.; Bruce, P. G. *Nature* **1996**, *381*, 499-500.
- (32) Kanno, R.; Shirane, T.; Kawamoto, Y.; Takeda, Y.; Takano, M.; Ohashi, M.; Yamaguchi, Y. *J. Electrochem. Soc.* **1996**, *143*, 2435-2442.
- (33) de Picciotto, L. A.; Thackeray, M. M.; David, W. I. F.; Bruce, P. G.; Goodenough, J. B. *Mater. Res. Bull.* **1984**, *19*, 1497-1506.

- (34) Thackeray, M. M.; de Picciotto, L. A.; David, W. I. F.; Bruce, P. G.; Goodenough, J. B. *J. Solid State Chem.* **1987**, *67*, 285-290.
- (35) Delmas, C.; Cognac-Auradou, H.; Cocciantelli, J. M.; Ménétrier, M.; Doumerc, J. P. *Solid State Ionics* **1994**, *69*, 257-264.
- (36) Murphy, D. W.; Christian, P. A.; DiSalvo, F. J.; Carides, J. N. *J. Electrochem. Soc.* **1979**, *126*, 497-499.
- (37) Nassau, K.; Murphy, D. W. *J. Non-Cryst. Solids* **1981**, *44*, 297-304.
- (38) Livage, J. *Mater. Res. Bull.* **1991**, *26*, 1173-1180.
- (39) Spahr, M. E.; Stoschitzki-Bitterli, P.; Nesper, R.; Haas, O.; Novak, P. J. *Electrochem. Soc.* **1999**, *146*, 2780-2783.
- (40) Ceder, G.; Aydinol, M. K.; Kohan, A. F. *Comput. Mater. Sci.* **1997**, *8*, 161-169.
- (41) Obrovac, M. N.; Mao, O.; Dahn, J. R. *Solid State Ionics* **1998**, *112*, 9-19.
- (42) Komaba, S.; Takei, C.; Nakayama, T.; Ogata, A.; Yabuuchi, N. *Electrochem. Commun.* **2010**, *12*, 355-358.
- (43) Massarotti, V.; Bini, M.; Capsoni, D.; Altomare, A.; Moliterni, G. G. *J. Appl. Crystallogr.* **1997**, *30*, 123-127.
- (44) Robertson, A. D.; Bruce, P. G. *Chem. Mater.* **2003**, *15*, 1984-1992.
- (45) Tarascon, J. M.; Armand, M. *Nature* **2001**, *414*, 359-367.
- (46) Rougier, A.; Saadoune, I.; Gravereau, P.; Willmann, P.; Delmas, C. *Solid State Ionics* **1996**, *90*, 83-90.
- (47) Armstrong, A. R.; Gitzendanner, R.; Robertson, A. D.; Bruce, P. G. *Chem. Commun.* **1998**, 1833-1834.
- (48) Rossen, E.; Jones, C. D. W.; Dahn, J. R. *Solid State Ionics* **1992**, *57*, 311-318.

- (49) Spahr, M. E.; Novak, P.; Schnyder, B.; Haas, O.; Nesper, R. *J. Electrochem. Soc.* **1998**, *145*, 1113-1121.
- (50) Liu, Z.; Yu, A.; Lee, J. Y. *J. Power Sources* **1999**, *81-82*, 416-419.
- (51) Lu, Z.; MacNeil, D. D.; Dahn, J. R. *Electrochem. Solid-State Lett.* **2001**, *4*, A200-A203.
- (52) Lu, Z.; Beaulieu, L. Y.; Donaberger, R. A.; Thomas, C. L.; Dahn, J. R. *J. Electrochem. Soc.* **2002**, *149*, A778-A791.
- (53) Lu, Z.; Dahn, J. R. *J. Electrochem. Soc.* **2002**, *149*, A815-A822.
- (54) Shin, S. S.; Sun, Y. K.; Amine, K. *J. Power Sources* **2002**, *112*, 634-638.
- (55) Robertson, A. D.; Bruce, P. G. *Chem. Commun.* **2002**, 2790-2791.
- (56) Kim, J. H.; Yoon, C. S.; Sun, Y. K. *J. Electrochem. Soc.* **2003**, *150*, A538-A542.
- (57) Park, Y. J.; Kim, M. G.; Hong, Y.; Wu, X.; Ryu, K. S.; Chang, S. H. *Solid State Commun.* **2003**, *127*, 509-514.
- (58) Kim, J. H.; Park, C. W.; Sun, Y. K. *Solid State Ionics* **2003**, *164*, 43-49.
- (59) Park, Y. J.; Hong, Y.; Wu, X.; Kim, M. G.; Ryu, K. S.; Chang, S. H. *J. Electrochem. Soc.* **2004**, *151*, A720-A727.
- (60) Johnson, C. S.; Kim, J. S.; Lefief, C.; Li, N.; Vaughey, J. T.; Thackeray, M. M. *Electrochem. Commun.* **2004**, *6*, 1085-1091.
- (61) Armstrong, A. R.; Holzapfel, M.; Novak, P.; Johnson, C. S.; Kang, S. H.; Thackeray, M. M.; Bruce, P. G. *J. Am. Chem. Soc.* **2006**, *128*, 8694-8698.
- (62) Bareño, J.; Lei, C. H.; Wen, J. G.; Kang, S. H.; Petrov, I.; Abraham, D. P. *Adv. Mater.* **2010**, *22*, 1122-1127.

- (63) Lei, C. H.; Wen, J. G.; Sardela, M.; Bareño, J.; Petrov, I.; Kang, S. H.; Abraham, D. *P. J. Mat. Sci.* **2009**, *44*, 5579-5587.
- (64) Lei, C. H.; Bareño, J.; Wen, J. G.; Petrov, I.; Kang, S. H.; Abraham, D. *P. J. Power Sources* **2008**, *178*, 422-433.
- (65) Jiang, J.; Eberman, K. W.; Krause, L. J.; Dahn, J. R. *J. Electrochem. Soc.* **2005**, *152*, A1879-A1889.
- (66) Lim, J.; Bang, H.; Lee, K.; Amine, K.; Sun, Y. *J. Power Sources* **2009**, *189*, 571-575.
- (67) Belharouak, I.; Sun, Y. K.; Liu, J.; Amine, K. *J. Power Sources* **2003**, *123*, 247-252.
- (68) Park, S. H.; Kang, S. H.; Belharouak, I.; Sun, Y. K.; Amine, K. *J. Power Sources* **2008**, *177*, 177-183.
- (69) Kang, Y. J.; Kim, J. H.; Lee, S. W.; Sun, Y. K. *Electrochim. Acta* **2005**, *50*, 4784-4791.
- (70) Wu, Y.; Manthiram, A. *Electrochem. Solid-State Lett.* **2006**, *9*, A221-A224.
- (71) Myung, S.; Izumi, K.; Komaba, S.; Yashiro, H.; Bang, H. J.; Sun, Y.; Kumagai, N. *J. Phys. Chem. C* **2007**, *111*, 4061-4067.
- (72) Wu, Y.; Murugan, A. V.; Manthiram, A. *J. Electrochem. Soc.* **2008**, *155*, A635-A641.
- (73) Wang, Q. Y.; Liu, J.; Murugan, A. V.; Manthiram, A. *J. Mater. Chem.* **2009**, *19*, 4965-4972.
- (74) Deng, H.; Belharouak, I.; Cook, R. E.; Wu, H.; Sun, Y.; Amine, K. *J. Electrochem. Soc.* **2010**, *157*, A447-A452.
- (75) Liu, J.; Manthiram, A. *J. Mater. Chem.* **2010**, *20*, 3961-3967.

- (76) Wu, Y.; Manthiram, A. *J. Power Sources* **2008**, *183*, 749-754.
- (77) Liu, J.; Reeja Jayan, B.; Manthiram, A. *J. Phys. Chem. C* **2010**, *114*, 9528-9533.
- (78) Liu, J.; Wang, Q.; Reeja-Jayan, B.; Manthiram, A. *Electrochem. Commun.* **2010**, *12*, 750-753.
- (79) Ito, A.; Li, D.; Ohsawa, Y.; Sato, Y. *J. Power Sources* **2008**, *183*, 344-346.
- (80) Ito, A.; Li, D.; Sato, Y.; Arao, M.; Watanabe, M.; Hatano, M.; Horie, H.; Ohsawa, Y. *J. Power Sources* **2010**, *195*, 567-573.
- (81) Shin, D. Y. U.S. Patent 5,587,139, **1996**.
- (82) Makimoto, K.; Sekimoto, M.; Fujikake, S.; Ishii, M. European Patent 0649818 A1, **1994**.
- (83) Konstantinov, K.; Zhong, S.; Wang, C.; Liu, H.; Dou, S. Australian Patent 2002100001 A4, **2002**.
- (84) Shin, D. Y. U.S. Patent 5,498,403, **1996**.
- (85) Ikoma, M.; Akutsu, N.; Enokido, M.; Yoshii, F.; Kaiya, H.; Tsuda, S. U.S. Patent 5,700,596, **1997**.
- (86) Aladjov, B. U.S. Patent 5,788,943, **1998**.
- (87) Wakao, S. U.S. Patent 5,861,131, **1999**.
- (88) Komatsu, K.; Makizoe, S.; Kamada, T.; Ochi, Y.; Okito, T. U.S. Patent 6,132,639, **2000**.
- (89) Cho, J. *Chem. Mater.* **2000**, *12*, 3089-3094.
- (90) Cho, J.; Park, B. *J. Power Sources* **2001**, *92*, 35-39.
- (91) Ito, M.; Usui, T.; Shimakawa, M.; Iida, T. U.S. Patent Application 2002/0063663 A1, **2002**.

- (92) Ying, J.; Wan, C.; Jiang, C.; Li, Y. *J. Power Sources* **2001**, *99*, 78-84.
- (93) Ohzuku, T.; Yoshizawa, H.; Nagayama, M. U.S. Patent Application 2003/0054250 A1, **2003**.
- (94) Lee, M. H.; Kang, Y. J.; Myung, S. T.; Sun, Y. K. *Electrochim. Acta* **2004**, *50*, 939-948.
- (95) He, P.; Wang, H.; Qi, L.; Osaka, T. *J. Power Sources* **2006**, *160*, 623-632.
- (96) Zhaorong, C.; Gongan, L.; Yujuan, Z.; Jianguo, C.; Yunchang, D. *J. Power Sources* **1998**, *74*, 252-254.
- (97) Junichi, I.; Yuri, K.; Tetsushi, M.; Toyoshi, I. U.S. Patent 6,040,007, **2000**.
- (98) Ovshinsky, S.; Aladjov, B.; Young, R.; Vankatesan, S.; Dhar, S. U.S. Patent 6,086,843, **2000**.
- (99) Cho, J.; Kim, G.; Park, Y.; Kim, S. U.S. Patent 6,773,852 B2, **2004**.
- (100) Sun, J.; Cheng, J.; Wang, C.; Ma, X.; Li, M.; Yuan, L. *Ing. Eng. Chem. Res.* **2006**, *45*, 2146-2149.
- (101) Guinier, A. In *X-Ray Diffraction in Crystals, Imperfect Crystals, and Amorphous Bodies*; Dover Publications, Inc.: New York, **1994**.
- (102) Jenkins, R.; Synder, R. L. In *Introduction to X-ray Powder Diffractometry*; John Wiley & Sons, Inc.: New York, **1996**.
- (103) Cullity, B. D.; Stock, S. R. In *Elements of X-Ray Diffraction*; Pentice Hall: New Jersey, **2001**.
- (104) Hunter, B. A. **1997**, Rietica for Windows, *vers. 1.7.7*.

- (105) Goldstein, J. I.; Newbury, D. E.; Echlin, P.; Joy, D. C.; Romig, A. D.; Lyman, C. E.; Fiori, C.; Lifshin, E. In *Scanning Electron Microscopy and X-Ray Microanalysis*; Plenum Press: New York, **1992**.
- (106) Brown, M. E., Ed.; In *Handbook of Thermal Analysis and Calorimetry: Principles and Practice*; Elsevier Science B. V.: Amsterdam, **2001**.
- (107) Calvet, E.; Pratt, H. In *Recent Progress in Microcalorimetry*; The Macmillan Company: New York, **1963**.
- (108) Barth, H. G., Ed.; In *Modern Methods of Particle Size Analysis*; John Wiley & Sons, Inc.: New York, **1984**; Vol. 73, pp 309.
- (109) Kaye, B. H., Ed.; In *Characterization of Powders and Aerosols*; Wiley-VCH: New York, **1999**.
- (110) Jiang, J.; Eberman, K. W.; Krause, L. J.; Dahn, J. R. *J. Electrochem. Soc.* **2005**, *152*, A1874-A1878.
- (111) Jiang, J.; Dahn, J. R. *Electrochim. Acta* **2005**, *50*, 4778-4783.
- (112) Lu, Z.; Chen, Z.; Dahn, J. R. *Chem. Mater.* **2003**, *15*, 3214-3220.
- (113) MacNeil, D. D.; Lu, Z.; Dahn, J. R. *J. Electrochem. Soc.* **2002**, *149*, A1332-A1336.
- (114) Barkhouse, D. A. R.; Dahn, J. R. *J. Electrochem. Soc.* **2005**, *152*, A746-A751.
- (115) Jiang, J.; Dahn, J. R. *Electrochim. Acta* **2006**, *51*, 3413-3416.
- (116) Jouanneau, S.; Eberman, K. W.; Krause, L. J.; Dahn, J. R. *J. Electrochem. Soc.* **2003**, *150*, A1637-A1642.
- (117) Jouanneau, S.; Dahn, J. R. *J. Electrochem. Soc.* **2004**, *151*, A1749-A1754.
- (118) Jouanneau, S.; Bahmet, W.; Eberman, K. W.; Krause, L. J.; Dahn, J. R. *J. Electrochem. Soc.* **2004**, *151*, A1789-A1796.

- (119) Yabuuchi, N.; Ohzuku, T. *J. Power Sources* **2003**, *119-121*, 171-174.
- (120) Wyckoff, R., Ed.; In *Crystal Structures*; **1982**; Vol. 1.
- (121) Butel, M.; Gautier, L.; Delmas, C. *Solid State Ionics* **1999**, , 271-284.
- (122) Sillen, L. G., Ed.; In *Stability Constants of Metal-Ion Complexes*; London, **1964**.
- (123) Crank, J. In *The Mathematics of Diffusion*; Oxford University Press: London, **1975**.
- (124) Atlung, S.; West, K.; Jacobsen, T. *J. Electrochem. Soc.* **1979**, *126*, 1311-1321.
- (125) Carslaw, H. S.; Jaeger, J. C. In *Conduction of Heat in Solids*; Oxford University Press: London, **1959**.
- (126) Cho, J.; Jung, H.; Park, Y.; Kim, G.; Lim, H. S. *J. Electrochem. Soc.* **2000**, *147*, 15-20.
- (127) Jang, Y.; Neudecker, B. J.; Dudney, N. J. *Electrochem. Solid-State Lett.* **2001**, *4*, A74-A77.
- (128) Zhang, L.; Takada, K.; Ohta, N.; Wang, L.; Sasaki, T.; Watanabe, M. *Mater. Lett.* **2004**, *58*, 3197-3200.
- (129) Yu, L. H.; Cao, Y. L.; Yang, H. X.; Ai, X. P.; Ren, Y. Y. *Mater. Chem. Phys.* **2004**, *88*, 353-356.
- (130) Kang, S. H.; Amine, K. *J. Power Sources* **2003**, *124*, 533-537.
- (131) Zhang, L.; Takada, K.; Ohta, N.; Fukuda, K.; Osada, M.; Wang, L.; Sasaki, T.; Watanabe, M. *J. Electrochem. Soc.* **2005**, *152*, A171-A178.
- (132) Dahn, J. R.; McKinnon, W. R.; Murray, J. J.; Haering, R. R.; McMillan, R. S.; Rivers-Bowerman, A. H. *Phys. Rev. B* **1985**, *32*, 3316-3318.
- (133) McKinnon, W. R.; Dahn, J. R.; Murray, J. J.; Haering, R. R.; McMillan, R. S.; Rivers-Bowerman, A. H. *J. Phys. C. : Solid State Phys.* **1986**, *19*, 5135.

(134) Murray, J. J.; Sleigh, A. K.; McKinnon, W. R. *Electrochim. Acta* **1991**, *36*, 489-498.

(135) Smith, A. J.; Burns, J. C.; Trussler, S.; Dahn, J. R. *J. Electrochem. Soc.* **2010**, *157*, A196-A202.

Appendix

Copyright Information

The copyright information is outlined in this section, with the permissions granted for figure use in this thesis.

Copyright permission for Figure 1.4.

THE AMERICAN ASSOCIATION FOR THE ADVANCEMENT OF SCIENCE LICENSE TERMS AND CONDITIONS

Jun 21, 2010

This is a License Agreement between Andrew TJ van Bommel ("You") and The American Association for the Advancement of Science ("The American Association for the Advancement of Science") provided by Copyright Clearance Center ("CCC"). The license consists of your order details, the terms and conditions provided by The American Association for the Advancement of Science, and the payment terms and conditions.

All payments must be made in full to CCC. For payment instructions, please see information listed at the bottom of this form.

License Number	2453690236229
License date	Jun 21, 2010
Licensed content publisher	The American Association for the Advancement of Science
Licensed content publication	Science
Licensed content title	Electrical Energy Storage and Intercalation Chemistry
Licensed content author	M. S. WHITTINGHAM
Licensed content date	Jun 11, 1976
Type of Use	Thesis / Dissertation
Requestor type	Other Individual
Format	Print and electronic
Portion	Figure
Number of figures/tables	1
Order reference number	
Title of your thesis / dissertation	Lithium-rich transition metal oxides for positive electrode materials in lithium-ion batteries
Expected completion date	Aug 2010
Estimated size(pages)	150
Total	0.00 USD
Terms and Conditions	

American Association for the Advancement of Science TERMS AND CONDITIONS

Regarding your request, we are pleased to grant you non-exclusive, non-transferable permission, to republish the AAAS material identified above in your work identified above, subject to the terms and conditions herein. We must be contacted for permission for any uses other than those specifically identified in your request above.

The following credit line must be printed along with the AAAS material: "From [Full Reference Citation]. Reprinted with permission from AAAS."

All required credit lines and notices must be visible any time a user accesses any part of the AAAS material and must appear on any printed copies and authorized user might make.

This permission does not apply to figures / photos / artwork or any other content or materials included in your work that are credited to non-AAAS sources. If the requested material is sourced to or references non-AAAS sources, you must obtain authorization from that source as well before using that material. You agree to hold harmless and indemnify AAAS against any claims arising from your use of any content in your work that is credited to non-AAAS sources.

If the AAAS material covered by this permission was published in Science during the years 1974 - 1994, you must also obtain permission from the author, who may grant or withhold permission, and who may or may not charge a fee if permission is granted. See original article for author's address. This condition does not apply to news articles.

The AAAS material may not be modified or altered except that figures and tables may be modified with permission from the author. Author permission for any such changes must be secured prior to your use.

Whenever possible, we ask that electronic uses of the AAAS material permitted herein include a hyperlink to the original work on AAAS's website (hyperlink may be embedded in the reference citation).

AAAS material reproduced in your work identified herein must not account for more than 30% of the total contents of that work.

AAAS must publish the full paper prior to use of any text.

AAAS material must not imply any endorsement by the American Association for the Advancement of Science.

This permission is not valid for the use of the AAAS and/or Science logos.

AAAS makes no representations or warranties as to the accuracy of any information contained in the AAAS material covered by this permission, including any warranties of merchantability or fitness for a particular purpose.

If permission fees for this use are waived, please note that AAAS reserves the right to charge for reproduction of this material in the future.

Permission is not valid unless payment is received within sixty (60) days of the issuance of this permission. If payment is not received within this time period then all rights granted herein shall be revoked and this permission will be considered null and void.

In the event of breach of any of the terms and conditions herein or any of CCC's Billing and Payment terms and conditions, all rights granted herein shall be revoked and this permission will be considered null and void.

AAAS reserves the right to terminate this permission and all rights granted herein at its discretion, for any purpose, at any time. In the event that AAAS elects to terminate this permission, you will have no further right to publish, publicly perform, publicly display, distribute or otherwise use any matter in which the AAAS content had been included, and all fees paid hereunder shall be fully refunded to you. Notification of termination will be sent to

the contact information as supplied by you during the request process and termination shall be immediate upon sending the notice. Neither AAAS nor CCC shall be liable for any costs, expenses, or damages you may incur as a result of the termination of this permission, beyond the refund noted above.

This Permission may not be amended except by written document signed by both parties.

The terms above are applicable to all permissions granted for the use of AAAS material. Below you will find additional conditions that apply to your particular type of use.

FOR A THESIS OR DISSERTATION

If you are using figure(s)/table(s), permission is granted for use in print and electronic versions of your dissertation or thesis. A full text article may be used in print versions only of a dissertation or thesis.

Permission covers the distribution of your dissertation or thesis on demand by ProQuest / UMI, provided the AAAS material covered by this permission remains in situ.

If you are an Original Author on the AAAS article being reproduced, please refer to your License to Publish for rules on reproducing your paper in a dissertation or thesis.

FOR JOURNALS:

Permission covers both print and electronic versions of your journal article, however the AAAS material may not be used in any manner other than within the context of your article.

FOR BOOKS/TEXTBOOKS:

If this license is to reuse figures/tables, then permission is granted for non-exclusive world rights in all languages in both print and electronic formats (electronic formats are defined below).

If this license is to reuse a text excerpt or a full text article, then permission is granted for non-exclusive world rights in English only. You have the option of securing either print or electronic rights or both, but electronic rights are not automatically granted and do garner additional fees. Permission for translations of text excerpts or full text articles into other languages must be obtained separately.

Licenses granted for use of AAAS material in electronic format books/textbooks are valid only in cases where the electronic version is equivalent to or substitutes for the print version of the book/textbook. The AAAS material reproduced as permitted herein must remain in situ and must not be exploited separately (for example, if permission covers the use of a full text article, the article may not be offered for access or for purchase as a stand-alone unit), except in the case of permitted textbook companions as noted below.

You must include the following notice in any electronic versions, either adjacent to the reprinted AAAS material or in the terms and conditions for use of your electronic products: "Readers may view, browse, and/or download material for temporary copying purposes only, provided these uses are for noncommercial personal purposes. Except as provided by law, this material may not be further reproduced, distributed, transmitted, modified, adapted, performed, displayed, published, or sold in whole or in part, without prior written permission from the publisher."

If your book is an academic textbook, permission covers the following companions to your

textbook, provided such companions are distributed only in conjunction with your textbook at no additional cost to the user:

- Password-protected website
- Instructor's image CD/DVD and/or PowerPoint resource
- Student CD/DVD

All companions must contain instructions to users that the AAAS material may be used for non-commercial, classroom purposes only. Any other uses require the prior written permission from AAAS.

Rights also extend to copies/files of your Work (as described above) that you are required to provide for use by the visually and/or print disabled in compliance with state and federal laws.

This permission only covers a single edition of your work as identified in your request.

FOR NEWSLETTERS:

Permission covers print and/or electronic versions, provided the AAAS material reproduced as permitted herein remains in situ and is not exploited separately (for example, if permission covers the use of a full text article, the article may not be offered for access or for purchase as a stand-alone unit)

FOR ANNUAL REPORTS:

Permission covers print and electronic versions provided the AAAS material reproduced as permitted herein remains in situ and is not exploited separately (for example, if permission covers the use of a full text article, the article may not be offered for access or for purchase as a stand-alone unit)

FOR PROMOTIONAL/MARKETING USES:

Permission covers the use of AAAS material in promotional or marketing pieces such as information packets, media kits, product slide kits, brochures, or flyers limited to a single print run. The AAAS Material may not be used in any manner which implies endorsement or promotion by the American Association for the Advancement of Science (AAAS) or Science of any product or service. AAAS does not permit the reproduction of its name, logo or text on promotional literature.

If permission to use a full text article is permitted, The Science article covered by this permission must not be altered in any way. No additional printing may be set onto an article copy other than the copyright credit line required above. Any alterations must be approved in advance and in writing by AAAS. This includes, but is not limited to, the placement of sponsorship identifiers, trademarks, logos, rubber stamping or self-adhesive stickers onto the article copies.

Additionally, article copies must be a freestanding part of any information package (i.e. media kit) into which they are inserted. They may not be physically attached to anything, such as an advertising insert, or have anything attached to them, such as a sample product. Article copies must be easily removable from any kits or informational packages in which they are used. The only exception is that article copies may be inserted into three-ring binders.

FOR CORPORATE INTERNAL USE:

The AAAS material covered by this permission may not be altered in any way. No additional printing may be set onto an article copy other than the required credit line. Any alterations must be approved in advance and in writing by AAAS. This includes, but is not limited to the placement of sponsorship identifiers, trademarks, logos, rubber stamping or self-adhesive stickers onto article copies.

If you are making article copies, copies are restricted to the number indicated in your request and must be distributed only to internal employees for internal use.

If you are using AAAS Material in Presentation Slides, the required credit line must be visible on the slide where the AAAS material will be reprinted

If you are using AAAS Material on a CD, DVD, Flash Drive, or the World Wide Web, you must include the following notice in any electronic versions, either adjacent to the reprinted AAAS material or in the terms and conditions for use of your electronic products: "Readers may view, browse, and/or download material for temporary copying purposes only, provided these uses are for noncommercial personal purposes. Except as provided by law, this material may not be further reproduced, distributed, transmitted, modified, adapted, performed, displayed, published, or sold in whole or in part, without prior written permission from the publisher." Access to any such CD, DVD, Flash Drive or Web page must be restricted to your organization's employees only.

FOR CME COURSE and SCIENTIFIC SOCIETY MEETINGS:

Permission is restricted to the particular Course, Seminar, Conference, or Meeting indicated in your request. If this license covers a text excerpt or a Full Text Article, access to the reprinted AAAS material must be restricted to attendees of your event only (if you have been granted electronic rights for use of a full text article on your website, your website must be password protected, or access restricted so that only attendees can access the content on your site).

If you are using AAAS Material on a CD, DVD, Flash Drive, or the World Wide Web, you must include the following notice in any electronic versions, either adjacent to the reprinted AAAS material or in the terms and conditions for use of your electronic products: "Readers may view, browse, and/or download material for temporary copying purposes only, provided these uses are for noncommercial personal purposes. Except as provided by law, this material may not be further reproduced, distributed, transmitted, modified, adapted, performed, displayed, published, or sold in whole or in part, without prior written permission from the publisher."

FOR POLICY REPORTS:

These rights are granted only to non-profit government agencies. Permission covers print and electronic versions of a report, provided the required credit line appears in both versions and provided the AAAS material reproduced as permitted herein remains in situ and is not exploited separately.

FOR CLASSROOM PHOTOCOPIES:

Permission covers distribution in print copy format only. Article copies must be freestanding and not part of a course pack. They may not be physically attached to anything or have anything attached to them.

FOR COURSEPACKS OR COURSE WEBSITES:

These rights cover use of the AAAS material in one class at one institution. Permission is valid only for a single semester after which the AAAS material must be removed from the Electronic Course website, unless new permission is obtained for an additional semester. If the material is to be distributed online, access must be restricted to students and instructors enrolled in that particular course by some means of password or access control.

FOR WEBSITES:

You must include the following notice in any electronic versions, either adjacent to the reprinted AAAS material or in the terms and conditions for use of your electronic products: "Readers may view, browse, and/or download material for temporary copying purposes only, provided these uses are for noncommercial personal purposes. Except as provided by law, this material may not be further reproduced, distributed, transmitted, modified, adapted, performed, displayed, published, or sold in whole or in part, without prior written permission from the publisher."

Permissions for the use of Full Text articles on third party websites are granted on a case by case basis and only in cases where access to the AAAS Material is restricted by some means of password or access control. Alternately, an E-Print may be purchased through our reprints department (brocheleau@rockwaterinc.com).

REGARDING FULL TEXT ARTICLE USE ON THE WORLD WIDE WEB IF YOU ARE AN 'ORIGINAL AUTHOR' OF A SCIENCE PAPER

If you chose "Original Author" as the Requestor Type, you are warranting that you are one of authors listed on the License Agreement as a "Licensed content author" or that you are acting on that author's behalf to use the Licensed content in a new work that one of the authors listed on the License Agreement as a "Licensed content author" has written.

Original Authors may post the 'Accepted Version' of their full text article on their personal or on their University website and not on any other website. The 'Accepted Version' is the version of the paper accepted for publication by AAAS including changes resulting from peer review but prior to AAAS's copy editing and production (in other words not the AAAS published version).

FOR MOVIES / FILM / TELEVISION:

Permission is granted to use, record, film, photograph, and/or tape the AAAS material in connection with your program/film and in any medium your program/film may be shown or heard, including but not limited to broadcast and cable television, radio, print, world wide web, and videocassette.

The required credit line should run in the program/film's end credits.

FOR MUSEUM EXHIBITIONS:

Permission is granted to use the AAAS material as part of a single exhibition for the duration of that exhibit. Permission for use of the material in promotional materials for the exhibit must be cleared separately with AAAS (please contact us at permissions@aaas.org).

FOR TRANSLATIONS:

Translation rights apply only to the language identified in your request summary above.

The following disclaimer must appear with your translation, on the first page of the article, after the credit line: "This translation is not an official translation by AAAS staff, nor is it endorsed by AAAS as accurate. In crucial matters, please refer to the official English-language version originally published by AAAS."

FOR USE ON A COVER:

Permission is granted to use the AAAS material on the cover of a journal issue, newsletter issue, book, textbook, or annual report in print and electronic formats provided the AAAS material reproduced as permitted herein remains in situ and is not exploited separately

By using the AAAS Material identified in your request, you agree to abide by all the terms and conditions herein.

Questions about these terms can be directed to the AAAS Permissions department permissions@aaas.org.

v 2

Gratis licenses (referencing \$0 in the Total field) are free. Please retain this printable license for your reference. No payment is required.

If you would like to pay for this license now, please remit this license along with your payment made payable to "COPYRIGHT CLEARANCE CENTER" otherwise you will be invoiced within 48 hours of the license date. Payment should be in the form of a check or money order referencing your account number and this invoice number RLNK10802986.

Once you receive your invoice for this order, you may pay your invoice by credit card. Please follow instructions provided at that time.

**Make Payment To:
Copyright Clearance Center
Dept 001
P.O. Box 843006
Boston, MA 02284-3006**

If you find copyrighted material related to this license will not be used and wish to cancel, please contact us referencing this license number 2453690236229 and noting the reason for cancellation.

Questions? customercare@copyright.com or +1-877-622-5543 (toll free in the US) or +1-978-646-2777.

Copyright permission for Figures 1.6, 1.7, 1.9, 1.15, 1.17, and 1.18.

06/18/2010 09:52 FAX 9024945191

DALHOUSIE PHYSICS DEPT

001/002

Request for Permission to Reproduce or Re-Publish ECS Material

Please fax this form to: The Electrochemical Society (ECS), Attn: Permissions Requests, 1.609.737.2743.
You may also e-mail your request to: copyright@electrochem.org. Include all the information as required on this form. Please allow 3-7 days for your request to be processed.

I am preparing a (choose one): paper chapter book thesis

entitled: Lithium-Rich Oxides for Lithium-Ion Batteries

to be published by: Dalhousie University

in an upcoming publication entitled: N/A

I request permission to use the following material in the publication noted above, and request nonexclusive rights for all subsequent editions and in all foreign language translations for distribution throughout the world.

Description of material to be used—Indicate what material you wish to use (figures, tables, text, etc.) and give the full bibliographic reference for the source publication. You may attach a separate list, organized by ECS title.

See separate list.

Signature:



Date: June 18, 2010

Name: Andrew van Bommel

Address: Department of Physics, Dalhousie University
6310 Coburg Rd., Halifax, NS, B3H 3J5

Telephone: 902-494-2991

Fax: 902-494-5191

E-mail: avb@dal.ca

Permission is granted to reproduce the above-referenced material. Please acknowledge the author(s) and publication data of the original material, and include the words: "Reproduced by permission of The Electrochemical Society."

June 21, 2010
Date



Ann F. Goedkoop, Director of Publications

Figure requested:

Figure 1 on Pg 2972

From the paper:

Ohzuku, T.; Ueda, A.

Solid-State Redox Reactions of LiCoO_2 (R-3m) for 4 Volt Secondary Lithium Cells

Vol. 141 No. 11 (1994) 2972-2977.

Journal of the Electrochemical Society

Figure requested:

Figure 2 on Pg 1864

From the paper:

Ohzuku, T.; Ueda, A.; Nagayama, M.

Electrochemistry and Structural Chemistry of LiNiO_2 (R-3m) for 4 V ^{Secondary} Lithium Cells

Vol. 140 No. 7 (1993) 1862-1870.

Journal of the Electrochemical Society

Figure requested:

Figure 9 on Pg 2440

From the paper:

Kano, R.; Shirane, T.; Kawamoto, Y.; Takeda, Y.; Takano, M.; Ohashi, M. Yamaguchi, Y.

Synthesis, Structure, and Electrochemical Properties of a New Lithium Iron Oxide, LiFeO_2 , with a Corrugated Layer Structure.

Vol. 143 No. 8 (1996) 2435-2442.

Journal of the Electrochemical Society

Figures requested:

Figure 1 on Pg A192, Figure 3 on Pg A192, and Figure 5 on Pg A193.

Lu, Z.; MacNeil, D.D.; Dahn, J.R.

Layered Cathode Materials $\text{Li}[\text{Ni}_x\text{Li}_{(1/3-2x/3)}\text{Mn}_{(2/3-x/3)}]\text{O}_2$ for Lithium-Ion Batteries

Vol. 4 No. 11 (2001) A191-A194.

Electrochemical and Solid-State Letters

Copyright permission for Figure 1.8.

NATURE PUBLISHING GROUP LICENSE TERMS AND CONDITIONS

Jun 21, 2010

This is a License Agreement between Andrew TJ van Bommel ("You") and Nature Publishing Group ("Nature Publishing Group") provided by Copyright Clearance Center ("CCC"). The license consists of your order details, the terms and conditions provided by Nature Publishing Group, and the payment terms and conditions.

All payments must be made in full to CCC. For payment instructions, please see information listed at the bottom of this form.

License Number	2453700241069
License date	Jun 21, 2010
Licensed content publisher	Nature Publishing Group
Licensed content publication	Nature
Licensed content title	Synthesis of layered LiMnO ₂ as an electrode for rechargeable lithium batteries
Licensed content author	A. Robert Armstrong, Peter G. Bruce
Volume number	
Issue number	
Pages	
Year of publication	1996
Portion used	Figures / tables
Number of figures / tables	1
Requestor type	Student
Type of Use	Thesis / Dissertation
Billing Type	Invoice
Company	Andrew TJ van Bommel
Billing Address	103 Prince Albert Road
	Dartmouth, NS B2Y 1M2
	Canada
Customer reference info	
Total	0.00 USD
Terms and Conditions	

Terms and Conditions for Permissions

Nature Publishing Group hereby grants you a non-exclusive license to reproduce this material for this purpose, and for no other use, subject to the conditions below:

1. NPG warrants that it has, to the best of its knowledge, the rights to license reuse of this material. However, you should ensure that the material you are requesting is original to

Nature Publishing Group and does not carry the copyright of another entity (as credited in the published version). If the credit line on any part of the material you have requested indicates that it was reprinted or adapted by NPG with permission from another source, then you should also seek permission from that source to reuse the material.

2. Permission granted free of charge for material in print is also usually granted for any electronic version of that work, provided that the material is incidental to the work as a whole and that the electronic version is essentially equivalent to, or substitutes for, the print version. Where print permission has been granted for a fee, separate permission must be obtained for any additional, electronic re-use (unless, as in the case of a full paper, this has already been accounted for during your initial request in the calculation of a print run). NB: In all cases, web-based use of full-text articles must be authorized separately through the 'Use on a Web Site' option when requesting permission.
3. Permission granted for a first edition does not apply to second and subsequent editions and for editions in other languages (except for signatories to the STM Permissions Guidelines, or where the first edition permission was granted for free).
4. Nature Publishing Group's permission must be acknowledged next to the figure, table or abstract in print. In electronic form, this acknowledgement must be visible at the same time as the figure/table/abstract, and must be hyperlinked to the journal's homepage.
5. The credit line should read:

Reprinted by permission from Macmillan Publishers Ltd: [JOURNAL NAME]
(reference citation), copyright (year of publication)

For AOP papers, the credit line should read:

Reprinted by permission from Macmillan Publishers Ltd: [JOURNAL NAME],
advance online publication, day month year (doi: 10.1038/sj.[JOURNAL
ACRONYM].XXXXX)

6. Adaptations of single figures do not require NPG approval. However, the adaptation should be credited as follows:

Adapted by permission from Macmillan Publishers Ltd: [JOURNAL NAME]
(reference citation), copyright (year of publication)

7. Translations of 401 words up to a whole article require NPG approval. Please visit <http://www.macmillanmedicalcommunications.com> for more information. Translations of up to a 400 words do not require NPG approval. The translation should be credited as follows:

Translated by permission from Macmillan Publishers Ltd: [JOURNAL NAME]
(reference citation), copyright (year of publication).

We are certain that all parties will benefit from this agreement and wish you the best in the use of this material. Thank you.

v1.1

Gratis licenses (referencing \$0 in the Total field) are free. Please retain this printable license for your reference. No payment is required.

If you would like to pay for this license now, please remit this license along with your payment made payable to "COPYRIGHT CLEARANCE CENTER" otherwise you will be invoiced within 48 hours of the license date. Payment should be in the form of a check or money order referencing your account number and this invoice number RLNK10803031.

Once you receive your invoice for this order, you may pay your invoice by credit card. Please follow instructions provided at that time.

**Make Payment To:
Copyright Clearance Center
Dept 001
P.O. Box 843006
Boston, MA 02284-3006**

If you find copyrighted material related to this license will not be used and wish to cancel, please contact us referencing this license number 2453700241069 and noting the reason for cancellation.

Questions? customercare@copyright.com or +1-877-622-5543 (toll free in the US) or +1-978-646-2777.

Copyright permission for Figures 1.11 and 1.13.

AMERICAN CHEMICAL SOCIETY LICENSE TERMS AND CONDITIONS

Jun 22, 2010

This is a License Agreement between Andrew TJ van Bommel ("You") and American Chemical Society ("American Chemical Society") provided by Copyright Clearance Center ("CCC"). The license consists of your order details, the terms and conditions provided by American Chemical Society, and the payment terms and conditions.

All payments must be made in full to CCC. For payment instructions, please see information listed at the bottom of this form.

License Number	2454190204764
License Date	Jun 22, 2010
Licensed content publisher	American Chemical Society
Licensed content publication	Chemistry of Materials
Licensed content title	Mechanism of Electrochemical Activity in Li ₂ MnO ₃
Licensed content author	Alastair D. Robertson et al.
Licensed content date	May 1, 2003
Volume number	15
Issue number	10
Type of Use	Thesis/Dissertation
Requestor type ¹¹	Not specified
Format	Print and Electronic
Portion	Table/Figure/Micrograph
Number of Table/Figure/Micrographs	2
Author of this ACS article	No
Order reference number	
Title of the thesis / dissertation	Lithium-rich transition metal oxides for positive electrode materials in lithium-ion batteries
Expected completion date	Aug 2010
Estimated size(pages)	150
Billing Type	Invoice
Billing Address	103 Prince Albert Road Dartmouth, NS B2Y 1M2 Canada
Customer reference info	
Total	0.00 USD
Terms and Conditions	

Thesis/Dissertation

ACS / RIGHTS LINK TERMS & CONDITIONS THESIS/DISSERTATION

INTRODUCTION

The publisher for this copyrighted material is the American Chemical Society. By clicking "accept" in connection with completing this licensing transaction, you agree that the following terms and conditions apply to this transaction (along with the Billing and Payment

terms and conditions established by Copyright Clearance Center, Inc. ("CCC"), at the time that you opened your Rightslink account and that are available at any time at <<http://myaccount.copyright.com>>).

LIMITED LICENSE

Publisher hereby grants to you a non-exclusive license to use this material. Licenses are for one-time use only with a maximum distribution equal to the number that you identified in the licensing process; any form of republication must be completed within 60 days from the date hereof (although copies prepared before then may be distributed thereafter).

GEOGRAPHIC RIGHTS: SCOPE

Licenses may be exercised anywhere in the world.

RESERVATION OF RIGHTS

Publisher reserves all rights not specifically granted in the combination of (i) the license details provided by you and accepted in the course of this licensing transaction, (ii) these terms and conditions and (iii) CCC's Billing and Payment terms and conditions.

PORTION RIGHTS STATEMENT: DISCLAIMER

If you seek to reuse a portion from an ACS publication, it is your responsibility to examine each portion as published to determine whether a credit to, or copyright notice of, a third party owner was published adjacent to the item. You may only obtain permission via Rightslink to use material owned by ACS. Permission to use any material published in an ACS publication, journal, or article which is reprinted with permission of a third party must be obtained from the third party owner. ACS disclaims any responsibility for any use you make of items owned by third parties without their permission.

REVOCAION

The American Chemical Society reserves the right to revoke a license for any reason, including but not limited to advertising and promotional uses of ACS content, third party usage, and incorrect figure source attribution.

LICENSE CONTINGENT ON PAYMENT

While you may exercise the rights licensed immediately upon issuance of the license at the end of the licensing process for the transaction, provided that you have disclosed complete and accurate details of your proposed use, no license is finally effective unless and until full payment is received from you (by CCC) as provided in CCC's Billing and Payment terms and conditions. If full payment is not received on a timely basis, then any license preliminarily granted shall be deemed automatically revoked and shall be void as if never granted. Further, in the event that you breach any of these terms and conditions or any of CCC's Billing and Payment terms and conditions, the license is automatically revoked and shall be void as if never granted. Use of materials as described in a revoked license, as well as any use of the materials beyond the scope of an unrevoked license, may constitute copyright infringement and publisher reserves the right to take any and all action to protect its copyright in the materials.

COPYRIGHT NOTICE: DISCLAIMER

You must include the following copyright and permission notice in connection with any reproduction of the licensed material: "Reprinted ("Adapted" or "in part") with permission from REFERENCE CITATION. Copyright YEAR American Chemical Society."

WARRANTIES: NONE

Publisher makes no representations or warranties with respect to the licensed material.

INDEMNITY

You hereby indemnify and agree to hold harmless publisher and CCC, and their respective officers, directors, employees and agents, from and against any and all claims arising out of your use of the licensed material other than as specifically authorized pursuant to this license.

NO TRANSFER OF LICENSE

This license is personal to you or your publisher and may not be sublicensed, assigned, or transferred by you to any other person without publisher's written permission.

NO AMENDMENT EXCEPT IN WRITING

This license may not be amended except in a writing signed by both parties (or, in the case of publisher, by CCC on publisher's behalf).

OBJECTION TO CONTRARY TERMS

Publisher hereby objects to any terms contained in any purchase order, acknowledgment, check endorsement or other writing prepared by you, which terms are inconsistent with these terms and conditions or CCC's Billing and Payment terms and conditions. These terms and conditions, together with CCC's Billing and Payment terms and conditions (which are incorporated herein), comprise the entire agreement between you and publisher (and CCC) concerning this licensing transaction. In the event of any conflict between your obligations established by these terms and conditions and those established by CCC's Billing and Payment terms and conditions, these terms and conditions shall control.

JURISDICTION

This license transaction shall be governed by and construed in accordance with the laws of the District of Columbia. You hereby agree to submit to the jurisdiction of the courts located in the District of Columbia for purposes of resolving any disputes that may arise in connection with this licensing transaction.

THESES/DISSERTATION TERMS

Publishing implications of electronic publication of theses and dissertation material
Students and their mentors should be aware that posting of theses and dissertation material on the Web prior to submission of material from that thesis or dissertation to an ACS journal may affect publication in that journal. Whether Web posting is considered prior publication may be evaluated on a case-by-case basis by the journal's editor. If an ACS journal editor considers Web posting to be "prior publication", the paper will not be accepted for publication in that journal. If you intend to submit your unpublished paper to ACS for publication, check with the appropriate editor prior to posting your manuscript electronically.

If your paper has already been published by ACS and you want to include the text or portions of the text in your thesis/dissertation in **print or microfilm formats**, please print the ACS copyright credit line on the first page of your article: "Reproduced (or 'Reproduced in part') with permission from [FULL REFERENCE CITATION.] Copyright [YEAR] American Chemical Society." Include appropriate information.

Submission to a Dissertation Distributor: If you plan to submit your thesis to UMI or to another dissertation distributor, you should not include the unpublished ACS paper in your thesis if the thesis will be disseminated electronically, until ACS has published your paper. After publication of the paper by ACS, you may release the entire thesis (**not the individual**

ACS article by itself) for electronic dissemination through the distributor; ACS's copyright credit line should be printed on the first page of the ACS paper.

Use on an Intranet: The inclusion of your ACS unpublished or published manuscript is permitted in your thesis in print and microfilm formats. If ACS has published your paper you may include the manuscript in your thesis on an intranet that is not publicly available. Your ACS article cannot be posted electronically on a publicly available medium (i.e. one that is not password protected), such as but not limited to, electronic archives, Internet, library server, etc. The only material from your paper that can be posted on a public electronic medium is the article abstract, figures, and tables, and you may link to the article's DOI or post the article's author-directed URL link provided by ACS. This paragraph does not pertain to the dissertation distributor paragraph above.

Other conditions:

v1.1

Gratis licenses (referencing \$0 in the Total field) are free. Please retain this printable license for your reference. No payment is required.

If you would like to pay for this license now, please remit this license along with your payment made payable to "COPYRIGHT CLEARANCE CENTER" otherwise you will be invoiced within 48 hours of the license date. Payment should be in the form of a check or money order referencing your account number and this invoice number RLNK10803535.

Once you receive your invoice for this order, you may pay your invoice by credit card. Please follow instructions provided at that time.

**Make Payment To:
Copyright Clearance Center
Dept 001
P.O. Box 843006
Boston, MA 02284-3006**

If you find copyrighted material related to this license will not be used and wish to cancel, please contact us referencing this license number 2454190204764 and noting the reason for cancellation.

Questions? customercare@copyright.com or +1-877-622-5543 (toll free in the US) or +1-978-646-2777.
